Erosion-Corrosion of Carbon Steel Pipework on an Offshore Oil and Gas Facility

Richard James Barker

Submitted in accordance with the requirements for the degree of
Doctor of Philosophy

The University of Leeds
Institute of Engineering Thermofluids, Surfaces and Interfaces
School of Mechanical Engineering

December 2012

The candidate confirms that the work submitted is his own, except where work which has formed part of jointly-authored publications has been included. The contribution of the candidate and the other authors to this work has been explicitly indicated overleaf. The candidate confirms that appropriate credit has been given within the thesis where reference has been made to the work of others.

Acknowledgements

I would like to express my gratitude to Prof. Anne Neville for all the supervision and encouragement she has provided throughout the course of this work. Without her kind support, insight and passion for engineering, none of this would have been possible.

I am extremely grateful to my co-supervisor Dr. Simon Hu for his invaluable day to day advice in the lab. Thank you Simon!

I wish to extend my thanks to my industrial supervisor Sue Cushnaghan for her guidance and support. I would also like to express my sincere appreciation to Shell U.K. Limited for their technical guidance and financial sponsorship throughout the course of the PhD.

A big thanks goes to the technical staff at iETSI, in particular Graham Jakeman for fixing my rig whenever it broke! I am also grateful to the Faculty of Biological Sciences and to Dr. Iain Manfield for allowing me to use the department facilities.

The support I received from my colleagues was tremendous and I wish to thank all my friends in the School of Mechanical Engineering, both past and present. I would especially like to thank Mohd, Thibaut, Frederick, Violette, Dave, Graham, Mike, James, Wendy, Juan, Laura, Louise, Jen, Andy, Ike, Akbar, Jon, Hui, Benissa, Eleftheria, Chun and Nasser.

A big thanks goes to my Mum, Dad, Grandma, Granddad, Jordan and Rachel for believing in me and helping me cope with the stress of writing up!

Finally, I would like to dedicate this thesis to Grandad Ronnie, Grandma Joan and Uncle Gary. Even though you are no longer with us, I know you would be proud!

Abstract

Erosion-corrosion is a destructive process which can be encountered in the oil and gas industry when carbon steel pipelines transport sand particles in CO_2-containing salt water and hydrocarbons. The high degradation rates attributed to this mechanism can create increased challenges to project economy and operation where material integrity, accurate corrosion rate prediction and long term performance are key concerns.

This thesis presents a project with a firm foundation in practical engineering problems, supported by strong generic engineering science which holds wider applications.

The research focuses on understanding and inhibiting the degradation processes occurring on a North Sea offshore facility which had experienced a number of unexpected failures and reportedly high degradation rates between 2005 and 2010.

An empirical erosion-corrosion model is developed for the facility to provide accurate assessment of degradation rate. The prediction tool is subsequently compared to commercially available CO_2 corrosion models and validated using inspection data.

An assessment of the corrosion inhibition strategy on the facility and the screening of numerous corrosion inhibitors are conducted through gravimetric analysis and *in-situ* AC/DC electrochemical techniques in static and dynamic conditions. The research discovers a more efficient chemical for controlling degradation processes on the facility whilst highlighting the ability of electrochemical techniques to help understand inhibition mechanisms and behaviour. The methods presented for interpreting the results using generic science demonstrate wider applications in both inhibited and non-inhibited environments.

A review of inhibition in more extreme erosion-corrosion environments is performed to elucidate the effect of increased levels of erosion on the degradation process. The application of *in-situ* electrochemistry in dynamic conditions allowed the individual contribution of erosion and corrosion components of mass loss to be quantified, producing information on the different mechanisms by which inhibitors mitigate degradation effects.

Finally, the optimum inhibitor in this study is broken down into is constituent components for individual analysis. A test matrix is implemented to determine the

effect of synergy between the individual components. The adsorption process of the most influential component onto carbon steel is studied and determined through the implementation of electrochemistry and Fourier Transform Infrared Spectroscopy (FT-IR) before a colorimetric technique is tailored for residual analysis purposes.

Table of Contents

List of Figures

List of Tables

Chapter 1 -
Introduction and Research Project Background

1.1 Project Background

CO_2 corrosion and erosion-corrosion of oil and gas pipework remain major operational obstacles to successful hydrocarbon production. The oil and gas industry continues its dependency on the use of carbon and low alloy steels as pipework materials based on their vast availability and ability to fulfil many of the mechanical, structural, fabrication and cost requirements. Although these materials represent an economical choice, a key issue for their effective use is their poor general corrosion and/or erosion-corrosion performance [1]. Accordingly, the injection of chemicals into the process fluid proves a necessity to control the corrosion rate of these susceptible materials.

Poor degradation resistance of carbon steel has been found to manifest itself in the lines of an offshore North Sea oil rig despite the application of chemical inhibition. These lines are an integral part of the field, allowing a link between the processing units on the platform to the storage cells on the sea bed. The high degradation rates and failures on the lines prompted an investigation into the degradation mechanisms encountered on the facility and necessitated a search to establish a robust means of mitigation through chemical inhibition.

1.2 Objectives

The objectives of this research are outlined in Figure 1.1. The aims of the study can be divided into those which are project specific (i.e. relating to the operators of the facility in question) and those that revolve around a generic fundamental understanding of the underlying erosion-corrosion and inhibition mechanisms.

Project Specific Objectives

- Understand the environmental and physical flow conditions on the offshore facility and develop an empirical erosion-corrosion model to predict degradation rates for the asset.
- Review the current inhibition strategy on the facility and assess the potential for new chemicals to control the level of degradation to acceptable levels whilst developing an understanding of the inhibitor mechanisms adopted.
- Determine the effects of changes in the degradation regime on the performance and behaviour of the chemicals reviewed (namely, the transition from static to flow-induced corrosion to erosion-corrosion, as well as the effects of pre-corrosion on inhibitor performance).

Generic Scientific Objectives

- Assess the interactions between erosion and corrosion in extreme environments when the two degradation processes occur simultaneously for a particular set of conditions.
- Understand the influence of chemical inhibition on erosion-corrosion interactions and their adopted mechanisms through the implementation of electrochemistry and surface analysis techniques.
- Determine the synergistic effect between inhibitor components for a specific corrosion inhibitor blend.
- Explore the possibility of a residual analysis technique for one of the active inhibitor components.

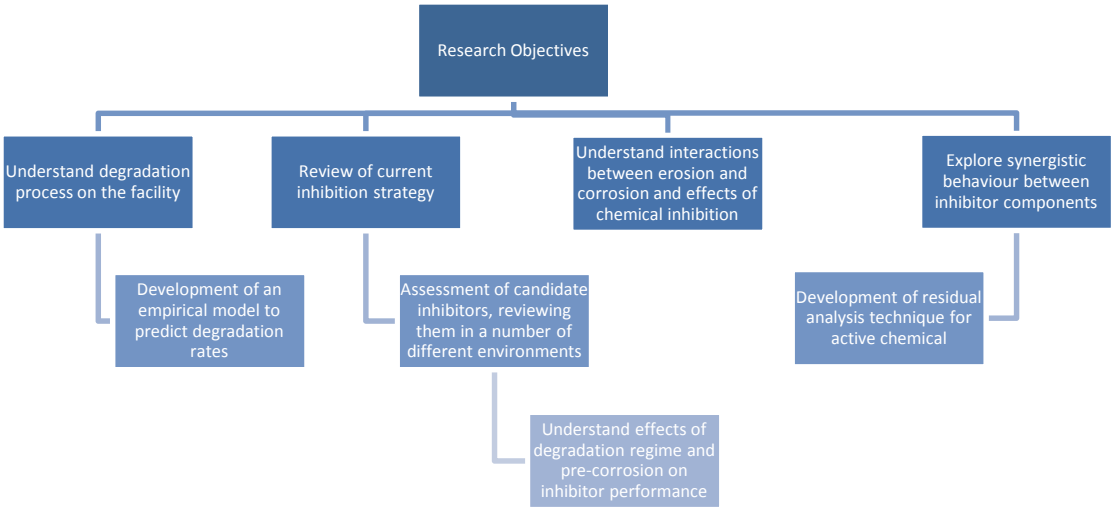

Figure 1.1: Research objectives for the thesis

1.3 Statement of Contribution to Literature

This thesis contributes to literature by providing a further understanding of erosion-corrosion processes in oil and gas production and demonstrates the ability of laboratory apparatus to accurately predict degradation rates on oil and gas facilities through the construction of an empirical erosion-corrosion model.

Furthermore, this research shows how chemical inhibition can mitigate the effects of erosion-corrosion by not only minimising the electrochemical corrosion reactions, but by also reducing the effects of mechanical damage attributed to the impingement of sand particles. The work presented discusses the number of mechanisms by which these chemicals mitigate corrosion and erosion processes, demonstrates how active components in inhibitor blends can be identified and

provides an example of how a residual analysis technique can be developed for one particular active ingredient.

1.4 Influence of Carbon Dioxide and Sand Production in the Oil and Gas Industry

Carbon dioxide (CO_2) remains an extremely influential constituent of oilfield production fluid, directly associated with the most prevalent form of corrosive degradation encountered in the oil and gas industry. CO_2 corrosion or 'sweet corrosion' of carbon and low alloy steels is not a recent problem and was first recorded in the United States oil and gas industry in the 1940s, with several investigations subsequently following [1]. The consequences of this particular corrosion mechanism have long been recognised and prompted extensive studies.

Although CO_2 occurs naturally, levels of the dissolved gas within produced fluids can increase through the implementation of such techniques as Enhanced Oil Recovery (EOR) by means of CO_2 injection [2].

In relation to the oil and gas industry, operational experience has indicated that sand production may be regarded as being inevitable in many reservoirs when their pressure falls below 1000 psi [3]. In many cases, sand only begins to appear late in the life of assets. Under these conditions, operators are reluctant to install sand exclusion systems because they can potentially lower production [3, 4]. Therefore, many operators tend to manage sand production by designing the facilities to mitigate its effects later in asset life. This can have implications in very low corrosivity environments, and is of particular concern in highly corrosive CO_2 systems as it creates what has become termed as an 'erosion-corrosion' environment.

Erosion-corrosion is receiving marked increased attention due to the current trends in operating with low concentrations of sand [5, 6]. Additionally, researchers have expressed interest in the synergistic effect which occurs between the two mechanisms; this means that essentially the degradation can be larger than the sum of the processes operating separately. However, in other cases, the formation of iron carbonate ($FeCO_3$) has been shown to reduce the effects of erosion [7-9]. These contrary observations mean models developed for CO_2 corrosion in the absence of erosion do not adequately describe many erosion-corrosion processes, presenting a significant problem for industry in terms of asset integrity management and accurate degradation rate prediction.

Erosion (and hence erosion-corrosion) problems will continue to increase in oil and gas production due to the increased tendency of operating with small levels of sand and the continual rise in water cut which inevitably puts pressure on engineers to increase total fluid production rates to maintain oil production. It is therefore imperative to develop an understanding of the interactions between erosion and corrosion and the various degradation mechanisms associated with erosion-corrosion in order to mitigate the effects through either chemical inhibition or material selection.

1.5 Analytical Assessment of Corrosion Failures in Industry

The wide-ranging environmental conditions present in the oil and gas industry provide a plethora of different degradation phenomena causing failures, with CO_2 corrosion and erosion-corrosion being two of the most pertinent types of attack. Other important categories of corrosion include H_2S corrosion [10-14], preferential weld corrosion [15-23] and pitting corrosion [24-26].

Corrosion-related failures constitute over 25% of failures experienced in the oil and gas industry. Almost half these failures are associated with sweet (CO_2) and sour (H_2S) producing fluids [27]. An analysis of failures during the 1980's is summarised in Table 1.1 and Table 1.2.

Table 1.1: Analysis of a selected number of failures in petroleum industries [27]

Type of Failure	Frequency (%)
Corrosion (all types)	33
Fatigue	18
Mechanical damage/overload	14
Brittle fracture	9
Fabrication defects (excluding weld defects)	9
Welding defects	7
Others	10

Table 1.2: Causes of corrosion-related failures in petroleum-related industries [27]

Type of Failure	Total Failure (%)
CO_2 related	28
H_2S related	18
Preferential weld	18
Pitting	12
Erosion-corrosion	9
Galvanic	6
Crevice	3
Impingement	3
Stress corrosion	3

Experience indicates that the majority of oilfield failures relating to corrosion occur as a result of lack of knowledge of its consequences, inadequate predictive capabilities and poor resistance of the material to the various forms of attack [27]. With the oil and gas industry so exposed to such a wide range of possible corrosion related failures, coupled with the variability in production conditions such as temperature, gas partial pressure, crude oil to brine ratio, brine composition etc., a stringent corrosion (or erosion-corrosion) management strategy is essential to not only reduce cost, but to prevent serious safety and environmental implications.

1.6 Financial Implications of Corrosion and its Relevance and Importance to Health, Safety and Environment

1.6.1 The Cost of Corrosion

The corrosion of metallic structures poses a significant threat to a company's economy [28, 29]. However, quantifying the cost of corrosion is by no means an easy task. Before exploring the associated costs, it can be considered that there are four main ways a company can incur expense as a result of corrosion:

- **Design Expenditure or Capital Expenditure (CAPEX) –** the investment incurred at the project stage associated with the additional capital outlay on controlling corrosion compared to the expenditure would it not exist at all. Nearly 8% of the total CAPEX for BP on their North Sea Projects was attributed to corrosion [27].

- **Operational Expenditure (OPEX) –** the day-to-day running costs associated with controlling corrosion, repairing equipment and maintenance. In 1988, 25-33% of maintenance costs of BP's oilfields in the U.K. Continental Shelf were corrosion-related [27].

- **Replacement Expenditure –** the expense incurred in replacing corroded plant equipment. In 1987, the cost of replacing the Forties field main oil line riser in the North Sea because of internal corrosion was $11.5 million [27].

- **Lost Revenue –** the decrease in revenue associated with lost/delayed production or contaminated products caused by corrosion related problems [27].

In terms of economic impact, two types of losses are attributed to corrosion [30]. Direct losses relate to replacement cost, including parts and labour. Protection costs such as the cost of alloying, corrosion inhibitors, coatings, cathodic protection and research & development are also included in this category [30], whereas indirect costs caused by failure tend to be significantly larger than direct costs. An exception to this rule is the case of offshore production, where the direct costs can be extremely high [30]. Indirect losses include lost revenue, lost product (from spills, fires, replacements etc.), lost efficiency, contamination of product, delays and lawsuits [30].

Figure 1.2: Examples of direct and indirect costs within the oil and gas industry

It is also common to divide these into expenditure which is 'avoidable' and 'unavoidable'. Applying the latest available technology, with greater corrosion

awareness make it possible to significantly reduce avoidable costs. By contrast, there are unavoidable costs because of the world in which we live [1, 27].

Experience also suggests that avoidable costs come as a result of lack of readily available information relating to the cost of corrosion failures, variable quality of information dissemination and a tendency to minimise initial capital outlay. Reduction of costs that are currently unavoidable or even potentially avoidable are dependent upon advances in technology, presenting challenges for research and development [27].

1.6.2 Battelle Columbus Laboratories and The National Institute of Science and Technology (1975 and 1995)

A landmark study was conducted by Battelle Columbus Laboratories and The National Institute of Science and Technology (NIST) in 1975 and updated in 1995 to highlight the cost of general corrosion for the United States. The original report, based on an elaborate model of more than 130 economic sectors, found that in 1975, the cost of metallic corrosion in the U.S. was $70 billion (4.2% of Gross National Product (GNP) in 1975). Furthermore, according to the study, $33 billion of this could have been avoided through application of existing technologies and best known practices [31, 32].

In 1995, the Battelle panel concluded it was necessary to update the original report, since there had been significant corrosion related changes in scientific knowledge and industrial practices over the past 20 years, which would have affected corrosion costs. This meant that some ‘unavoidable’ corrosion losses could be re-categorised as ‘avoidable’ and the some of the initial ‘avoidable’ outlay could be eliminated [31]. The updated study reflected that the total cost of metallic corrosion in 1995 was reduced by 14% (from what it would have been in 1975) to $296 billion. The avoidable category, which amounted to 40% in 1975, was estimated at 35% and accounted for $104 billion a year in 1995 [31].

1.6.3 The Federal Highway Administration and NACE International (2002)

The U.S. Federal Highway Administration (FHWA) released a break-through 2-year study in 2002 on the direct costs associated with metallic corrosion in nearly every U.S. sector [29]. Initiated by NACE International and mandated by the U.S. congress in 1999 as part of the Transportation Equity Act, the study provides information on the overall cost of corrosion by analysing 26 industrial sectors in

which corrosion is known to exist, and extrapolating the results for a nationwide estimate.

Results of the study showed that the total annual estimated direct cost of corrosion in the U.S. amounted to $276 billion (3.1% of Gross Domestic Product (GDP)) [29]. The U.S. economy was broken down into five major sectors. The categories were infrastructure, utilities, transportation, production and manufacturing, and government. When added together, the total direct losses attributed to corrosion for these sectors was $137.9 billion as shown in Figure 1.3.

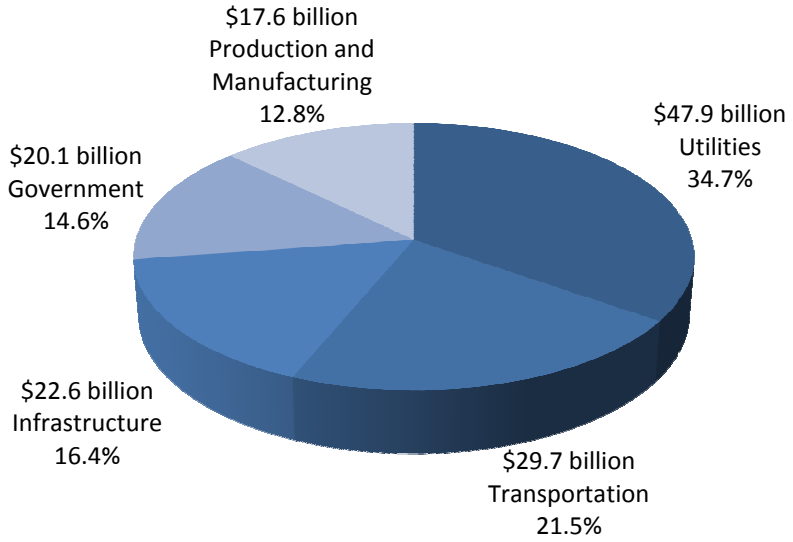

Figure 1.3: Percentage and dollar contribution to the total cost of corrosion for the five U.S. economic sectors [29]

As part of the review into production and manufacturing ($17.6 billion), the oil and gas exploration and production sector was reviewed. The total cost of corrosion in the U.S. oil and gas production industry was estimated to be $1.372 billion annually (Figure 1.4). This comprised of $589 million for surface piping and facilities, $463 million in downhole tubing expenses and $320 million in capital expenditures related to corrosion [29].

Today, corrosion costs in one year are generally still believed to be around 3% of GDP for developed countries [27]. Were this to be directly translated onto an oil and gas company's balance sheet as a percentage of turnover, it would represent an enormous expense in one year.

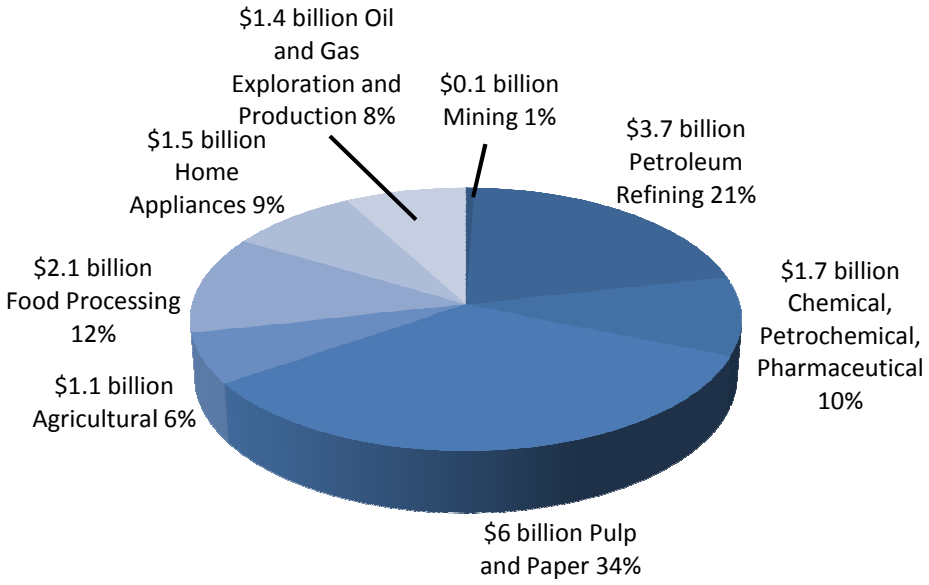

Figure 1.4: Annual cost of corrosion in the production and manufacturing category [29]

1.6.4 The Impact of Corrosion on Health, Safety and Environment

Although expense is a significant consequence of poor corrosion management, of equal, if not higher importance is that of Health, Safety and the Environment (HSE). Poorly managed corrosion or unchecked equipment can seriously affect asset integrity and serviceability, in turn increasing the possibility of liquid and gas leaks [27]. Many of these fluids have unacceptable environmental properties as a result of production chemicals added to aid processing and transportation (e.g. scale inhibitors, corrosion inhibitors and demulsifiers), which places demands on the importance of managing corrosion effectively and efficiently [27].

Since the 1980's, there has been an increasing awareness of the environmental implications associated with industrial discharge. Today, in the oil and gas exploration and production industry, the use of chemicals is essential to the successful operation of fields, thus increasing the risk if they were to enter the surrounding environment. As government bodies are becoming more informed of these risks, they continue to invoke tighter controls, together with a far more 'greener' public awareness [27]. Stronger legislation is emerging and the appropriateness of certain types of chemical inhibition is being questioned [27].

It is imperative that research is sustained in the field of corrosion mitigation. Researchers are presented with the challenge of reducing unavoidable costs through advancements in technology whilst searching for more environmentally

friendly products for industry to use. Researchers also adopt a significant role in ensuring industries remain up to date with the latest technological advancements to diminish the avoidable costs. Studies into corrosion mitigation techniques can help to reduce problems relating to HSE and make industries more aware of the consequences of poor corrosion management.

Research into the mechanisms that cause corrosion and determining how to treat forms of degradation effectively is essential to reduce both the impact on HSE and the expenditure of industries. With the growing environmental awareness and imposed international legislation, corrosion issues within the oil and gas industry are becoming increasingly more prevalent, highlighting the necessity for intensive research [27].

Chapter 2 - Fundamentals of Aqueous Corrosion

2.1 Definition of Corrosion

The deterioration of materials due to reactions with their environment is the currently accepted broad definition of ‘corrosion’ [33]. In terms of this thesis, a more appropriate definition would be ‘the chemical or electrochemical deterioration of a metal in an aggressive environment’ [34, 35].

In general, the mechanism of corrosion is the actual atomic, molecular, or ionic transport process that occurs at the material interface. These processes usually involve more than one definable step, and therefore interest is directed toward the slowest step which essentially controls the overall corrosion mechanism [33]. These processes cannot be directly observed on an atomic scale, making it necessary to infer possible mechanisms based on indirect measurements and observations such as weight loss, rate of corrosion product formation or changes in surface appearance. When electrochemical corrosion is occurring, mechanisms can be identified through the implementation of electrical potential and/or current measurements [33].

An important electrochemical mechanism involves the corrosion of metals in an aqueous solution, where atoms at the surface of the metal depart their lattice and enter the solution as metal ions. Subsequently, electrons migrate through the metal to a site where, to sustain the reaction, they are consumed by electrochemically active species in contact with the metal surface [33]. In more complicated cases, the metal ions move into the solution by forming complex ions, or combine with other species in the solution and precipitate compounds.

This chapter focuses on the theory associated with aqueous corrosion. Achieving a sound understanding of the principles behind this concept is essential in interpreting the electrochemical behaviour of metals subjected to CO_2 corrosion.

2.2 Thermodynamics of Aqueous Corrosion Reactions

2.2.1 Free Energy

Engineering metals are unstable and given the opportunity they will corrode. Metals try to lower their energy by spontaneously reacting to form solutions or compounds with greater thermodynamic stability [33, 36].

The driving force for metallic corrosion is the Gibbs free energy change (ΔG), which is the change in free energy of the metal and environment combination brought

about by corrosion [33]. If a reaction is spontaneous, then ΔG must be negative [33].

The term ΔG is only the difference between the Gibbs energies of the final and initial states of the reaction process, making it independent of the various intermediate stages [33]. Therefore, the corrosion reaction can be arbitrarily divided into either real of hypothetical steps to find out the true Gibbs energy change for the reaction.

2.2.2 The Corrosion Cell

Aqueous corrosion is electrochemical and the principles of electrochemistry, established by Michael Faraday in the early 19th century, are essential to develop an understanding of corrosion and its prevention.

Every electrochemical corrosion cell consists of four key components:

- The anode, which is the corroding metal [33]
- The cathode, which is a metal or another electronic conductor whose surface provides sites for the environment to react [33]
- The electrolyte (the aqueous environment), in contact with both the anode and cathode to provide a path for ionic conduction [33]
- The electrical connection between the anode and cathode to allow electrons to flow between them [33]

If any of these components are missing in the cell, electrochemical corrosion will not occur.

2.2.3 Anode and Cathode Reactions

Corrosion reactions can be separated into anode and cathode half-cell reactions to better understand the corrosion process. The anode reaction of a corroding metal 'M' is of the form:

$$\mathrm{M} \rightarrow \mathrm{M}^{n+} + \mathrm{ne}^{-} \qquad (2.1)$$

where n is the number of electrons (e^-) released by the metal. The electrons produced do not flow into the solution. They remain on the corroding metal and migrate through the electronic conductor to the cathode [33].

The cathodic reaction consumes electrons produced by the anode. This is achieved through reducible species in the electrolyte adsorbing onto the metal surface and removing the electrons [33].

The anodic and cathodic processes are capable of occurring on the same metal surface and the free energy differences for each reaction are measurable as electrical potentials and current flow [37].

Faraday derived an equation which relates potential difference and charge transported with the Gibbs free energy change of the corrosion process:

$$\Delta G = (-nF)E \tag{2.2}$$

where ΔG is the free energy change for the corrosion reaction in $kJmol^{-1}$, n is the number of electrons exchanged in the corrosion reaction, F is Faraday's constant (96,494 Coulombs/mole) and E is the potential difference at non-standard conditions in Volts.

By using the superscript (^{o}), the equation can be rewritten to represent standard conditions at a temperature of 273.15K and a pressure of one atmosphere:

$$\Delta G^o = (-nF)E^o \tag{2.3}$$

Values of E^o are available for all metals as well as many other half cell redox reactions and are listed in the *electrochemical series.* Examples of some standard half cell potentials are provided in Table 2.1. The most noble metals, such as gold, have the most positive reduction potentials. Metals at the negative end corrode readily and tend to be anodes.

Table 2.1: Standard electrode *reduction* potentials versus a Standard Hydrogen Electrode (SHE) [37]

Electrode	Standard Electrode Potential E^o (V) (SHE)
$Au^{3+} + 3e^- = Au$	+1.50
$½O_2 + 2H^+ + 2e^- = H_2O$	+1.228
$Fe^{3+} + e^- = Fe^{2+}$	+0.771
$2H^+ + 2e^- = H_2$	0.000 (by definition)
$Ni^{2+} + 2e^- = Ni$	-0.250
$Fe^{2+} + 2e^- = Fe$	-0.440
$Cr^{3+} + 3e^- = Cr$	-0.740
$Zn^{2+} + 2e^- = Zn$	-0.763

2.2.4 The Nernst Equation and Cell Potential

All corrosion reactions are dependent upon temperature, which is proportional to the free energy state of the species. Additionally, these half cell potentials change with respect to the concentration of ions present in reactions.

By using thermodynamic principles, the value of ΔG at any given temperature or concentration can be defined as:

$$\Delta G = \Delta G° - RT\ln\frac{[a_{products}]}{[a_{reactants}]} \tag{2.4}$$

where R is the ideal gas constant (8.314 $Jmol^{-1}K^{-1}$), T is the absolute temperature in Kelvin (K) and $[a_{products}]$ or $[a_{reactants}]$ are the concentrations or pressures of all the product or reactant species multiplied together in moles or atm.

By combining Equation (2.4) with Faraday's Law, the Nernst equation can be created, which allows for the correction of standard reduction potentials based on the environmental concentrations:

$$E = E° - \frac{RT}{nF}\ln\frac{[a_{products}]}{[a_{reactants}]} \tag{2.5}$$

Electrode potentials can be combined arithmetically to give cell potentials consisting of both anodic and cathodic reactions. Galvanic cells which operate spontaneously will produce a positive cell voltage if the difference is calculated as follows:

$$E_{cell} = E_{cathodic} - E_{anodic} \tag{2.6}$$

where E_{cell} is the cell potential in Volts, $E_{cathodic}$ is the reduction potential of the cathodic reaction and E_{anodic} is the reduction potential of the anodic reaction.

A spontaneous reaction, such as corrosion must result in a reduction in Gibbs energy, so ΔG must be negative. Therefore, E_{cell} must be positive for corrosion to occur.

2.3 Electrochemistry of Aqueous Corrosion and the Electrical Double Layer (EDL)

When a metal is immersed into an aqueous solution, local anodic and cathodic regions are generated instantaneously at the solid/liquid interface as a result of differences in free energy states between reacting sites.

As previously discussed, when a metal corrodes, ions depart their lattice, leaving behind their electrons. Water molecules then surround the metal ions as they escape the lattice, hydrating them. The hydrated ions are then free to diffuse away from the metal. The surface of the metal becomes negatively charged due to excess electrons and tends to attract some of the positively charged ions. This means that a certain percentage of ions remain near the surface, instead of diffusing into the bulk electrolyte. The water layer around the ions helps prevent them from making contact with the excess surface electrons and subsequently being reduced to metal atoms. Positive ions already in the electrolyte are also attracted to the negatively charged surface [38].

Consequently, the electrolyte layer adjacent to an electrode surface contains water molecules and ions from both the metal and bulk electrolyte, providing it with a distinctly different chemical composition than the bulk solution. This negatively charged surface and the adjacent electrolyte layer are collectively referred to as the electrical double layer (EDL) [38].

The physical separation of two oppositely charged planes created by the EDL causes it to produce capacitor-like behaviour, with the level of capacitance being determined by the metal and electrolyte composition. The metal also resists transferring excess electrons to the electrochemically active ions, which allows the EDL to also behave as a resistor [38]. A simple electrical circuit can be used to represent the properties of an EDL as shown in Figure 2.1. This is referred to as an equivalent electrical circuit model (EECM).

Figure 2.1: Equivalent electrical circuit model which represents the properties similar to the electrical double layer. C_{edl} is a capacitor and represents the capacitive reactance of the EDL. R_{ct} is the charge-transfer resistance which can be thought of as being similar to corrosion resistance and R_s represents the solution resistance

The charge separation in an EDL undoubtedly creates an electrical potential. The existence of a measurable electrical potential difference and the involvement of electron transfer in corrosion suggest there is a relationship between the EDL chemical composition, voltage and electric current [38].

2.3.1 The Relationship between EDL Chemistry, Voltage and Current

The potential at which the sum of the anodic and cathodic reaction rates are equal to zero is termed the free corrosion potential (E_{corr}) which is dependent on the metal and the nature of the solution. The corresponding current density is called the corrosion current density (i_{corr}) [2].

E_{corr} values change when EDL composition changes and applied voltages change EDL composition. The Nernst equation mathematically relates EDL behaviour to electrical potential:

$$E = E° - \frac{RT}{nF} \ln \frac{[a_{products}]}{[a_{reactants}]} \tag{2.7}$$

It is possible to replace the chemical activity components of the reaction ($[a_{products}]$ and $[a_{reactants}]$) with the activity coefficient (γ) multiplied by the concentrations of species represented by an element symbol in brackets (e.g. $[Fe^{2+}]$). Consequently, the equation can be rewritten as:

$$E = E° - \frac{RT}{nF} \ln \frac{\gamma_p [products]}{\gamma_r [reactants]} \tag{2.8}$$

Where γ_p and γ_r are the activity coefficients for products and reactants, respectively.

The measured potential is dependent upon the concentrations of both the metal ions and electrochemically active species in the EDL. The magnitude of a measured potential will therefore change with EDL chemical composition. Hence, E_{corr} will change if the bulk electrolyte composition is changed in such a way that it alters the EDL composition [38, 39].

The Nernst equation does not express a relationship for electrical current (an important variable to engineers as it has the potential to be converted into a rate of metal penetration by corrosion). Rather the Nernst equation expresses the tendency of a material to corrode, not the rate at which the material will deteriorate.

If the EDL has both a voltage and a resistance, Ohm's Law states that it must have a current. The following relationship, known as the Butler-Volmer equation, is experimentally observed between applied current density and potential for corroding electrodes in the absence of competing reduction-oxidation reactions [40]. The applicability of this relationship relies on the presence of a single charge-

transfer-controlled cathodic reaction and a single charge-transfer-controlled anodic reaction:

$$i_o = i_{corr}\left[e^{\left(\frac{(1-\alpha)nF(E-E_{corr})}{RT}\right)} - e^{\left(\frac{-\alpha nF(E-E_{corr})}{RT}\right)}\right] \quad (2.9)$$

where E_{corr} is the free corrosion potential in Volts, i_o is the external current in Amps/cm^2 flowing to or from the electrode because of an applied potential, i_{corr} is the corrosion current density in Amps/cm^2 that occurs when the electrode is at E_{corr}, E is the applied potential in Volts, α is a coefficient ranging from 0 to 1 and R, T, n and F have been defined previously.

Alternatively, the equation can be expressed in term of Tafel slopes (β_a and β_c) which are given by the gradients of the polarisation curves in the anodic and cathodic regions for a plot of E vs log(i) i.e. (dE/dlog(i)):

$$i_o = i_{corr}\left[e^{\left(\frac{2.303(E-E_{corr})}{\beta_a}\right)} - e^{\left(\frac{-2.303(E-E_{corr})}{\beta_c}\right)}\right] \quad (2.10)$$

This relationship provides the basis for the electrochemical polarisation technique for a corroding electrode at its free corrosion potential [40].

2.3.2 Electrochemical Measurement Techniques

2.3.2.1 Direct Current – Linear Polarisation Resistance

Many investigators have observed the linear relationship between applied voltage and current within a few millivolts of polarisation from E_{corr}. Stern and Geary [41] simplified the kinetic expression to provide an approximation to the charge-transfer-controlled reaction kinetics given by Equation (2.10) for the case of small overpotentials with respect to E_{corr}. Equation (2.10) can be linearised mathematically by taking its series expansion (e.g. $e^x = 1 + x + x^2/2! + x^3/3!...$) and by neglecting higher terms. This simplified relationship has the following form:

$$R_p = \left[\frac{\Delta E}{\Delta i}\right]_{(E-E_{corr})\to 0} = \frac{1}{2.303 i_{corr}}\left[\frac{\beta_a\beta_c}{\beta_a+\beta_c}\right] \quad (2.11)$$

Rearranging this equation gives:

$$i_{corr} = \frac{1}{2.303 R_p}\left[\frac{\beta_a\beta_c}{\beta_a+\beta_c}\right] = \frac{B}{R_p} \quad (2.12)$$

where R_p is the polarisation resistance (Ohm·cm^2) given by the gradient of the polarisation plot at small overpotentials (dE/di) for a plot of E vs I. Since charge-

transfer is assumed in Equation (2.12), R_p is equal to the charge-transfer resistance (R_{ct}). The B factor is dominated by the smaller of the two anodic and cathodic Tafel slopes (β_a and β_c) if unequal.

Knowledge of R_p, β_a and β_c enables direct determination of the corrosion rate at any instant in time [40]. The measured current is approximately linear within a potential range of ±5-20 mV of E_{corr}. Consequently, this method is commonly called the linear polarisation technique.

2.3.2.2 Direct Current – Tafel Plots

Although linear polarisation curves are useful for predicting the effects of long-term general corrosion without having to routinely replace electrodes, the corrosion rates are only estimates of actual rates when the Tafel slopes are unknown. It is also sometimes desirable to know more about corrosion than just the rate. Tafel plot measurements use a wider DC potential spectrum (around 200 to 500 mV) and provide more information than linear polarisation tests [38].

The resulting currents from the varied potentials are plotted on a logarithmic scale as shown in Figure 2.2, producing two branches. Polarisation plot structures can vary in that they can be activation controlled (controlled by the reaction rate) or diffusion controlled (dictated by the rate of diffusion of species to and from the surface).

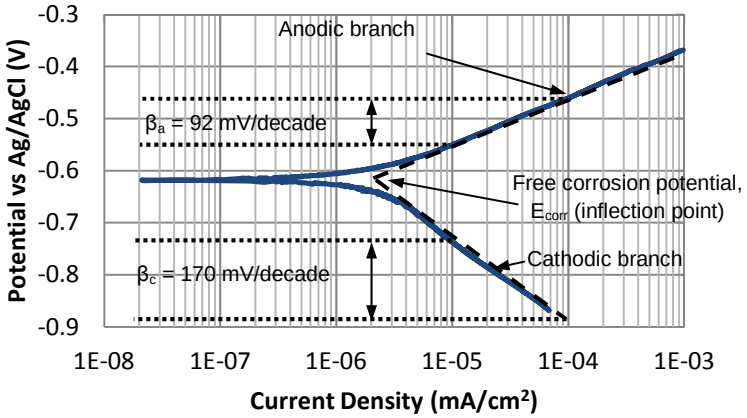

Figure 2.2: Tafel plot for activation controlled corrosion rates, indicating how to determine Tafel slopes

By measuring Tafel slopes, it is possible to determine the corrosion rate of a metal more accurately. Tafel slopes have units of mV/decade (the decade is associated with the current) and this can simply be found by determining the gradient of the anodic and cathodic slopes from the linear parts of the E-log(i) plot, as indicated in

Figure 2.2. When this information is used in conjunction with linear polarisation data and the Stern-Geary equation, a value of corrosion rate can be calculated [42]. Alternatively, corrosion current density, i_{corr}, can simply be read directly from a Tafel plot.

By determining the corrosion current, it is possible to use Faraday's Law to determine the corrosion rate of the material. Faraday stated that the mass of a substance altered at an electrode during electrolysis is directly proportional to the quantity of electricity transferred at that electrode. Faraday also stated that for a given quantity of electric charge, the mass loss of an elemental material altered at an electrode is directly proportional to the elements equivalent weight. This law can be summarised using the following equation:

$$m = \frac{QM}{nF} \tag{2.13}$$

where m is the mass of the substance liberated at an electrode in grams, Q is the total electric charge passed through the substance in Coulombs and M is the molar mass.

An alternative way of expressing this equation is as follows:

$$\text{Corrosion Rate } (\text{moles} \cdot m^{-2}s^{-1}) = \frac{i_{corr}}{nF} \tag{2.14}$$

Using this expression along with conversion factors, the corrosion rate can be expressed in mm/year:

$$\text{Corrosion Rate } (mm/y) = \frac{3.27 \times 10^3 (i_{corr})M}{n\rho} \tag{2.15}$$

where 3.27 x 10^3 is a combination of several conversion terms, i_{corr} is the corrosion current density in Amps/cm^2 and ρ is the metal density in g/cm^3.

It is worth noting that Tafel plots cannot be used to study or measure localised corrosion. Much larger anodic polarisations are required for these types of observation [38].

2.3.2.3 Alternating Current (AC) Methods

The AC impedance method is conducted over a range of low magnitude polarising voltages in a similar approach to linear polarisation. Typically, a small-amplitude sinusoidal potential perturbation is applied to the working electrode at a number of

discrete frequencies (ω). For each applied frequency, the resulting current waveform will exhibit a sinusoidal response that is out of phase with the applied potential. Each frequency produces values of resistance and capacitance and these quantities can provide information on the corrosion behaviour and rates, but also an insight into the corrosion rate-controlling mechanisms at the material surface within an electrolyte (especially in the presence of an adsorbed film or material coating).

AC voltages have variable magnitudes with both anodic and cathodic polarity in each polarisation cycle. The voltage amplitude can range typically between 5 and 20 mV centred around E_{corr}. Voltage frequencies for impedance measurements range from 100 kilohertz to a few millihertz.

As previously discussed, an EDL can have electrical properties similar to those for a simple electrical circuit composed of resistors and a capacitor (i.e. the equivalent circuit previously shown in Figure 2.1). A capacitor takes time to reach full charge which produces a shift between the voltage and current amplitude curves. This shift (or phase angle) and its magnitude are different for each polarising voltage frequency and tend to be plotted as positive quantities for EIS data despite their values being negative.

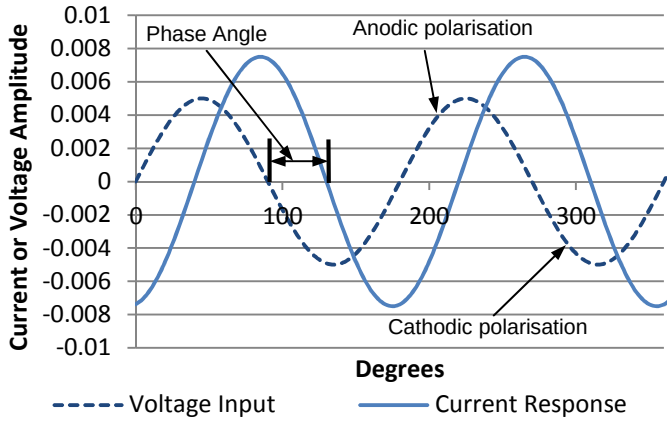

Figure 2.3: AC voltage and current response

AC (and DC) current and voltage are vectors and consequently so is impedance. An impedance vector can be resolved into components as shown in Figure 2.4, where the impedance is a solid arrow and the components are dashed arrows.

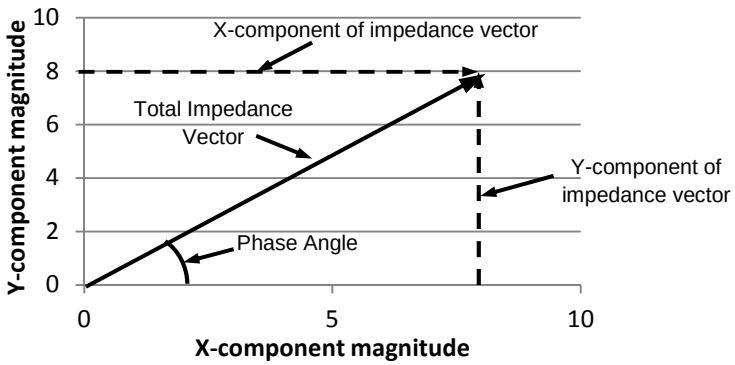

Figure 2.4: Vector nature of impedance

The total impedance magnitude of the electrochemical interface for the equivalent circuit in Figure 2.1 can be represented as:

$$Z(\omega) = Z' + jZ'' = R_s + \frac{R_{ct}}{1 + (\omega R_{ct} C_{edl})^2} + \frac{j(-\omega {R_{ct}}^2 C_{edl})}{1 + (\omega R_{ct} C_{edl})^2} \qquad (2.16)$$

where Z' is the real impedance magnitude (first and second term) and Z'' is the imaginary impedance magnitude (third term). R_{ct} is the charge-transfer resistance in Ohm•cm^2, ω is the multiple of 2π and the applied voltage frequency in Hz and C_{edl} is the capacitance of the EDL.

Equation (2.16) illustrates that each polarising voltage frequency produces a different magnitude for phase angle, total impedance and the component vectors.

Unlike DC polarisations, which cause ions to move in one direction for each DC magnitude and polarity, AC voltages cause ions to move back and forth between counter and test electrodes in response to the changes in polarity during an AC cycle. Therefore electron transfer also cycles to and from the test electrode and electrochemically active species during polarisation.

By polarising the sample using an AC voltage, the EDL is forced to try and change its chemical composition as fast as the polarising voltage frequency changes. The EDL takes time to change to a composition that corresponds to a given polarising voltage magnitude [43]. A range of frequencies exist where the time it takes for a full polarisation cycle to be completed is similar to the time taken for the EDL composition to change. It is reasonable to assume that the EDL time constant will be part of this frequency range and essentially determine its location. The response of the EDL to these frequency changes will be different to frequency ranges outside of this region.

It must be noted that the EDL is not the only source of time constants and a given electrode can possess much more than one. Inhibitor films or corrosion products such as iron carbonate ($FeCO_3$) can have capacitive reactance and resistance properties. Water and ions are capable of moving through porous films in response to AC polarisation and the movement of these species is hindered by the morphology of the film which produces a pore resistance. Figure 2.5 indicates the equivalent circuit for a corroding, coated metal which would produce two time constants. The circuit for metallic corrosion is nested inside the coating circuit. Nested circuits are used as opposed to series circuits to indicate that pores in the coating, or regions that are not protected by the coating can cause metallic corrosion as these are areas where the electrolyte has direct access to the metal surface.

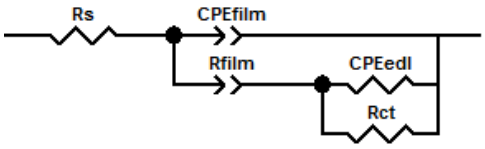

Figure 2.5: Equivalent circuit used to represent a corroding, coated metal. C_{edl} is the EDL capacitance. R_{ct} is the charge-transfer resistance, C_{film} is the capacitance of the film, R_{film} is the resistance of the film and R_s represents the solution resistance

Chapter 3 - Literature Review I: CO_2 Corrosion of Carbon Steel

Corrosion remains a key hindrance to successful operation in oil and gas production. Its occurrence affects both the economy and can have severe consequences with respect to the safety of people and integrity of facilities [44]. The need to control corrosion is centred on these two considerations. Machines, equipment and products may fail due to corrosion, potentially resulting in personal injury or harm to the environment. The implementation of safety measures not only reflect humanitarian concerns but also economics. With all economic decisions, there is a compromise between the benefits generated and the cost that would result if the level of corrosion protection was not maintained [33].

CO_2 corrosion is by far the most prevalent form of attack found in upstream oil and gas operations. The majority of failures attributed to CO_2 corrosion of carbon and low alloy steels come as a consequence of inadequate knowledge/predictive capability and poor resistance of carbon and low-alloy steel to this specific form of attack [44]. A thorough understanding of CO_2 corrosion, as well as its prediction and control are vital to ensure the sound design, operation and integrity of facilities. Intense research efforts have been made with the aim of understanding corrosion mechanisms caused by various corrosive species that promote or inhibit corrosion. Although some issues remain unclear, the majority of the steps associated with CO_2 corrosion are now understood.

This Chapter outlines the current understanding of CO_2 corrosion mechanisms for carbon and low-alloy steels in hydrocarbon production and highlights key parameters which influence CO_2 corrosion behaviour. Additionally, this section presents and reviews a number of popular mechanistic, semi-empirical and empirical models which can be used to help predict CO_2 corrosion rates.

3.1 CO_2 Corrosion Mechanism

CO_2 corrosion is a complex process in which a number of chemical reactions, electrochemical reactions and transport processes occur simultaneously [45], which can be divided into both anodic and cathodic reactions:

3.1.1 Cathodic Reactions

The presence of CO_2 in an aqueous solution promotes the hydrogen evolution reaction, increasing the rate of corrosion of iron [46].

CO_2 is soluble in water:

$$\mathrm{CO_{2(g)} \leftrightarrow CO_{2(aq)}} \tag{3.1}$$

When CO_2 dissolves in water, it associates to give carbonic acid (H_2CO_3), a weak acid compared to mineral acids, since it does not fully dissociate [2, 47]:

$$\mathrm{CO_{2(g)} + H_2O_{(l)} \leftrightarrow H_2CO_{3(aq)}} \tag{3.2}$$

H_2CO_3 is diprotic and partially dissociates in two steps to form bicarbonate and carbonate ions [46, 47]:

$$\mathrm{H_2CO_3 \leftrightarrow H^+ + HCO_3^-} \tag{3.3}$$

$$\mathrm{HCO_3^- \leftrightarrow H^+ + CO_3^{2-}} \tag{3.4}$$

This process is then followed by hydrogen evolution:

$$\mathrm{2H^+ + 2e^- \leftrightarrow H_2} \tag{3.5}$$

The homogenous dissociation reactions (3.3) and (3.4) proceed much faster than other simultaneous processes in the system. Both the CO_2 dissolution (3.1) and the CO_2 hydration (3.2) reaction have been known to be much slower [45].

The hydrogen evolution reaction (3.5) is believed to be one of the main cathodic reactions. This reaction is limited by the rate at which H^+ can be transported from the bulk solution to the steel surface [45].

Higher corrosion rates are often observed in CO_2 corrosion systems compared to strong acid solutions of the same pH. However, for practical CO_2 corrosion systems where pH > 4 the limiting flux for this reaction would be small due to the low concentration of H^+. This suggests that CO_2 influences H^+ reduction. The homogenous dissociation of H_2CO_3 provides an additional reservoir for H^+ ions, which can be adsorbed onto the steel surface and be reduced according to reaction (3.5) [45]. Any rapid consumption of H^+ can be readily replenished by the dissociation reactions. Therefore, at pH levels greater than 4, the presence of CO_2 creates a much more corrosive environment than that found in a solution of strong acid at the same pH [45].

In CO_2 systems at low pH (< 4), the dominant process is the cathodic reduction of H^+ because of the high concentration of H^+. At intermediate concentrations (4 < pH

< 6), which is the range of interest in this work, a new cathodic reaction becomes important in addition to the reduction of H^+ [46]. This is the direct reduction of H_2CO_3 [2, 46]:

$$2H_2CO_3 + 2e^- \rightarrow H_2 + 2HCO_3^- \quad (3.6)$$

The rate of this additional hydrogen evolution due to CO_2 is mainly controlled by the hydration step (3.2) and is strongly related to H_2CO_3 concentration which depends on the partial pressure of CO_2 [45].

This additional reaction is also believed to be another cause of H_2CO_3 being more corrosive than a completely dissociated acid at the same pH [48] as it allows hydrogen evolution to occur at a much higher rate. This reaction is just an alternative pathway for the same cathodic reaction – hydrogen evolution as addition of reactions (3.3) and (3.5) leads to reaction (3.6). The distinction is only the pathway.

This cathodic reaction has a limiting current (i_{lim}) that is controlled by the hydration of CO_2. This i_{lim} is not sensitive to flow and at currents above i_{lim} for H^+ or H_2CO_3 reduction, the dominant cathodic reaction changes to the direct reduction of water [49]:

$$2H_2O + 2e^- \rightarrow H_2 + 2OH^- \quad (3.7)$$

In comparison to the previous cathodic reactions described, this pathway is very slow and often can be neglected in CO_2 corrosion environments. However, under low partial pressures (P_{CO2} << 0.1 bar) and high pH (pH > 6), this reaction may become significant and contribute to the overall reaction process [45]. It is also believed that the direct reduction of bicarbonate ions can become important under these conditions:

$$2HCO_3^- + 2e^- \rightarrow H_2 + 2CO_3^{2-} \quad (3.8)$$

3.1.2 Anodic Reactions

The anodic dissolution of iron in acid solutions:

$$Fe \rightarrow Fe^{2+} + 2e^- \quad (3.9)$$

has been studied extensively by researchers, with several multi-step mechanisms being used to explain experimental results. The anodic dissolution of iron in aqueous CO_2 solutions was not the subject of detailed mechanistic studies until the

late 90's, but the majority of research articles appear to support the mechanism suggested by Bockris et al. [50], which represents the behaviour of the metal in strong acidic conditions. According to Bockris et al. [50] the iron is oxidised in the first two steps, with the final third step creating Fe^{2+}:

$$\mathrm{Fe} + \mathrm{H_2O} \leftrightarrow \mathrm{FeOH} + \mathrm{H^+} + \mathrm{e^-} \tag{3.10}$$

$$\mathrm{FeOH} \xrightarrow{\mathrm{RDS}} \mathrm{FeOH^+} + \mathrm{e^-} \tag{3.11}$$

$$\mathrm{FeOH^+} + \mathrm{H^+} \rightarrow \mathrm{Fe^{2+}} + \mathrm{H_2O} \tag{3.12}$$

The second step is considered as the rate determining step for the overall anodic reaction and the equations produce an anodic Tafel slope of 40 mV/decade at 25°C [51].

The de Waard and Milliams model [46] for aqueous corrosion assumes the same mechanism as Bockris et al. [50], producing values of Tafel slopes between 30-40 mV/decade in the absence and presence of CO_2.

In a far more recent study by Nešić et al. [49], it was reported that the anodic dissolution of iron is affected by the presence of CO_2, and the different kinetics of iron dissolution in CO_2 solutions for strong acids are explained. The disparity is believed to be associated with carbonic species acting as chemical ligands and catalysing the dissolution of iron. This effect was found to be independent of pH. As H_2CO_3 and CO_2 are the only carbonic species which are not dependent upon pH for their concentration, and CO_2 was vastly more concentrated, it was assumed that the ligand Fe_L denotes the complex Fe-CO_2 formed as an adsorbed species at the electrode surface which catalyses the dissolution of iron. Several multi-step models were used to explain a series of findings. The one most applicable to this project was that used to explain the experimental results for pH > 5:

$$\mathrm{Fe} + \mathrm{CO_2} \leftrightarrow \mathrm{Fe_L} \tag{3.13}$$

$$\mathrm{Fe_L} + \mathrm{H_2O} \leftrightarrow \mathrm{Fe_LOH_{ad}} + \mathrm{H^+} + \mathrm{e^-} \tag{3.14}$$

$$\mathrm{Fe_LOH_{ad}} \xrightarrow{\mathrm{RDS}} \mathrm{Fe_LOH_{ad}^+} + \mathrm{e^-} \tag{3.15}$$

$$\mathrm{Fe_LOH_{ad}^+} + \mathrm{H_2O} \leftrightarrow \mathrm{Fe_L(OH)_{2ad}} + \mathrm{H^+} \tag{3.16}$$

$$\mathrm{Fe_L(OH)_{2ad}} \leftrightarrow \mathrm{Fe_L(OH)_{2sol}} \tag{3.17}$$

$$Fe_L(OH)_{2sol} + 2H^+ \leftrightarrow Fe^{2+} + CO_2 + 2H_2O \quad (3.18)$$

The overall corrosion reaction is:

$$Fe + 2H_2CO_3 \rightarrow Fe^{2+} + 2HCO_3^- + H_2 \quad (3.19)$$

For pH < 4, it was postulated that Reaction (3.15) would increase and the desorption step (3.17) will become the new rate determining step.

3.2 Key Factors Influencing CO_2 Corrosion

The rate at which carbon steel corrodes in a CO_2 environment is affected by a number of different factors and the most common variables are reviewed within this section.

3.2.1 Water Chemistry

One of the most influential parameters affecting CO_2 corrosion is the solution chemistry. The solution composition can vary from simple, such as those found in gas condensate systems, to very complex, with numerous species in the solution such as formation water accompanied by the presence of crude oil [49]. The latter case can be further complicated by the species which partition into the water from the oil phase. Typical dissolved species include ions such as carbonic, bicarbonate, hydrogen, hydroxide, iron, chloride, sodium, potassium, calcium, magnesium, barium, strontium, acetate and sulphate as well as dissolved gases such as CO_2 and H_2S [49]. In some cases, the concentration of dissolved salts can be very high (> 10 wt.%) making the solution non-ideal [49]. Organic acids can also be present in the system [52] and acetic acid in particular can influence the corrosion rate [18, 49, 52-54].

A complete understanding of brine chemistry and the effect this can have on CO_2 corrosion rate is an important precondition. The influence of different brine chemistries will be discussed further in Chapter 6.

3.2.2 CO_2 Corrosion Products

CO_2 corrosion of carbon and low alloy steels is strongly dependant on the surface films formed during the corrosion process. The protectiveness, rate of precipitation and stability of the film dictate the corrosion rate and its nature [1, 54].

If the solubility of any of the salts within the near-surface solution is exceeded they can precipitate onto the surface of the steel [54]. The most notable of these are iron

carbonate ($FeCO_3$), and various types of scale rich in calcium ($CaCO_3$, $CaSO_4$) and barium ($BaSO_4$) [49].

The nucleation of iron carbonate can occur at the surface or inside the pores of the present film when Fe^{2+} ions react with carbonate (CO_3^{2-}) and bicarbonate (HCO_3^-) ions in the solution [45]:

$$Fe^{2+} + CO_3^- \rightarrow FeCO_{3(s)} \tag{3.20}$$

Therefore a high supersaturation of Fe^{2+} and CO_3^{2-}/HCO_3^- is necessary for the formation of protective films [54, 55].

Iron carbonate precipitation can inhibit the corrosion kinetics by either creating a diffusion barrier for species participating in the corrosion process or by covering a region of the steel surface [1, 45, 56, 57]. To achieve successful protection, the film must be adherent and cover the whole surface. Localised corrosion can occur if parts of the scale break down and cannot reform [54].

Iron carbonate growth and its protectiveness depend on the characteristic of the material (metal composition and microstructure) and the environment (temperature, CO_2 partial pressure, pH etc.). The rate of precipitation heavily influences the properties of the $FeCO_3$ film [49].

As the steel corrodes under the $FeCO_3$ layer, corrosion continuously undermines the scale. As voids are created, they are filled by continuous precipitation [49]. When precipitation exceeds the rate of corrosion, dense protective scales are created (sometimes as thin as 1 µm, but still protective). Alternatively, when the corrosion process challenges the newly formed scale such that the rate of dissolution is faster than the rate at which voids can be filled, a porous and unprotective film is formed. This film can have a thickness over 100 µm and still not offer protection [49].

The formation of iron carbonate films are governed by many factors, but two of the most influential aspects are the solution chemistry and operating temperature [49]. The supersaturation with respect to iron carbonate needs to be exceeded in order to obtain appreciable enough levels of precipitation [49]. At room temperature, precipitation is slow and even at high supersaturation an unprotective film containing voids and grain boundaries will be produced unless pH is very high. Above 60°C, film protectiveness increases with temperature. The rise in temperature reduces $FeCO_3$ solubility and increases precipitation rate, resulting in

the formation of a dense, protective scale, even at low supersaturation. In reality, high supersaturation cannot be sustained for long periods at high temperature as the accelerated precipitation process will tend to rapidly return the solution to thermodynamic equilibrium.

Recent developments in the study of CO_2 corrosion have indicated decisive influences of variations in the protectiveness of corrosion layers [26]. Crolet et al. [26] found that corrosion layers containing the same solid components can be extremely protective, very little so, or even corrosive [26].

Studies by Crolet and co-workers [26] on St52 grade carbon-manganese steels showed that corrosion layers are composed of the insoluble iron carbonate and/or an undissolved component from the steel, namely cementite (Fe_3C).

Crolet et al. [26] observed that iron carbonate could precipitate on both the steel and Fe_3C, enabling $FeCO_3$ to precipitate at a certain distance from the steel, as well as directly on the material. They found that the main difference between protective and unprotective corrosion layers is the presence of empty Fe_3C in contact with the steel. It was suggested that neither the thickness of the Fe_3C layer, nor the distance of the $FeCO_3$ layer from the steel had any effect on the un-protectiveness of the film. Similarly, for protective layers, the presence of Fe_3C seemed to be of no importance. A summary of the findings of Crolet et al. [26] are provided in Figure 3.1.

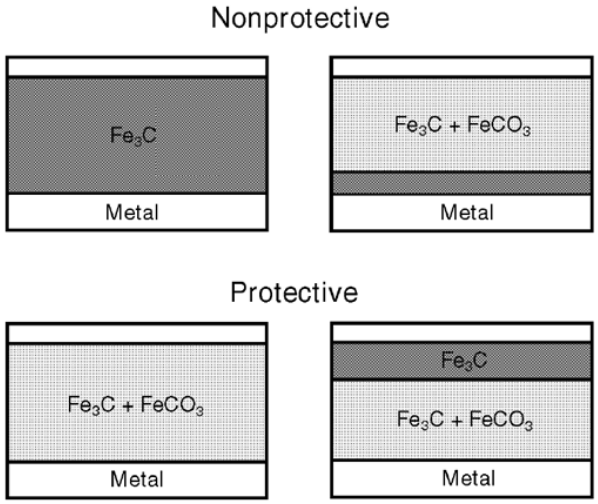

Figure 3.1: Different morphologies observed for protective and non-protective corrosion layers – from Crolet et al. [26]

3.2.3 pH

The pH has the most effect indirectly on corrosion rate through its relationship with the formation of $FeCO_3$ scales [58]. Studies have shown that increasing the pH of a solution from 4 to 5 reduces the solubility of Fe^{2+} by approximately a factor of 5. A further increase in pH from 5 to 6 reduces solubility 100 times [1]. Dugstad et al. [55] showed how CO_2 partial pressure and pH can influence the level at which $FeCO_3$ saturation was attained and these results are summarised in Figure 3.2.

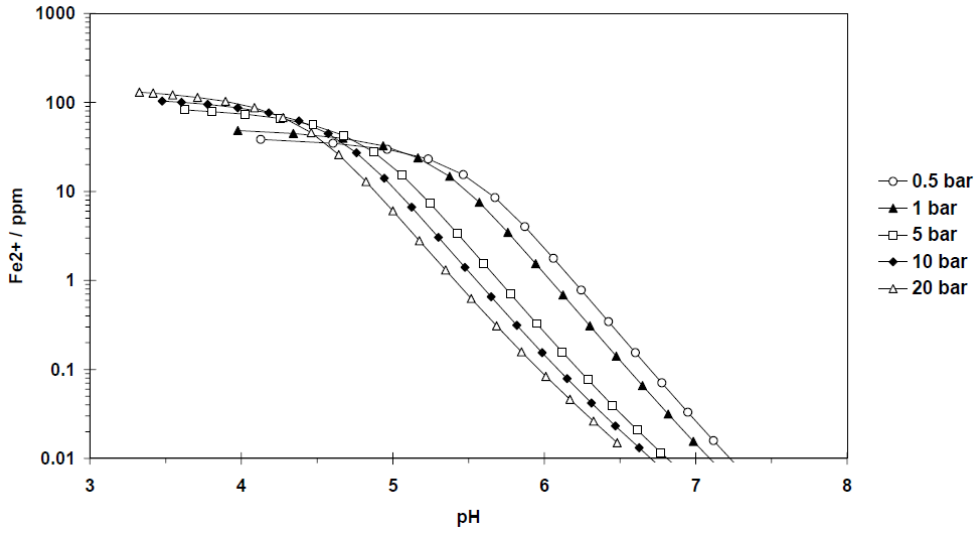

Figure 3.2: Quantity of Fe^{2+} needed to be produced by corrosion to reach $FeCO_3$ saturation plotted as a function of pH. The brine pH is the pH before corrosion has started – from Dugstad et al. [55]

A low solubility can correspond to higher super-saturation, which accelerates the precipitation and formation of $FeCO_3$ films. Therefore, for pH > 5, as is the case with most CO_2-saturated brines, the probability of film formation is increased, which can contribute to a lower corrosion rate [1, 49].

3.2.4 Partial Pressure

In the case of scale-free CO_2 corrosion, an increase of CO_2 partial pressure (P_{CO2}) tends to result in a rise in corrosion rate. It is generally considered that with increasing P_{CO2}, the concentration of H_2CO_3 increases, accelerating the cathodic reaction, and ultimately the corrosion rate [49]. However, when conditions are favourable for the formation of iron carbonate scales, increasing P_{CO2} can have a beneficial effect. At high pH, high P_{CO2} can accelerate precipitation and scale formation by increasing the bicarbonate and carbonate ion concentration [1].

De Waard et al. [58] stated the importance of acknowledging the fugacity of CO_2 as opposed to the partial pressure in high pressure systems as the non-ideality of the gas plays an increasing role.

3.2.5 Operating Temperature

Temperature accelerates all the processes (electrochemical, chemical, mass transport etc.) involved in corrosion. The rate of corrosion steadily increases with temperature at low pH when the precipitation of iron carbonate and other protective scales do not form [49]. The situation changes significantly when the conditions mean the solubility of iron carbonate (or other salts) is exceeded, which typically occurs at higher pH. In these conditions, increasing temperature accelerates the kinetics of precipitation and protective scale formation, decreasing the corrosion rate. Peaks in corrosion rate are usually seen between 60°C and 80°C depending upon the solution chemistry and flow behaviour and this is referred to as the 'scaling temperature' [58]. The precipitation of $FeCO_3$ in itself does not necessarily result in the formation of a protective film. At higher temperatures, the film becomes different in texture, more crystalline and generally more protective [59]. At lower temperatures (below 60°C), the corrosion product has a smudge-like texture and is easily removed by flowing fluid [58].

3.2.6 Wettability and Corrosion Inhibition by Crude Oil

CO_2 corrosion occurs as a result of water being present in the system which wets the steel surface. The intensity of the CO_2 attack increases with the time during which the water phase is in contact with the steel surface. Therefore the water content (or water cut) and the notion of water wetting is an important consideration when examining CO_2 corrosion [1].

It has been shown that emulsions can form in oil/water systems. If a water-in-oil emulsion is created and the water is held in the emulsion, then the water wetting of steel is significantly reduced, lowering the corrosion rate [60]. However, if an oil-in-water emulsion is fashioned, water wetting of the steel will occur. The transition between these two regimes is believed to occur at around 30% to 40% water [1, 60]. This change in regime of emulsified liquids can apparently become very obvious in terms of a large increase in corrosion rate but the water cut threshold depends primarily on the maturity of the hydrocarbon and the nature of its kerogen [1, 49, 60].

The presence of crude oils can modify the morphology, composition and compaction of the corrosion products for different oil/water ratios. Hydrocarbons have been shown to destabilise protective films, accelerating local corrosion [1, 61].

CO_2 corrosion rates seen in the field in the presence of crude oil tend to be lower than those in laboratory tests where oil is omitted or synthetic oil is used [49]. Crude oil has been shown to help reduce CO_2 corrosion through its interaction with the steel surface, as well as it reducing the surface wettability [1]. Corrosion inhibition is offered by certain components of the crude oil that reach the steel surface, either through direct contact, or partitioning into the water phase. Recent studies [62, 63] have related the degree of inhibition quantitatively to the chemical composition of the crude oil and specifically to the concentration of compounds such as saturates, aromatics, resins and asphaltenes.

3.2.7 Effect of Flow

The relationship between flow and CO_2 corrosion still remains a contentious area in the prediction process [49]. When conditions do not result in the formation of a protective scale, the main role of the turbulent flow is to enhance transport of species towards and away from the metal surface, leading to an increase in corrosion rate [49, 54]. When iron carbonate forms on the surface, or when an inhibitor film is present, the main effect of the flow is to interfere with the formation of films or partially remove them, leading to an increase in corrosion rate.

Flow accelerated corrosion effects are generally aggravated by flow disturbances such as valves, constrictions, expansions and bends [49]. These changes in flow behaviour can induce sporadic changes in the wall shear stresses, which can remove a protective scale or an inhibitor film [49].

The operating conditions in the oil and gas industry are such that two- or three-phase flow tends to be exhibited. Multiphase flow in CO_2 environments can produce a series of flow patterns, the most common being stratified, slug and annular flow [49]. Different flow patterns can affect the water wetting capability of the process fluid, significantly affecting corrosion [49].

Multiphase flow can lead to high fluctuating mass transfer and shear stress rates. It has been suggested that the Froude number (the ratio of inertia forces on a fluid element to its weight) can be an important ratio which can help characterise the effect of multiphase flow on CO_2 corrosion [64].

3.2.8 Metallurgical Parameters

The importance of chemical composition and microstructure on CO_2 corrosion of carbon steel has been widely recognised [65]. Regrettably, different aspects are still uncertain and some contradictory results can be found in literature [65]. This is believed to have emerged due to the complexity of the problem and the issues with describing the involved corrosion mechanisms.

Chemical composition and microstructure are not independent variables. The same microstructure can be created with different chemical compositions and vice versa [65]. The fact that authors tend to report the effect of one parameter without taking into account other variables can produce misleading conclusions about the behaviour witnessed. Additionally, tests conditions can vary widely, making the behaviour impossible to compare. The review for this section presents findings which are generally agreed upon in terms of the relationship between CO_2 corrosion rate and microstructure/composition.

3.2.8.1 Alloying Elements and Chemical Composition

It is widely acknowledged that the addition of chromium to low-alloy steels can offer improved corrosion resistance in CO_2 conditions through the formation of a stable chromium oxide film [1]. A study by Kermani in 2003 [66] presented the development of novel carbon and low alloy steels with superior CO_2 corrosion resistance. The process involved a systematic and extensive development programme focusing on metallurgical conditioning and micro-alloying additions. The philosophy behind the work involved lowering carbon content and adding carbide forming alloying elements to maximise the effect of chromium, vanadium and molybdenum whilst achieving desired properties through microalloying additions and mechanical heat treatments [66]. The intention was that the addition of stronger, carbide-forming elements would preferably combine with carbon in a given steel leaving chromium, vanadium and molybdenum uncombined in the ferrite phase to provide improved corrosion protection [66]. The presence of silicon and nickel was used to bring back the strength of the material caused by the lack of carbon. The work concluded that vanadium-microalloyed steel containing Cr, Si, Mo, V, and Cu is the most promising elemental structure to produce the required corrosion resistance and material properties. However, the weldability of this structure was an issue for this particular composition and its use was therefore only readily suitable for downhole applications [66].

The data indicated that the presence of free chromium and vanadium is generally a good indication of CO_2 corrosion resistance of the material [66].

3.2.8.2 Microstructure

The driving force for corrosion in an aqueous environment is the difference in potential of areas where heterogeneities exist in the material. These heterogeneities can be as small as atoms to several hundred microns in scale, and can arise from factors such as defects in the crystal structure, chemically different phases, segregation on elements/phases and non-metallic inclusions [67]. It has been reported that these heterogeneities are predominantly controlled by the elemental composition, thermal and mechanical history of the material [67].

Different phases in a steel microstructure provide sites for anodic and cathodic reactions [67, 68]. Therefore, it is sensible to suggest that the shape, size and distribution of these phases affect the corrosion rate.

3.3 An Assessment and Comparison of CO_2 Corrosion Prediction Models

Many different mathematical models exist for CO_2 corrosion which are used by engineers in the oil and gas industry. Some are described in open literature while others are proprietary models. The latter tend to be variations of publicly available models or empirical correlations based on practical experience [49]. The models available offer a large scatter in the prediction due to the different theories, assumptions and modelling strategies.

With so many models existing, only a handful can be reviewed here. However, the models considered have been chosen either because they are well-known and widely used by industry or reflect the variety of different categories of models available.

It is possible to classify CO_2 corrosion models into three broad categories based on how firmly they are grounded to theory. These categories are as follows:

- **Mechanistic models:** possessing a strong theoretical background and describe the mechanism of the underlying reactions. Models include the SPPS:CO_2 model by Dayalan et al. [69] at Tulsa University, the Kjeller Sweet Corrosion (KSC) model developed at the Institute for Energy (IFE) by Nešić et al. [70-72], as well as the MULTICORP [73] and FREECORP [45] models also created by Nešić whilst at Ohio University.

- **Semi-Empirical models:** partly based on firm theoretical hypotheses which tend to be calibrated with large and reliable experimental data, generally allowing for good interpolation prediction, however, extrapolation can lead to unreliable results. New knowledge can be introduced to these models with moderate effort using re-calibration or correction factors. Semi-empirical models include those developed by de Waard and Milliams [46, 58-60, 74], the BP Cassandra model [75] and the Shell HYDROCORR model [76].

- **Empirical models:** possessing very little or no theoretical background and possess constants with no physical meaning. These models can provide good interpolation results if they are calibrated with a large and reliable experimental database. One of the most popular empirical models is the NORSOK M-506 model developed at IFE [77, 78]

3.3.1 Mechanistic Electrochemical Models – Nešić et al. and Turgoose et al.

Since CO_2 corrosion is an electrochemical process, it is not surprising that many researchers initially based mathematical models on the electrochemistry occurring at the metal surface. Mechanistic models are completely different to both empirical and semi-empirical models since they do not rely on any measured corrosion rate data. The calculations are purely predictive but they can be extrapolated well and the theory extended to new systems. The problem with these models is the implementation work and specialised knowledge required to extend the models to new systems [79]. There is no guarantee the models will reproduce measured corrosion rates, but they can be validated against experimental data. Fosbøl et al. [79] produced a complete list of mechanistic corrosion models developed since 2009. They indicate that the majority of models were developed by groups within universities, suggesting they are time consuming to implement. It may also prove difficult to emulate certain mechanistic models based on the lack of published information relating to them. These reasons are why mechanistic models may not have received the same level of industrial attention as semi-empirical and empirical models.

3.3.1.1 Theory of Mechanistic Models

The core of all mechanistic models are their governing electrochemical kinetic equations. The models are based on the fact that CO_2 dissolves into the liquid phase, is hydrated and dissociates to create HCO_3^- and CO_3^- which produces an acidic solution. H_2CO_3 then diffuses to the pipe surface and participates in cathodic reactions outlined earlier in this Chapter, leading to the production of H_2.

These reactions only proceed if electrons are supplied by other reactions, namely, the anodic reaction involving the dissolution of iron.

The produced species diffuse away from the surface and, depending upon the environmental conditions, $FeCO_3$ may precipitate on the pipe wall, forming a protective scale. The presence of this carbonate film can act as a diffusion barrier as shown in Figure 3.3. This lowers the reaction rate due to the lack of H_2CO_3, meaning electron transfer is smaller and the rate of dissolution of iron is reduced [79].

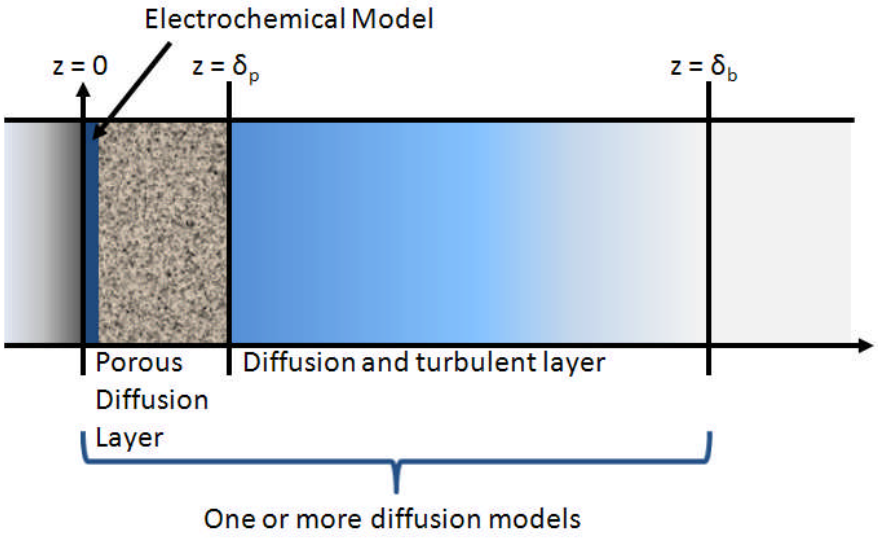

Figure 3.3: The principles of CO_2 corrosion mechanistic models. Distances to the interfaces are δ_p and δ_b from the surface [79]

The electrochemical reactions at the surface are typically formulated in a manner similar to the Butler-Volmer equation:

$$i_{net} = \sum_k i_{0,k} \left\{ e^{\left(\frac{(1-\alpha_k) n_k F (E - E_k^o)}{RT} \right)} - e^{\left(\frac{-\alpha_k n_k F (E - E_k^o)}{RT} \right)} \right\} \qquad (3.21)$$

Various empirical variations exist for this equation. In this general structure, $i_{0,k}$ is the k'th electrochemical surface reaction. It is calculated based on the concentrations of species at the steel surface, which can differ greatly from that of the bulk solution. The above equation is solved for the unknown potential, E. When E is calculated, the current related to the dissolution of iron can be ascertained and converted into a rate of thickness loss.

3.3.1.2 Nešić et al. – 1996

The model developed by Nešić et al. [48] couples four cathodic reactions, (the reduction or hydrogen ions, carbonic acid, water and oxygen (if present)), with a single anodic reaction representing the dissolution of iron. The aim was to develop an overall electrochemical model for the CO_2 corrosion process. The corrosion rate was determined when the sum of the cathodic current contribution equalled that of the rate of iron dissolution:

$$i_{H^+} + i_{H_2CO_3} + i_{H_2O} + i_{O_2} = i_{Fe} \tag{3.22}$$

The model requires the user to input the temperature, pH, P_{CO2}, oxygen concentration, steel type and flow geometry. 'Pipe flow' or 'Rotating Cylinder Electrode' (RCE) can be selected. 'Pipe flow' requires inputs of velocity and pipe diameter, while 'RCE' requires the rotating speed and cylinder diameter.

Once the input parameters are determined, the program generates anodic and cathodic Tafel curves. The intersection of the curves gives the corrosion potential, which is found by solving Equation (2.10). The program calculates i_{corr} based on the known E_{corr} and the anodic curve. Values of corrosion rate determined by the model as a function of temperature and CO_2 fugacity are provided in Figure 3.4.

The model provides an understanding for the effect of key parameters on the CO_2 corrosion mechanism. The majority of the constants used in the model have a physical meaning and the fact the model is theoretical leaves it open for the inclusion of new concepts such as film formation and/or inhibitor effects.

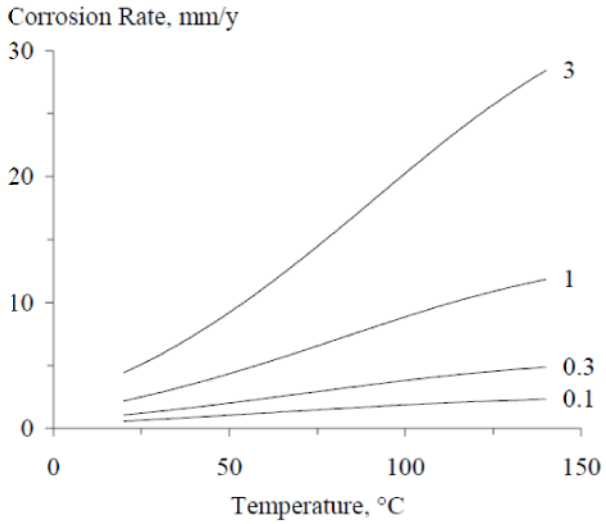

Figure 3.4: Corrosion rate prediction for the 1996 Nešić et al. [48] model for a range of fugacity from 0.1-3 bar - from Woollam [80]

Based on this approach, the FREECORP mechanistic model was developed by Nešić et al. in 2009 [45] aimed at elevating the level of understanding of carbon steel corrosion. The model is capable of predicting uniform corrosion of carbon steel in environments containing CO_2, H_2S, organic acids and/or oxygen.

The approach by Nešić et al. [45] is similar to that of work by Anderko et al. [81] and George et al. [82]. All models of this type have a limitation in that although they can adequately describe the electrochemical processes occurring on the metal surface, the treatment of the transport processes in the boundary layer is potentially oversimplified [49]. This is particularly crucial when a reliable prediction of protective scale formation is sought.

3.3.1.3 Transport Based Electrochemical Models

The challenge of mechanistic models lies in the calculation of surface concentrations. Describing the transport processes in the boundary layer for CO_2 corrosion has been considered a much more realistic method. The relatively new approach of coupling transport and electrochemical behaviour has long been established in other areas of electrochemistry and crevice corrosion [49], but Turgoose et al. [83] were the first to pave the way for a more realistic way of interpreting the transport processes in the boundary layer for the case of CO_2 corrosion. Although the electrochemical reactions were somewhat simplified, the subsequent studies of Nordsveen [70] and Nešić [84] rectified this issue.

In corrosion, certain species are 'created' at the steel surface (e.g. Fe^{2+}) and some are depleted (e.g. H^{+}) by the electrochemical reactions. This process inevitably leads to concentration gradients and diffusion of species to and from the corroding material surface.

The concentration of each species is governed by mass conservation. A universal, one-dimensional form of the equation which describes transport for species 'j' in the presence of chemical reactions (valid in both the liquid boundary layer and porous scale) is:

$$\frac{\partial \varepsilon c_j}{\partial t} = -\frac{\partial}{\partial z}\left(\varepsilon^{1.5} D_j^{eff} \frac{\partial c_j}{\partial z}\right) + \varepsilon R_j \qquad (3.23)$$

where the three groups of terms correspond to accumulation, net flux and a source/sink due to chemical reactions. ε is the porosity of the scale, c_j is the concentration of species 'j' in kmol/m^3, t is the time in seconds, D_j^{eff} is the molecular diffusion coefficient in m^2/s, x is a spatial co-ordinate in m and R_j is a source or sink in kmol/m^3s due to chemical reactions.

One transport equation of the form of Equation (3.23) can be written for each species in the solution. The resulting set of equations are solved in space and time. The boundary conditions for the partial differential equations are:

- At the steel surface: flux of species determined from the rate of the electrochemical reactions
- In the bulk: equilibrium concentrations of species as obtained based on chemical reactions of species in the brine based on their equilibrium constants

As Equation (3.23) is transient, initial conditions are generally defined as a bare metal surface with the solution in chemical equilibrium. Once the set of equations is solved for any given time step, the corrosion rate can be calculated as the flux of Fe^{2+} ions at the metal surface.

The CO_2 corrosion process involves a number of chemical reactions. Changes in the surface concentrations of species can significantly alter the rate of electrochemical processes and hence, the corrosion rate. This is particularly true in situations where the solubility limit is exceeded due to high local concentrations and precipitation occurs.

The rate of precipitation of iron carbonate (R_{FeCO3}) can be described as:

$$R_{FeCO_{3(s)}} = \frac{A}{V} \cdot f(T) \cdot K_{sp} \cdot f(S) \tag{3.24}$$

where A/V is the surface area to volume ratio in m^{-1}, T is absolute temperature in Kelvin, K_{sp} is the solubility limit and S is the supersaturation, defined as:

$$S = \frac{c_{Fe^{2+}} c_{CO_3^{2-}}}{K_{sp}} \tag{3.25}$$

where the 'c' values represent the concentration of Fe^{2+} and CO_3^{2-}.

Iron carbonate growth depends primarily on the precipitation rate as well as undermining which is governed by the corrosion rate. This process can also be expressed through a partial differential mass balance equation in terms of the volumetric scale porosity, ε:

$$\frac{\partial \varepsilon}{\partial t} = -\frac{M_{FeCO_{3(s)}}}{\rho_{FeCO_{3(s)}}} R_{FeCO_{3(s)}} - CR\frac{\partial \varepsilon}{\partial x} \tag{3.26}$$

where M_{FeCO3} is the molar mass in g/mol, ρ_{FeCO3} is the density in kg/m^3 and CR is the corrosion rate.

Solving this equation along with the transport equation and electrochemical equation allows the calculation of porosity, scale thickness and also the protective properties of the layer.

3.3.2 Semi-Empirical Models – De Waard and Milliams

3.3.2.1 De Waard and Milliams – 1975

One of the first and most widely used semi-empirical models developed for predicting CO_2 corrosion is that proposed by de Waard and Milliams in 1975 [74], based on the assumption of the direct reduction of H_2CO_3. The authors presented a correlation for the corrosion rate as a function of temperature and CO_2 partial pressure derived from gravimetric and linear polarisation measurements. Assuming a charge-transfer-controlled reaction between carbon steel and carbonic acid, an Arrhenius relationship was formulated along with an associated nomogram provided in Figure 3.5 [59].

$$\log V_{cor} = 7.96 - \frac{2320}{T + 273} - 5.55 \times 10^{-3} T + 0.67 \log P_{CO_2} \tag{3.27}$$

where V_{cor} is the corrosion rate in mm/year, T is the temperature in °C and P_{CO2} is the partial pressure of CO_2 in bar.

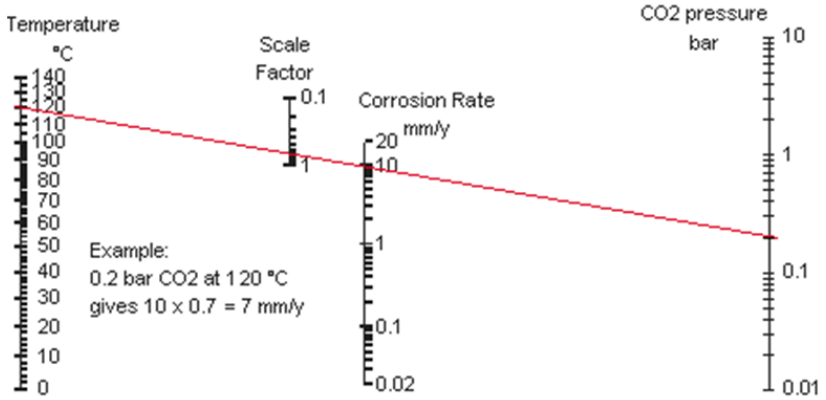

Figure 3.5: De Waard and Milliams nomogram for CO_2 corrosion [74]

The equation was derived on the assumption that pH was a function of CO_2 partial pressure only i.e. that all H^+ ions in the solution come from the dissolution of carbonic acid, which is now known to be incorrect for salt water solutions [46, 74]. Additionally, it was assumed that the anodic dissolution proceeded via a pH dependant mechanism, which was later proven to be invalid.

Although the de Waard and Milliams nomogram of 1975 has proved to be reasonably successful in predicting CO_2 corrosion rates, it has become apparent that limitations exist within the model. The sets of data used to derive Equation (3.27) were obtained through the gravimetric analysis of cylindrical samples in stirred solutions and it is believed that the pH of the solution was affected by dissolved corrosion products. It was stated that the nomogram failed to account for factors such as the presence of crude oil, glycol and condensing water at the top of a pipeline [58].

3.3.2.2 De Waard and Milliams – 1991

Following the initial study in 1975 [46], de Waard and Milliams refined the original model throughout the early 1990's by essentially recalibrating the constants against more reliable experiments and introducing various correction factors to quantify the influence of physical and environmental properties under various conditions.

In 1991, de Waard et al. [58] re-evaluated the data used by the first model and demonstrated it was possible to simplify the equation for the corrosion rate (V_{cor}):

$$\log V_{cor} = 5.8 - \frac{1710}{T + 273} + 0.67 \log f_{CO_2} \quad (3.28)$$

where f_{CO2} is the fugacity of CO_2 in bar.

It was stated that with increasing pressure, the non-ideality of the natural gas will play an increasing role, and that the fugacity of CO_2 should be used instead of the partial pressure [58].

The model proposed in 1991 systematically modified the prediction from Equation (3.28) by multiplying it with factors, each of which are associated with an individual physical or chemical effect. Separate equations were proposed for the calculation of each of the factors, which accounted for the effects of high temperature protective films, Fe^{2+} concentration, pH, glycol injection and chemical inhibition. Combinations of these effects were also discussed by de Waard et al. [58].

Woollam and Hernandez [80] considered the behaviour of corrosion rate for the model as a function of temperature and fugacity. The rates are determined over ranges of 20-140°C and 0.1-3 bar, as highlighted in Figure 3.6. This allows a direct comparison with the predicted rates of Nešić et al. [48] shown previously in Figure 3.4.

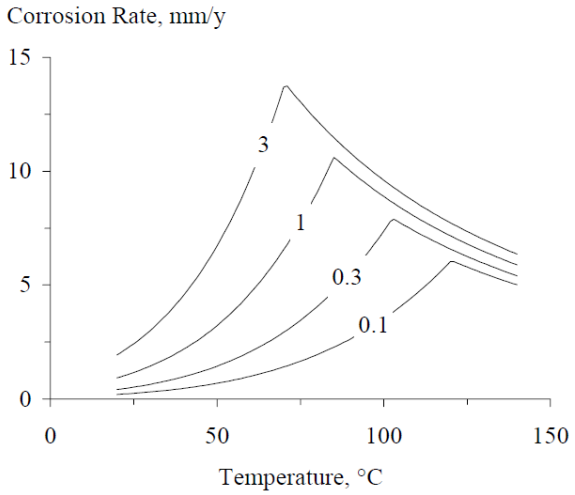

Figure 3.6: Corrosion rate prediction from the 1991 de Waard, Lotz and Milliams model [58] for a range of fugacity from 0.1-3 bar using a 'scale factor' - from Woollam [80]

3.3.2.3 De Waard and Milliams – 1993 and 1995 Parallel Resistance Models

De Waard et al. [59] stated that every corrosion reaction consists of two consecutive steps; the transport of the corrosive species through a hydrodynamic or

concentration boundary layer to the metal surface (mass transfer coefficient), and the reaction of the species at the metal's surface (reaction rate constant). In 1993, de Waard and Lotz [59] used this theory to develop a parallel resistance model to determine the effect of velocity on corrosion rate in the absence of surface scales. The model essentially combined the flow-independent kinetics of the corrosion reaction with the flow-dependent mechanism relating to mass transfer of dissolved CO_2:

$$\frac{1}{V_{cor}} = \frac{1}{V_r} + \frac{1}{V_m} \tag{3.29}$$

where V_r represents the rate of the electrochemical processes and V_m denotes mass transfer.

The first term on the right of Equation (3.29) represents the rate of the electrochemical process and the second term is related to the mass transfer rate.

In 1995, de Waard et al. [85] further refined the model from 1993 to provide the following values for V_r and V_m:

$$\log V_r = 4.93 - \frac{1119}{T + 273} + 0.58 \log P_{CO_2} - 0.34(pH_{actual} - pH_{CO_2}) \tag{3.30}$$

$$V_m = 2.45 \frac{U^{0.8}}{d^{0.2}} P_{CO_2} \tag{3.31}$$

For Equation (3.30), T is the temperature in ˚C, P_{CO2} is the partial pressure in bar and pH_{actual} and pH_{CO2} are the pH values of the aerated solution in the presence of dissolved salts and with dissolved CO_2, respectively. For Equation (3.31), U is the flow velocity in m/s and d is the pipe diameter in m.

It should be noted that the results used to develop the 1993 and 1995 models were the first set of substantial data to become available pertaining to the effect of velocity on CO_2 corrosion under well defined turbulent conditions. Tests were performed using coupons mounted within pipes and the environmental conditions were not influenced by the accumulation of corrosion products.

Woollam [80] also compared the behaviour of corrosion rate for the 1995 model over the same conditions as the previous Figures, which enables a direct comparison.

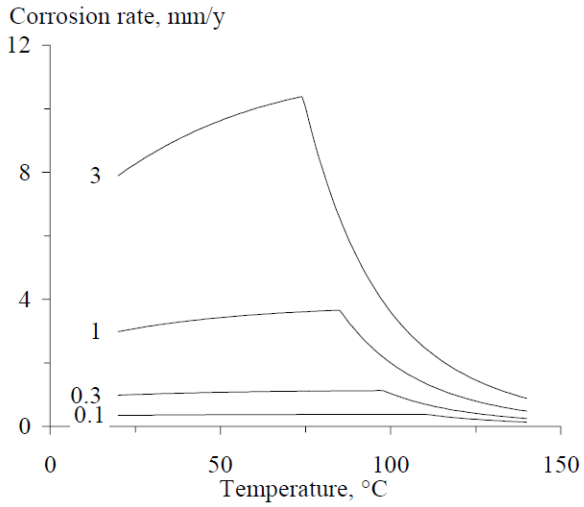

Figure 3.7: Corrosion rate prediction from the 1995 de Waard, Lotz and Dugstad model [85] for a range of fugacity from 0.1-3 bar - from Woollam [80]

3.3.2.4 De Waard and Milliams – 2001 and 2003

In 2001 and 2003, de Waard et al. [60, 86] updated the original de Waard and Lotz empirical correction for water wetting from 1995 and proposed the introduction of a new factor based on the emulsion breakpoint approach. The new empirical correction took into account the API gravity, emulsion stability and water wetting of steel by an oil-water mixture. Unfortunately, this model does not take into account pipe diameter, oil density, oil viscosity or operating temperature on the critical velocity of the flowing oil phase required for entrainment.

Users of the nomogram models tend not to appreciate the fact that it fails to account for erosion-corrosion, even though the guidelines state that ‘’judgement must be made for situations where erosive flow is present’’. It must also be stressed that these CO_2 studies are only helpful in the oil and gas industry for estimating corrosion rates if the applied material properties and the environmental parameters are extremely similar to those in the study.

Over the years, the de Waard and Milliams model of 1975 [74] has been revised on several occasions [58-60, 85, 86], extending its validity into areas where protective scales are involved and to account for changes in high pH in brines, velocity, water wetting etc.. These modifications, which have been implemented using correction factors, violate the assumption under which the original equation was derived, introducing a new form of semi-empirical model.

Despite the theoretical shortcomings, de Waard and Milliams' work has marked one of the important reference points for CO_2 corrosion research over the past three decades, and its most recently revised form is still used informally by industries today.

3.3.3 Empirical Models - Dugstad et al. and the Norsok Model

3.3.3.1 Dugstad et al. and the Norsok M-506 Model - 1994

One of the most frequently encountered empirical models is that by Dugstad et al. [87]. The model is based on the same empirical database as that of de Waard et al. [85]. The work by Dugstad uses a polynomial fit to determine a temperature dependant "basic equation". This basic equation is then multiplied by various correction factors to account for CO_2 partial pressure, pH, shear stress and steel chromium content. This simple empirical model is at the core of the NORSOK M-506 model. A detailed explanation of the model is provided by Olsen et al. [77], as well as by Halvorsen and Sontvedt [88] but can be summarised simply by the following equation:

$$\mathrm{CR_T} = \mathrm{K_T} f_{\mathrm{CO_2}}^{0.6} \left(\frac{\mathrm{S}}{19}\right)^{0.15+0.03\log(f_{\mathrm{CO_2}})} \mathrm{f(pH)_T} \tag{3.32}$$

where CR_T is the corrosion rate at a specific temperature in mm/year, K_T is a constant dependent upon temperature, f_{CO2} is the fugacity of CO_2 in bar, S is the wall shear stress in Pa and $f(pH)_T$ is a constant dependent upon pH.

Values for K_T and $f(pH)_T$ can be found using tables such as those provided by Halvorsen and Søntvedt [88]. Figure 3.8 shows the predicted corrosion rates for the NORSOK model for the same conditions as previous graphs in this section.

Despite the apparent advantage of these particular types of model, the key problem with fully empirical models is that they are somewhat regarded as "black boxes". The fact their prediction algorithms offer virtually no meaningful insight into the reasons behind the prediction means they cannot be, or should not be, used outside of the parameters which they have been validated experimentally. Adding new data to these models is also time consuming and requires recalibration of the entire model with all the data.

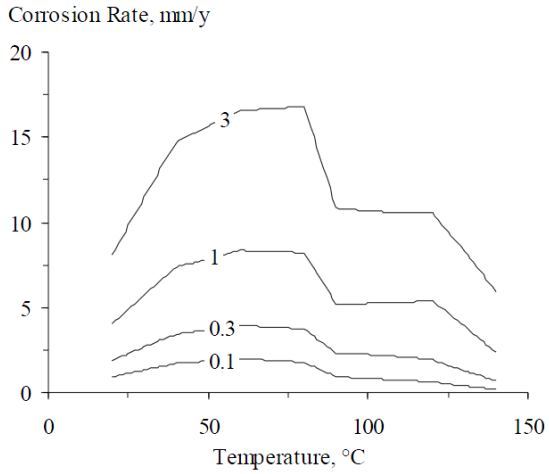

Figure 3.8: Corrosion rate prediction from the NORSOK M-506 model [88] for a range of partial pressures from 0.1-3 bar - from Woollam [80]

3.4 Summary of CO_2 Corrosion

The mechanism of carbon steel corrosion in a CO_2-containing environment has been studied and debated for decades. Hundreds of papers related to CO_2 corrosion have been published, with a number of different corrosion rates and mechanisms being reported.

The understanding of CO_2 corrosion has come a considerable way over the past two to three decades. The influence of a number of important electrochemical, hydrodynamic, chemical and metallurgical parameters have been investigated, but challenges still exist in this field.

The electrochemistry of steel dissolution in CO_2 solutions has been largely understood, although issues related with H_2S environments still required further consideration. The formation of protective and unprotective $FeCO_3$ scales has been identified and the influence of various parameters on this phenomenon has been studied.

The influence of pH, temperature, partial pressure and organic acids has been considered for general corrosion, but the prediction of localised corrosion and erosion-corrosion in CO_2 systems are areas requiring further attention.

A number of models (mechanistic, semi-empirical and empirical) exist to predict CO_2 corrosion in literature. They all consist of differing levels of complexity and different theoretical bases leading to a potentially inconsistent assessment of CO_2 corrosion risk. Sometimes, the basis and applicability limits of these prediction models are misunderstood which can lead to incorrect prediction. The differences in

values between models depends on how different parameters are treated and how much conservatism is built into each model [55].

The models reviewed here do not account for sand production in CO_2 systems. Sand particle presence in process fluid is becoming increasingly common and as will be demonstrated in the next Chapter, it can have significantly adverse effects on degradation rates. Sand production can result in the break-down of these CO_2 models and render them useless in terms of predicting pipeline failures, particularly in high temperature environments.

Chapter 4 -
Literature Review II: Sand Production and Erosion By Solid Particle Impact

Reductions in sediment consolidation and pore pressure, increasing production rate and reservoir fluid viscosity and rises in water cut can all influence and trigger sand production from oil and natural gas wells. Operational experience indicates that sand production is regarded as almost inevitable in reservoirs when their formation strength falls below 1000 psi [4]. In many cases, sand production only becomes apparent late in the life of assets. In these situations, operators are reluctant to install sand exclusion systems because they can potentially lower production rates [3, 4].

As an alternative, many operators tend to manage sand production by designing the facilities to handle sand when production commences. This can have implications in very low corrosivity environments, but becomes a particular concern in highly corrosive systems as it creates what has become termed as an 'erosion-corrosion' environment (which will be discussed in due course). Erosion (and hence erosion-corrosion) problems will continue to increase in oil and gas production due to the increasing trends of operating with sand laden fluids, coupled with the continual increase in water cut which inevitably puts pressure on operators to increase total fluid production rates to maintain oil production.

This Chapter presents an understanding of pure aqueous erosion and the factors which influence the level of material removal associated with this particular mechanism. A number of models are reviewed for purely erosive systems, along with other various approaches for predicting the rates of material loss when corrosion rates are low or have negligible influence.

4.1 Definition of Aqueous Erosion

For the purpose of this research, erosion can be defined as 'the mechanical removal of material from a metal surface'. It is worth noting that the degradation process attributed to erosion is considerably different to that of corrosion, which involves a chemical or electrochemical reaction [89].

Researchers believe that the first step towards understanding the complexities of erosion–corrosion is to understand erosion alone, i.e. under conditions where corrosion rates are very low. Once researchers attain a quantitative understanding of the effects of erodent particle interactions with the wearing surface in the

absence of corrosion, the added complexities of erosion-corrosion can be tackled with a real hope of achieving a quantitative understanding [90].

4.2 Aqueous Erosion Mechanisms

Studies focussing on the impact damage of single particles onto metal surfaces by Hutchings [89] showed three basic types of impact damage which are illustrated in Figure 4.1. Impacts at high angles of impingement (90°), are capable of plastically deforming and cold working the surface of the sample as identified by Bitter [91, 92] in tests using hardened steel balls on carbon steel surfaces. In these situations, further impacts around this area lead to the detachment of heavily strained material from the rim or lip of the crater created.

The deformation caused by an angular particle depends on the orientation of the particle when it comes into contact with the surface and whether the particle rolls forward or backwards during contact. In the 'type I' cutting mode, the particle rolls forward, indenting the material and producing a prominent lip, which is susceptible to removal by nearby impacts. In this mode, wear rate increases with increasing impact angle [93].

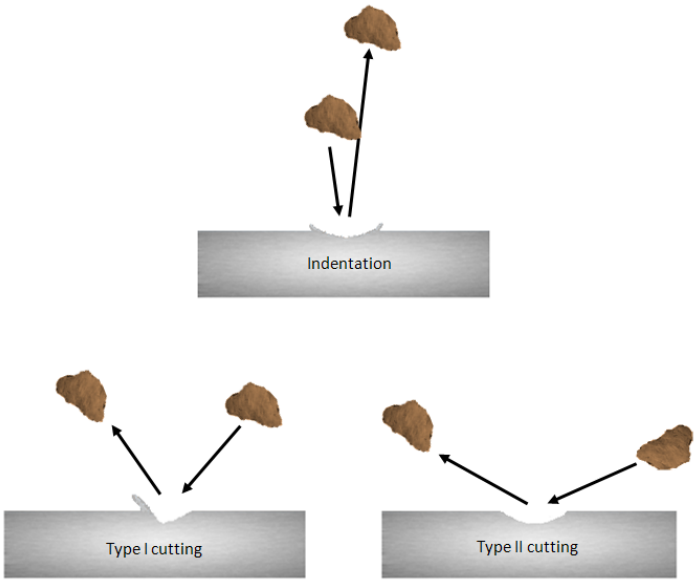

Figure 4.1: Schematic diagram of cross-sections through impact sites formed by hard particles on a ductile metal, showing typical shapes. Impacts are from left to right. (a) Indentation (plastic deformation); (b) Type I cutting by an angular particle, rotating forwards during impact; (c) Type II cutting by and angular particle rotating backwards during impact [89]

At low impact angles, a critical impact angle is observed, below which the cutting action does not contribute as significantly to erosive wear. In these situations, the particle is believed to scratch the surface, form the wear scar, but leave the surface whilst still cutting [94]. This type of mechanism only occurs over a finite range of particle geometries and impact orientations [89].

While it is possible to clearly distinguish between the three types of deformation for single particle impacts, classification is more difficult when randomly orientated particles of irregular shape impinge on an eroded or roughened surface [89]. In practice, Bitter [91, 92] and Clarke [95] have both shown that multiple wear processes tend to occur simultaneously.

4.3 Key Factors Influencing Aqueous Erosion

The oil and gas industry rely heavily upon the transportation of fluids with entrained particles. It is important to have an understanding for which factors influence erosion behaviour, as well as possessing a method for determining the erosion rate for specific operating conditions to prevent failures from occurring. Accurate prediction of erosion rates allows the user to estimate component service life, but also enables engineers to determine locations in pipework geometry where high erosion rates are likely to occur [96].

Table 4.1: Factors influencing the erosion rate of slurries [90, 95, 97-100] – the five factors in bold were classed by Clark [90] as being very influential towards erosion rates

Flow Field	Particles
Target-particle velocity	**Concentration**
Angle of impact	**Size range**
Boundary layer properties	Shape-angularity
Particle-particle interactions	Hardness
Particle rebound	Density
Target	**Liquid**
Ductility-brittleness	Viscosity
Melting point	Density
Metallographic structure	Surface activity-lubricity
Work hardening	Temperature
Residual Stress	

Hutchings [89] and Clark [98] proposed that the erosive resistance of a material subjected to solid particle erosion is strongly dependent upon a series of factors which include properties of the liquid, erosive particles, target and flow-field. Table 4.1 lists some of the factors that have been shown to influence erosion rates.

Clark [98] stated that many of the factors listed in Table 4.1 are not only interrelated but intimately entangled such that they cannot be investigated independently. Being unable to control single variables independently, even in a laboratory, presents a major obstacle to the development of a comprehensive understanding of the erosion process through experimental work alone [98]. The following sections focus on some of the main factors which are particularly influential in term of erosion rate.

4.3.1 Flow Field

The wear process of aqueous erosion manifests itself when a surface experiences a loss of material by the repeated impact of suspension particles [98]. In erosion, several forces of different origins may act on a particle contacting a solid surface, as illustrated in Figure 4.2 [101]. The particle experiences a gravitational force and reaction forces (including any frictional forces) when pressing onto the surface [102]. Additionally, the particle will experience drag forces due to the relative motion of the fluid and particle.

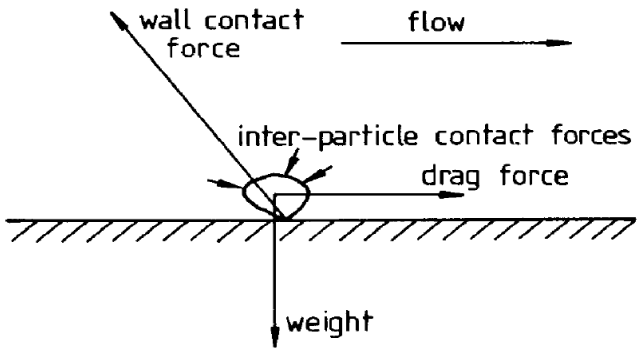

Figure 4.2: Schematic diagram of forces acting on a particle at a solid boundary – from Hutchings [102]

The main contact force on erosive particles which is responsible for their deceleration from initial impact velocity is usually the contact force exerted by the surface, although the weight and buoyancy forces will also be present [89]. The magnitude of this force is important as it is responsible for the deformation of the surface and ultimately, for wear and is influenced by the interactions between the particle and its neighbours, gravity, buoyancy and fluid drag forces. The magnitude

of wear will therefore be influenced by all of these variables, as well as the particle and target properties.

The effect of drag forces is an important concept as it can significantly alter particle velocity, impact angle and impact frequency upon a target from the values calculated based on the free-stream velocity [90]. Clark [98] stated that dense particles moving at high velocities in liquids of low viscosity will be least diverted from a direct collision path with the specimen. Conversely, small, slow moving particles of low density in a viscous liquid will be most likely to follow fluid streamlines and avoid collision with targets.

4.3.2 Fluid Density and Viscosity

Increasing liquid density and viscosity both increase the drag force on particles. A liquid with high viscosity will exert a greater drag force on a particle than that of a low viscosity. As the liquid of high viscosity begins to flow onto a surface, it will be more effective in moving particles laterally around the specimen than a low viscosity fluid. High viscosity liquids would therefore only allow few particles to collide with the specimen, reducing the collision efficiency as well as particle impact velocity. Clark [100] confirmed this strong dependence of collision efficiency and particle impact velocity on viscosity by conducting tests with dilute water-glycerin suspensions of glass beads with copper rod specimens, as shown in Figure 4.3.

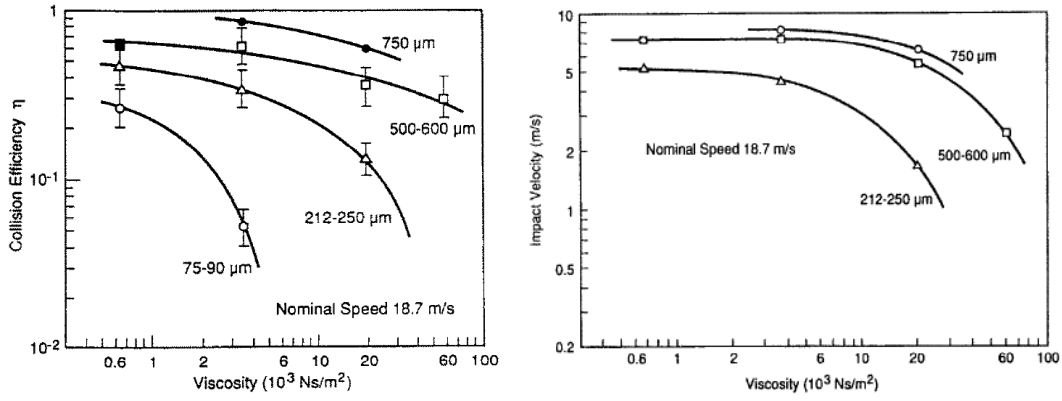

Figure 4.3: The variation in (a) collision efficiency and (b) calculated impact velocity with viscosity for the impact of glass beads on copper rod specimens in a slurry pot tester - from Clark [100]

4.3.3 Particle Velocity

The relationship between fluid velocity and erosion rate has continued to be researched ever since the early 1960's work published by Finnie [103], in which he

demonstrated the strong correlation between the amount of material removed in erosion by gas-borne particles and the square of velocity.

It is frequently seen that the erosion rate is related to a change in velocity using an exponent, n, in the following relationship:

$$\text{Erosion Rate} = V^n \tag{4.1}$$

Values of n vary significantly depending upon the conditions of slurry erosion (from 0.34 to 4.83), but for dilute suspensions (less that 5 wt.%) and ductile target materials, the exponent is around 2.5 [98].

Unfortunately, the relationship between velocity and other parameters affecting erosion is not simple. For example, doubling test speed does not always double particle impact velocity. Secondly, if the nominal test speed is changed the impact angle and collision efficiency become affected. In addition, if it is believed that the rate of material loss is a function of the rate of kinetic energy dissipation, erosion must be a function of velocity squared for constant particle sizes. Therefore, other values of the exponent reflect changes in other parameters which make data obtained at different speeds no longer directly comparable. Clark [100] concluded that either the laboratory tests must allow for particle impact analysis or the approach must be taken to treat particle impact, size effects and slurry erosion as a whole system to determine the severity and distribution of damage.

4.3.4 Particle Impact Angle

Research suggests the rate of mass loss in erosion is a function of particle impact angle. Impact angles of particles are usually defined relative to the plane of the surface. As shown in Figure 4.4, the erosion of ductile materials depends strongly upon impact angle, showing a maximum at 10º to 20º. For brittle materials, the maximum rate is at normal impact (90º), with the rate steadily declining with decreasing impact angle [89].

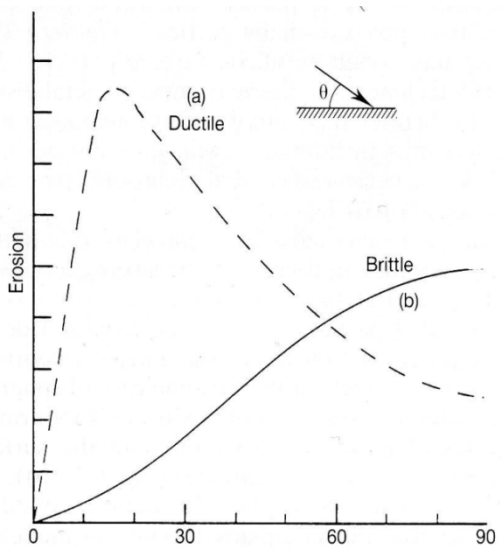

Figure 4.4: Typical dependence of erosion on impact angle, θ. Ductile metals commonly show peak erosion at shallow impact angle (curve (a)), while brittle materials often show maximum wear at higher angles of incidence (curve (b)) – from Hutchings [89]

For ductile materials, erosive wear is associated with the detachment of metal from raised craters or lips through the process of plastic rupture. Finnie [103] suggested that at low angles, the idealised particles strike the surface, form a crater and leave the surface. Finnie's research showed that particles remove a chip through metal cutting, whilst others leave material piled up on the side of craters. It was suggested that although each impact can cause displacement of the metal, the material will often not become detached as wear debris until it has been subjected to several cycles of plastic deformation and become severely work-hardened. Finnie [103] suggested that impact angles at 90° cause surfaces to become roughened so that subsequent particle impacts strike the surface with a variety of different angles.

It is worth noting that when using a jet impingement system, control over the impact angle is uncertain. It is strongly believed, that with jet impingement rigs using particles of sizes less that 500 µm, all impact angles between 0˚ and 90˚ would be present [98]. Particles at the centre of the sample will collide at 90˚ whilst those towards the edge of the sample will collide only at glancing angles, or not at all. The number of particles impacting a unit area will decrease with distance from the centre of the jet as the collision efficiency decreases.

A further complication with the jet impingement system is the requirement for particles that have already hit the surface of the sample to move out of the path of incoming particles.

4.3.5 Particle Size, Shape, Concentration and Density

The effect of particle size on erosion rates by slurries has been repeatedly examined [99, 100, 104]. It is generally agreed from results of laboratory experiments that an increase in particle size will result in an increase in erosion rate, which tends to a limiting value, while very small particle sizes result in diminishingly small rates [99]. Particle size can be related to erosion rate by the following relationship:

$$\text{Erosion Rate } \alpha \text{ (Particle Size)}^{m} \tag{4.2}$$

where 'm' may be referred to as the particle size exponent.

Unfortunately, prediction of the effect of particle size is less straightforward for irregularly shaped particles [98] and in addition, Clark [99] stated that experiments which involve the change of erodent particle size in typical laboratory test equipment, while revealing a decrease in erosion rate with decreasing erodent size, can also produce significant changes in the slurry flow conditions and particle impact conditions and hence change the experiment. This means that results from experiments with different particle sizes, (even under the same nominal tests conditions) are no longer directly comparable [99]. Unless these changes are evaluated properly, they may mask the true influence of particle size on slurry erosion.

The shape of the abrasive particles can also influence the pattern of plastic deformation around indentations made by particles as well as the proportion of material displaced from each indentation, which forms a rim or lip. Rounded particles produce less localised deformation, and more impacts are required to remove each fragment of debris. This has a very similar effect to changes in impact angle [103].

Experimental data relating to the effects of particle concentration of slurry erosion rates has been the subject of many investigations [105]. It has been suggested that once particle concentration goes above 5 wt.% for sand-water suspensions, significant particle-particle interactions can be expected [98]. Humphrey [97] believed that particles failed to interact with each other in concentrations of less than 0.25 wt.% for quartz sand in water.

Increasing particle concentration above 10 wt.% has indicated a decline in erosion rate with the use of jet techniques [105]. The mechanism related to this reduction in

erosion rate has been attributed to particle-particle interference and possibly impact angle [98]. Particles suffer a high loss in velocity normal to the target surface at low impact angles, but retain a significant amount of velocity parallel to it. Normal impact causes particles to come instantaneously to rest on the surface and require removing before further impact can take place at that exact site [98].

It has been postulated that for high solid loadings, layers of particles could build up on the surface, preventing direct impact and consequently causing material removal via abrasion as this layer is dragged across the surface [98]. Conversely, even at low concentrations, particles with low velocities could become captured by the liquid layer adjacent to the surface. Particles with insufficient velocity may not have enough energy to rebound clear of the target from further incoming particles. Erosion studies usually assume that suspensions are homogeneous, but it is worth noting that particle concentration effects may occur at the target surfaces, which are worthy of study, especially when material loss measurements are involved.

It still appears that little or no research has been published relating to the effect of particle density on slurry erosion. It has been suggested by Clark [98, 100] that this may be due to the problem of obtaining conditions under which the effect of density could be measured. An increase in particle density, however, will result in an increase in particle inertia, so one could expect that, for a given test condition, the number of particles impacting the specimen will increase as will the impact velocity, producing higher erosion rates.

4.3.6 Material Hardness

Hardness is the most commonly used property to seek correlation with erosion rates for materials. When hard angular particles strike a soft target, the material will deform plastically [89]. Erosion damage tends to decrease with hardness of the material [89]. During an impact, when the yield strength of a material is locally exceeded, plastic deformation takes place at the region of impact. Multiple impacts can have the effect of creating a plastically deformed layer near the eroded surface with increased yield strength as a result of strain hardening, which can reduce erosion rates [106]. Hutchings [106] has suggested that erosion processes require an understanding of the strain rate sensitivity and mechanical properties of a surface. High energy solid particle erosion can cause significant strain rate deformation on a surface [106].

4.4 An Assessment and Comparison of Aqueous Erosion Models and Guidelines

Sand erosion prediction models are a requirement for oil and gas companies as they allow users to establish tolerable sand production and well flow rates. They also help determine the inspection strategy for facilities. Establishing the optimum production rate whilst remaining within safety levels and ensuring asset integrity is a balancing act that companies continuously strive to achieve.

4.4.1 API Guidelines

The high cost and long duration of erosion experiments has meant that the use of prediction models is a necessity. Sand erosion is complicated and as shown previously, a wide range of factors contribute to erosion severity.

Solid particle erosion models have been developed by many researchers to predict erosion rates by implementing their understandings of solid particle erosion mechanisms. Most methods are based on limited amounts of experimental data, so these models are only applicable to specific conditions [96]. Due to the lack of an accurate and general erosion prediction model, design guidelines are adopted by industries which usually lead to designs which are too conservative or unrealistic [107].

One of the most well-known guidelines in the oil and gas industry is the American Petroleum Institute Recommended Practice 14E (API-RP-14E). The practice recommends limiting the maximum production velocity in two-phase flow systems to a value defined by the following empirical equation to avoid severe erosion:

$$V_e = \frac{C}{\sqrt{\rho}} \tag{4.3}$$

For a sand-free, two-phase flow situation, the C factor is limited to 100 for continuous flow and 125 for intermittent flow. The API-RP-14E recommends using an unspecified value of C for fluids containing sand. The equation was evaluated by Salama and Venkatesh [108], who showed that the value of C, as recommended by API was extremely conservative.

The only variable accounted for directly by API-RP-14E is fluid density, therefore the equation is not capable of incorporating all the important factors involved such as sand production rate and fluid/particle properties.

4.4.1.1 Limitations of API-RP-14E

In 1998, Jordan [107] reviewed the performance of API-RP-14E against a collection of industrial field data. By comparing the field information collected by the Southwest Research Institute with API-RP-14E, Jordan was able to draw two conclusions about the practice:

- API-RP-14E is too conservative and can be seen to unnecessarily limit production. This is illustrated by the high number of 'lack of failure' points to the right of the line in Figure 4.5.
- In other cases, API-RP-14E is not conservative enough. A large number of data points representing failure are to the left of the line.

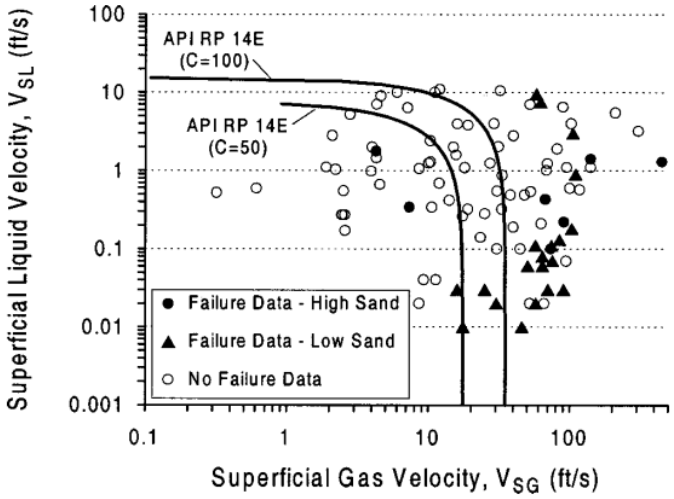

Figure 4.5: Field experience reported by the Southwest Research Institute in comparison to the API-RP-14E limit - from Jordan [107]

4.4.2 Mechanistic Models

4.4.2.1 Finnie – 1960

As opposed to calculating erosion based on empirical information, it is possible to model erosion based on several physical parameters and mechanisms. In 1960, Finnie [103] analysed the erosion of ductile materials by considering the equations of particle motion for a single abrasive particle impacting the surface. By comparing his equation with experimental data, he was able to model the volume of material removed as a result of particle impingement using the following equations:

$$W \approx \frac{MV^2}{8p}(\sin 2\alpha - 3\sin^2\alpha) \quad \alpha \leq 18.5° \tag{4.4}$$

$$W \approx \frac{MV^2}{24p}(\cos^2\alpha) \quad \alpha \geq 18.5° \tag{4.5}$$

where W is the mass of material removed by a number of particles, α is the impact angle, p is the plastic flow stress reached upon particle impact, M is the total mass of particles and V is the particle velocity.

This simple model accurately describes the physics of erosion by solid particles, but the influence of the particle hardness, size and velocity together with the hardness of the target are believed to require further consideration [103].

4.4.3 Semi-Empirical Models

4.4.3.1 Erosion-Corrosion Research Centre Model and its Variations – 1999-2002

In 1999, McLaury et al. [109-111] developed a semi-empirical model to predict erosion severity which can be used for a broad range of operating conditions. The model computes the maximum penetration rate in carbon steel elbows:

$$h = F_M F_S F_P F_{\frac{r}{D}} \frac{W V_L^{1.73}}{\left(\frac{D}{D_o}\right)^2} \tag{4.6}$$

where h is the penetration rate in m/s, F_M is an empirical constant that accounts for material hardness, F_S is an empirical sand sharpness factor, F_P is the penetration factor for steel in m/kg, $F_{r/D}$ is the penetration factor for elbow radius, W is the sand production rate in kg/s, V_L is the characteristic particle impact velocity in m/s and D/D_o is the ratio of pipe diameter in inches to a one inch pipe.

The relation was developed based on extensive empirical information gathered at the Erosion-Corrosion Research Centre at The University of Tulsa and data gathered at Texas A & M University whom have been investigating erosion for a number of years.

Predicting erosion in single phase flow is challenging without the addition of another phase into the system. However, the Erosion-Corrosion Research Centre model can also be applied to multiphase flow with a few modifications. This involves replacing the fluid properties (density and viscosity) with mixture properties and changing the average fluid velocity for an equivalent flowstream velocity. More information can be found in the paper by McLaury and Shirazi [111].

In 1998, Jordan [107] introduced a slightly different version of McLaury and Shirazi's equation, breaking up the sand production (W) into the weight fraction (w) and the production rate of the fluid (Q_F) as shown below:

$$W = wQ_F \tag{4.7}$$

In 2002, Ramachandran et al. [112] expanded on the work by McLaury and Jordan, by introducing an empirical inhibitor factor (F_i) to account for the reduction of erosion by inhibition:

$$h = F_i F_M F_S F_P F_r \frac{wQ_F V_L^{1.73}}{\left(\frac{D}{D_o}\right)^2} \tag{4.8}$$

4.4.4 Empirical Models

4.4.4.1 Salama et al. – 2000

In 2000, Salama [113] proposed an alternative to the API-RP-14E velocity limits for sand-laden fluids:

$$ER = \frac{1}{S_m} \frac{WV_m^2 d}{D^2 \rho_m} \tag{4.9}$$

where ER is the erosion penetration rate in mm/year, W is the sand flow rate in kg/day, V_m is the fluid mixture velocity in m/s, d is the sand size in micrometers (typically 250 µm), S_m is a geometry-dependant factor determined experimentally (approximately 0.05 for pipe bends), D is the pipe internal diameter in mm and ρ_m is the fluid mixture density in kg/m^3.

This empirical model has been shown to agree well with experimental data and is simple to use. Salama also presented the foregoing equation in terms of sand concentration, M (ratio of mass of sand to mass of fluid). The empirical equation proposed by Salama, when rearranged in terms of mixture velocity (V_m) becomes:

$$V_m = \left[\frac{(ER)(S_c)}{M d_p}\right]^{\frac{1}{3}} \tag{4.10}$$

where M is in ppm and S_c is a geometry dependant constant related to S_m and is 20,000,000 for elbows.

Unfortunately, the applicability of empirical models, like those proposed by Salama, tends to be limited to the flow conditions of the experiments.

4.4.5 CFD Modelling in Erosion Rate Prediction

The problem of erosion was summarised well by Finnie [103] in 1960:

“The erosion of a surface by abrasive particles in an inert fluid should depend on the number of particles striking the surface, their velocity and their direction relative to the surface. These quantities are largely determined by the flow conditions...” [103].

As stated previously, Clark [112] concluded that if an understanding of erosion rates is desired, it is imperative to know the number of particles striking a unit area, the velocity of the particles and their impact angle. It is believed that particle impact dynamics must be analytically modelled for us to fully understand erosion behaviour.

Acknowledgement has to be afforded to the original findings above. A more comprehensive approach to modelling erosion and determining the above mentioned parameters can be attained using Computational Fluid Dynamics (CFD). This method consists of flow modelling, particle tracking and erosion equations. Work by Chen et al. [96, 114] is an excellent example of how CFD can be used to allow the prediction of erosion rate within geometries such as elbow and plugged tees, two sections of pipework that are particularly vulnerable in erosion environments. A flow model is used to determine the flow field for a given geometry and particle tracking is used to determine the trajectories in the flow. Impingement information, such as particle impact speed, angle and locations are used along with empirical equations to predict erosion rates. Unfortunately, this technique requires expertise in CFD as well as a great deal of time [115]. Examples of the particle tracking are provided in Figure 4.6.

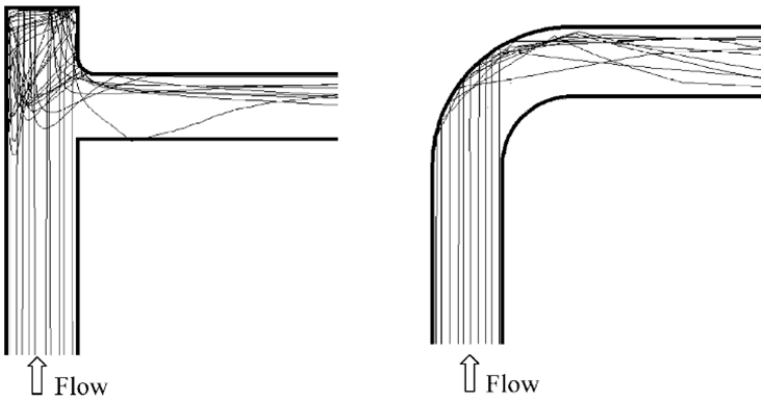

Figure 4.6: Predicted particle impact trajectories in a plugged tee and elbow – from Chen et al. [115]

Work conducted by Gnanavelu et al. [116] involved a different approach to that of Chen et al. [96, 114] by combining jet impingement experiments with CFD. Initially a universal wear map is generated for the material in question using the jet impingement test to create a wear scar. The local wear rate from the surface profile is interpreted using a CFD simulation of the test, which produces a map giving local wear rates as a function of particle impact angle and velocity. A CFD simulation is then calculated for a series of different erosion configurations to provide particle impact data at each point on the surface. The wear maps from the jet impingement tests are then used to calculate the local wear rates.

4.5 Summary of Aqueous Erosion

It is evident that numerous studies on aqueous erosion have been conducted, with work focussing on the effects of factors such as liquid viscosity and density, particle size and concentration, target shape and impact angle etc.. However, there are many uncertainties attributed to erosion testing, including the size range and distribution of particles, the shape of the particles, the local turbulence of slurry flow, details of particle-target and particle-particle interactions and the change in wear rate with respect to time. Additionally, many of these parameters are not only interrelated but intimately entangled such that they cannot be investigated independently.

A number of mechanistic, semi-empirical and empirical models exist in literature for aqueous erosion in environments where corrosion rates are low. However, when facilities transporting highly corrosive solutions begin to produce sand, a transition from a flow-induced corrosion to an erosion-corrosion environment can occur. Material loss rates can become significantly larger than the sum of the individual processes operating independently. Consequently, neither corrosion models, erosion models, nor their summation of material loss rates can accurately predict the level of degradation. The ways in which erosion and corrosion processes interact with each other and methods of controlling this degradation regime are reviewed in the following Chapter.

Chapter 5 - Literature Review III - Erosion-Corrosion and Chemical Inhibition

In oil and gas production, it is not uncommon to find sand present in a corrosive process fluid. The onset of sand production promotes a transition from a flow-induced corrosion environment to that of an erosion-corrosion environment. In these situations, models which have been developed to predict purely CO_2 flow-induced corrosion break down and can fail to capture the severity of degradation. This can result in the models drastically under-estimating the degradation rates, leading to ambiguity surrounding asset integrity. Unfortunately, erosion-corrosion degradation rates are notoriously difficult to predict because the combined effect of CO_2 corrosion and sand erosion create more damage than the sum of the individual effects acting alone.

5.1 Definition of Erosion-Corrosion

Erosion-corrosion is a form of tribo-corrosion material loss mechanism caused by flowing fluid (in the presence or absence of solid particles) which can damage the surface layers as well as the base metal [117]. The mechanism of erosion-corrosion results from interactions between electrochemical and mechanical processes. Mechanisms associated with material loss can occur through a combination of the following processes:

- chemical dissolution (which can be accelerated by increased mass transfer at the surface) [117],
- mechanical erosion caused by fluid flow and/or impingement of particles on the pipe wall [117],
- electrochemical corrosion can enhance erosion [117],
- erosion can enhance the corrosion process [117].

The total mass loss as a result of erosion-corrosion therefore tends to be divided into four aspects:

$$\mathrm{TML} = \mathrm{E} + \mathrm{C} + \mathrm{dE_C} + \mathrm{dC_E} \tag{5.1}$$

where TML is the total mass loss, E is pure erosion in the absence of any corrosion and C is the corrosion in the absence of any erosion. dC_E is the effect of erosion on

corrosion (often referred to as the additive effect) and dE_C is the effect of corrosion on erosion (usually termed synergistic effect) [118].

Erosion-corrosion is receiving greater attention because of its destructive nature and the fact that this regime of degradation is becoming more prevalent due to the increasing severity of conditions attributed to exploring deeper wells and the ageing of wells with associated higher sand production rates. In addition, the trend of operating with small quantities of sand in the system is becoming increasingly more common.

5.2 Erosion-Corrosion Regimes and Erosion-Corrosion Maps – Stack et al.

Early work relating to erosion-corrosion focused on describing the process in terms of different regimes of behaviour. Since the mechanism of material loss in an erosion-corrosion environment is dependent on which process predominates, it is useful to classify erosion-corrosion behaviour in terms of regimes [119]. By identifying transitions between different regimes for a given set of conditions it can help to determine whether the material requirement is predominantly for an erosion- or corrosion- resistance material [119]. Such a technique can act as a guide to the selection of the most appropriate material for the exposure conditions.

Considerable notable work on defining erosion-corrosion regimes has been performed by Stack et al. [7, 119-131], beginning in the early 1990's.

The early work of Stack and colleagues directed their attention towards establishing erosion-corrosion regimes for alloys subjected to erosion in the presence of high temperature, oxidising gases [119, 125]. Stack et al. [119, 127] chose to classify erosion-corrosion into four regimes which were:

- erosion-dominated
- erosion-corrosion dominated
- corrosion-dominated 1
- corrosion-dominated 2

These regions were determined by considering how temperature influences the rate of the oxidation process of alloys and are shown in the schematic diagram provided in Figure 5.1. The 'erosion-dominated' regime exists when erosion is the dominant process [119]. An increase in temperature would increase the level of oxidation between erosion events causing erosion of both scale and the substrate. The

temperature at which an increase in degradation is observed marks the transition to the 'erosion-corrosion dominated' regime [119]. Further increase in temperature marks the critical temperature at which the system becomes dominated by corrosion [119]. This is defined as the region where erosion-corrosion rate begins to reduce with temperature. Stack and Stott [119] subdivided the 'corrosion dominated' regime into two categories to distinguish between high erosion rates (just above the critical temperature, termed 'corrosion dominated 1') and low erosion rates (termed 'corrosion dominated 2') where the overall weight change is zero or greater (although the overall mass loss is not zero) [119, 125].

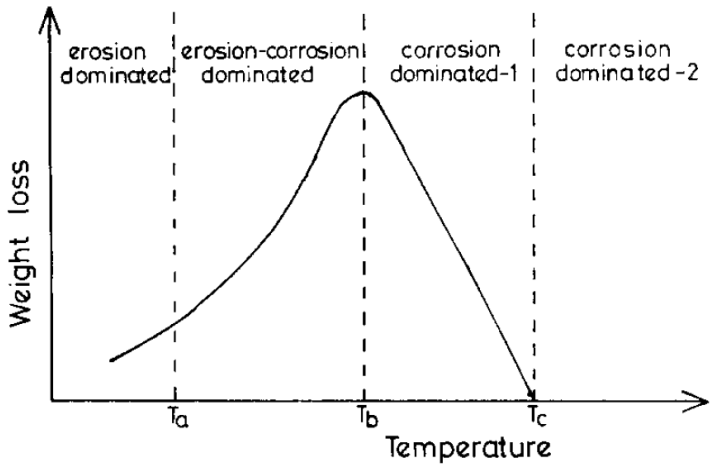

Figure 5.1: Schematic diagram of weight change vs. temperature for an alloy exposed to low velocity erosion-corrosion conditions – from Stack and Stott [119]

Stack et al. also directed their attention towards establishing the transition in erosion-corrosion regimes in aqueous environments using a methodology based around rotating cylinder electrode experiments [127]. This work was the first study to define erosion-corrosion regimes in a 'wet' environment. Stack et al. [127] showed conclusively that electrochemical techniques could be used to identify transitions between erosion-corrosion regimes for mild steel in a 0.5 M Na_2CO_3 + 0.5 M $NaHCO_3$ electrolyte. By considering the current density and erosion-corrosion rate of mild steel at various applied potentials, it was possible to create aqueous erosion-corrosion maps which highlighted the differing erosion-corrosion regimes as shown in Figure 5.2.

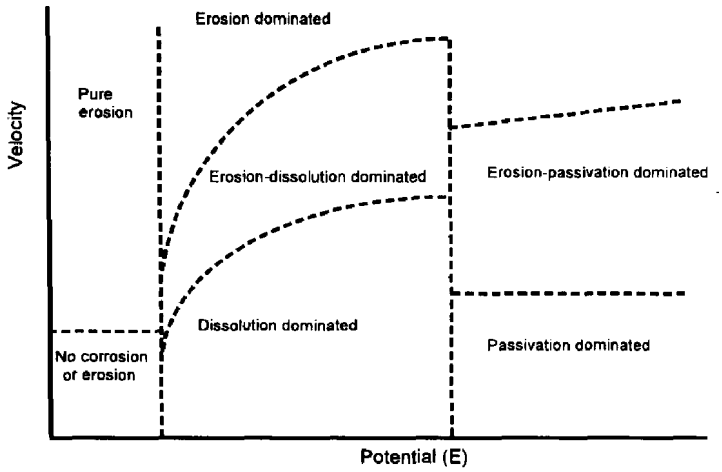

Figure 5.2: Schematic diagram indicating different erosion-corrosion regimes for Fe in $NaHCO_3/Na_2CO_3$ solution as a function of applied potential and flow velocity – from Stack et al. [127]

In the late 1990's Stack and colleagues [123] began to quantitatively define erosion-corrosion regimes by classifying them based on the ratio of corrosion rate to erosion rate (K_c/K_e). It was suggested that the regimes can be classified as follows:

- erosion dominated ($K_c/K_e < 0.1$)
- erosion-corrosion ($0.1 < K_c/K_e < 1$)
- corrosion-erosion ($1 < K_c/K_e < 10$)
- corrosion dominated ($K_c/K_e > 10$)

These regions were further subdivided based on the corrosion processes taking place on the surface of the material. Numerous erosion-corrosion maps were constructed to highlight the sensitivity of erosion-corrosion regime boundaries to particle size, solution pH and particle concentration for iron in water. These erosion-corrosion maps ultimately led to the development of process control maps which indicate bands of differing levels of material wastage. Stack et al. [121] also showed that these maps could be constructed by combining certain parameters into dimensionless groups, helping users deal with the large number of variables associated with erosion-corrosion.

In 2004, Stack and Pungwiwat [126] introduced the notion of 'positive' and 'negative' synergy. The ability to define the conditions where this transition occurs is important when minimising the wastage of materials. Erosion-corrosion maps were developed to show the transitions between low, medium and high synergy for iron

in aqueous slurries as a function of applied potential and velocity using results from an erosion-corrosion rig with a built in electrochemical cell [126].

Stack and Jana [124] considered the erosion-corrosion behaviour of a range of pure metals in aqueous slurries, developing computational maps for Ni, Cu and Al. From the sets of data collected using computational techniques, material performance maps such as those shown in Figure 5.3 could be constructed, highlighting regions where wastage rates are low for particular materials.

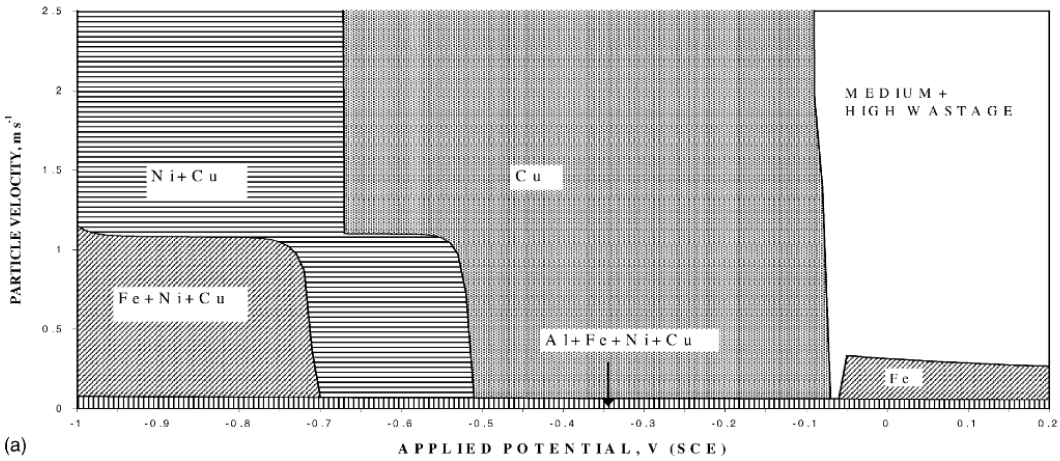

Figure 5.3: Material performance map indicating regions of 'low' wastage for various pure metals at pH 5 - from Stack and Jana [124]

Telfer et al. [128] continued the use of this technique in 2012 to evaluate the influence of particle concentration and size on the erosion-corrosion of the aforementioned pure metals in aqueous slurries.

Since 2010, Stack and Abdulrahman [129, 130] have focused their attention towards developing erosion-corrosion maps in crude oil conditions such as those found in oilfield production. Through the implementation of *in-situ* potentiodynamic polarisation for carbon steel material in an erosion-corrosion test rig, the ratio of erosion to corrosion damage could be quantified and wastage maps, as well as additive-synergism maps could be generated. These studies [129, 130] have focused on the effect of impact angle, applied potential and impact velocity on the erosion-corrosion regimes in three environments: reservoir water, crude oil and 20% water/crude oil.

5.3 Synergistic Effects in Erosion-Corrosion Environments

The reasoning behind erosion-corrosion creating such a destructive process is predominantly attributed to the synergistic effects occurring between erosion and

corrosion. In various circumstances, the effects of synergy have been shown to contribute to over 50% of the overall damage in specific environments [132]. Table 5.1 highlights some of the factors which can contribute towards this dramatic increase in degradation rate.

Table 5.1: Different mechanisms resulting in erosion-corrosion synergy

Erosion-enhanced corrosion	Corrosion-enhanced erosion
Local acidification in the erosion pits, accelerating corrosion rates and prohibiting film formation [133]	The removal of work hardened material by corrosion, exposing a softer metal [133]
Increased ion transportation by high turbulence levels caused by surface roughening as shown by Dave et. al [6]	Preferential corrosive attack at grain boundaries, resulting in grain loosening as suggested by Reyes and Neville [134]
When the protective film (corrosion product or inhibitor film) is continually removed by the impacting particle, exposing fresh material to the corrosive environment as shown by Zheng et al. [135]	
The disturbance of solid particles in flow field can enhance the transport process of both reactants and corrosion products, and then promote the corrosion process [133]	

In CO_2 environments, erosion-corrosion of carbon steel is the most significant cause of damage when iron carbonate protective films are removed by high levels of shear or the impingement of sand particles. For this to occur, a critical velocity (or shear stress) must be exceeded. The localised removal of iron carbonate films exposes fresh steel which corrodes at an exceptionally higher rate than surrounding steel, leading to localised attack and rapid failure. Figure 5.4 highlights the different scenarios of erosion for iron carbonate films.

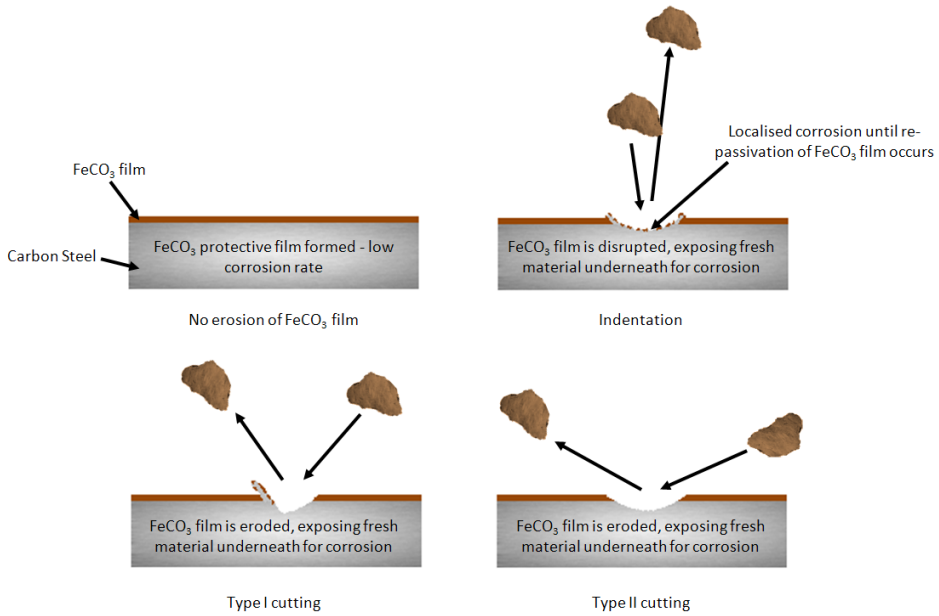

Figure 5.4: Various erosion mechanisms of iron carbonate films

Erosion-corrosion of materials in aqueous solutions is a complex process involving a large number of variables. Predicting the erosion-corrosion behaviour of a material and the level of synergy has been considered by some researchers as somewhat of a 'black art' due to the parameter size which is involved in such processes [120]. Additionally, Barik et al. [136] indicated that in some environments, the synergy can be extremely difficult to quantify experimentally as multiple experiments are required, generating considerable errors outweighing values of synergy contribution.

Notable work on understanding erosion-corrosion and its processes, particularly in CO_2-saturated environments, has been performed at the Erosion-Corrosion Research Centre at the University of Tulsa [137-141] and the University of Leeds [134, 142-144]. Other considered publications are those of Southampton [133, 145-148] and Cambridge University [93, 94] who have considered the effects of erosion-corrosion on stainless steels in non-CO_2 containing environments. However, focus is directed here towards CO_2 systems, therefore the work of these authors will not be reviewed here.

From 1996 to 1998, Shadley and co-workers at the University of Tulsa [141] set out to characterise erosion-corrosion behaviour of a carbon steel elbow over a range of environmental conditions through the use of an empirical model. They applied the results of the study, along with published erosion and corrosion models, to predict erosion-corrosion penetration rates for a carbon steel elbow. Shadley et al. [139,

141] made strong reference to the 'threshold velocity'. They believe that the first step in predicting erosion-corrosion penetration rates is to compute the threshold velocity, because below this velocity the protective $FeCO_3$ scale remains intact, and above the velocity, the scale breaks down. Shadley et al. [141] examined thirteen sets of environmental conditions in flow loop tests. For each set of conditions, erosion parameters (sand size, sand concentration and flow velocity) were varied. If scale formed everywhere in the elbow, then the erosivity of the next test was increased. If pitting or uniform corrosion was observed, the erosion severity was reduced. The objective was to determine the erosion-corrosion resistance i.e. define the highest erosion rate that the system could tolerate without eroding the protective scale [141]. The erosion-corrosion resistance was then calculated from the parameters using published prediction models. This enabled the threshold velocity to be calculated. Once the threshold velocity was identified, erosion and corrosion rates corresponding to selected flow velocities could be estimated [141].

Three types of behaviour were identified from the flow loop tests performed on the carbon steel elbow. At low velocities, a protective iron carbonate film was formed over all surfaces of the elbow, and corrosion rates were very low. At high velocities, the impingement of sand particles prevented the formation of a protective film anywhere on the surface. Accordingly, corrosion rates were recorded as extremely high and uniform over the entire elbow. At intermediate velocities, a protective film was formed over the surface, except at localised regions, promoting pitting and high wall penetration rates as shown in Figure 5.5.

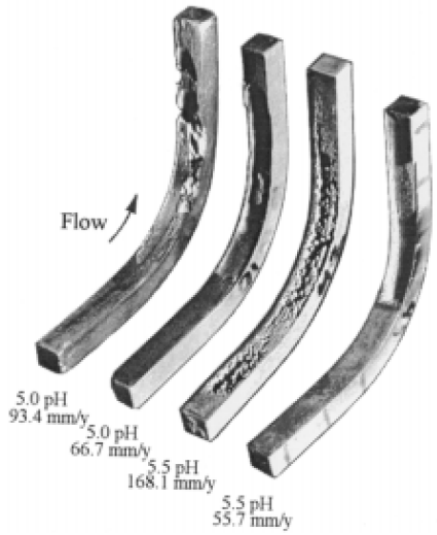

Figure 5.5: Photographs of sections of a carbon steel elbow in different conditions highlighting regions of localised attack – from Shadley et al. [139]

5.4 Modelling of Erosion-Corrosion – Erosion-Corrosion Research Centre – 2012

Very few researchers have tackled the challenge of modelling erosion-corrosion and predicting expected degradation rates over the expanse of operating conditions, particularly in CO_2-containing environments. This is conceivably related to the complexity of the degradation process and the large number of erosion and corrosion parameters that need to be accounted for.

One notable approach towards predicting erosion-corrosion degradation rates over a range of conditions in CO_2 environments was that of the Erosion-Corrosion Research Centre [149] who pursued an interesting mechanistic approach. Al-Mutahar et al. [149] presented a model which accounts for iron carbonate scale formation in multiphase flow by modelling the competition between scale growth by precipitation and scale removal by erosion. The mechanistic corrosion prediction model, Sand Production Pipe Saver, SPPS:CO_2 and the mechanistic erosion model SPPS were the basis of the erosion-corrosion model. These two tools were integrated into one model for predicting erosion-corrosion in multiphase flow under steady state conditions. An example of how the model functions is provided in Figure 5.6.

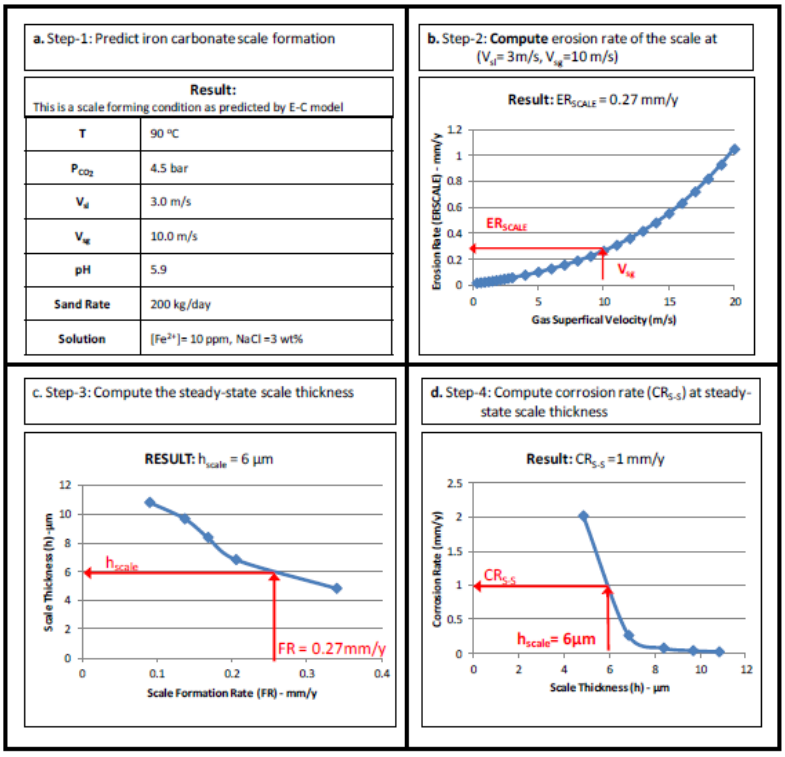

Figure 5.6: Calculation procedure and sample of results for erosion-corrosion model developed by Al-Mutahar et al. [149]

5.5 Implementation of CFD in Erosion-Corrosion Modelling

Erosion-corrosion investigations are typically quite daunting due to the vast number of experimental parameters involved affecting the synergistic behaviour. The presence of multiphase flow provides further complications with respect to hydrodynamics and modelling of the processes. This produces an overall lack of predictivity for these types of studies [150].

The introduction of CFD to study the degradation of materials under erosion-corrosion is proving useful, with the approach currently being dominated by the analysis of single-phase flow with a particulate solid, usually in two-dimensional geometry [151]. CFD is suitable for providing local evaluations of mechanical action of the fluid flow and the parameters related to the impacting solids suspended in the flow. The erosion mechanism needs to be linked with electrochemical information related to the corrosion of the material in its environment in order to fully represent the effects witnessed in an erosion-corrosion regime.

CFD has currently developed into one of the more promising approaches for the analysis and solution of a wide range of flow problems. CFD codes are capable of solving the full set of fluid mechanics balancing equations (usually in Navier-Stokes formulation for momentum balance). Turbulence can also be accounted for using a variety of models. In particular, the FLUENT code solves the balance equations via domain discretisation, using a control volume approach to convert partial differential equations into algebraic equations, which are solved numerically. The FLUENT solution procedure involves integrating the balance equations over the control volume to obtain discrete equations. FLUENT is also capable of simulating complex flows in two and three-dimensions, also accounting for turbulence.

In the recent work, Stack and colleagues [120] combined various models of solid particle erosion with those for aqueous corrosion. These models were then incorporated into a simulated flowing environment using CFD techniques to predict the erosion-corrosion behaviour of pure metals. The technique provides a means of mapping the level of degradation of components undergoing erosion-corrosion and enables the superimposition of erosion-corrosion maps onto real surfaces. The results presented a new technique for mapping erosion-corrosion regimes onto real pipes.

The erosion-corrosion boundaries were defined using ratios of corrosion damage to erosion damage. Predictions from the model were mapped onto a pipe elbow and indicated that there were significant differences between erosion-corrosion regimes,

with dissolution and dissolution-erosion being the dominant mechanisms for pure iron. The methodology also allowed wastage maps to be generated to indicate regions that were most susceptible to degradation, as shown in Figure 5.7.

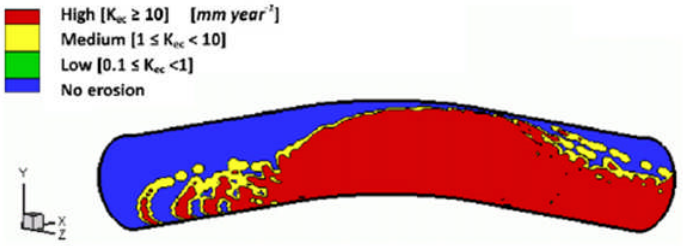

Figure 5.7: Erosion-corrosion wastage maps for the outer surface of elbow-pipe made from iron at pH 7, E_{ap} = -0.6 V (SCE), particle size 1000 µm and concentration of 22.88% - from Stack et al. [120]

5.6 Corrosion Inhibition

One of the most imperative methods of minimising corrosion today is the use of corrosion inhibitors. The use of corrosion inhibition techniques is extensive in industry and many plant operators are heavily dependent upon their successful application.

A corrosion inhibitor can be defined as a substance that, when added in small concentrations to a corrosive system, effectively reduces the corrosion rate of a metal exposed to that environment [152, 153].

Corrosion inhibition has developed from something of a practical art in early times, to today, where it has reached sufficient maturity and scientific status as our understanding of the complex system of metal/electrolyte/inhibitors continuously improves.

5.6.1 Inhibitor Mechanisms and Classification

Corrosion inhibitors are not universally applicable. This statement is somewhat supported by the vast number of chemicals available. The fact that one inhibitor performs well in one set of conditions does not mean it will be effective in another. For the classification of an inhibitor as well as for a discussion of the mechanisms involved, both the metal and environment must be specified. Inhibition usually results from the formation of an adsorption layer or protective film, influencing the electrochemical reactions at the metal-electrolyte interface. In other instances, the chemicals can promote passivation of the metal or modify the solution chemistry [153].

Corrosion rates are determined by the anodic and cathodic reactions, both of which can be influenced by inhibition. Inhibitors can be referred to as anodic, cathodic or mixed depending upon the electrochemical reactions affected. In all these cases, inhibition can result in a reduction in the rate of the rate-determining step, or introduce a new rate-determining step [153].

The addition of a chemical which directly affects the anodic reaction i.e. the metal dissolution process is termed an ‘anodic inhibitor’. The addition of an anodic inhibitor can either lower the rate of the anodic reaction or influence the anodic reaction mechanism, which would result in a change in the Tafel slopes compared to the inhibitor-free solution [153]. This results in an anodic shift of the free corrosion potential.

In a similar way, inhibitors can interfere with the cathodic reactions, creating a negative shift in potential. This can be achieved by either reducing the rate or changing the mechanism of the cathodic reaction. Cathodic inhibitors can also become effective under diffusion controlled conditions by turning the system into a reaction-controlled environment or by reducing the surface concentration of active species e.g. the formation of surface films which reduce mass transport [153].

Certain inhibitors are able to promote the passivation of metals by shifting the corrosion potential into the range positive of the critical passivation of the metal. Inhibitors which are easily reduced can increase the cathodic current density, which can help to induce passivation. However, most passivating inhibitors work by decreasing the current density by restricting the anodic reaction and shifting the anodic potential into regions where passivation would occur. Inhibitors can also be directly involved by forming passive films which differ strongly from those in uninhibited conditions [153]. These films can contain the inhibitor or reaction products formed by the interaction of the inhibitor with the corrosion products.

When designing an organic corrosion inhibitor, a thorough understanding of the corrosion processes and organic chemistry is essential. It is believed that a strong candidate for an effective inhibitor is one which will bond to both cathodic and anodic sites i.e. ‘mixed’ inhibitors.

5.6.2 Chemisorption and Physisorption

Riggs [154] suggested that organic molecules inhibit corrosion by becoming adsorbed at the metal-solution interface. The level of adsorption depends on the

chemical nature of the inhibitor, the environment, the metal surface condition and the electrochemical potential at the interface [155].

The adsorption process of an inhibitor is governed by the residual charge on the surface of the metal and by the chemical structure of the inhibitor. Organic inhibitors tend to be adsorbed either through physical means or by chemisorption [152].

Physical adsorption is due to the electrostatic attraction between the inhibiting ions and the electrically charged surface of the metal. The surface charge is defined by the position of the free corrosion potential of the metal with respect to its potential of zero charge. If the metal potential is greater than the potential of zero charge, the metal is positively polarised and the adsorption of anions is preferred. Conversely, the adsorption of cations is preferred if the free corrosion potential is below the potential of zero charge [155]. The forces in electrostatic adsorption are generally weak and can be desorbed easily as the ions are not in direct contact with the metal. A layer of water molecules separates the metal from the ions [152].

In chemisorption, the inhibitor molecules are in contact with the metal surface. A co-ordinate bond involving electron transfer between the inhibitor and the metal is assumed to take place. The chemisorption process is slower than electrostatic adsorption, possessing a higher activation energy and higher efficiency at elevated temperatures [155]. Unlike electrostatic adsorption, it is specific for certain metals and the types of material and inhibitor place a decisive effect on the bond. When inhibitor molecules have an unshared, lone pair of electrons on the donor atom of the functional group, electron transfer is facilitated from the inhibitor to the metal [152]. Chemisorption usually involves significant charge transfer which results in a shift in the zero charge potential.

The adsorbed inhibitor may not cover the entire surface, but occupies sites which are electrochemically active, thereby reducing the degree of some reactions. The corrosion rate is believed to decrease proportionally with the quantity of sites blocked by the inhibitor [152].

5.7 Mitigation of Erosion-Corrosion Using Film-Forming Inhibitors

A number of corrosion inhibitors are capable of forming protective 3D films on the metal surface. The films may consist of adsorbed multilayers, salts, or reaction products formed as a result of the interaction between the inhibitor and solution species at the metal surface [153].

Thick corrosion inhibiting layers are capable of forming via precipitation from the solution. This can be a result of precipitation of oxides/hydroxides, the reaction of the inhibitors with metal ions in the solution or the reduction/decomposition of the inhibitor at the metal surface followed by precipitation [153].

Protective films may also be formed directly at the metal-solution interface via a 3D growth mechanism. The first step of this process is usually the monolayer adsorption of the inhibiting species. The process is then followed by multilayer adsorption (hydrophobic interactions) or by a reactive growth process, in which ions of the protected metal are incorporated into the film [153].

The performance of film–forming inhibitors is intrinsically connected to the persistence and/or regeneration of the protective film and will be a function of the aggressive environments around them. Main factors which effect the active mechanism of these substrates include CO_2 partial pressure, temperature and particularly the hydrodynamic flow and presence of sand particles in the process fluid [156].

Chemical inhibitors are used throughout the world to mitigate the effects of corrosion in aggressive environments. However, there are concerns surrounding inhibitors capabilities in high velocity flows or in systems containing sand particles.

Studies by Dave et al. [6] found that an amidoamine fatty acid inhibitor was able to significantly reduce the corrosion component of material loss in erosion-corrosion environments at 50°C, 13 m/s and 1 wt.% sand. However, the presence of sand disrupted the inhibitor film and increased the rate of dissolution of the carbon steel as shown in Figure 5.8. Although sand presence did increase the corrosion rate in the system, increasing inhibitor concentration reduced the effect of film disruption and improved the level of corrosion protection. Despite this increase in overall efficiency, the inhibitor failed to reduce the level of erosion damage on the surface. In inhibited erosion-corrosion systems where sand concentration is high, the metal loss rates could be higher than the target ranges due to the mechanical damage component alone.

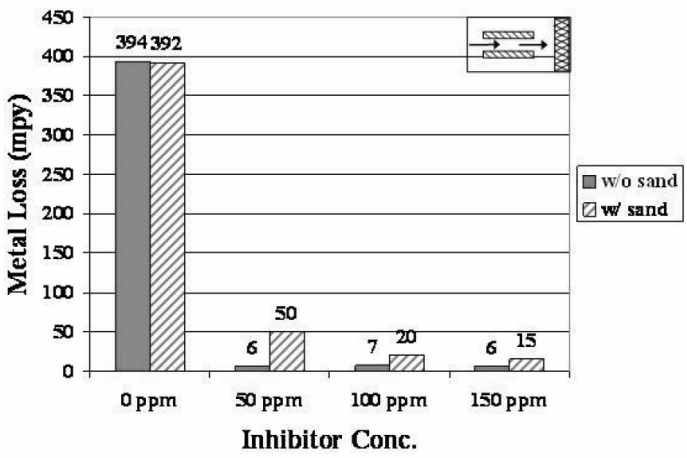

Figure 5.8: *In-situ* corrosion rates in an erosion-corrosion environment at 50°C, 13 m/s and 1 wt.% sand – from Dave et al. [6]

Many authors have also found that chemical inhibition can significantly reduce the corrosion component of damage in erosion-corrosion environments, but fails to offer little or no resistance to pure erosion [112, 157-160]. With the increasing trend of oil and gas companies operating with small levels of sand in CO_2 systems, there is an ever increasing demand for corrosion inhibitors in erosion-corrosion environments which can reduce the mechanical damage as well as the dissolution of the material.

Indeed, there are aspects of the literature suggesting there is potential for inhibitors to meet this requirement, especially in environments where $FeCO_3$ formation occurs. Jasinski [161] found that an amine based corrosion inhibitor was able to transform the morphology of the corrosion product scale that forms in CO_2 conditions, making the scale a lot more compact. Shadley et al. [139] speculated that the denser scales formed under the presence of inhibitors in environment such as these may possess more erosion resistant properties than ones formed without inhibitor, suggesting inhibitors may be capable of reducing the erosion component associated with erosion-corrosion processes.

Despite significant work being conducted by the University of Leeds [117, 118, 132, 142-144, 162-165], the ECRC at the University of Tulsa [6, 109, 137-141, 166] and Baker Petrolite [112, 157-160] on erosion-corrosion inhibition, only a limited number of these studies have focused on whether chemicals do exist to control the mechanical erosion mechanism in an erosion-corrosion environment.

Certainly, research by Wang et al. [142, 162, 167] and Akbar et al. [8, 9] at Leeds University has suggested that the application of high shear CO_2 corrosion inhibitors may help to reduce the erosion component as well as the synergy which exists

between erosion and corrosion. However, this area is in need of further attention to elucidate whether certain chemicals can control these types of systems effectively and establish the various mechanisms by which this is achieved.

5.8 Summary of Erosion-Corrosion and its Inhibition

In CO_2 environments containing sand, the level of damage can be significantly increased when protective $FeCO_3$ films are removed, exposing fresh surfaces to corrosion attack. This can result in severe localised corrosion. An erosion-corrosion regime can result in a breakdown of models which are developed solely for CO_2 corrosion or pure aqueous erosion. There is therefore a requirement for a model which takes into account both processes occurring simultaneously.

Different researchers have applied computational, empirical and experimental methods to understand and investigate the phenomenon of erosion-corrosion. However, the development of a generic erosion-corrosion model for the oil and gas industry is something which has received little attention. Part of the reason behind this is that erosion-corrosion is a complex process because of the number of factors influencing the degradation mechanism.

In recent years, studies of erosion-corrosion have yielded significant advancements in the modelling of its processes. Although it is still not fully understood mechanistically, various modelling approaches have been developed, concentrating on different kinds of output data. Certainly, predictions of erosion-corrosion must account for variables affecting both corrosion and erosion mechanisms. Corrosion rate predictions account for variables such as pH, water chemistry, fluid properties, flow conditions, flow geometry and target material properties. If solid particle erosion is included, then additional variables such as sand size, shape and concentration need to be included in the modelling approach.

Numerous researchers have highlighted the capabilities of inhibitors to be effective in erosion-corrosion environments. However, the inhibitors tend to work by reducing only the corrosion component of damage, leaving the erosion component unaffected. This is far from ideal if the level of mechanical damage in the system already exceeds the target set by industry.

Research has suggested that certain inhibitors may be able to reduce the mechanical damage attributed to erosion-corrosion, but this aspect requires further study and an understanding of the mechanisms is paramount to aid the development of chemicals to control these harsh environments.

Chapter 6 - Industrial Problem - Development of an Erosion-Corrosion Model to Quantify Degradation Rate on an Offshore Facility

6.1 Introduction

The influence of CO_2 corrosion has been extensively studied since first recorded over 70 years ago in the United States oil and gas industry [1]. The effects of this prevalent form of attack and its consequences have long been recognised, with significant research being directed towards understanding the mechanisms by which carbon steel corrodes in a CO_2 environment [48, 51].

Since the development of de Waard and Milliams' first CO_2 corrosion model in the 1970's [46], laboratory tests, coupled with field experience have been used to further understand the mechanisms attributed to this particular form of corrosion. A complete understanding of CO_2 corrosion is paramount to enable researchers to ensure its control and prevention [168].

In terms of CO_2 prediction, de Waard and Milliams [46, 85] led the way and their studies have provided reference points for many CO_2 corrosion researchers over the past few decades.

Today, numerous mechanistic [48, 70, 83, 84], semi-empirical [46, 58, 59, 85] and empirical models [88, 169] have been developed to predict CO_2 corrosion rates. Company corrosion mitigation strategies and inspection regimes rely heavily on the predictive capabilities of these models. Commercially available prediction tools used by industry, such as the Norsok model [77] and the parallel resistance model proposed by de Waard and Milliams [85] offer an excellent interpretation of how changes in some of the key parameters affect corrosion rates. Their main limitation is that they are generic in nature and cannot account for changes in some of the more specific environmental properties of process fluids, especially variations in brine chemistry. A culmination of changes in solution chemistry and even changes in material composition can result in very different rates of corrosion observed to those predicted by commercially available models [77].

A more accurate and reliable approach to predicting the rate of material thickness loss for a facility is to conduct laboratory experiments which replicate the environmental and physical conditions on the facility more precisely. Evidently, this is not possible when constructing a generic model, but if prediction is required over

a set of very specific conditions on one field, this is undoubtedly a superior approach.

Although predictive models exist for CO_2 corrosion, far less research has focused on the modelling of erosion-corrosion in CO_2-containing environments, even though this form of degradation has become important in the oil and gas industry. A combination of the corrosive medium and the presence of sand particles creates an erosion-corrosion environment which can result in exceptionally high rates of material loss if production rates are above a certain threshold velocity [139]. This can lead to CO_2 corrosion models under-estimating the rate of material loss, leading to ambiguity surrounding asset integrity. The demand for erosion-corrosion models within the oil and gas industry is increasing, especially with the rising trend of operating facilities with small concentrations of sand [6].

Regrettably, erosion-corrosion models which do exist [139, 149, 170] tend to be for very specific conditions because of the complex degradation processes involved. As a result, problems then tend to arise if these models are used outside of the regions in which they have been experimentally validated.

Other, more generic erosion-corrosion models which pursue a mechanistic approach or involve computational fluid dynamics (CFD) [7, 151] cannot be readily used by industry because certain information on the approach adopted remains withheld in publications, making it difficult for companies to accurately predict degradation rates on facilities which produce sand without specific laboratory tests. Ultimately the corrosion management strategy can become affected and this can result in a potential increase in the risk of failure or overcompensation with respect to factors such as material specification and inhibitor dose rate.

6.2 Problem Background and Chapter Outline

Between 2005 and 2010, the carbon steel pipelines on a particular offshore facility in the North Sea were reported to be suffering from high uniform degradation as well as several failures attributed to localised attack. The lines were known to be carrying small concentrations of sand which were believed to be accelerating the degradation process. The company requested that the influence of sand presence on the system degradation rate was explored and that an empirical model be generated to determine the rates of pipework thickness loss on the facility.

The research presented in this Chapter focuses on the development of an empirical erosion-corrosion model generated using data from submerged impinging jet

laboratory apparatus. The program of experiments set out to create a means of prediction using the material loss data from submerged impinging jet tests over a range of conditions replicating those on the facility. The model is compared with two commercially available CO_2 corrosion models and its performance is reviewed against inspection data for the facility. Consideration was also given to the current use of inhibition on the facility at its dose rate of 10 ppm, which was subsequently incorporated into the model.

An analysis of why the Leeds model predicts the degradation rates more effectively on the facility compared to other models is presented using Computational Fluid Dynamics (CFD). The limitations of the model are discussed, along with suggestions for ways to develop the Leeds model further. A schematic outlining the course of the work in this Chapter is provided in Figure 6.1.

It is worth noting that this Chapter establishes an industrial framework and forms the transition from an industrial problem into scientific research for the subsequent Chapters.

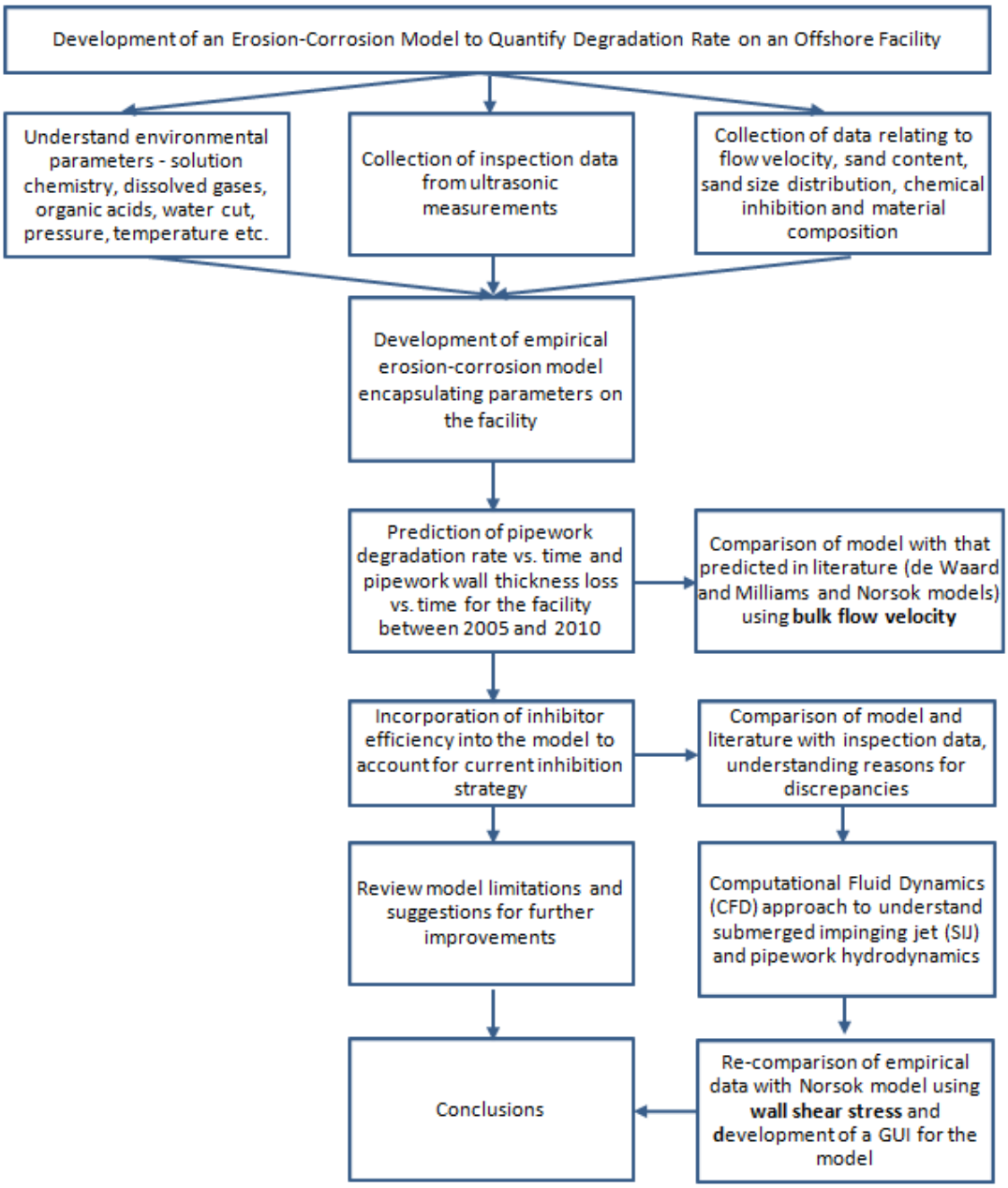

Figure 6.1: Outline of Chapter 6

6.3 Initial Pipework Inspection

Since 2005, a number of leaks were reported on the carbon steel pipelines of an offshore facility in the North Sea. Various spools of the pipework removed from the line were not only found to experience high uniform degradation rates, but regions of severe localised attack. Examples of typical failure mechanisms on the facility are provided in Figure 6.2(a)–(d).

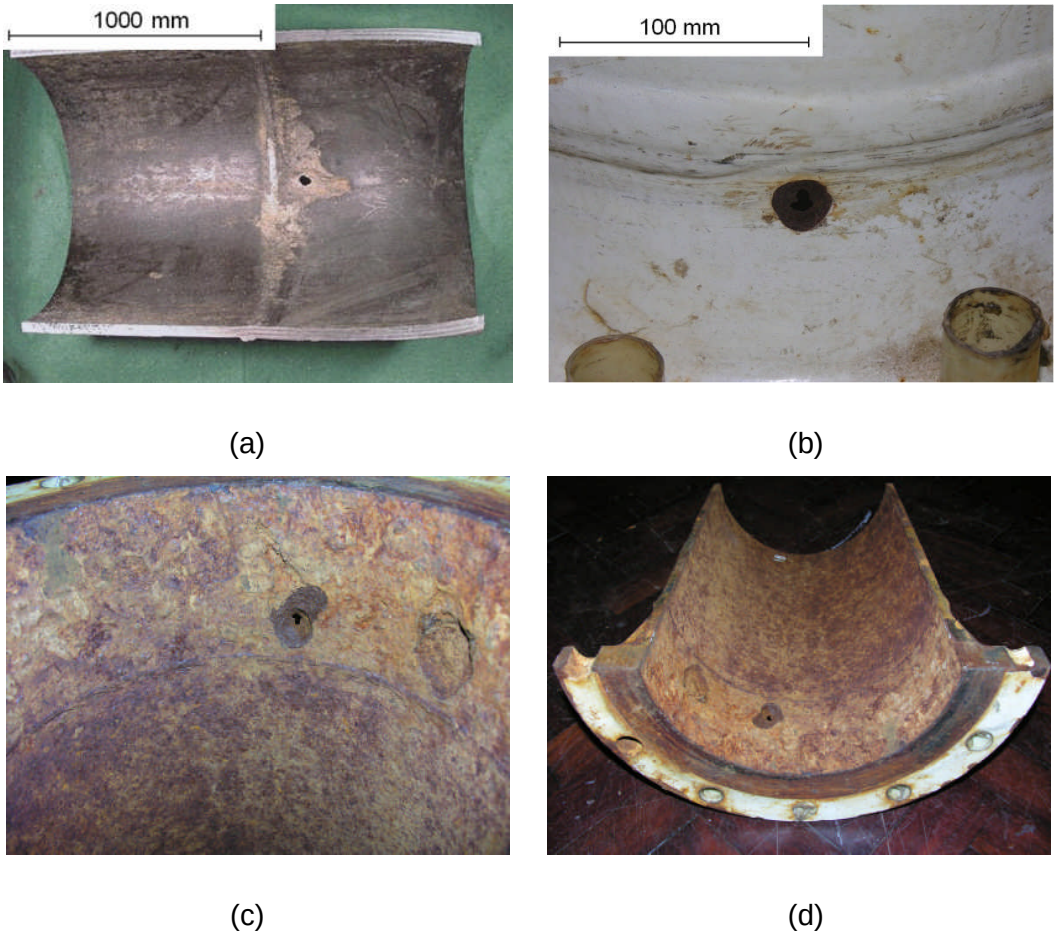

Figure 6.2: Images of pipework from an offshore facility showing points of failure and severity of degradation

6.4 Operating Conditions of the Field

Information relating to environmental and physical properties of the process fluid on the facility was gathered to ensure that tests represented field conditions. This section details the operating conditions for the facility in question.

6.4.1 Solution Chemistry

6.4.1.1 Dissolved Salts

Understanding brine chemistry is one of the most important preconditions for predicting CO_2 corrosion behaviour [49]. It was essential to achieve a strong representation of the process fluid chemistry to allow as accurate corrosion prediction as possible. Various process fluid compositions were provided by the company from a number of wells. Table 6.1 shows the most recent brine composition measurement on the line which was used throughout the course of this research. Based on a comparison with other compositions, the values measured were typical of the line. Table 6.1 indicates the maximum and minimum concentrations measured during the lifetime of the wells.

Table 6.1: Recent brine composition of produced fluid from the offshore facility in comparison to minimum and maximum concentrations recorded

Ion	Recent measurement (mg/L)	Minimum over last 5 years (mg/L)	Maximum over last 5 years (mg/L)
Sodium	10700	7794	11687
Potassium	370	156	403
Calcium	378	300	696
Magnesium	1113	830	1387
Barium	9	0	25
Strontium	11	5	53
Chloride	19570	13507	20702
Sulphate	2382	278	2839
Bicarbonate	221	97	268

6.4.1.2 Dissolved Gases

The brine solution in Table 6.1 has a pH of 7.7 when aerated and a pH of 5.4 when fully saturated with CO_2. The pH of the solution on the facility was estimated at between 5.5 and 6.0 depending upon the line and CO_2 content.

The levels of H_2S within the majority of the wells used by the facility are between 0.1 and 1 mg/L. It is well known that the presence of H_2S in a CO_2 environment can influence the corrosion mechanism [44]. At low concentrations, H_2S is capable of increasing the CO_2 corrosion process by acting as an accelerant of the anodic dissolution through sulphide adsorption as well as reducing the pH [44]. H_2S is also capable of decreasing the corrosion rate through the formation of a protective sulphide scale [44]. The exact influence H_2S has on the anodic dissolution reaction in the presence of CO_2 is still not fully understood [44].

As a general rule for CO_2 environments, the presence of H_2S can:

- Increase the risk of corrosion through:
    - the facilitation of localised corrosion [44], or
    - the preferential formation of an FeS corrosion product which offers less protection that an iron carbonate film [44]
- Reduce the risk of corrosion by:

- forming a FeS corrosion product which replaces a less protective iron carbonate film [44]
- forming a combined protective layer of FeS and $FeCO_3$ [44]

In the presence of both gases, the corrosion process tends to be governed by the dominant acid gas. A notion has been introduced which considers three different corrosion domains based on the dominance of the corrosion mechanism [44]. These are shown in Table 6.2.

Table 6.2: Corrosion domains determined by relative concentrations of CO_2 and H_2S [44]

CO_2/H_2S < 20	Corrosion dominated by H_2S
20 < CO_2/H_2S < 500	Mixed CO_2/H_2S dominance
CO_2/H_2S > 500	CO_2 corrosion dominates

H_2S was not included in the brine chemistry because of the hazards associated with dealing with this particular gas. For a fully CO_2-saturated solution at 45°C and atmospheric pressure, 1 litre of brine would contain 480 cm^3 of CO_2 which is approximately 0.8 g (or 800 mg in one litre). This gives a CO_2/H_2S ratio of approximately 800, indicating that the corrosion process is dominated by CO_2 and justifying the omission of H_2S in this circumstance. Additionally, studies by Nešić et al. [84] indicated that the presence of H_2S in concentrations below 10 ppm led to a reduction in corrosion rate, meaning that the data determined from the jet impingement tests would be likely to represent a 'worst case' scenario.

6.4.1.3 Organic Acids

No information was provided on the levels of organic acids in the system (particularly acetic acid (HAc)). The presence of acetic acid has been shown to influence the corrosion process [171]. Although HAc is a weak acid, it is stronger than carbonic acid [52, 53]. It has been reported that HAc can mildly increase the cathodic reaction of the corrosion process [171], but other researchers have reported that HAc can work as an inhibitor [53]. It is this authors opinion that temperature appears to be a key influence on the corrosion rate when HAc is present in process fluids. Experiments conducted by Gulbransen and Bilkova [53] in

systems at 25°C showed that HAc caused ennoblement of the potential of carbon steel and a reduction in corrosion rate, signifying anodic inhibition. For concentrations of 60 ppm and above, the corrosion rate decreased with increasing HAc content. Conversely, tests performed by Hedges and McVeigh [171] at 60°C showed that HAc had no significant impact on corrosion rate until concentrations of 2000 ppm were reached. Concentrations above this value saw a dramatic increase in corrosion rate. When tests were conducted at 80°C by Gulbrandsen and Bilkova [53], corrosion rate increased dramatically at concentrations of 60 ppm and higher.

It is generally accepted that enhanced corrosion by HAc is caused by a decrease in the pH and increase in the solubility of Fe^{2+} which reduces iron carbonate film thickness and its propensity to form [171]. The presence of HAc tends to be influential at high temperatures (above 60°C). Gulbrandsen and Bilkova [53] stated that the formation of acetate complexes of Fe^{2+} and Ca^{2+} should be considered at high temperatures because they can reduce the driving force for the formation of protective films.

The assumption was made that HAc did not significantly affect the corrosion process in this specific environment based on the fact that:

- the solution pH in the SIJ was already slightly below that measured in the well (therefore the pH effect of HAc could be neglected)
- the concentration of HAc was too low to be of concern (based on other facilities measuring less than 150 ppm HAc on other North Sea wells)
- the temperature was too low (no protective scale formation should occur at this temperature, so protective film formation is of no significance)

6.4.1.4 Presence of Crude Oil

The pipework transports a mixture of crude oil and water from a low pressure separator with a relatively steady water cut of approximately 95%. Water cut levels have remained the same for at least the past 10 years. A recent analysis of process fluid samples from the facility indicated an oil presence of 7.2 and 2.2%. Tests for generating the empirical model were performed without the presence of crude oil. It was assumed that such a high water cut would result in the crude oil having no effect in terms of reducing water wetting based on the work by de Waard et al. [85]. The presumption was also made that the inhibition effects offered by the presence of the crude oil (if any) were negligible.

6.4.2 System Pressure

Known pressures throughout the line are included in Table 6.3.

Table 6.3: Pressure in the line of the offshore facility

Position	Pressure (bar)
Low Pressure Separator	1.1
Oil Cooler Inlet	1.55
Oil Cooler Outlet	1.24
LCV Outlet	2.6
Top of Line	1.7

One of the limitations of the submerged impinging jet is that it is not capable of operating above atmospheric pressure. Seeing as pressures in the line were close to atmospheric, the use of the SIJ was deemed acceptable.

6.4.3 Flow Velocity

Outputs from a flow rate indicator positioned on the line enabled the volumetric flow rate in m^3/day to be obtained between 2005 and 2010. This was converted into a flow velocity based on the pipework diameter and is provided in Figure 6.3 for one of the lines.

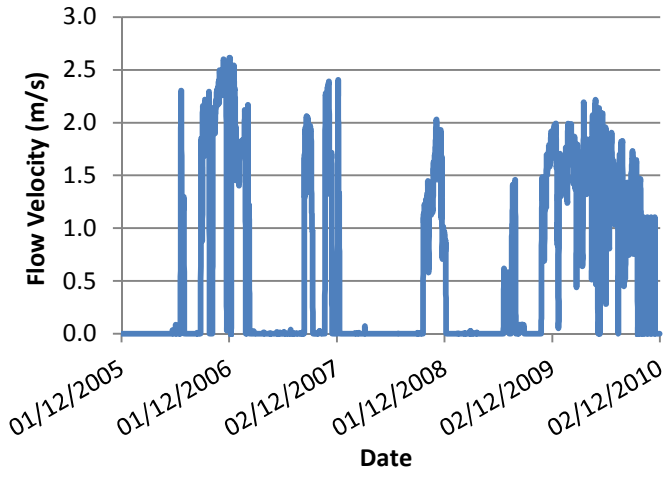

Figure 6.3: Variation in flow velocity over a 5 year period for lines on offshore facility

6.4.4 Temperature

A temperature sensor positioned before the process fluid reaches the run-down lines provided data for between 2005 and 2010 as shown in Figure 6.4. The

average temperature on the lines is generally between 42 and 45°C. Temperature excursions are sometimes experienced due to dewaxing, meaning that temperatures can rise to 50°C for brief periods.

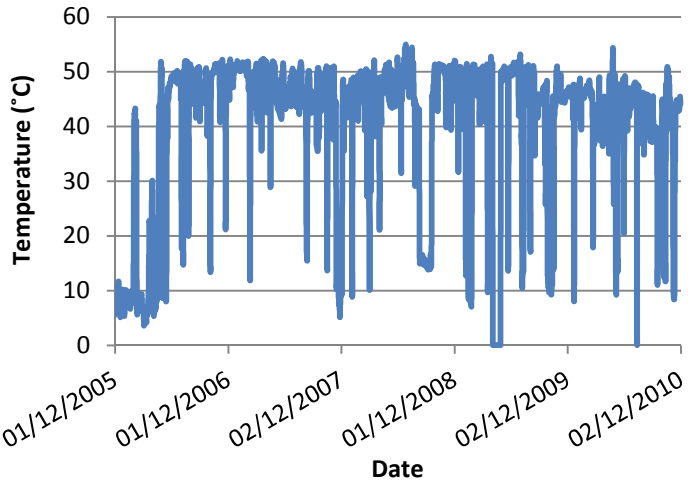

Figure 6.4: Variation in temperature over a 5 year period for lines on offshore facility

6.4.5 Sand Content and Size Distribution

Sand concentration in the system is measured and monthly totals are obtained through the use of acoustic sand monitors. The average sand production for one line is shown in Figure 6.5. The graph shows that sand content has not risen above 30 mg/L in the past 5 years based on monthly records for this particular line. However, sand levels have been recorded around 400 mg/L on other lines on the same facility. This information proved essential when determining the sand loading parameter range for the submerged impinging jet experiments.

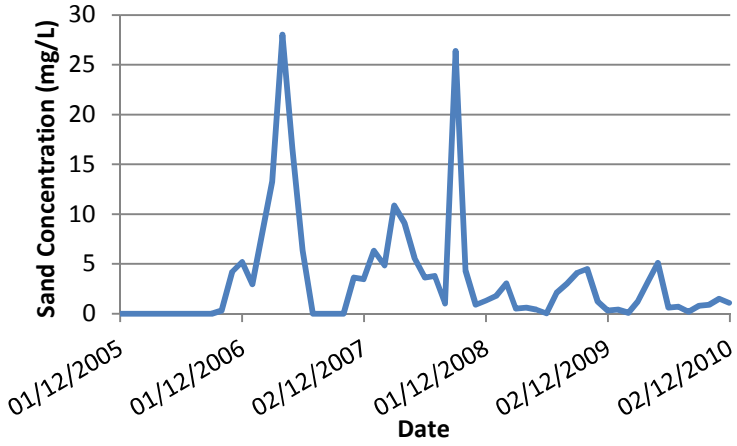

Figure 6.5: Monthly sand concentrations on offshore facility over a 5 year period

Two samples of sand were taken from the system for particle size analysis and the distributions are provided in Figure 6.6. Both samples possessed very similar distributions, with the mean particle size around 250 µm. HST60 sand was chosen for use in the laboratory tests as it possessed a very similar particle size distribution to the two samples, with the average diameter occurring around 250 µm. An SEM image of the HST60 sand particles is shown in Figure 6.7.

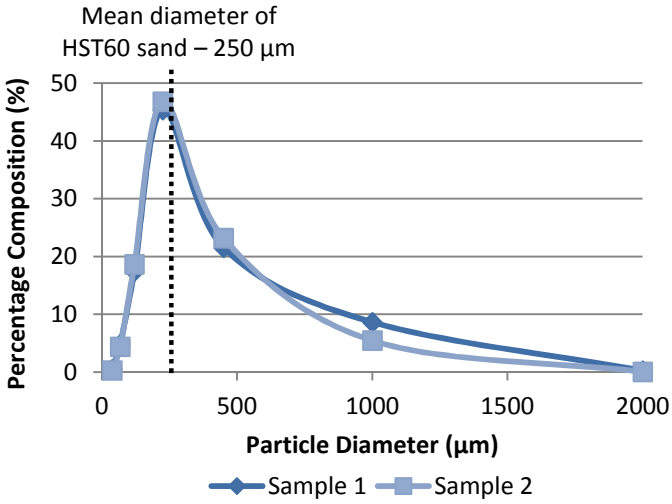

Figure 6.6: Sand particle size distribution for two samples taken from an offshore facility

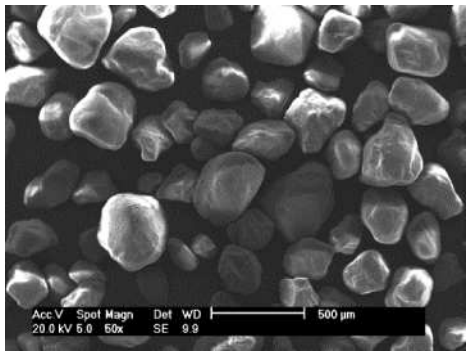

Figure 6.7: SEM image of HST60 sand particles used in jet impingement tests – average diameter of 250 µm

Consideration of particle size distribution is important as Jordan [107] showed that erosion rates increase with increasing particle size (over and above the mass increase effect). It is believed that above 300 µm, the erosion rate no longer increases with particle size [107].

Although the hardness of the sand particles was not determined, the assumption was made that this variable did not influence the degradation rate due to the

ductility of carbon steel. Finnie [103] commented that for ‘soft’ steels, the erosion rate increases with particle hardness until it exceeds that of the steel. As a guide, the typical Vickers hardness of silica sand is approximately 590, where as the carbon steel for these tests was measured between 130 and 140 using a micro-indenter.

6.4.6 Chemical Inhibition

Chemical inhibition is used in an attempt to mitigate the effects of degradation on the facility. This has been administered at a dose rate of 10 ppm since before 2005. The inhibitor chosen (referred to as ‘Inhibitor A’ from here onwards) is known to contain a blend of chemicals listed in Table 6.4. To respect confidentiality, the exact type and composition of some of the chemicals was withheld. However, the information provided is sufficient for the purpose of the thesis.

Table 6.4: Composition/information on chemical components of Inhibitor A

Chemical Name	Content
2-(2-Butoxyethoxy)ethanol	5 - 10%
Ethandiol	5 - 10%
Ethoxylated Amine Salt	10 - 30%
Propan-2-ol	< 1%
Quaternary Ammonium Salts	1 - 5%

6.4.7 Inspection Data for Pipework

Inspection data for the facility came in the form of manual ultrasonic inspection (UT) and measurements using Time Of Flight Diffraction (TOFD) for the welded regions.

6.4.7.1 Ultrasonic Testing

Ultrasonic testing is a form of non-destructive test which uses high frequency sound energy to detect flaws, characterise materials or determine the thickness of particular objects, allowing the user to monitor pipework corrosion [172].

Pulse-echo ultrasonic measurements such as manual normal beam ultrasonics (MUT) can detect corrosion defects reliably from a 2 mm depth onwards for the application on this facility. In UT inspection, a high frequency ultrasonic wave is introduced and propagates through the pipe wall. When a discontinuity (e.g. localised corrosion) is reached, part of the energy is reflected back from the

corroded surface [172]. The duration the signal takes to be reflected back can be directly related to the distance travelled and hence, the wall thickness.

The performance of UT is operator-dependent and extensive knowledge is required for the development of inspection procedures [172]. An advantage of the technique is that information about the location, size and orientation can be gathered. Only single-side access is required when using the pulse-echo technique [172].

As for the use of the TOFD method of ultrasonic inspection, this technique is suited to the non-destructive testing on and around welded regions. In the TOFD system, probes are placed on either side of the weld. One probe emits an ultrasonic pulse that is detected by the other probe. The signals detected by the receiver come in the form of two waves (one from along the surface and one reflecting from the far wall). Attack at or around the welded region causes the waves to diffract. Based on the time of flight of the pulse, the depth of the attack can be calculated.

Unfortunately for both these techniques, materials which are rough, have an irregular shape or are hard to access are difficult to measure. A number of problems with performing UT and TOFD inspection on the facility was the lack of access to specific areas and the difficult circumstances on the facility.

Based on the data which was collected via UT and TOFD, two rates of degradation can be obtained for the facility (as shown on each axis in Figure 6.8) which indicate vital information. The left axis determines the degradation rate on the facility based on how long the pipework has been in service. The right hand axis expresses material thickness loss in terms of how long fluid has been flowing through the pipelines i.e. the time spent in production. This type of analysis presumes that the pipework does not corrode when there is no fluid flow. With fluid only travelling through the pipework a small percentage of the time, the difference between the two interpreted degradation rates is significant. Errors bars in Figure 6.8 are provided to express the degree of ambiguity over the initial wall thicknesses of the pipework and to incorporate the uncertainty surrounding the type of measurement technique implemented.

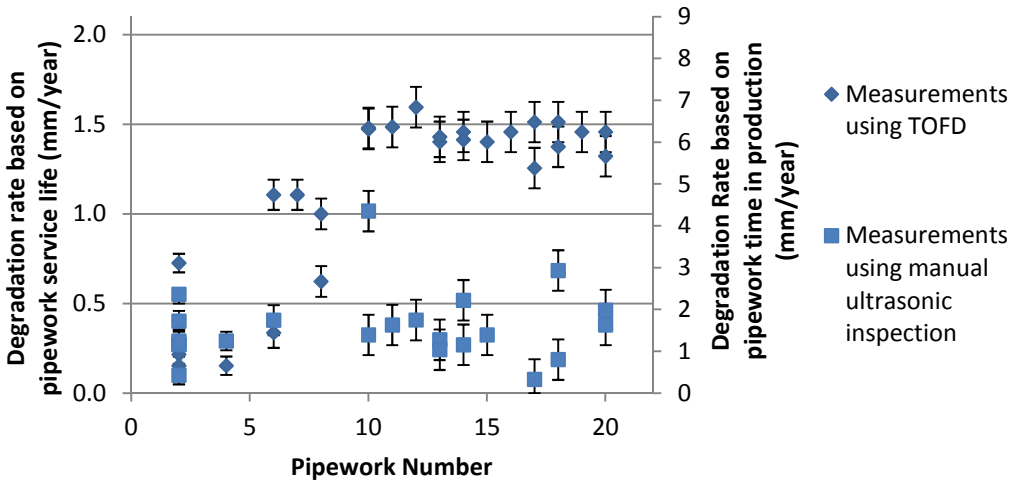

Figure 6.8: Inspection data for pipework based on results from manual ultrasonic inspection (UT) and time of flight diffraction (TOFD) – axes show degradation rate based on service life (left) and time in production (right)

6.5 Experimental Procedure

6.5.1 Material

All carbon steel samples tested were cut from one section of pipework which had been taken out of service from the system of the offshore facility. The chemical composition of the material is provided in Table 6.5. An optical microscope image of the parent metal is provided in Figure 6.9 after etching for 10 seconds in 2% nital solution. This image reflects a uniform distribution of pearlite (α-ferrite and cementite) and ferrite phases. These images are taken from the radial perspective and therefore show the distribution of ferrite and pearlite exposed to the process fluid. Examining the distribution from a perspective perpendicular to this indicated a banded distribution of pearlite and ferrite. Mishra et al. [168] and Al-Hassan et al. [68] believed a higher corrosion rate can be predicted when the distributions of pearlite in a ferrite matrix are more evenly distributed as opposed to being present in bands. This was attributed to the increase in interfacial area between the phases.

Prior to starting every experiment, the brine solution was sparged with CO_2 for a minimum of 12 hours to achieve an oxygen concentration of below 20 ppb.

Table 6.5: Composition of carbon steel parent metal (wt.%)

Element	Composition (wt.%)
Carbon	0.120
Silicon	0.210
Manganese	0.960
Phosphorus	0.019
Sulphur	0.003
Chromium	0.060
Molybdenum	0.030
Nickel	0.090
Aluminium	0.035

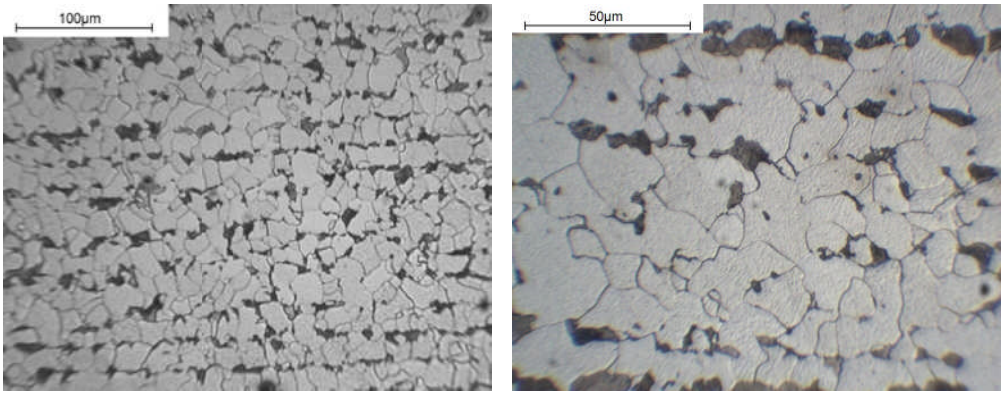

(a) (b)

Figure 6.9: Optical microscope images of carbon steel parent metal after being polished and etched in 2% nital solution for 10 seconds indicating a fine grained ferrite (lighter) and pearlite (darker) microstructure

6.5.2 Flow-Induced Corrosion and Erosion-Corrosion Tests

Flow-induced corrosion and erosion-corrosion tests were conducted using a submerged impinging jet (SIJ) apparatus shown in Figure 6.10. The vessel has a 70 litre capacity and operates at atmospheric pressure. A re-circulating system is adopted by the rig which enables the mixture of fluid and sand to be delivered through a dual nozzle arrangement which impinges onto a flat specimen at an angle of 90˚. The nozzle is 8 mm in diameter and was positioned at a fixed distance of 5 mm from the specimen. The carbon steel specimens were cut from the pipework, machined to 20x20x6 mm pieces and wet-ground up to 1200 silicon carbide abrasive paper. Prior to starting experiments, the working electrodes were

degreased with acetone, rinsed with distilled water and dried with compressed air before weighing.

Weight loss measurements were taken using a balance accurate to 0.01 mg and then converted into a thickness loss based on the total surface area of the sample exposed to the jet.

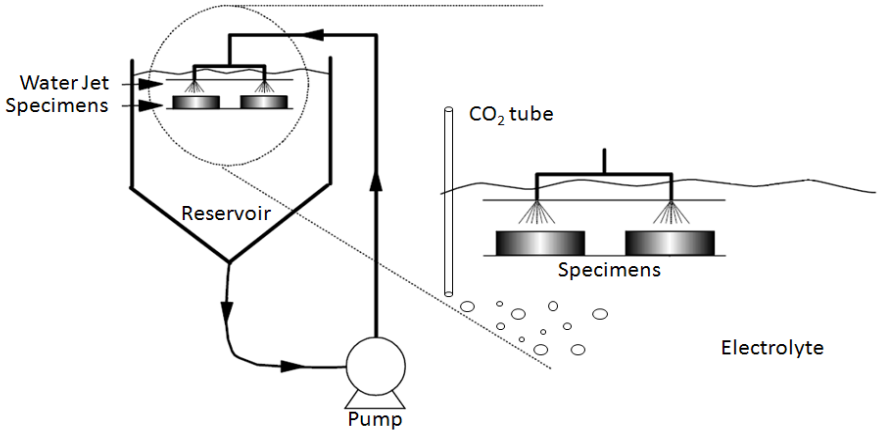

Figure 6.10: Re-circulation rig for CO_2 flow-induced corrosion and erosion-corrosion weight loss experiments

Tests ran for 4 hours and specimens were weighed before and after the test (after cleaning the surface with Clarke's solution which comprised of 1000 ml HCl, 20 g antimony trioxide (Sb_2O_3) and 50 g stannous chloride ($SnCl_2$) [173]) to determine the total weight loss. The vessels were sealed in every test and CO_2 was bubbled into the system throughout the experiment to keep the solution fully saturated and the pH at 5.4. Tests were conducted at flow velocities of 1-5 m/s in 1 m/s increments and a fixed temperature of 45°C. Tests were performed without solid loading for flow-induced corrosion tests and with the addition of 100 mg/L and 500 mg/L of sand to represent erosion-corrosion environments.

6.6 Weight Loss Experiments for Empirical Model

6.6.1 Prediction of Thickness Losses without Inhibition

Mass loss results from the submerged impinging jets are provided in Figure 6.11 for velocities from 1-5 m/s and sand loadings of 0, 100 and 500 mg/L. Although most velocities on the facility were between 1 and 3 m/s and sand loadings tended to be below 100 mg/L, it was decided to include tests at higher velocities and sand loadings. This would mean that the developed prediction tool could be used on other pipelines and for the current lines in the future should production rate or sand

loading increase. Figure 6.11 also shows the predicted corrosion rates from the de Waard and Milliams 1995 model [85] and the Norsok model [88] as a comparison.

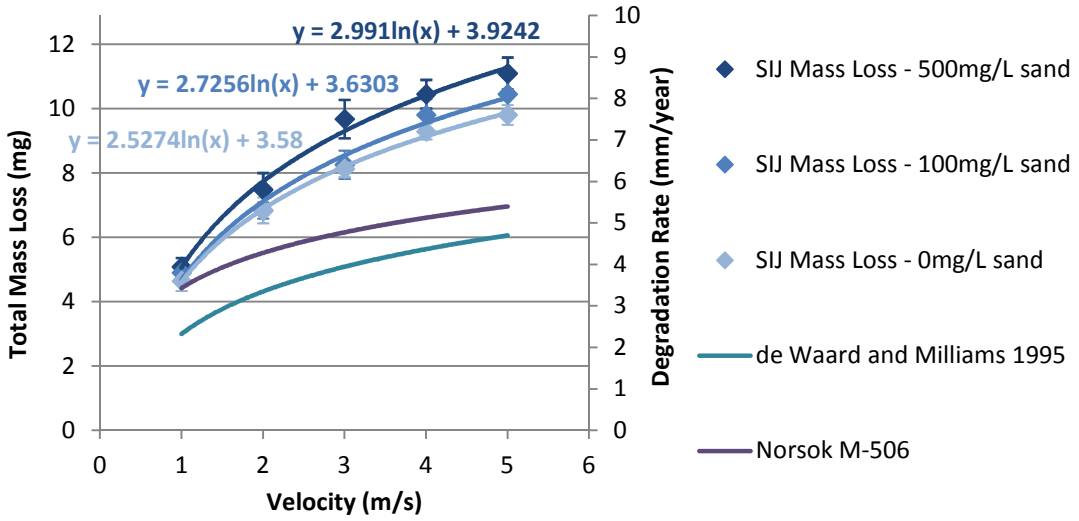

Figure 6.11: Mass loss results from tests conducted at velocities from 1-5 m/s and sand loading from 0 mg/L to 500 mg/L in comparison to commercially available CO_2 corrosion models for the same conditions, which do not consider sand content

Flow-induced corrosion rates (very light blue line in Figure 6.11) recorded using the submerged impinging jet were higher than both of the two commercially available prediction models. Tests with and without sand follow a logarithmic trend comparable with that of the Norsok and de Waard and Milliams models provided in Figure 6.11.

The Norsok model is purely an empirical model based on single phase flow loop experiments. A detailed description of the model is provided by Halvorsen and Søntvedt [88]. Essentially, the model is based on a number of curves fitted to data from a database containing over 2400 data points at various temperatures, partial pressures, pH's and wall shear stresses. Linear interpolation is used in order to predict corrosion rates between temperatures. The equation and factors used for various temperatures are provided in the manual for the standard [78]. The model does not take into account the presence of HAc or H_2S and is meant primarily as a guidance tool for material selection and for the determination of required corrosion allowance. Input parameters for the calculation of the corrosion rate include pressure, pH, temperature and shear stress as shown in the interface in Figure 6.12(a). Values of shear stress are calculated by the model based on the environmental conditions and pipe geometry (Figure 6.12(b)).

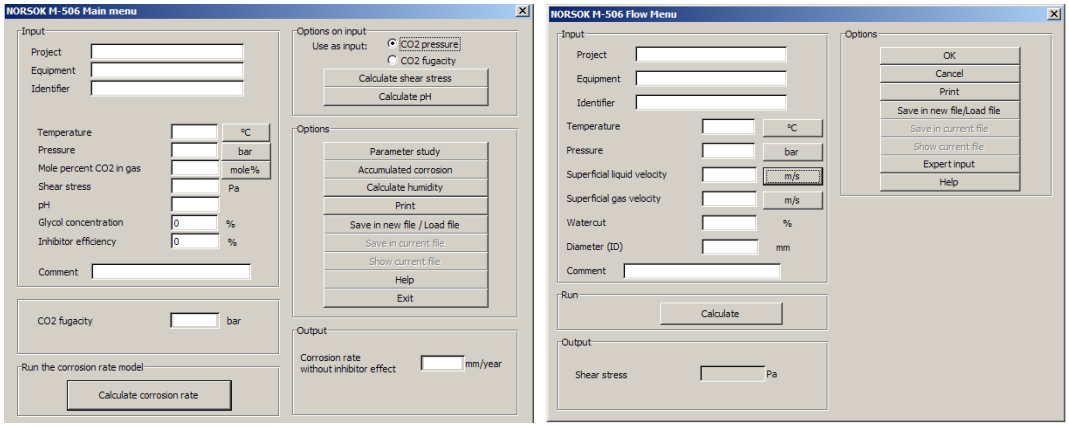

(a) (b)

Figure 6.12: Interface for the Norsok model

The de Waard and Milliams semi-empirical model from 1995 [85] is also based on a large number of flow loop tests. The model combines both flow dependent and independent mechanisms through a resistance model which is a refined version of the model from 1993 [59]:

$$\frac{1}{V_{cor}} = \frac{1}{V_r} + \frac{1}{V_m} \tag{6.1}$$

$$\log V_r = 4.93 - \frac{1119}{T + 273} + 0.58 \log P_{CO_2} - 0.34(pH_{actual} - pH_{CO_2}) \tag{6.2}$$

$$V_m = 2.45 \frac{U^{0.8}}{d^{0.2}} P_{CO_2} \tag{6.3}$$

where the first term on the right (V_r) in Equation (6.1) represents the rate of electrochemical process, the second term (V_m) denotes the mass transfer rate and V_{cor} represents the corrosion rate. For Equation (6.2), T is the temperature in ˚C, P_{CO2} is the partial pressure in bar and pH_{actual} and pH_{CO2} are the pH values of the aerated solution in the presence of dissolved salts and with dissolved CO_2, respectively. For Equation (6.3), U is the flow velocity in m/s and d is the pipe diameter in m.

The addition of sand to the jet impingement system caused degradation rate to increase for each velocity. The visible logarithmic trend established for the data in Figure 6.11 with 100 and 500 mg/L sand (similar to that for flow-induced corrosion) was believed to occur because the system was dominated by corrosion as a result of the low test velocity. Previous research by Hu et al. [143] indicated that at higher velocities (above 7 m/s), the erosion component of material loss tends to become

more significant and increase rapidly with velocity, suggesting that at higher velocities, the relationship observed would not hold. Therefore the use of this prediction tool is strictly limited to the parameters over which it has been experimentally validated (as with most empirical prediction models).

By adopting the mass loss data in Figure 6.11 and the logarithmic relationships established, it was possible to create an empirical model by linearly interpolating between each of the three curves over constant values of velocity, but varying levels of sand loading. The values encompassed all possible conditions on the offshore facility in terms of flow velocity and sand loading.

A 3D plot was produced for degradation rate which is sensitive to both velocity and sand concentration at 45°C (Figure 6.13). Fluctuations in temperature were disregarded as this was relatively stable in the system when process fluid was flowing. The inclusion of this parameter would have also significantly increased the size of the test matrix.

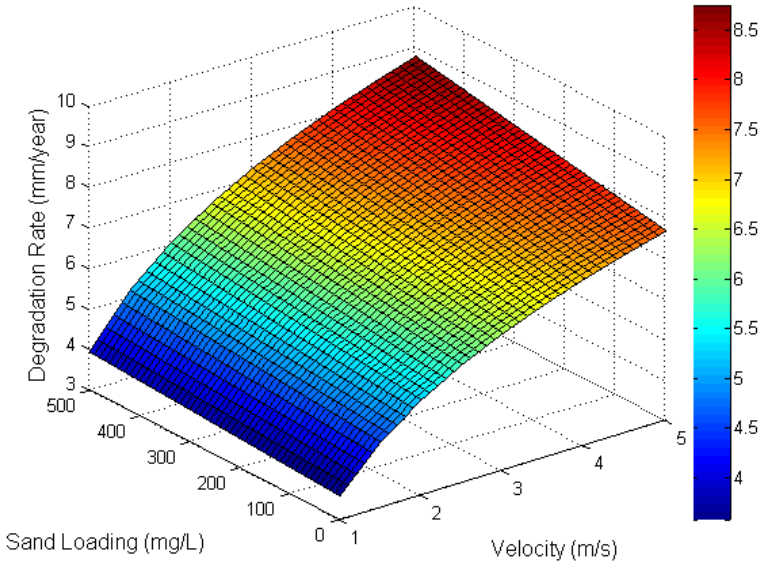

Figure 6.13: 3D plot of degradation rate as a function of sand loading and fluid velocity

A program was created using the model which was capable of extracting values of flow velocity and sand loading for each day on the facility and determining the daily degradation rate. Degradation rate as a function of time could then be plotted for the facility over a 5 year period from 2005 to 2010. The plot is shown in Figure 6.14 and compared to the behaviour predicted from the two commercially available models.

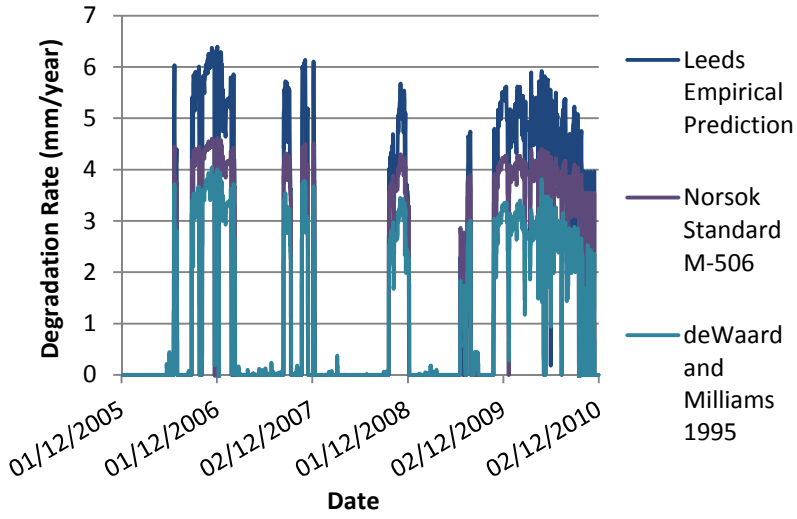

Figure 6.14: Predicted degradation rates as a function of time on the offshore facility from various models over 5 years; comparison of Leeds empirical model with commercially available Norsok and de Waard and Milliams models

When these fluctuations in degradation rate are compared to the Norsok and the de Waard 1995 models in Figure 6.14, it is clear that the average rate of degradation is greater for the Leeds empirical model. The program can also calculate the cumulative thickness loss of pipework as a function of time for pipework based on the daily degradation rates, shown in Figure 6.15.

It is worth noting here that for very rare cases when the velocity in the system fell below 1 m/s, the corrosion rate at 1 m/s was still employed by the program. With the bulk flow velocity rarely falling below this value, there was no significant effect on the prediction model.

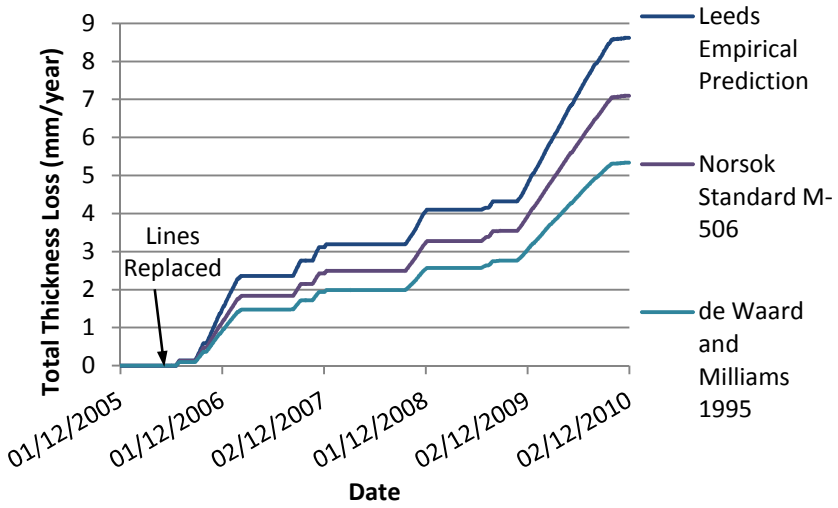

Figure 6.15: Predicted thickness loss as a function of time on the offshore facility over 5 years; comparison of Leeds empirical model with commercially available Norsok and de Waard and Milliams models

6.6.2 Prediction of Thickness Losses with Inhibition

It was important to incorporate the effects of chemical inhibition into the model. In particular, considering the application of 10 ppm of the current inhibitor was crucial to provide a more accurate interpretation of degradation rates on the facility.

It is likely that the efficiency of the inhibitor will change depending upon the bulk flow velocity and sand content. However, repeating the entire experimental matrix with the addition of 10 ppm would be very time-consuming.

Time constraints meant that the decision was made to conduct one set of jet impingement tests at 10 ppm in more severe conditions than those encapsulated by the empirical model (7 m/s and 500 mg/l sand) and apply the determined efficiency to the entire model. Using this technique significantly reduced the number of required experiments and ensured that the approximation of inhibitor efficiency was conservative and adopted a ‘worst case scenario’ approach. Results of the tests at 7 m/s are displayed in Figure 6.16.

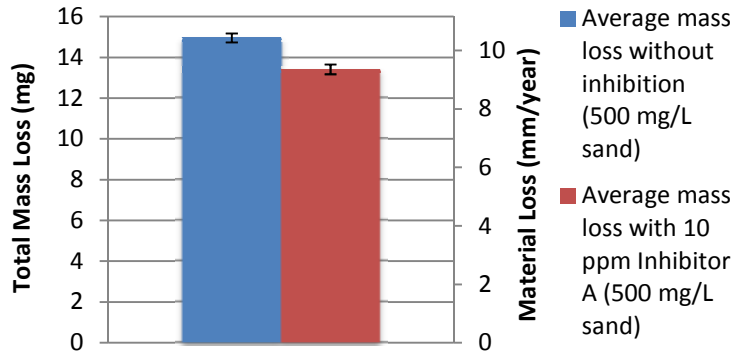

Figure 6.16: Average thickness loss from SIJ tests at 7 m/s, 500 mg/L sand and 45°C in blank condition and with the addition of 10 ppm Inhibitor A

The results produced an inhibitor efficiency of 11.5% for the application of 10 ppm Inhibitor A. Assuming this efficiency is also applicable at lower velocities and sand loadings, the inhibitor efficiency can be incorporated into the model and applied to the blank degradation rates as shown in Figure 6.17.

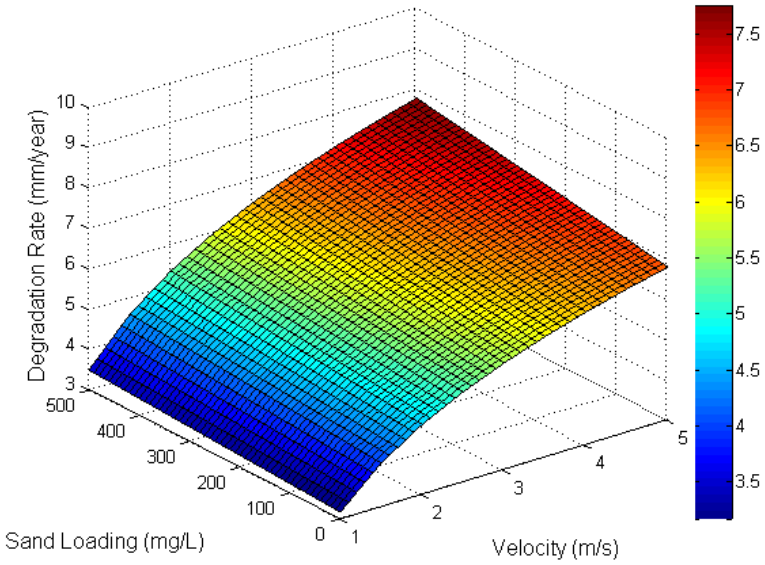

Figure 6.17: 3D plot of degradation rate as a function of sand loading and fluid velocity with the application of 10 ppm Inhibitor A

The new 3D plot was used to determine the thickness losses under the application of 10 ppm Inhibitor A (Figure 6.18).

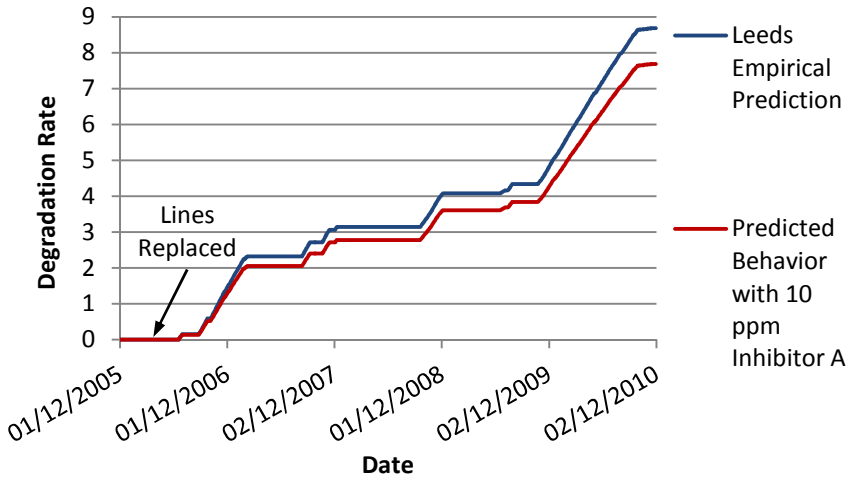

Figure 6.18: Predicted thickness loss as a function of time on the offshore facility with and without the application of 10 ppm Inhibitor A

6.6.3 Comparison of Model Prediction Capabilities with Inspection Data and Pipework Failures

Figure 6.19 shows the predicted average degradation rates between 2005 and 2010 using the Leeds empirical model in comparison to inspection data, including those using the Norsok and de Waard and Milliams models. Average degradation rates were calculated by taking the final thickness loss predicted by each model on 02/12/2010 and dividing it by the duration which the pipework had been in service.

Figure 6.19 indicates that the Leeds empirical prediction overestimates the degradation rate on the facility. When account is taken for the addition of 10 ppm Inhibitor A, the estimated values match the highest degradation rates more closely. The Norsok and de Waard and Milliams models underestimate a number of the higher degradation rates even without accommodating for the presence of Inhibitor A. It is worth noting here that both the Norsok and de Waard and Milliams models are capable of accounting for inhibitor efficiencies. For the de Waard and Milliams model, the corrosion rate is simply divided by an inhibitor efficiency factor i.e. for an efficiency of 90%, the corrosion rate is divided by 10. The Norsok model works in a similar way in that the user is able to enter the efficiency directly into the program which is then applied as a reduction factor.

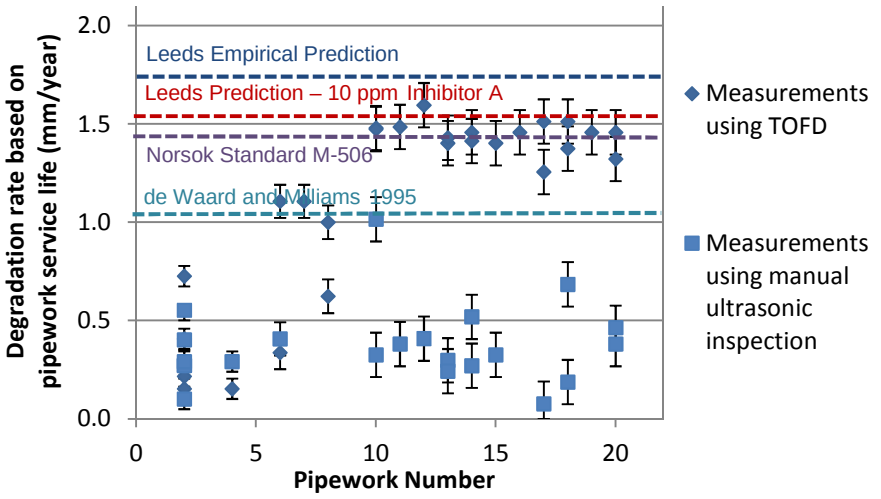

Figure 6.19: Inspection data for pipework compared with average degradation rates predicted by the Leeds empirical model and the commercially available Norsok and de Waards and Milliams models

Only one leak was detected on the line for which the flow velocity data is presented here. The spool associated with the failure was in operation for 5 years which relates to a degradation rate of approximately 1.64 mm/year based on the service life of the spool. There is a strong agreement between the prediction data and the failure.

It is clear that the use of the SIJ offers a close prediction for this particular application. The degradation rates predicted by the empirical model are higher than both the Norsok and de Waard and Milliams models.

6.7 Understanding Reasons behind Discrepancies between Leeds Model and Commercially Available Models

With the Leeds Model being able to account for the presence of sand, it is not surprising that the degradation rates predicted are greater than those predicted by the two corrosion models which do not account for the presence of solid particles.

However, the noticeable difference between the flow-induced corrosion rates for the Leeds and commercially available models appears to be the prime reason behind the significant difference in predictive capability.

The main differences between the SIJ setup and the experiments which the de Waard and Milliams and Norsok models are based on are (i) the specific brine chemistry used in the experiment (ii) material composition i.e. the type of carbon

steel evaluated and (iii) the hydrodynamic conditions of the system. These are discussed in the following sections.

6.7.1.1 Influence of Different Brine Chemistry

Both the Norsok and de Waard and Milliams models are based on tests conducted in 0.1% NaCl solutions with no other salts present. The test medium in the SIJ consisted of 3% NaCl combined with various other salts combining to give 3.5% of total dissolved salts. The increase in salt concentration is potentially one of the reasons why the Leeds model predicts a higher degradation rate. It is generally believed that the corrosivity of water containing dissolved salts increases with increasing concentration until a maximum is reached. This can be partly attributed to the increased electro-conductivity in the system [53]. Figure 6.20 shows the mass loss based corrosion rates as a function of NaCl concentration at 80°C and 0.5 bar CO_2 conducted by Gulbrandsen and Bilkova [53]. The results in Figure 6.20(a) demonstrated that an increase in salt concentration from 0.1% to 3% NaCl caused an increase in corrosion rate from 42 mm/year to 66 mm/year (an increase of 57%). The polarisation curves in Figure 6.20(b) for 0.3 and 3% NaCl also indicated that the increase in brine concentration caused an increase in both the anodic and cathodic currents.

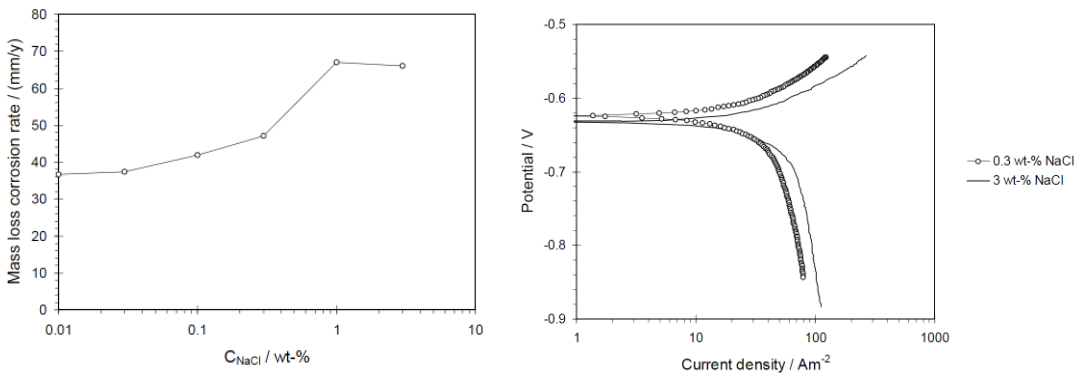

(a) (b)

Figure 6.20: (a) Mass loss corrosion rate as a function of NaCl concentration and (b) Potentiodynamic polarisation curves at 0.3% and 3% NaCl measured at the end of the test; 80°C and 0.5 bar CO_2 – from Gulbrandsen and Bilkova [53]

6.7.1.2 Influence of Different Material Compositions

The majority of tests for the Norsok and de Waard and Milliams models were performed with St 52 grade carbon steel. The composition of this steel is provided in Table 6.6. Olsen et al. [77] mentioned that different types of steel were tested and very different corrosion rates were observed for various steels. The decision to

select the St 52 type steel was based on the fact that the *majority* of data obtained for this type of steel gave the highest corrosion rates. However, the material considered in this thesis is ASTM A106 Grade B carbon steel, which appears to have an even more basic composition and therefore has the potential to be even more susceptible to corrosion than St 52 in the same environment.

A number of interesting comparisons can be made between the two materials compositions which are shown in Table 6.6. The first observation is the higher carbon content of the steel considered in this research. Gulbrandsen et al. [174] found higher carbon content can lead to increased corrosion rates of steel exposed to CO_2 environments between the temperatures of 20 and 50°C. This was attributed to the formation of iron carbide which accelerated the dissolution process - an aspect which will be discussed in detail later in the thesis.

The St 52 steel contains significantly higher quantities of elements such as Silicon, Manganese, Nickel and Aluminium, all of which been shown to improve carbon steel CO_2 corrosion resistance [66].

Table 6.6: Comparison of carbon steel in this research compared with St 52 grade carbon steel

	Carbon steel in this work ASTM A106 Grade B	**St 52**
Carbon	0.17	0.13
Silicon	0.20	0.38
Manganese	0.78	1.29
Phosphorus	0.010	0.015
Sulphur	0.003	0.008
Chromium	0.10	0.07
Molybdenum	0.030	0.01
Nickel	0.030	0.09
Aluminium	0.032	0.05
Vanadium	-	0.035
Copper	-	0.34
Tin	-	0.015

Additional elements were present in St 52 that were not detected in the carbon steel taken from the offshore facility. These were Vanadium, Copper and Tin. Based on

extensive research by Kermani et al. [66], addition of Vanadium has the greatest effect on reducing corrosion rate, closely followed by Chromium and then Copper, as summarised in Figure 6.21. This suggests that St 52 would be more corrosion resistant than the steel considered here. It is likely that the difference in composition has contributed partly to the difference in observed corrosion rates.

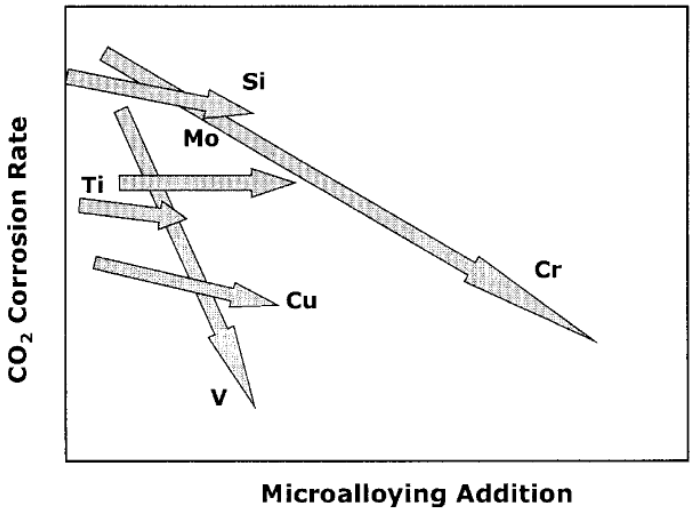

Figure 6.21: Schematic representation of relative effect of additional microalloying elements on the corrosion rate of carbon and low allow steels – from Kermani et al. [66]

6.7.1.3 Influence of Different Hydrodynamic Conditions

The goal of the experiments performed in this Chapter were to effectively simulate the flow turbulence in the operating system to investigate whether the corrosion rates could accurately be predicted in the field. The comparison of corrosion rates between the SIJ, the Norsok model and the operating system was based on the values of flow velocity of the process fluid, despite the very different flow geometries.

It is clear that the hydrodynamic conditions over the carbon steel sample in the SIJ will not be the same as those in pipeflow, nor those in the single phase flow loop used by the Institute for Energy Technology (IFE) for the same test velocity. This poses the question as to whether a comparison of corrosion rates using flow velocity is a suitable approach and whether comparison of corrosion rate using another parameter more closely related to the turbulence in the fluid acting on the wall could be conducted.

Fluid velocity has long been the primary parameter for comparison of laboratory test results to field applications, but this concept has evolved since the work published by Efird [169, 175] in which he considered the use of hydrodynamic parameters to correlate with corrosion rates.

Many corrosion engineers and authors [64, 77, 88, 176] are of the belief that flow-accelerated corrosion must be expressed in terms of geometry independent fluid parameters which are common to all hydrodynamic systems to allow the application of laboratory test data to what is observed in the field. The parameters which are most frequently used to draw comparisons are the wall shear stress, τ_w [169, 175-177], and the mass transfer coefficient, k [169, 175-179]. Considering that fluid flow is a complex combination of near wall hydrodynamics and mass transfer, not necessarily indicative of the bulk flow and fluid parameters, the majority of the changes with regards to fluid stresses, turbulence, mass transfer and fluid interaction occur within the boundary layer. This suggests that using a geometry independent parameter acting on the test specimen surface can help to investigate fluid flow effects on corrosion for any system that can be hydro-dynamically characterised [169].

The jet impingement system (and the IFE flow loop for that matter) does not measure corrosion under equilibrium conditions, but measures corrosion in a steady state environment [176]. The technique measures the effect of flow turbulence without the diffusion boundary layer reaching equilibrium. The system reaches a steady state, which simulates the effect of flow disturbances where equilibrium conditions are destroyed [176]. In this case, Efird [176] stated that the mass transfer conditions do not apply and the wall shear stress equations must be used to allow correlation to field operations.

Efird [169] stated that laboratory tests should be conducted in a way to allow hydrodynamic calculations of τ_w or k. These corrosion rates are then applied to the field for identically calculated values of these parameters as shown in Figure 6.22. The fundamental assumption is that the selected parameter is directly related to the corrosion rate, and that scaling of this parameter for flow-induced corrosion is valid [169]. Efird [169] found that using shear stress to determine corrosion rates in pipeflow was a valuable approach.

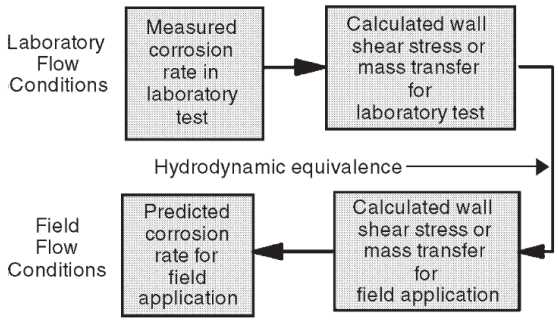

Figure 6.22: The process for determining field corrosion rates from laboratory data using hydrodynamic parameters - from Efird [169]

In hindsight, relating the Leeds empirical model to the commercially available models and the operating system through flow velocity was not an ideal approach. The SIJ, the 200 mm diameter offshore pipework and the 60 mm diameter IFE flow loop are very different systems, which would subject the material surface to different hydrodynamic conditions and different levels of shear stress for the same bulk flow velocity. Relating the material degradation rates in flow-induced corrosion environments through a geometry independent parameter such as shear stress would be a much more suitable approach.

In order to consider this relationship, Computational Fluid Dynamics (CFD) was employed to compare the levels of shear stresses in the SIJ and the pipework on the facility. These could then be related to the shear stress values calculated by IFE in the Norsok model for the 60 mm diameter flow loop. The approach adopted for this process is reviewed in the following section which contains details of the CFD modelling employed along with validation of the model.

6.8 Hydrodynamic Characterisation of SIJ and Offshore Pipework

To investigate the differences between the submerged impinging jet and the pipework on the offshore facility in terms of hydrodynamics, CFD was used to model the flow behaviour. This allowed a comparison between levels of wall shear stress, a parameter which is believed to be very influential in determining degradation rates attributed to flow-induced corrosion [175].

FLUENT was chosen as the CFD program to characterise the different systems. This software uses the finite volume method with the second order upwind interpolation scheme selected for this particular approach. Various geometries were modelled for the lines, simulating 90˚ turns, 45˚ bends and vertical flow over internal

weld beads, as well as modelling the submerged impinging jet. Models were established for bulk flow velocities of 1-5 m/s in 1 m/s increments for each case.

To resolve turbulence, the k-ε model [180] was used with standard wall functions applied to represent near wall effects. A converged solution to the models was obtained after 20 minutes on a 3 GHz dual core desktop PC for all models.

6.8.1 Submerged Jet Impingement Model

CFD modelling of the submerged impinging jet was undertaken extensively by Gnanavelu [116] at the University of Leeds. The same methodology is adopted in the work presented here, although simulations are conducted for different nozzle diameters and for different inlet velocities. A detailed discussion of the creation of geometry, mesh generation, selection of fluid properties, specification of boundary conditions and turbulence model, as well as verification of the computational mesh and domain size can be found in the work by Gnanavelu [181]. A brief overview of these features is provided here for clarity and an independent validation of the model has also been conducted here through comparisons with literature.

6.8.1.1 Geometry and Mesh Generation

The jet impingement and sample configuration simulated in this study are assumed to be axisymmetric about the centreline of the nozzle. A 2D model was used to model the impingement at 90°. Hence, the resulting flow domain on any particular plane along this centreline and perpendicular to the test surface is expected to be representative of the entire flow domain. This was the same approach adopted by Gnanavelu [116] in which the 2D, incompressible, steady state model was used. Adopting this technique helped to minimise computing resources without compromising solution accuracy. Figure 6.23 indicates how the physical domain has been represented using a computational domain.

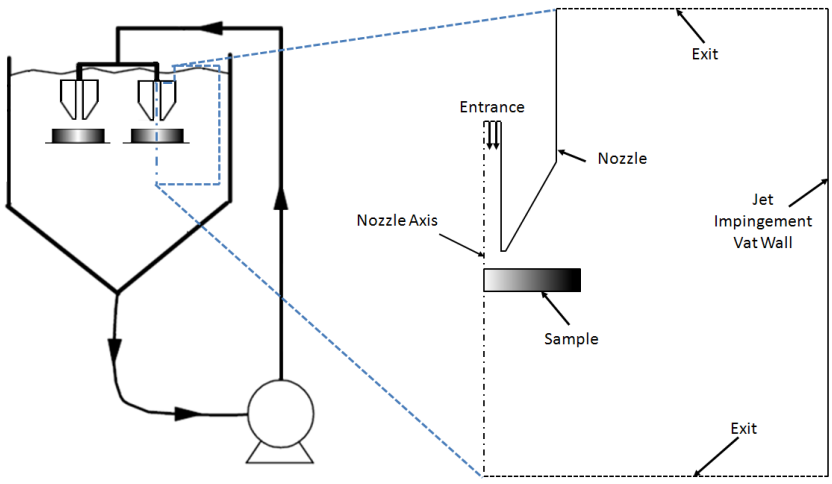

Figure 6.23: Representation of the physical domain (left) and the computational domain (right) for the submerged impinging jet

Fluid exiting the nozzle undergoes dramatic changes in direction once it comes into contact with the sample surface. It is advisable that the majority of computational cells should be use to resolve this region in particular, especially as the wall shear stress of the sample is the main parameter of interest in this study. The computational mesh generated is shown in Figure 6.24 and consists of approximately 130,000 triangular elements mapping the whole domain, with the mesh becoming finer around the specimen surface. The computational mesh was refined to ensure that the boundary layer was adequately resolved and grid independence obtained.

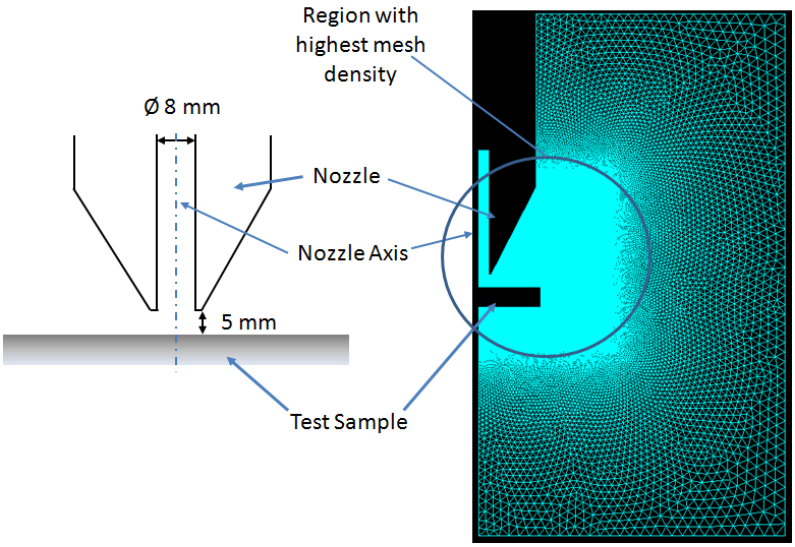

Figure 6.24: Representation of actual geometry (left) and flow domain simplified to 2D using Gambit (right) (Domain size is 120 mm x 220 mm and mesh consists of approximately 130,000 elements)

6.8.1.2 Specification of Boundary Conditions and Selection of Fluid Properties

The nature of the implemented boundary conditions are shown in Figure 6.25 for the consideration of a viscous, turbulent, incompressible and isothermal fluid. All solid walls in the system are defined as such, and by definition the velocities are zero for the walls bounding the fluid domain. For the inflow condition, the mean fluid jet velocity at which the fluid enters the domain is specified. The length of the inlet was adjusted to at least 10 times the internal diameter of the jet to ensure the flow became fully developed within the nozzle [181]. The outflow boundaries are defined in Figure 6.25. Only one outlet condition is specified with atmospheric pressure being the property imposed in this case. The symmetry condition was used along the nozzle axis to reduce computational time. The final condition to assign to the system was to associate the interior of the computational domain as being representative of the fluid solution within the reservoir.

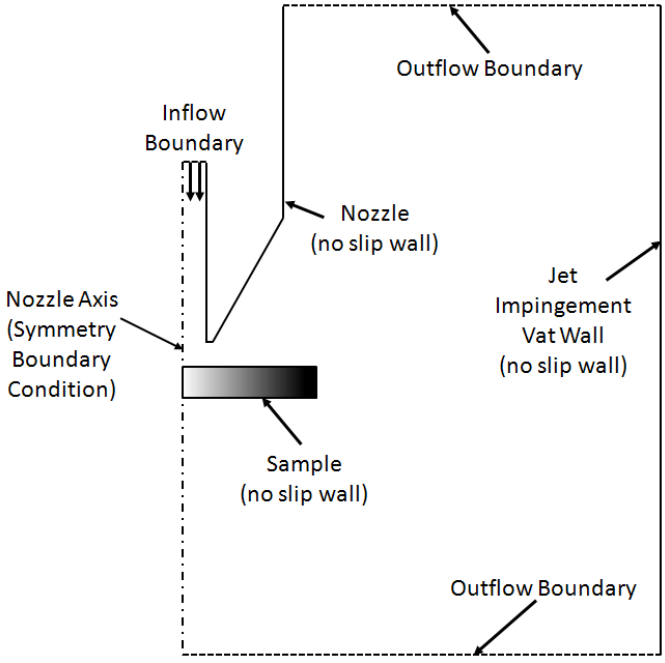

Figure 6.25: Illustration of the computational domain developed using Gambit with the relevant boundary conditions imposed for the submerged impinging jet (diagram is not to scale)

Regarding fluid properties, the density of the saltwater solution (1019 kg/m^3) and the dynamic viscosity (6 x 10^{-4} Pa.s) at 45°C was used throughout every simulation.

6.8.1.3 Modelling Turbulence Effects and Convergence Criteria

The k-ε model was chosen to numerically simulate the effects of turbulence within the submerged impinging jet. All numerical simulations were solved using the second order upwind interpolation scheme. The SIMPLE algorithm was also employed to guarantee a cross linkage between the pressure and velocity, which predominantly accounts for the mass conservation within the flow domain. All numerical simulations were converged when the residuals of all flow parameters fell below 1×10^{-5}.

6.8.1.4 Validation of SIJ CFD Model

Use of jet impingement to study flow-accelerated corrosion is a common test technique. The flow field for a circular jet impinging onto a flat plate with the jet's central axis perpendicular to the plate is provided in Figure 6.26. At the intersection of the nozzle axis and the plate, a stagnation point exists, with the flow being symmetrical about this axis. Only the flow properties in the radial direction need to be considered because of the axisymmetric flow.

When considering Figure 6.26, Region A is the free jet region, in which the primary velocity is axial. The local velocity field is complex and flow vectors change rapidly as radial distance increases, making it difficult to experimentally characterise the wall shear stresses in this region [182]. Region B is the impingement region and is an area of rapidly increasing turbulence, which is characterised by significant changes in flow direction [182]. Region C is the wall jet region which is characterised by a large velocity gradient and high wall shear stresses. The boundary layer gradually thickens with increasing radial distance from this region onwards [182].

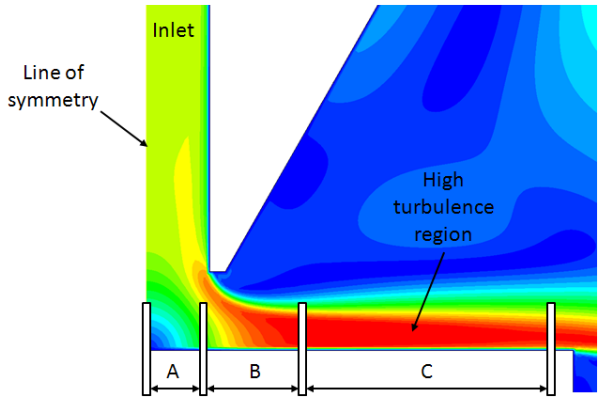

Figure 6.26: CFD model of submerged jet impingement system

It was important to validate the CFD simulations with experimental work, particularly the values of shear stress determined. In 1975, Giralt and Trass [183] proposed an equation for wall shear stress in the wall jet region, which is commonly referred to by corrosion engineers. This equation, with numerical constants recalculated for the use of the jet radius instead of the jet diameter as the normalising factor, is written as:

$$\tau_w = 0.179\rho U_0^2 Re^{-0.182}\left(\frac{r}{r_0}\right)^{-2.0} \quad (6.4)$$

where the jet Reynolds number is defined as:

$$Re = \frac{2r_0 U_0}{\nu} \quad (6.5)$$

where r_0 is the jet radius, r is the distance from the centre of the sample, U_0 is the velocity at the stagnation point and v is the kinematic viscosity.

However, the range of applicability for this equation needs to be taken into account when using it to validate the CFD simulation. Giralt and Trass [183] stated that the application of this equation was only valid for the conditions tested (nozzle height to jet diameter ratio of H/D = 8, jet diameters of D = 2.54 and 5.08 mm and Reynolds numbers of between 22,900 and 152,000). The data published highlighted that the range of applicability for this equation ranges for values of x/r_0 (x = distance from jet axis, r_0 = jet radius) between 2 and 5. Although the Reynolds numbers over which this equation is verified cover the majority of the range of values in these tests for 1-5 m/s (Re = 13,197 - 65,987), the nozzle height to diameter ratio of H/D = 8 is not comparable to that in these experiments (here H/D = 0.625).

Although this equation is not applicable for this particular case, work published by Giralt et al. in 1977 [184] considered the dimensionless wall shear stress distributions produced along a plate from different nozzle heights. The lowest value of H/D considered by Giralt et al. [184] was 1.2, which produced a markedly different distribution to that for H/D = 8. The dimensionless distribution determined by Giralt et al. [184] for H/D = 1.2 was used to help verify the shear stress calculations from the CFD model as this was the closest comparable work available. The correlation between the two sets of data is provided in Figure 6.27. Unfortunately, the equation was only considered over a range which corresponds to a 0 – 7.1 mm in term of radial distance from the jet centreline for this application.

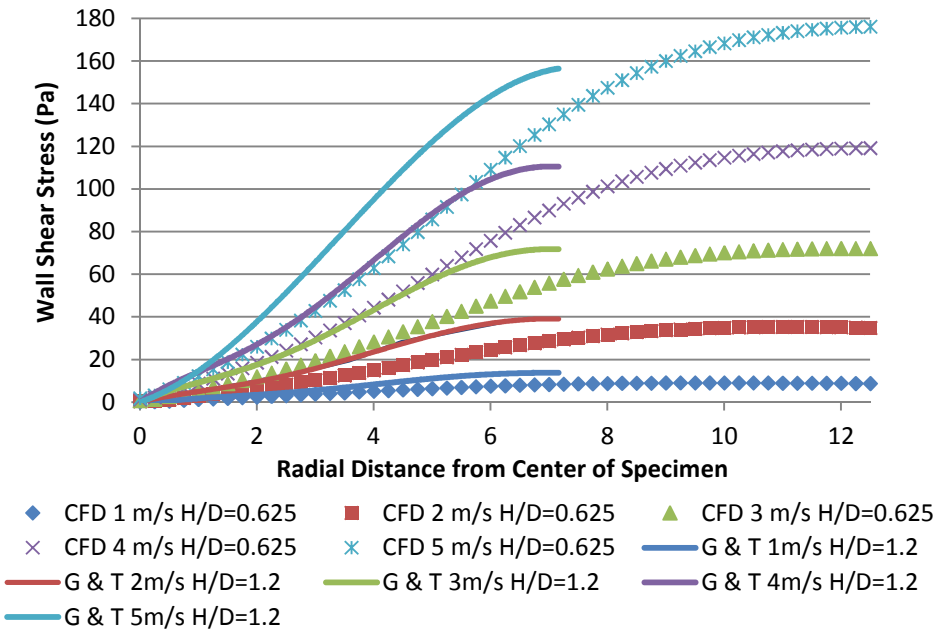

Figure 6.27: Comparison of predicted wall shear stress distributions for submerged impinging jet and published work by Giralt et al. [184]

It is evident that the correlation between the distribution proposed by Giralt and Trass [184] and that of the CFD show very similar shapes and maximum values of shear stress. Two noticeable differences are the fact that the distributions of Giralt et al. [184] predict higher shear stresses at smaller radial distances and the maximum wall shear stress value is reached closer to the centreline than the prediction from the CFD model. The difference in behaviour can be partly attributed to the fact that the model by Giralt et al. [184] predicts behaviour at a greater value of H/D than the CFD model.

Giralt et al. [184] established trends in the dimensionless wall shear stress distribution as the nozzle to plate distance was reduced. They showed that as the nozzle approaches the surface of the specimen, the maximum shear stress increases and is shifted further away from the centre of impingement. Values of shear closer to the centre of impingement (before this maximum peak value) reduced as the height decreased and values of shear after the peak value increased with reducing H/D. This trend is depicted by the graphs with solid lines in Figure 6.28 which are the dimensionless wall shear stress distributions publicised by Giralt et al. [184] in 1977.

The wall shear stress distribution extracted from the CFD simulation was non-dimensionalised using Equations (6.6) and (6.7) and is inserted into Figure 6.28.

$$\text{dimensionless wall shear stress} = \frac{\tau}{1/2\,\rho V_s^2}\sqrt{\frac{V_s r_{1/2}}{\nu}} \tag{6.6}$$

where τ is the wall shear stress, V_s is the flow velocity at the stagnation point, ρ is the fluid density and $r_{1/2}$ is the jet half radius, calculated by:

$$r_{1/2} = D_0\left(0.5 + \frac{0.006H}{D_0}\right) \tag{6.7}$$

where D_0 is the nozzle diameter and H is the stand-off distance.

By considering the trend and change in distribution as H/D is reduced from 8 to 1.2, it is possible to envisage what impact a further reduction in H/D would have on the wall shear stress distribution and compare this to the CFD prediction for the smallest value of H/D. The distribution predicted by CFD produces what could be argued as a likely distribution following the trends of the previous graphs. As a final check for a direct comparison with the data, simulations were conducted for conditions representative of those analysed by Giralt et al. [184] i.e. simulations with values of H/D at 8, 5 and 1.2. The dimensionless shear stress distributions are provided in Figure 6.29. The distributions obtained are reasonably similar in shape and magnitude to those proposed by Giralt et al. [184]. This information helps to ensure the validity of the simulation at smaller nozzle to surface distances.

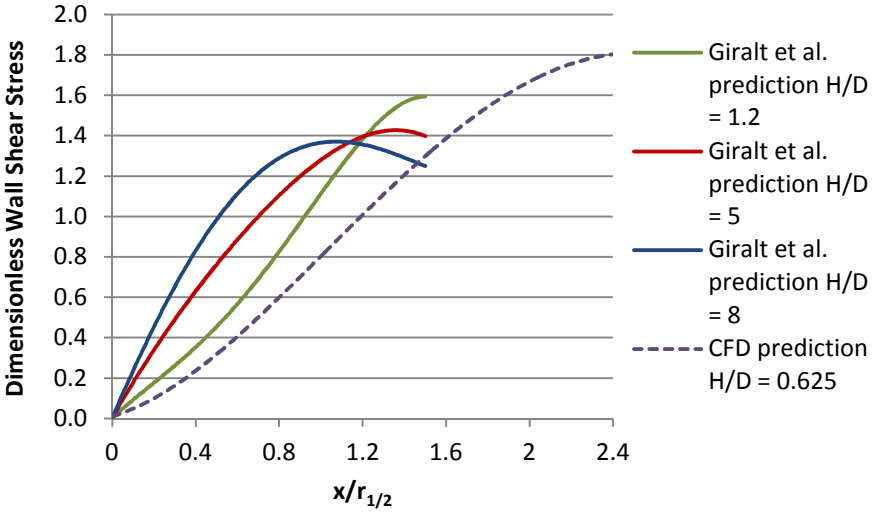

Figure 6.28: Dimensionless wall shear stress distributions along a sample for different nozzle heights; a comparison between CFD prediction and published work by Giralt et al. [183]

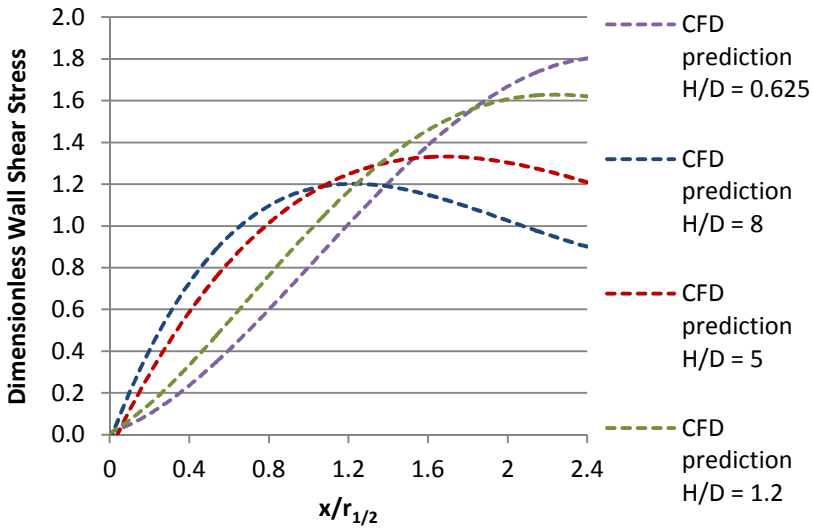

Figure 6.29: Dimensionless wall shear stress distributions along a sample for different nozzle heights; all distributions were determined from the CFD simulations

6.8.1.5 CFD Modelling of Flow Through Facility Pipework

Common sections of pipework found on the facility lines were also modelled using a similar approach. Simulations were conducted for three geometries, namely; vertical flow over an internal weld bead, flow round a 90° bend and flow through a sharp turn of 45°. Again, grid independence was achieved to determine the number of elements required for the simulations and the same solution methods and controls were used as in the jet impingement setup. The boundary conditions imposed on each of the three pipework geometries are provided in Figure 6.30.

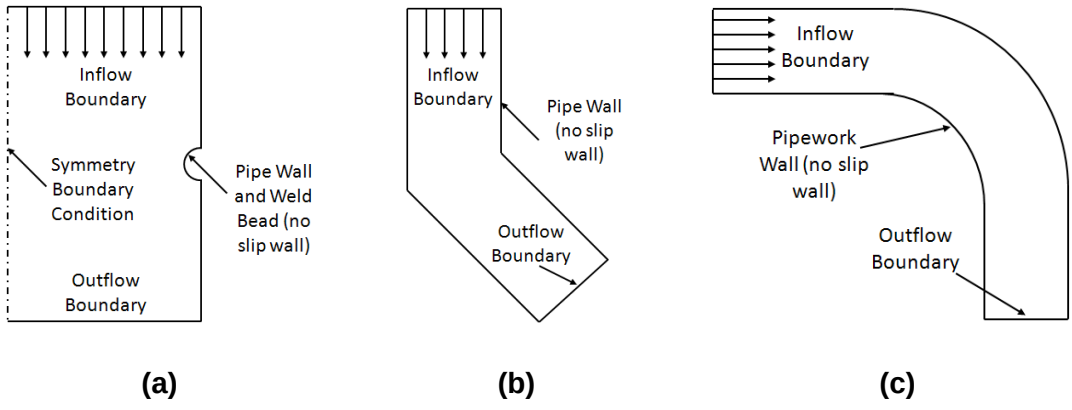

Figure 6.30: Illustration of the computational domain developed using Gambit with the relevant boundary conditions imposed for (a) flow over an internal weld bead, (b) flow through a 45° sharp bend and (c) flow round a 90° bend (diagrams are not to scale)

The number of elements within the mesh, the domain size, and various other parameters pertaining to the modelling of the submerged impinging jet and pipework geometry can be found in Table 6.7.

Table 6.7: Parameters related to all CFD simulations for various geometries

	Jet Impingement	Weld Bead	45 sharp bend	90 degree bend
Domain size (mm)	120 x 220	100 x 250	400 x 700	2000 x 1000
No. Of Elements (approx.)	130,000	32,000	13,000	62,000
Inlet Flow Velocity (m/s)	1, 2, 3, 4, 5			
Dynamic Viscosity (Pa s)	6×10^{-4}			
Fluid Temperature (°C)	45			
Fluid Pressure (Pa)	Atmospheric (101325)			
Turbulence Model	k-ε			
Convergence Criteria	1×10^{-5}			

6.8.1.6 Correlating Laboratory Data to Operating Systems

Wall shear stress is commonly perceived as a force which acts to remove corrosion products from the surface of a metal. This belief is incorrect, with the parameter being a direct measure of viscous energy loss within a turbulent boundary layer [175]. Wall shear stress is related to the intensity of turbulence acting on a wall.

Wall shear stress (τ_w) is the isothermal pressure loss in turbulent fluid flow due to fluid friction resulting from contact with a stationary wall within an incremental distance. The mathematical expression is defined as:

$$\tau_w = \mu \left(\frac{\delta u}{\delta y}\right)_{y=0} \tag{6.8}$$

where μ is the dynamic viscosity, u is the flow velocity parallel to the wall and y is the distance to the wall.

The CFD simulations were used to compare the hydrodynamics of the submerged impinging jet and various sections of the pipework and review the calculation of shear stress by the Norsok model in an effort to explain the correlation between the Leeds empirical model and the field data. Simulations were conducted for four geometries, namely; the jet impingement rig, flow over an internal weld bead, flow round a 90° bend and vertical flow turned through 45°. In addition to each of the shear stress distributions extracted from the four geometries, the wall shear stress

in purely vertical flow with no geometry changes was simulated for each of the velocities between 1 and 5 m/s for comparison with the Norsok model.

Examples of the velocity contours and shear stresses are provided for the submerged impinging jet in Figure 6.31, flow over the weld bead in Figure 6.32, flow through a sharp 45° turn in Figure 6.33 and flow round a 90° bend in Figure 6.34.

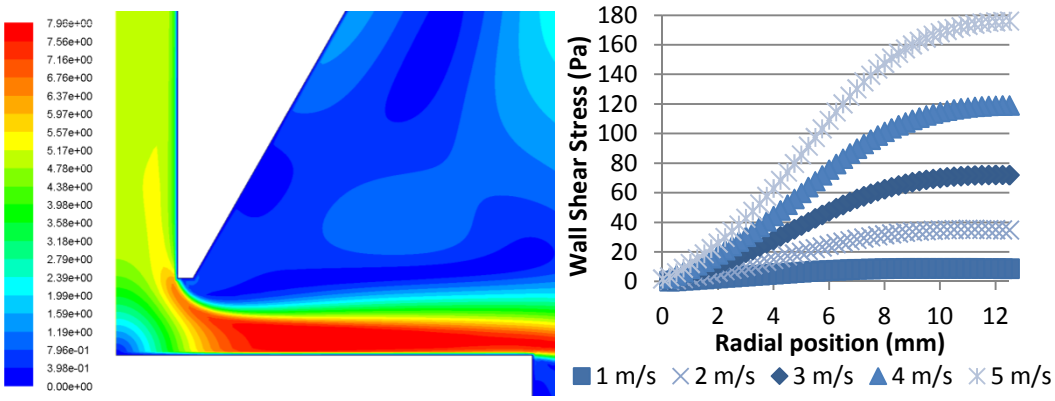

(a) (b)

Figure 6.31: (a) Velocity profile of submerged impinging jet at inlet velocity of 5 m/s, (b) Shear stress distributions over submerged impinging jet sample between 1 and 5 m/s

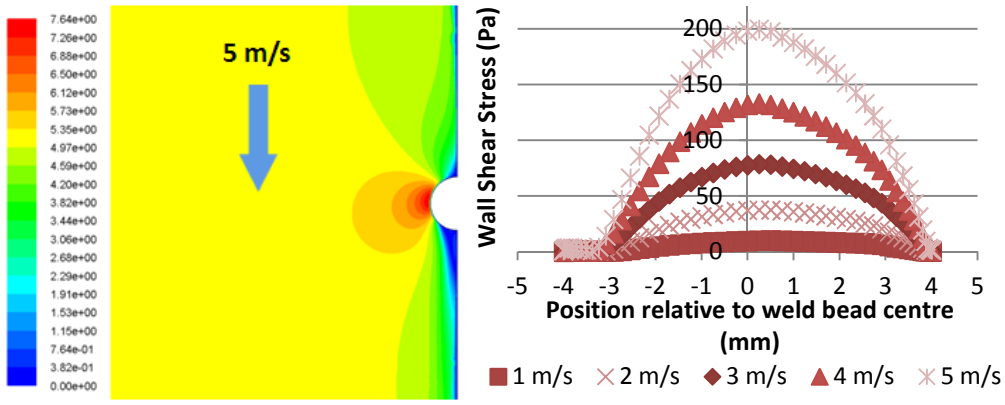

(a) (b)

Figure 6.32: (a) Velocity profile over a 4 mm radius weld bead at inlet velocity of 5 m/s, (b) Shear stress distributions over weld bead between 1 and 5 m/s

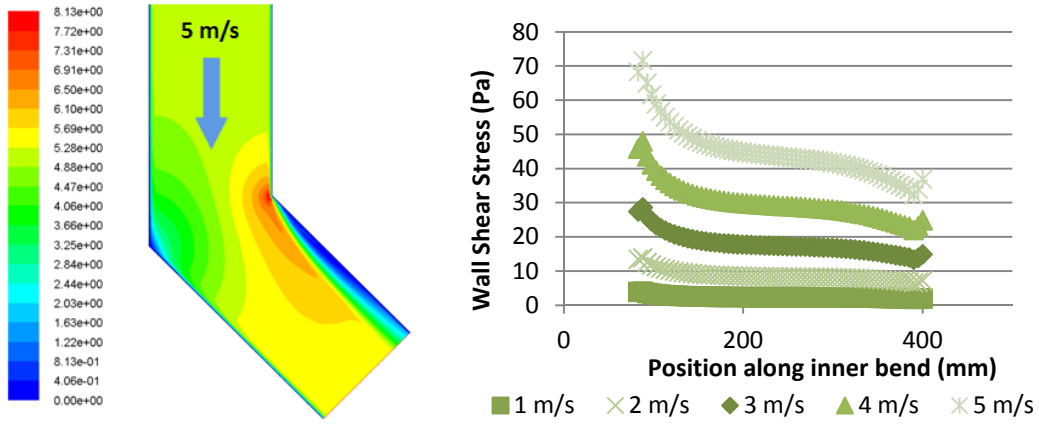

(a) (b)

Figure 6.33: (a) Velocity profile for a 45˚ bend with an inlet velocity of 5 m/s, (b) Shear stress distributions over inner 45˚ bend between 1 and 5 m/s

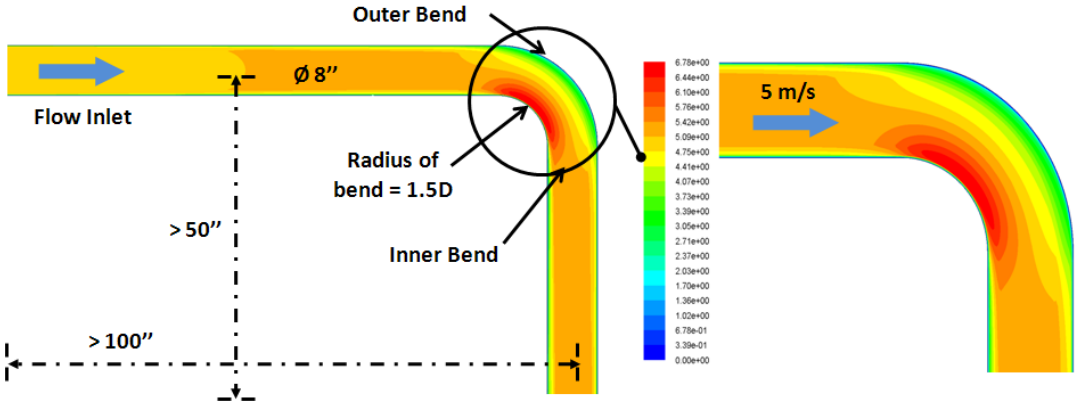

(a)

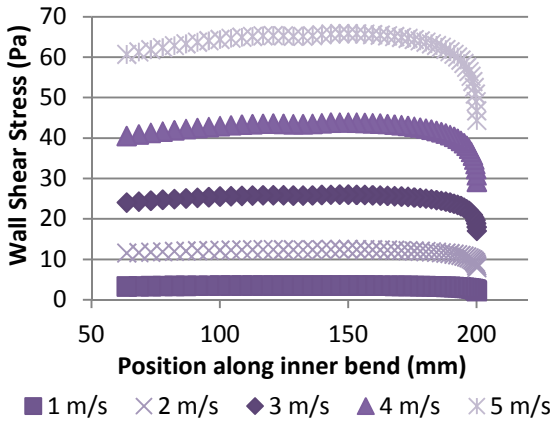

(b)

Figure 6.34: (a) Velocity profile of pipework bend of radius 1.5D at inlet velocity of 5 m/s, (b) Shear stress distributions over inner wall of pipework between 1 and 5 m/s

The maximum and average wall shear stress values extracted from the simulations are presented in Table 6.8 and Table 6.9, respectively.

By considering the values presented in the tables, it is clear that all geometries simulated produce higher values of wall shear stress than in purely vertical flow because of the flow disturbances. The submerged impinging jet produced the highest average shear stress, whilst the wall shear stress over the weld bead produced the highest maximum value for each velocity.

With flow-induced corrosion contributing towards the majority of material degradation in the submerged impinging jet experiments (especially at low velocities), it could be argued that the accurate predictive capability of the model is influenced by the correlation in shear stress values between the turbulent regions in the pipework and the jet impingement rig over the same velocities (Figure 6.31 and Figure 6.32). Therefore, for a given velocity, the empirical model is able to predict the degradation rates for regions where high turbulence and shear stress are present in the system.

It is purely coincident that the shear stress on the impinging jet sample surface is similar to the shear stress in the most turbulent areas on the offshore pipework for the same flow velocity. This effect may explain why the empirical model predicts some of the localised degradation rates (i.e. the higher rates of material loss) so effectively and the de Waard and Milliams and Norsok models fail to do so.

Table 6.8: Maximum shear values for various geometries modelled using CFD

Geometry Modelled	**Maximum Shear Stress (Pa)**				
	1 m/s	**2 m/s**	**3 m/s**	**4 m/s**	**5 m/s**
Submerged Jet Impingement	9.0	35.3	72.1	119.2	176.1
1.5D Bend Inner Wall	3.6	12.5	26.0	43.4	65.9
Weld Bead	10.1	37.4	78.5	133.0	199.7
45˚ Sharp Bend	4.0	13.9	28.7	48.0	71.7
Undisturbed Vertical Flow	2.5	8.7	18.0	30.1	44.9

Table 6.9: Average shear values for various geometries modelled using CFD

Geometry Modelled	Average Shear Stress (Pa)				
	1 m/s	**2 m/s**	**3 m/s**	**4 m/s**	**5 m/s**
Submerged Jet Impingement	6.3	22.2	43.9	71.0	103.3
1.5D Bend Inner Wall	3.2	11.4	23.7	40.1	60.2
Weld Bead	4.2	15.8	33.6	57.2	86.6
45˚ Sharp Bend	1.9	5.1	12.1	20.2	30.1
Undisturbed Vertical Flow	2.5	8.7	18.0	30.1	44.9

Through studying the degradation mechanisms on the facility, there appear to be two main degradation processes. There are high general corrosion rates, highlighted by the UT inspection on the pipework, and there are also regions of localised attack after weld beads and step changes in pipework, shown by the TOFD measurement.

Based on work by Efird [176], weld beads and steps in pipework are common areas where higher rates of attack and failure can occur because of increased turbulent activity as a result of disturbed flow. Schematic diagrams are provided in Figure 6.35 which highlight these modes of attack.

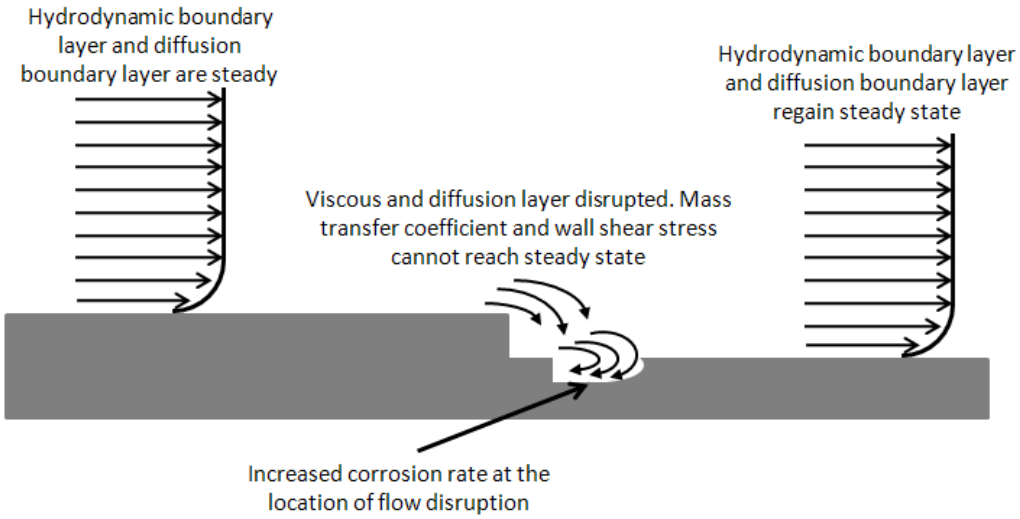

(a)

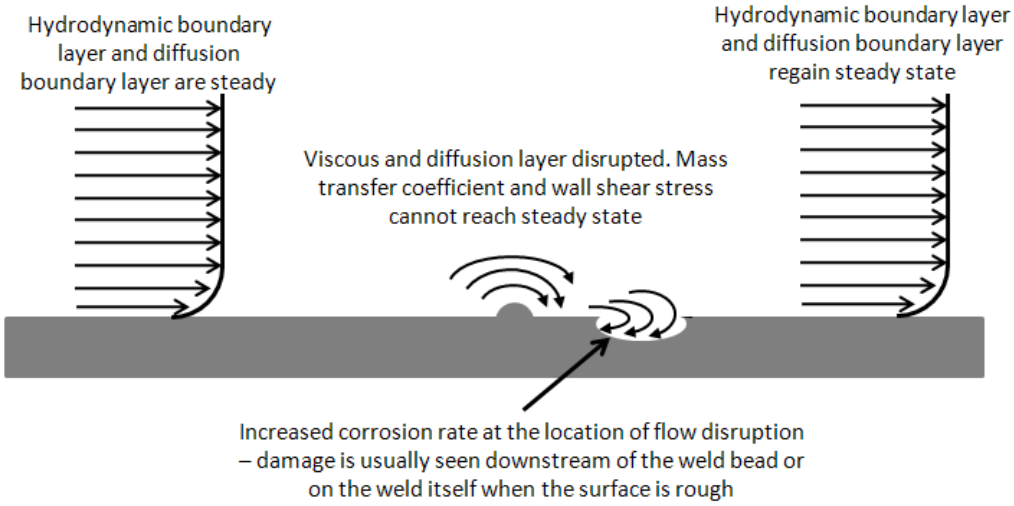

(b)

Figure 6.35: Wall shear stress and mass transfer for turbulent flow over a metal surface containing (a) a step change and (b) an internal weld bead [176]

It is evident that the Leeds model is capable of predicting the localised degradation rates on the facility in its current format by simulating the effects in highly turbulent regions of the offshore pipework.

6.8.2 Norsok Model Comparison Through Shear Stress

The Norsok model interprets corrosion rates through the calculation of shear stress for the system. The model is capable of calculating the shear stress in the system based on input parameters of pipe diameter, water cut, flow velocity, pressure, temperature and water cut. A comparison between the shear stress calculated by the CFD model of vertical pipe flow and that determined by the Norsok model is provided in Table 6.10. Both models are in good agreement over the level of shear stress in undisturbed flow.

It is perhaps unreasonable to have compared the Leeds empirical model with the Norsok model using the geometry dependant value of velocity when considering the differences in shear stress presented here. It is suggested that the reason for the large discrepancy between the Leeds and Norsok models exist because of the large different in wall shear stress for the same flow velocity. This is a result of the two different geometries of the systems used to establish corrosion rates.

Table 6.10: Comparison of shear stresses calculated by CFD and Norsok model for undisturbed pipe flow

Model	Shear Stress (Pa)				
	1 m/s	2 m/s	3 m/s	4 m/s	5 m/s
CFD for undisturbed pipe flow	2.5	8.7	18.0	30.1	44.9
Norsok Model	2.0	8.0	18.0	31.0	49.0
CFD Submerged Jet Impingement - average	6.3	22.2	43.9	71.0	103.3
CFD Submerged Jet Impingement - maximum	9.0	35.3	72.1	119.2	176.1

The calculated shear stress from the Norsok model is used to determine the shear stress factor, f(S), using Equation (6.9):

$$\mathrm{f(S)} = \left(\frac{\mathrm{S}}{19\ \mathrm{Pa}}\right)^{0.15+0.03\log\left(\mathrm{fCO_2}\right)} \tag{6.9}$$

where $\frac{\mathrm{S}}{19\ \mathrm{Pa}}$ is the actual wall shear stress S (Pa) relative to 19 Pa. Corrosion rate is then found using Equation (6.10):

$$\mathrm{CR_T} = \mathrm{K_T\ x\ fCO_2}^{0.6}\ \mathrm{x\ f(S) x\ f(pH)_T} \tag{6.10}$$

where K_T and $f(pH)_T$ are constants for a given temperature and pH, respectively. These constants can be found in tables provided by Halvorsen and Søntvedt [88].

To achieve a better understanding of how the SIJ data compares to that of the Norsok model, the corrosion rate predicted by each model is considered as a function of shear stress (Figure 6.36). The corrosion rates match much more closely and help to reinforce the belief by Efird that wall shear stress is a valuable parameter to help apply laboratory corrosion test data to operating systems in hydrodynamic systems.

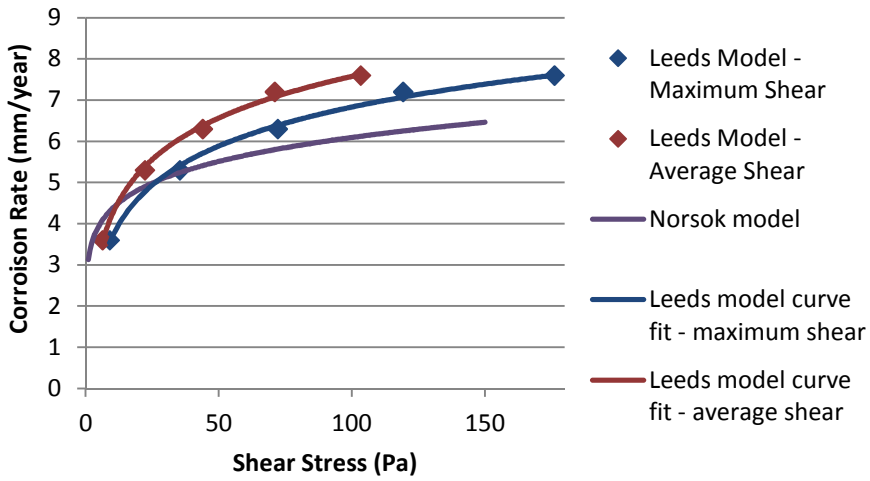

Figure 6.36: Comparison of Norsok model with SIJ data through levels of shear stress. Tests conditions were for a CO_2-saturated brine at atmospheric pressure, 0 mg/l sand and 45°C

It is evident that for this model to be used effectively in the field, it should be linked with CFD and the calculation of corrosion rate should be determined through levels of shear stress in the system, not bulk flow velocity.

6.8.3 Limitations of Leeds Model and Suggested Improvements

Although the model offers a very good prediction for this particular scenario, it is not without its limitations. Obviously, numerous suggestions for improvements to the model can be made, but focus here is directed towards incorporating features into the model which are deemed to be the most influential towards the rate of erosion-corrosion for this facility and nearby platforms. Two main parameters which vary across the other lines on the facility are that of temperature and crude oil to brine ratio.

At present, the model fails to account for changes in temperature for the system. This factor was not regarded as a priority due to the stable temperature on this particular line, but it does pose a limitation if the model is intended to be used on other similar systems on the facility/field which operate at a range of different temperatures. It is well documented that operating temperature can dramatically affect the nature, characteristics and morphology of the surface film, which, in turn, influences the corrosion and erosion processes [1, 139].

The line in question produces process fluid with an exceptionally high water cut (95%). Experiments were performed without the presence of hydrocarbon to generate the empirical model, therefore the model does not take water to

hydrocarbon ratios into consideration. The intensity of CO_2 corrosion attack is influenced by the time in which water is in contact with the steel surface. The water cut and the notion of water wetting are important variables to consider [1]. It is known that emulsions can form in oil/water systems and a water-in-oil emulsion can prevent or greatly reduce corrosion rate. However, if an oil-in-water emulsion is formed, then water wetting of steel will still occur. The transition from water-in-oil to oil-in-water occurs at water cuts of around 30-40%, causing an obvious increase in corrosion rate [1]. As a general rule, water cuts below 30% have a significantly lower corrosion rate, although exceptions to this do occur [1]. With the water cut on this particular facility being so high, it was assumed that the oil did not affect the water wetting of the steel significantly, nor the corrosion rate.

It can be argued that the empirical model provides a 'worst case scenario' in terms of prediction when water cut is concerned, as the presence of hydrocarbons will more often than not contribute to a reduction in erosion attributed to sand particle impingement as well as corrosion rate [86, 132]. However, incorporation of this particular feature may be worthwhile to provide a more accurate degradation rate estimate should it be applied to lines containing higher quantities of hydrocarbons.

Finally, the efficiency of the inhibitors is known to vary as a function of velocity [6]. To build a more accurate interpretation of degradation rate as a function of time when inhibition is used, it would be ideal to test the inhibitor at every velocity and every sand concentration within the model to provide a more accurate interpretation. The addition of this feature would be incredibly time consuming, therefore testing the inhibitor at more severe erosion-corrosion conditions than within the model, and applying the resulting efficiency throughout the entire model appears a logical choice for a 'worst case scenario'. The evaluation and incorporation of a number of inhibitors into the model may be a valuable introduction for corrosion engineers.

6.9 Generation of Graphical User Interface

Based on the model, a graphical user interface was developed in Matlab® which essentially takes the sand loading and velocity data and uses it to predict the pipework thickness loss and degradation rate as a function of time. The user is able to specify the inhibitor efficiency and availability over that period and can also specify single values of sand loading and velocity to determine individual degradation rates. Figure 6.37 shows the interface developed for the model.

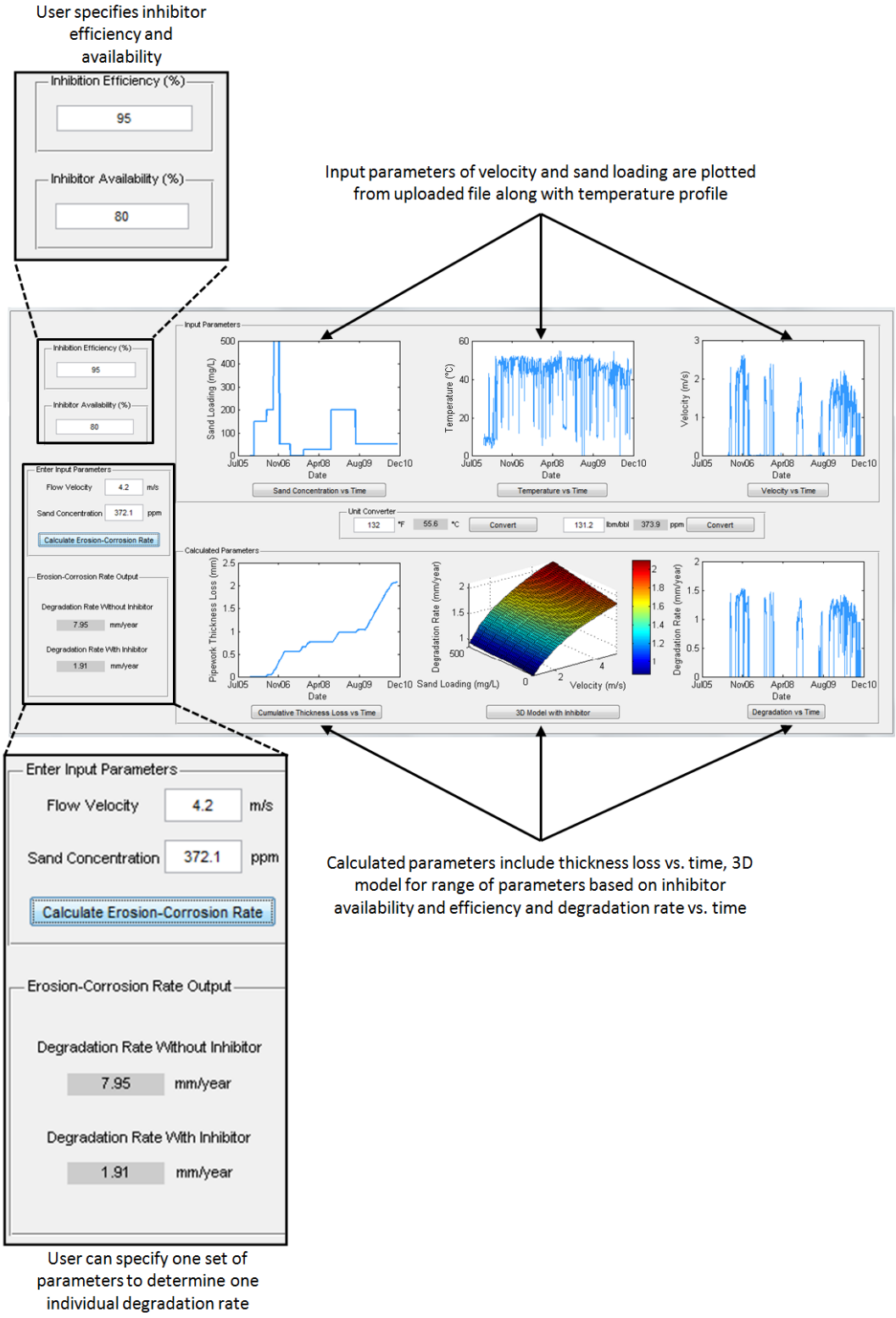

Figure 6.37: Graphical user interface for the Leeds Erosion-Corrosion Model

6.10 Conclusions

- An empirical model has been developed to predict the erosion-corrosion degradation rate of carbon steel in sand containing CO_2 environments on an offshore facility.

- The model inputs include both flow velocity and sand concentration. The range of inputs encapsulates velocities between 1 and 5 m/s and sand concentrations between 0 to 500 mg/L.

- The model was used to predict degradation rate on the offshore facility as a function of time between 2005 and 2010 and was capable of determining the thickness loss of the pipework as a function of time.

- Comparison of the prediction data with the Norsok and de Waard and Milliams models showed that the developed model predicted significantly higher degradation rates which were closer to those seen on the facility based on ultrasonic inspection.

- The implementation of CFD showed that degradation rates were higher potentially because of the higher levels of turbulence and shear stress in the jet impingement system. Correlating the Leeds model with the Norsok model through calculated values of shear stress showed that the models were in much better agreement with each other.

- A review of the current inhibition strategy allowed the efficiency of the currently used chemical to be incorporated into the model. Once this factor was accounted for, the empirical model predicted degradation rate even more closely when compared to the inspection data.

- The main limitations of the model which are preventing it from being used on other similar lines are that it does not take into account changes in temperature and hydrocarbon content.

- The research indicated that the jet impingement system is a useful tool for predicting degradation rates. The model also helped to enforce the belief that wall shear stress is a valuable parameter when correlating laboratory corrosion rates with the field.

Chapter 7 - Inhibitor Selection Process for an Offshore Facility – An Understanding of Inhibitor Mechanisms

7.1 Introduction and Chapter Outline

Inhibitors evaluated in laboratories do not always behave as intended in the field. Research into factors which limit a chemical's performance is paramount when evaluating inhibitors for the oil and gas industry. The development of reliable and representative testing methods are essential for the selection and quantification of inhibitors so that the user has the utmost confidence in the product and its application [185].

This Chapter examines the efficiency of three commercially available CO_2 corrosion inhibitors using gravimetric methods and a variety of electrochemical techniques (both AC and DC). All inhibitors are either currently used or considered for application in the North Sea to mitigate the effects of CO_2 corrosion. The performances of the inhibitors are compared in both static, flow-induced corrosion and erosion-corrosion conditions at concentrations between 10 and 100 ppm to demonstrate the difference in inhibitor performance with changes in the physical and environmental properties of the process fluid. The influence of pre-corrosion in flow-induced corrosion conditions and the implications this has on inhibitor efficiency are also considered.

Electrochemical impedance spectroscopy (EIS) is used to study the corrosion mechanisms and inhibitor film formation for different inhibitor concentrations (10, 25, 50, 75 and 100 ppm) under dynamic conditions. Impedance data was fitted to equivalent electrical circuit models (EECMs) yielding information pertaining to the capacitive, inductive and resistive properties of the electric double layer, corrosion behaviour, inhibitor films and diffusion characteristics, providing an insight into a number of inhibition mechanisms adopted by the chemicals. The EIS results are also evaluated against gravimetric measurements.

The inhibitors are tested in an erosion-corrosion environment at their optimum concentrations and scanning electron microscopy (SEM) along with *in-situ* corrosion measurements are used to help review the inhibitors' performance and consider the degradation mechanisms. The behaviour of the most efficient chemical is then incorporated into the Leeds empirical model and the notion of inhibitor availability is introduced. Figure 7.1 provides an outline of the approach adopted within this Chapter.

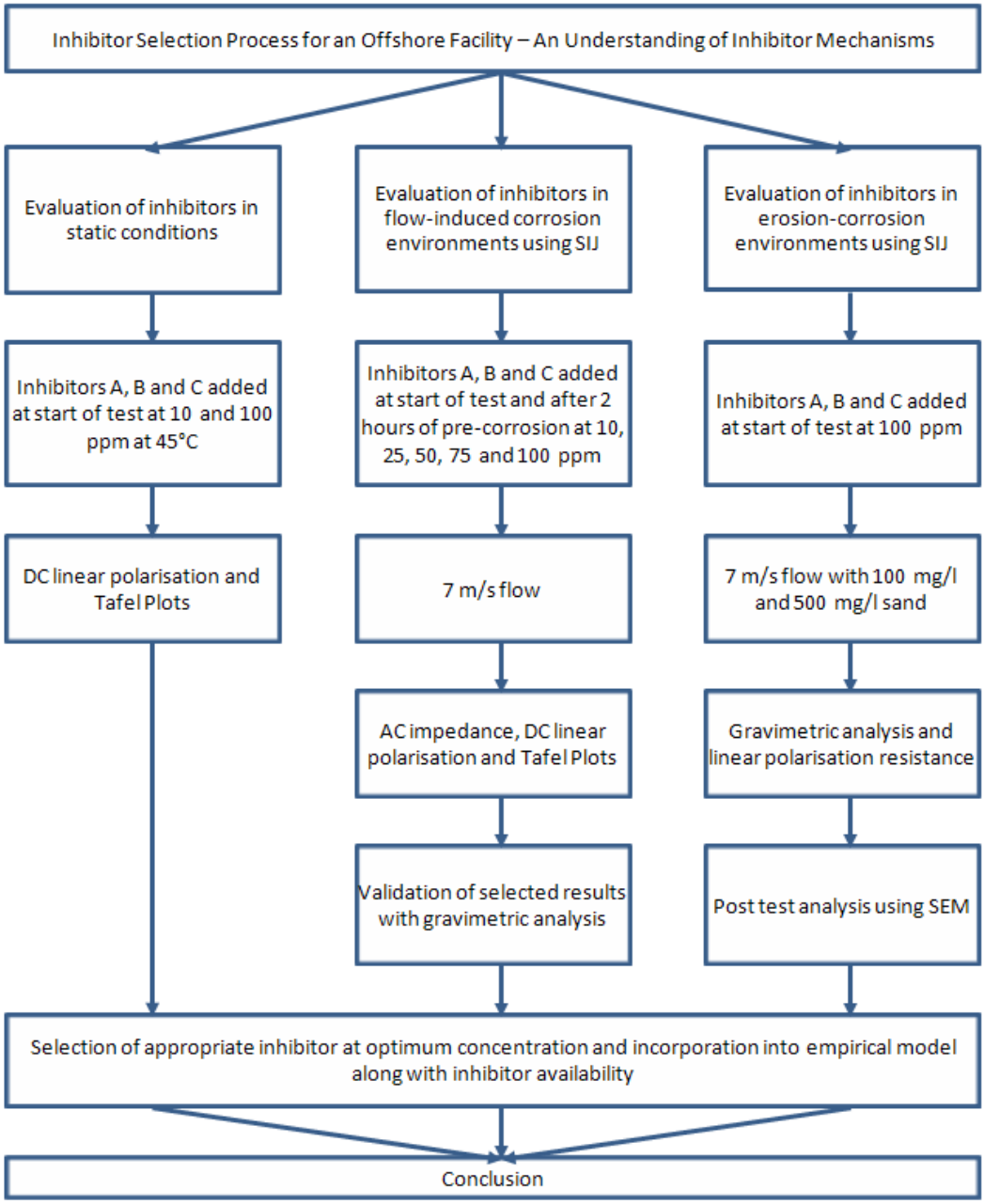

Figure 7.1: Outline of Chapter 7

7.2 Static Corrosion Testing Using Linear Polarisation

Two experimental techniques were used to evaluate the inhibitors. Static tests were performed in glass cells, whilst the flow-induced corrosion and erosion-corrosion experiments were conducted in a submerged impinging jet (SIJ). The experimental setup and results of the static tests are provided in this section.

7.2.1 Experimental Static Setup

Static tests formed a baseline for the flow-induced corrosion and erosion-corrosion experiments and were conducted in the brine solution shown previously in Table 6.1. Experiments were performed at atmospheric pressure in a 1 litre glass cell. The apparatus is shown in Figure 7.2. The corrosion process was studied by means of the DC linear polarisation technique using a computer controlled ACM Gill 8 potentiostat. A three electrode cell was used comprising of a Ag/AgCl reference electrode, a platinum auxiliary electrode and the specimen working/test electrode. The pH was monitored with an electrode immersed in the electrolyte. Temperature was monitored with a probe which also served as an input for the temperature regulating system, comprising of a hotplate and a magnetic stirrer.

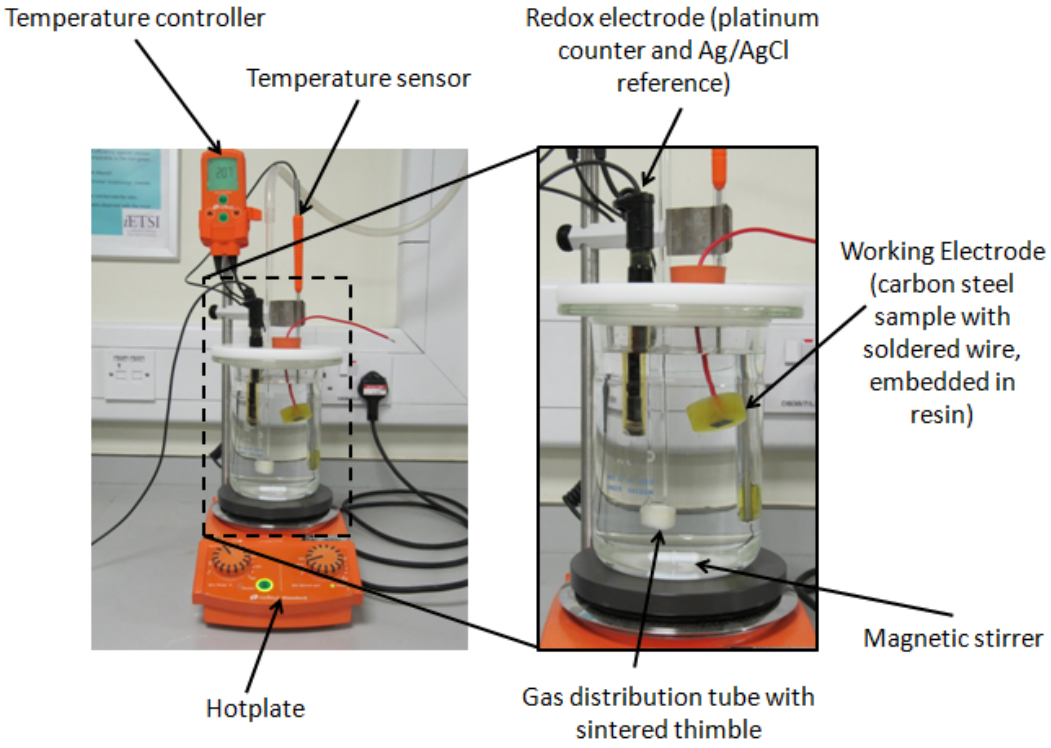

Figure 7.2: Diagram of three-electrode cell used in static experiments

7.2.2 Sample Preparation

Carbon steel samples/working electrodes were cut from the pipework, machined down to 10x10x6 mm pieces and soldered to wires before embedding them in a non-conductive resin. The exposed area of the specimen was 1 cm^2. The chemical composition of the steel has been previously provided in Table 6.6.

7.2.3 Inhibitors

Three inhibitors were evaluated in static conditions. These are referred to as Inhibitors A, B and C. The constituents of the three inhibitors are summarised in Table 7.1.

Table 7.1: Composition/information on chemical components of Inhibitors A, B and C

Chemical Name	Inhibitor A	Inhibitor B	Inhibitor C
2-(2-Butoxyethoxy)ethanol	(5-10%)	-	
Ethandiol	(5-10%)	-	(10-30%)
Ethoxylated Amine Salt	(10-30%)	-	-
Propan-2-ol	(< 1%)	(< 1%)	-
Quaternary Ammonium Salts	(1-5%)	(1-5%)	-
Anhydride/Polyamine Reaction Product	-	(1-5%)	-
Ethoxylated Imidazoline	-	(5-10%)	(10-30%)
2-Mercaptoethanol	-	(1-5%)	(1-5%)
2-Aminoethanol	-	-	(1-5%)
Salts of Carboxylic Acid	-	-	(5-10%)

7.2.4 Experimental Procedure for Static Tests

The glass cells were filled with 1 litre of electrolyte and CO_2 was bubbled through the solution for a minimum of 12 hours before starting the test as well as throughout the experiment to ensure complete saturation. The temperature was maintained at 45±1˚C in all experiments.

Before starting each experiment, the steel working electrode was wet-ground up to 1200 silicon carbide abrasive paper, degreased with acetone and rinsed with distilled water before immersing in the test solution. The free corrosion potential (E_{corr}) was followed immediately after immersion and stabilised within 1-5 minutes.

When inhibition was used, chemicals were added once E_{corr} had stabilised and polarisation measurements were subsequently started. Polarisation resistance measurements were conducted by polarising the working electrode ±15 mV from E_{corr} and scanning at a rate of 0.25 mV/s in accordance with ASTM-G102 [42]. Measurements were performed approximately every 6-7 minutes. Solution resistance (R_s) was measured for each test using AC impedance and was subsequently subtracted from the polarisation resistance (R_p) to ensure the corrosion rate was accurately quantified.

At the end of each experiment, potentiodynamic sweeps were conducted. Cathodic and anodic sweeps were performed by starting from E_{corr} and finishing at either ±250 mV from E_{corr}. Only one sweep (either anodic or cathodic) was performed for a single working electrode at the end of the test since significant polarisation can alter the specimen surface and high anodic potentials can contaminate the electrolyte with dissolved iron.

7.2.5 Characterisation of Carbon Steel in Blank, Static Conditions

The first section of tests focused on the behaviour of the material in static conditions without chemical inhibition (referred to as blank tests). R_p measurements over 4 hours (Figure 7.3) indicated no significant change in corrosion rate, although an increase in E_{corr} of approximately 4-5 mV over the 4 hour period was observed.

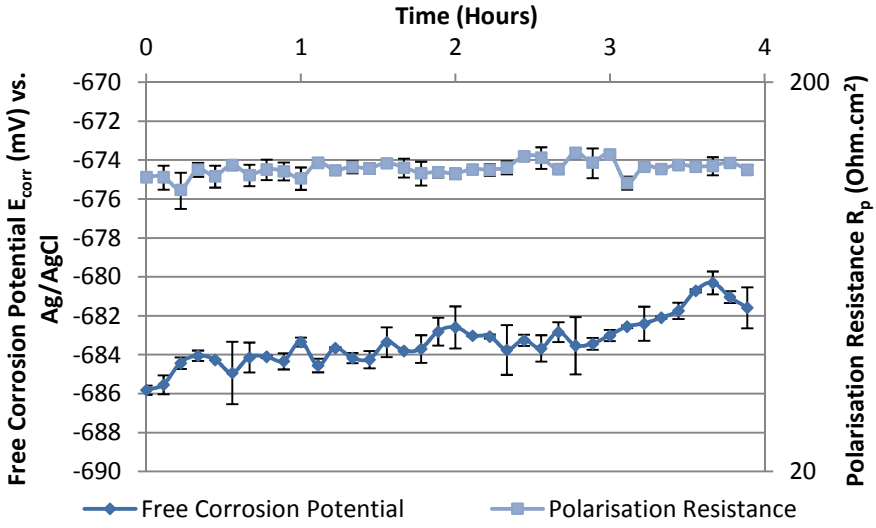

Figure 7.3: Free corrosion potential and polarisation resistance of carbon steel sample over 4 hours in a blank brine solution. Test conditions were: static, 45°C and CO_2-saturated at 1 bar

Tafel measurements from four separate tests (two anodic and two cathodic) in the blank solution are provided in Figure 7.4 to indicate the reproducibility of the tests.

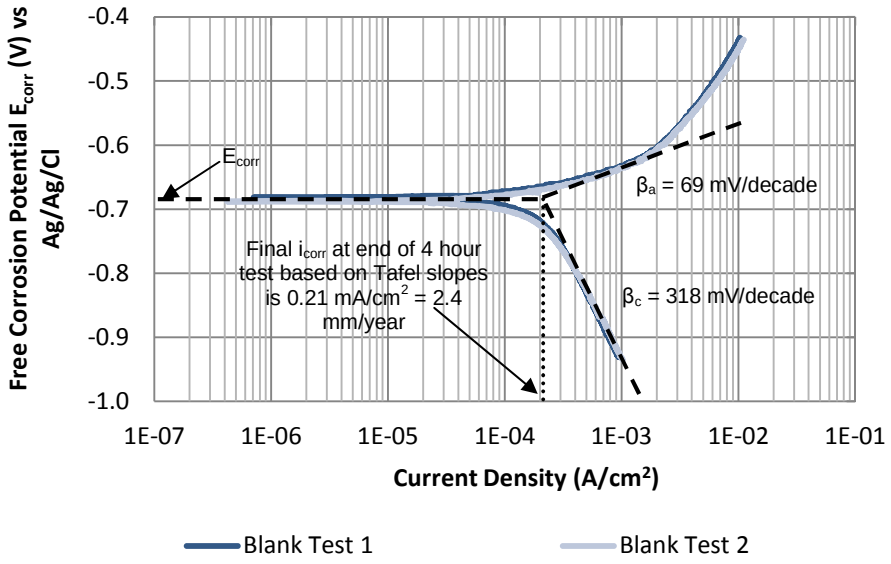

Figure 7.4: Repeated Tafel plots for carbon steel in blank brine solution after 4 hours. Tests conditions were: static, 45°C and CO_2-saturated at 1 bar

By using measured values of Tafel constants, the Stern-Geary coefficient was calculated at 24.6 mV/decade using the following equation:

$$\mathrm{B\ (Stern-Geary\ coefficient)} = \frac{1}{2.303}\left[\frac{\beta_a \beta_c}{\beta_a + \beta_c}\right] \tag{7.1}$$

The corrosion current density could then be determined using this coefficient and the R_p values using:

$$i_{corr} = \frac{B}{R_p} \tag{7.2}$$

Finally, corrosion rates were quantified by converting the corrosion current density into a rate of thickness loss using:

$$\mathrm{Corrosion\ Rate\ (mm/y)} = \frac{3.27 \times 10^3 (i_{corr}) M}{n\rho} \tag{7.3}$$

The corrosion rate as a function of time is provided in Figure 7.7 and indicates the stability of the corrosion rate over the initial 4 hours.

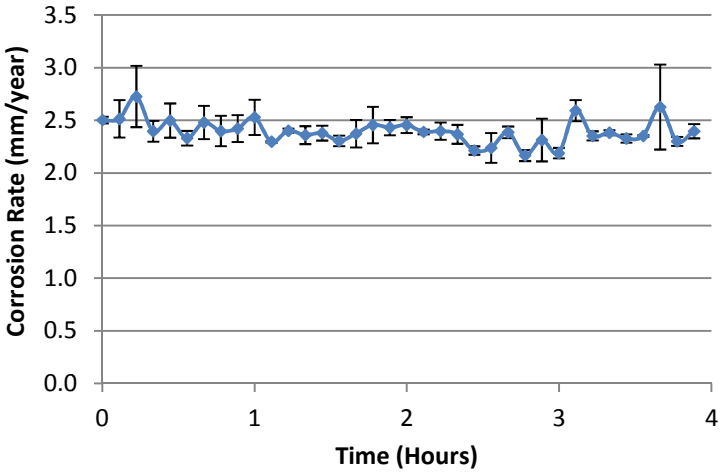

Figure 7.5: Corrosion rate of carbon steel sample over 4 hours in a blank brine solution. Tests conditions were: static, 45°C and CO_2-saturated at 1 bar

Upon inspection of the working electrode surface after the 4 hour test, a black iron carbide network (Fe_3C) was visible on the surface of the sample. Figure 7.6 shows an optical microscope image of the network. These types of formation are attributed to the dissolution of the ferrite phase from the sample, leaving behind the Fe_3C phase protruding from the surface. Nešić et al. [48] explained that the presence of Fe_3C has the ability to cause an increase in E_{corr} and that iron carbide films can also increase corrosion rate. For the tests performed in static conditions, an increase in potential was observed, but no discernible change in corrosion rate was seen over 4 hours.

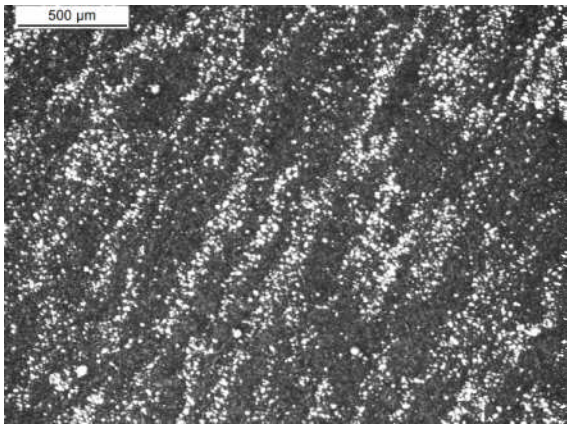

Figure 7.6: Optical microscope image of iron carbide network on the surface of carbon steel after exposure to static conditions for 4 hours

7.2.6 Inhibitor Performance at 10 ppm

All three inhibitors were tested in static conditions at 10 ppm. Chemicals were administered to the brine solution no more than 5 minutes after submerging the working electrode into the solution. Electrochemical measurements were started immediately after administering chemicals to the test solution. Values of R_p and E_{corr} were recorded against time for all tests.

Results for the application of Inhibitors A and B at 10 ppm are provided in Figure 7.7 and Figure 7.8, respectively. Both chemicals display similar behaviour in that the addition of 10 ppm resulted in a gradual and continual increase in both R_p and E_{corr}. The value of E_{corr} begins to plateau after 2 hours, reaching a higher potential than in the blank tests. The overall increase in potential suggests that the inhibitors are predominantly anodic in behaviour i.e. suppress the anodic reaction more than the cathodic reaction.

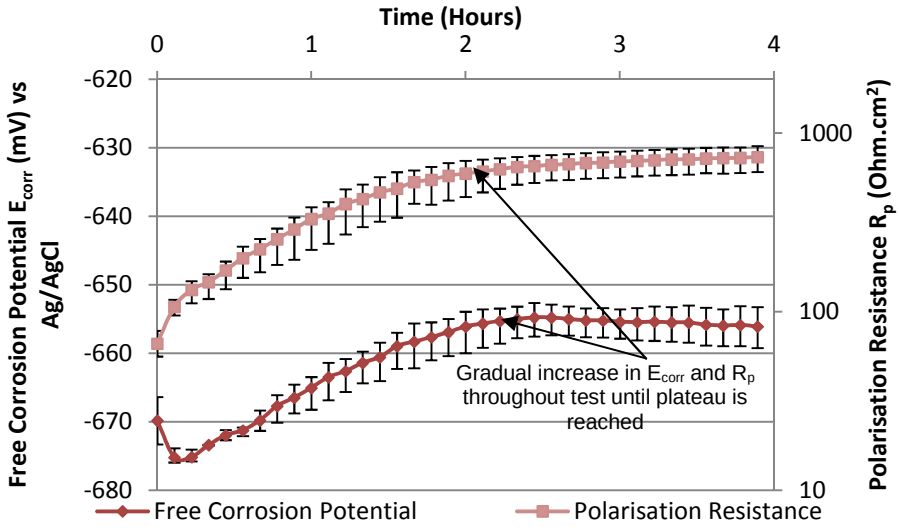

Figure 7.7: Free corrosion potential and polarisation resistance of carbon steel sample over 4 hours after the addition of 10 ppm Inhibitor A. Test conditions were: static, 45°C and CO_2-saturated at 1 bar

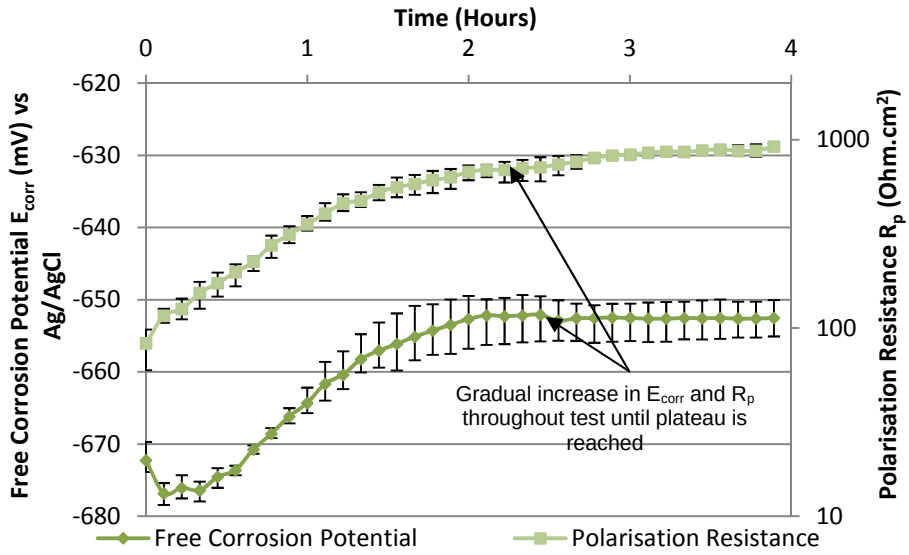

Figure 7.8: Free corrosion potential and polarisation resistance of carbon steel sample over 4 hours after the addition of 10 ppm Inhibitor B. Test conditions were: static, 45°C and CO_2-saturated at 1 bar

The addition of Inhibitor C at 10 ppm produced different adsorption characteristics to that of A and B. Figure 7.9 indicates that the addition of 10 ppm of Inhibitor C resulted in what could almost be described as a 'two-step' adsorption mechanism. One can notice in Figure 7.9 that a fast initial adsorption step occurs over the first hour, corresponding to a fast increase in E_{corr} and a corresponding rise in R_p. This process is subsequently followed by a much slower adsorption process which results in a further reduction in the corrosion rate (i.e. an increase in R_p). Interestingly, the initial rapid adsorption step is associated with an increase in E_{corr} and the second step coincides with a smaller (approximately 5-10 mV) decrease in potential. It is suggested that the anodic reaction is rapidly inhibited in this first adsorption process, followed by a much slower reduction of the cathodic process in the second step.

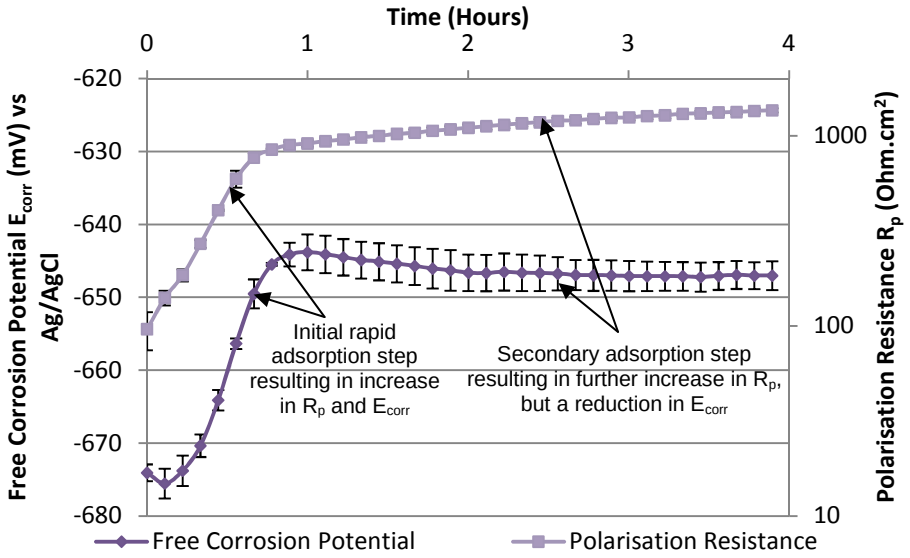

Figure 7.9: Free corrosion potential and polarisation resistance of carbon steel sample over 4 hours after the addition of 10 ppm Inhibitor C. Test conditions were: static, 45°C and CO_2-saturated at 1 bar

Figure 7.10 indicates the Tafel measurements which were performed at the end of each of the blank and inhibited tests at 10 ppm.

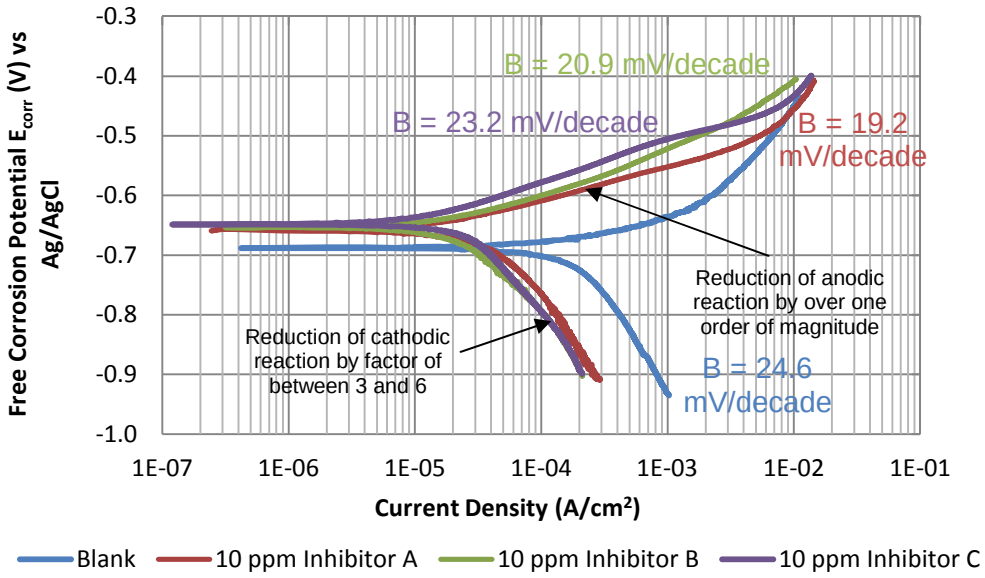

Figure 7.10: Tafel plots after 4 hours in static conditions with Inhibitors A-C at 10 ppm (anodic and cathodic curves were constructed using separate samples). Test conditions were: static, 45°C and CO_2-saturated at 1 bar

From Figure 7.10, it is clear that the values of E_{corr} at the end of the inhibited tests were all higher than that of the blank solution, indicating predominantly anodic inhibition behaviour. As a rough initial statement from the Tafel slopes in Figure

7.10, one can say that all inhibitors act similarly by slowing down both the cathodic and anodic reactions. The effect of the inhibitors on the anodic reaction appears much stronger, which would explain the increase in E_{corr} observed. The cathodic reaction is inhibited by a factor of between 3 and 6 for the three chemicals where as the anodic reaction is reduced by over one order of magnitude.

By considering the plots of E_{corr} and R_p as a function of time in conjunction with the Tafel plots, it can be proposed that Inhibitors A and B adopt slightly different inhibition mechanisms to that of Inhibitor C at a concentration of 10 ppm. Chemical packages A and B display a gradual and relatively slow increase in E_{corr} throughout the test (visible in Figure 7.7 and Figure 7.8) which stabilises after 2 hours. The corrosion rate gradually reduces and the adsorption process appears to occur in one smooth step.

Inhibitor C (Figure 7.9) has an initial adsorption step, corresponding to an ennoblement of E_{corr} which peaks within less than one hour, signifying suppression of the anodic reaction. Once a maximum value of potential is reached, a slow reduction in potential is observed with a continual decrease in corrosion rate.

For Inhibitor C (Figure 7.9) the continual reduction in corrosion rate despite the initial increase and then decrease in E_{corr} suggests that the anodic reaction is initially suppressed the most during the rise in potential. After the peak in E_{corr}, the cathodic process becomes the focus of attention for the inhibitor which is manifested by the reduction in potential.

It is difficult to propose an accurate explanation for this observation of fluctuating potential. However, it can be speculated that the majority of inhibitor molecules are initially attracted to the anodic sites, leading to a reduction in the iron dissolution rate, without affecting the cathodic reaction directly. This accounts for the initial rapid adsorption process. The second, slower process is either a result of the attraction of cathodic inhibitors to the surface as a result of chemicals which have already adsorbed onto the surface, or potentially the lateral interactions between the chains of adsorbed molecules hinder the transport of the cathodic species to the surface and subsequently decrease the rate of the cathodic reaction. Similar behaviour was witnessed by Nešić et al. [186] for one amine based and one imidazoline based inhibitor.

The measured values of Tafel slopes were used in conjunction with the Stern-Geary Equation [41, 187] and Faraday's Law to determine the corrosion rate of the

carbon steel as a function of time (Figure 7.11). None of the three inhibitors were able to reach the target commonly set by industry of 0.1 mm/year within the test period.

The 'two-step' mechanism proposed for Inhibitor C is clearly visible within the corrosion rate measurements as a function of time (Figure 7.11). There is a distinct and relatively rapid initial decrease in corrosion rate followed by a slower adsorption process resulting in a slower reduction in the rate of dissolution.

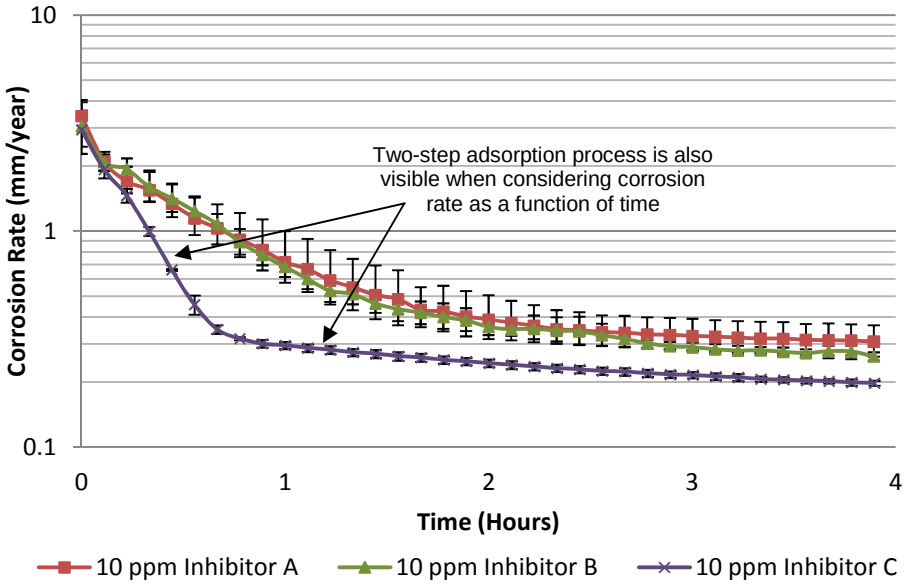

Figure 7.11: Corrosion rates of carbon steel as a function of time for the application of Inhibitors A-C at 10 ppm in static solutions with inhibitor addition at the start of the test. Test conditions were: static, 45°C and CO_2-saturated at 1 bar

7.2.7 Inhibitor Performance at 100 ppm

In an effort to achieve corrosion rates below 0.1 mm/year, the inhibitor concentrations were increased to 100 ppm. Measurements of E_{corr} and R_p as a function of time are provided from Figure 7.12 to Figure 7.14 for Inhibitors A to C. By studying the potential changes as a function of time for the three inhibitors at 100 ppm, the behaviour can be related to that observed for Inhibitor C at 10 ppm (Figure 7.9). A rapid increase in potential is observed at the start of the test when 100 ppm of each inhibitor is used. This signifies suppression of the anodic reaction and occurs over the first 5-10 minutes of the test, after which the potential peaks. The point at which the potential reaches a maximum is around 50 minutes faster than tests at 10 ppm, indicating that the initial adsorption process is far more rapid as a result of the increase in concentration.

The peak in potential effectively represents the switch in adsorption steps [186]. Subsequently, there is a slow reduction in E_{corr} and a continual rise in R_p (or continuous reduction in corrosion rate). This step is believed to result in inhibition of predominantly the cathodic process during this period [186].

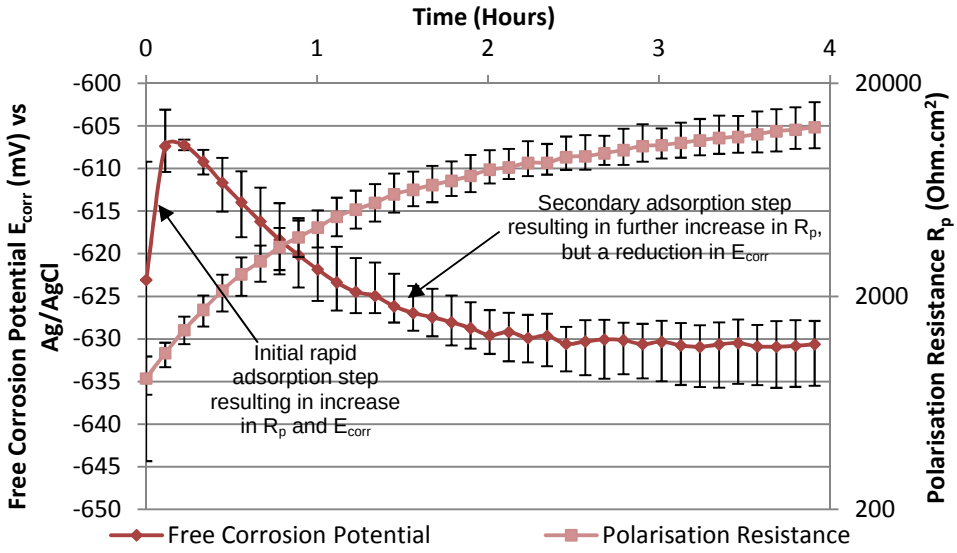

Figure 7.12: Free corrosion potential and polarisation resistance of carbon steel sample over 4 hours after the addition of 100 ppm Inhibitor A. Test conditions were: static, 45°C and CO_2-saturated at 1 bar

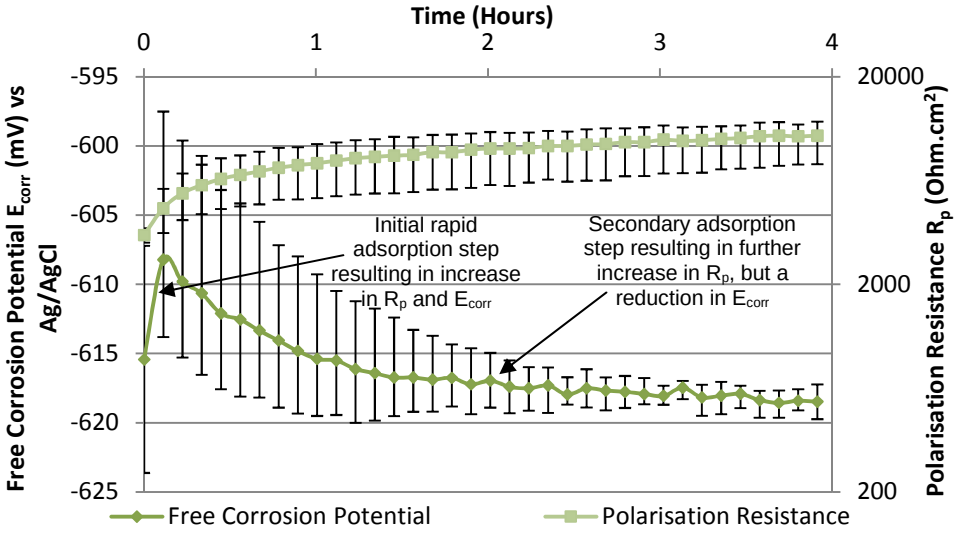

Figure 7.13: Free corrosion potential and polarisation resistance of carbon steel sample over 4 hours after the addition of 100 ppm Inhibitor B. Test conditions were: static, 45°C and CO_2-saturated at 1 bar

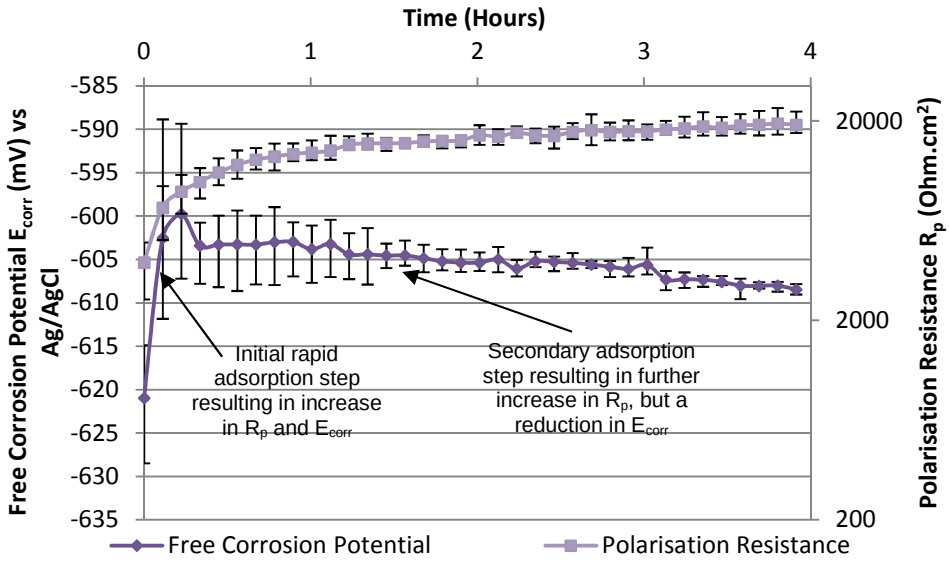

Figure 7.14: Free corrosion potential and polarisation resistance of carbon steel sample over 4 hours after the addition of 100 ppm Inhibitor C. Test conditions were: static, 45°C and CO_2-saturated at 1 bar

The Tafel plots for tests at 100 ppm are provided in Figure 7.15 along with a plot for the blank solution. It can be seen that increasing the inhibitor concentrations to 100 ppm reduces the cathodic reaction by over one order of magnitude and the anodic process by over two orders of magnitude. Interestingly, based on the anodic Tafel slope measurements in Figure 7.15, Inhibitor A fully desorbs from the surface at higher anodic potentials.

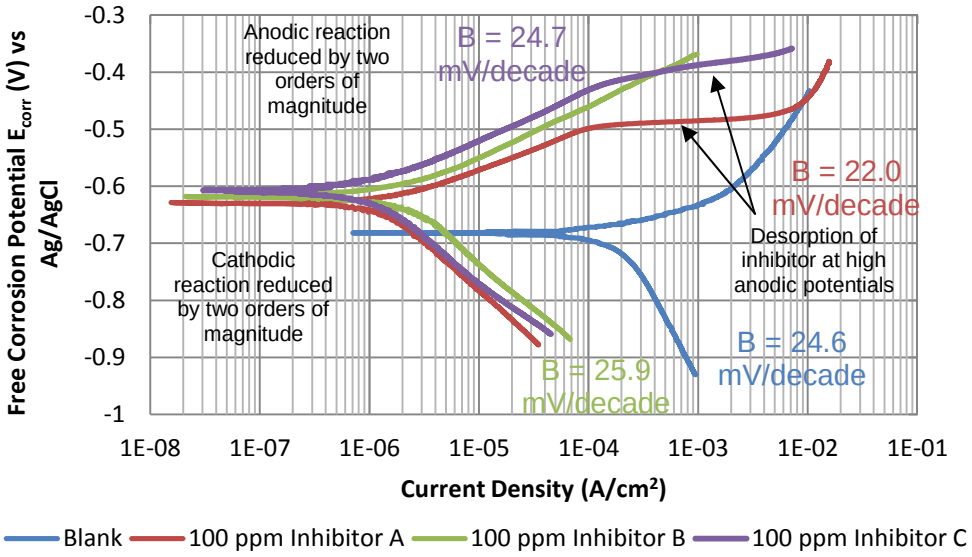

Figure 7.15: Tafel plots after 4 hours in static conditions with Inhibitors A-C at 100 ppm (anodic and cathodic curves were constructed using separate samples). Test conditions were: static, 45°C and CO_2-saturated at 1 bar

Corrosion rate as a function of time for the inhibitors is provided in Figure 7.16. The rate at which corrosion inhibition is achieved is significantly faster than at 10 ppm, so much so that the benchmark of 0.1 mm/year is achieved for two of the inhibitors even before the potentiostat began monitoring the corrosion rate.

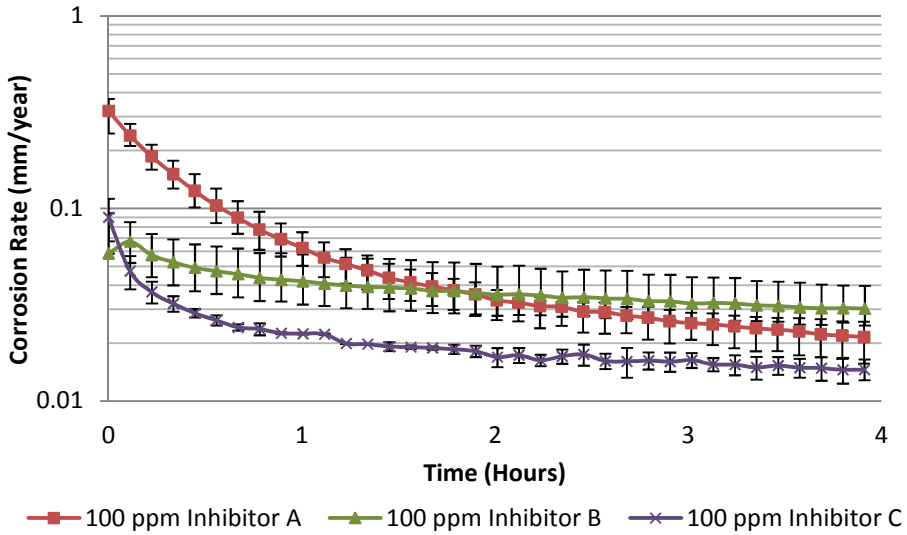

Figure 7.16: Corrosion rates of carbon steel as a function of time for the application of Inhibitors A-C at 100 ppm in static solutions with inhibitor addition at the start of the test. Test conditions were: static, 45°C and CO_2-saturated at 1 bar

7.2.8 Summary of Static Results

Figure 7.17(a) summarises the final E_{corr} at the end of each test in blank conditions and with each inhibitor at 10 ppm. Figure 7.17(b) provides the inhibitor efficiency at 10 ppm based on the reduction in corrosion rate. This was calculated using the equation:

$$\text{Inhibitor Efficiency} = \frac{CR_{NI} - CR_{WI}}{CR_{WI}} \quad (7.4)$$

where CR_{NI} is the blank corrosion rate and CR_{WI} is the final corrosion rate reading at the end of the inhibited test.

The red dashed line in Figure 7.17(b) indicates the required efficiency to reach 0.1 mm/year. Static corrosion tests therefore indicated that 10 ppm was insufficient to reduce corrosion rate to below this target. Based on Figure 7.17(a), all inhibitors increased the E_{corr} of the material from that of the blank solution, indicating they predominantly suppress the anodic reaction. Inhibitors A and B at 10 ppm produced a 'slow' adsorption process with continual increase in E_{corr} throughout the test,

signifying one dominant adsorption step. Inhibitor C at 10 ppm displayed a 'two-step' mechanism whereby the first step was dominated by suppression of the anodic reaction and the second mechanism focused on reducing the cathodic process. These two stages are visible for Inhibitor C in the plot of corrosion rate vs. time shown previously in Figure 7.11. This behaviour was attributed to the initial adsorption of anodic (or predominantly anodic) inhibitor components, followed by either the preferential adsorption of a chemical onto cathodic sites, or the build up of lateral interactions between inhibitor chains resulting in the hindrance in transport of cathodic species to the surface, ultimately suppressing the cathodic reaction.

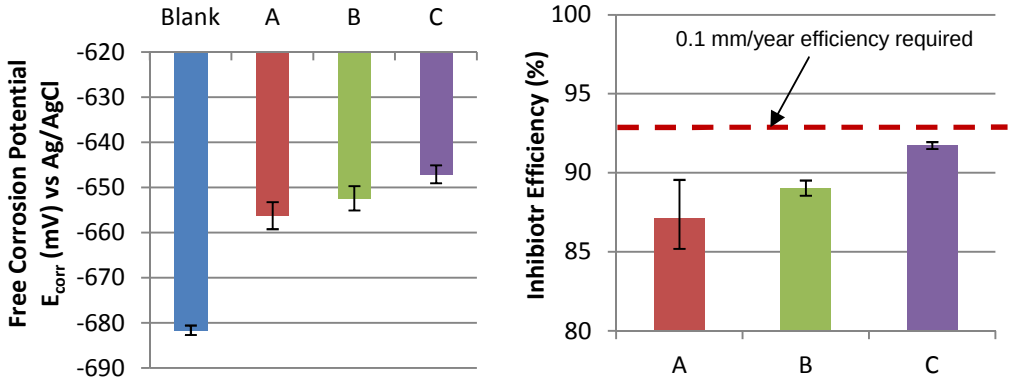

(a) (b)

Figure 7.17: (a) Free corrosion potential measurements at the end of the 4 hour tests and (b) Inhibitor efficiencies based on the final corrosion rate at the end of the experiment at 10 ppm. Test conditions were: static, 45°C and CO_2-saturated at 1 bar

Final E_{corr} measurements and inhibitor efficiencies at 100 ppm are provided in Figure 7.18(a) and Figure 7.18(b), respectively. At higher concentrations of 100 ppm, all inhibitors followed the two-stage adsorption process. Suppression of the anodic reaction was rapid (within a few minutes) as opposed to the test at 10 ppm with Inhibitor C (1 hour). The majority of the test duration comprised of a decrease in the potential as a function of time after an initial sudden rise, along with an increase in R_p (or reduction in corrosion rate).

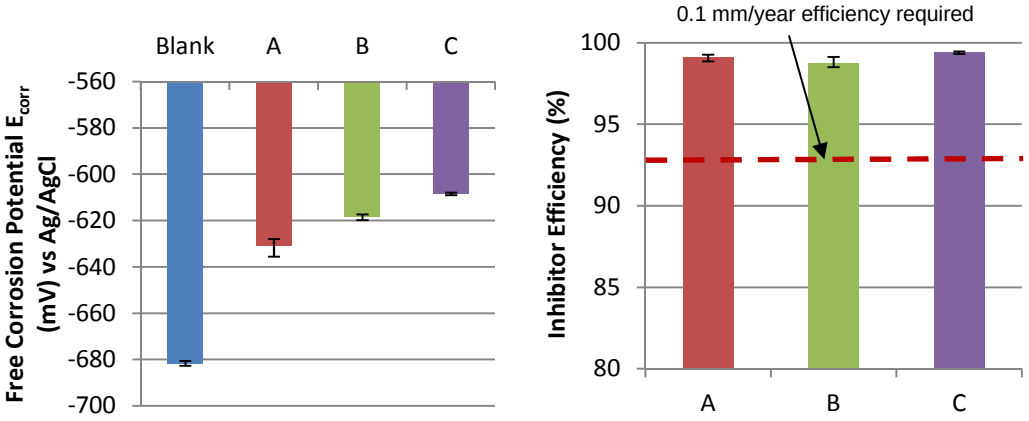

(a) (b)

Figure 7.18: (a) Free corrosion potential measurements at the end of the 4 hour tests and (b) Inhibitor efficiencies based on the final corrosion rate at the end of the experiment at 100 ppm. Test conditions were: static, 45°C and CO_2-saturated at 1 bar

7.3 Flow-Induced Corrosion Tests Using the SIJ

Based on the static corrosion tests performed, any one of the three chemicals would be sufficient to suppress corrosion rate in the system to below the target level of 0.1 mm/year at 100 ppm. Unfortunately, the behaviour in static conditions does not represent the hydrodynamic severity experienced in pipe flow on the facility. Often inhibitors tend to be validated in laboratory conditions which are not representative of those in the field. To demonstrate this misrepresentation of efficiency and determine the effect of fluid hydrodynamics on the system, tests were conducted in a more severe, high shear environment using a submerged impinging jet.

7.3.1 Experimental Flow-Induced Corrosion Setup

Flow-induced corrosion tests were conducted using the submerged impinging jet (SIJ) apparatus shown in Figure 7.19. A re-circulating system is adopted by the rig which enables the fluid to be delivered through a dual nozzle arrangement, which impinges onto a flat specimen at an angle of 90˚. The nozzle is 4 mm in diameter and positioned at a fixed distance of 5 mm from the specimen.

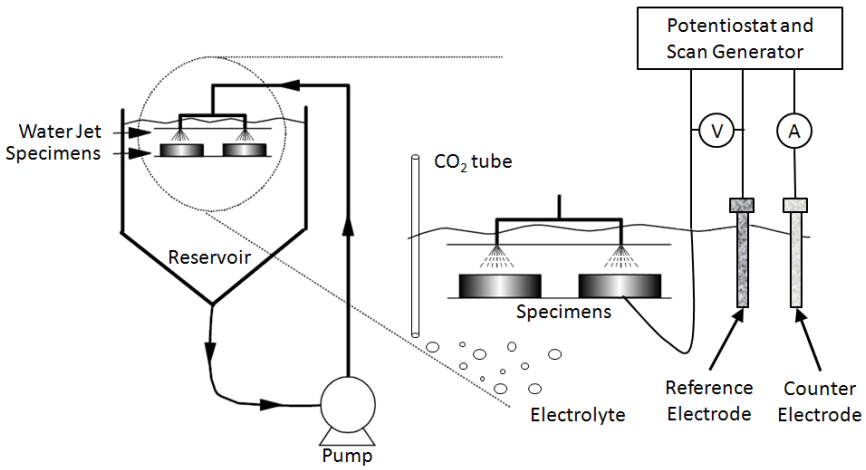

Figure 7.19: Re-circulation rig for CO_2-saturated flow-induced corrosion experiments

The corrosion processes were studied using the same three electrode cell as in static tests. The pH was monitored with an electrode immersed in the electrolyte. Temperature was monitored with a probe which also served as an input for the temperature regulating system comprising of a control box and a heating filament.

7.3.2 Sample Preparation and Inhibitors

Carbon steel test samples/working electrodes were cut from the pipework, machined to 20x20x6 mm pieces and soldered to wires before embedding them in a non-conductive resin. The exposed area of the sample was 4 cm^2.

The three inhibitors studied in the static tests were all considered in the flow-induced corrosion tests.

7.3.3 Experimental Procedure for Flow-Induced Corrosion Tests

The SIJ vessel was filled with 70 litres of electrolyte and CO_2 was bubbled through the solution for a minimum of 12 hours before starting the test as well as throughout the experiment to ensure it remained fully saturated. The temperature was maintained at 45±1˚C and all flow-induced corrosion experiments in this section were conducted at a flow velocity of 7 m/s.

Before starting each experiment, the carbon steel working electrode was wet-ground up to 1200 silicon carbide abrasive paper, degreased with acetone, rinsed with distilled water and dried with compressed air before being fixed into sample holders positioned under the jet nozzles. E_{corr} was followed immediately after immersion and stabilised within 1-5 minutes, after which the motor was started.

When inhibition was used, E_{corr} was allowed to stabilise with the motor running before chemicals were added to the rig. This usually took less than one minute. In the case where samples were pre-corroded, inhibitor was introduced to the system after 2 hours of exposure to blank conditions.

AC impedance was chosen along with DC linear polarisation as the electrochemical method to determine corrosion rate in the system, as this approach was capable of providing a further insight into the dissolution and inhibitor mechanisms as well as the *in-situ* corrosion rates. The AC impedance measurements were performed using a Solartron 1280 potentiostat which applied an oscillating potential to the working electrode of 10 mV about E_{corr} using a frequency range of 20 kHz to 100 mHz with 10 points per decade. Nyquist, Bode and Phase plots were analysed using Zview^{TM} software. Linear polarisation was applied in the same manner as the static tests to help verify impedance measurements.

At the end of each experiment, potentiodynamic sweeps were conducted. Cathodic and anodic sweeps were performed by starting from E_{corr} and finishing at either ±250 mV from E_{corr}. Only one sweep (either anodic or cathodic) was performed for a single working electrode at the end of the test.

7.3.4 Data Fitting and Model Validation for AC Impedance Results

Impedance circuits are often modelled using electrical circuits which are capable of producing a similar spectrum. The electrical components selected for these circuits are then matched to the physical characteristics of the measured cell. There are often several equivalent circuits that will produce the same impedance spectrum, meaning that there is no way to distinguish a correct model from a single data spectrum. Therefore, a certain degree of knowledge of the physical system needs to be implemented to attain meaningful data.

A number of models selected from literature were used to fit the physical properties of the cell. Each proposed circuit was fitted to the spectra using the Zview^{TM} software. The spectra were assessed using three criteria, in that the model:

- had to have been previously proposed in literature
- needed to make physical sense
- had to have the lowest χ^2 value possible to indicate a sufficient fit to the experimental data

7.4 Characterisation of Carbon Steel in Blank Solution at 7 m/s

7.4.1 AC Impedance Plots

Initially, it was important to characterise the dissolution behaviour of the carbon steel in the blank solution and determine the baseline corrosion rate prior to tests with chemical inhibition. Impedance measurements were conducted every 24 minutes for 4 hours on the blank sample subjected to 7 m/s flow to monitor the dissolution process. Figure 7.20 displays selected Nyquist plots obtained between 0 and 4 hours along with the Bode phase plot as a function of frequency. Further beyond 3 hours, the plots remained similar to those at 192 minutes and have been omitted for clarity.

The AC impedance measurements in Figure 7.20 helped to provide an insight into the corrosion mechanism occurring at the interface of the sample. The mechanism displayed through the AC impedance measurements represents that of an active-adsorption state similar to that obtained by Farelas et al. [188]. Tests conducted in 3% NaCl in static conditions with C1018 steel at 0.5 m/s and 80°C by Farelas et al. [188] produced Nyquist and Bode plots markedly similar to that observed here and are shown in Figure 7.21 for the purpose of comparison.

Both the work by Farelas et al. (Figure 7.21) and the work presented here (Figure 7.20) illustrate similar dissolution behaviour despite the differing conditions. Two time constants can be identified during the exposure of carbon steel to the electrolyte; a capacitive semicircle in the high to medium frequency range, and an inductive loop in the low frequency range. The capacitive loop amplitude decreases with respect to time in both Figures, indicating that the charge-transfer process becomes increasingly favourable. The Nyquist plots suggest that the corrosion kinetics at the electrode surface are gradually accelerated and it has been shown that this increase in the dissolution process can be attributed to the revealing of iron carbide (Fe_3C) on the surface of the material [26, 188].

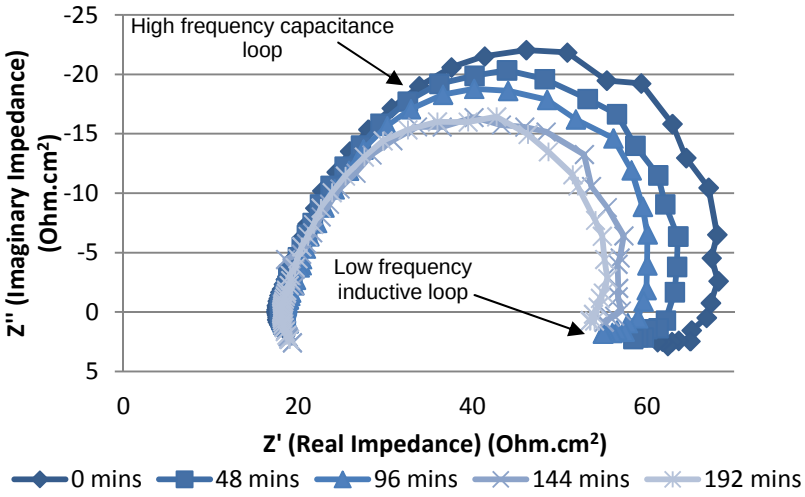

(a)

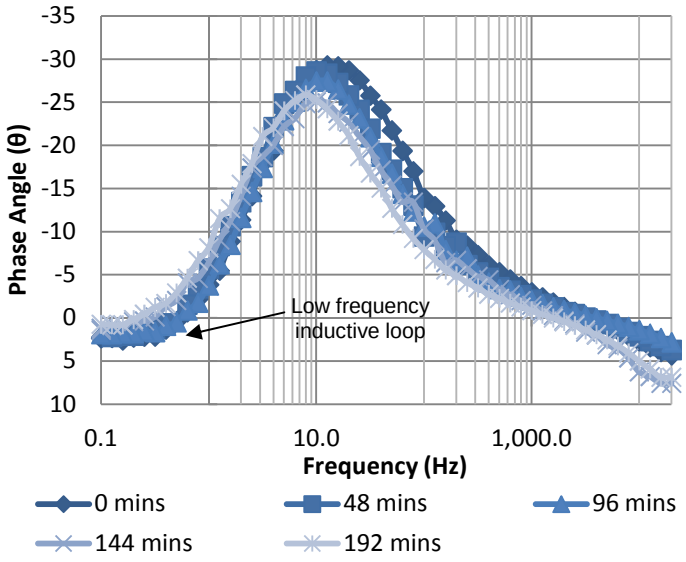

(b)

Figure 7.20: (a) Nyquist and (b) Bode phase plot for carbon steel in the blank solution. Test conditions were: 7 m/s, 45°C and CO_2-saturated at 1 bar

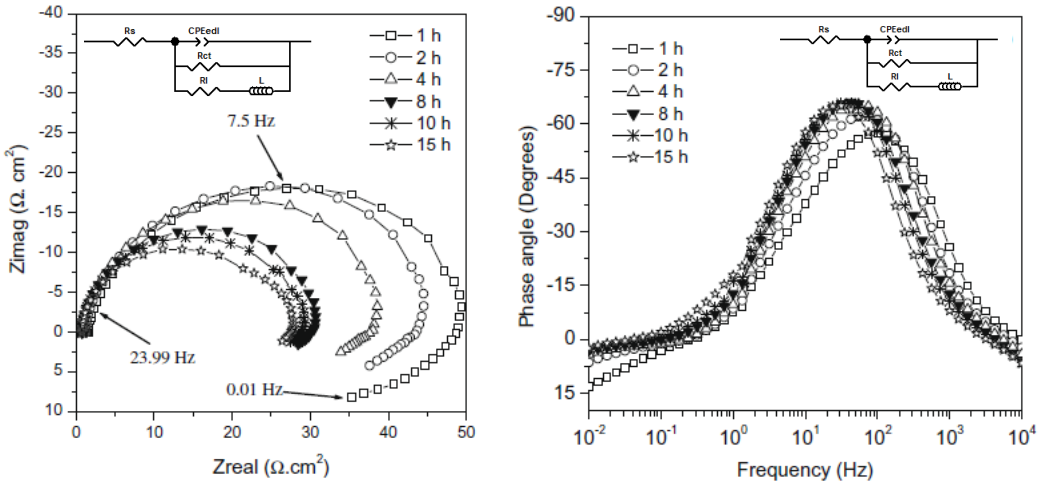

Figure 7.21: (a) Nyquist and (b) Phase plots obtained by Farelas et al. [188] for a C1018 steel at different exposure times under 0.5 m/s flow in a 3% NaCl solution saturated with CO_2 – from Farelas et al. [188]

When samples were removed from the SIJ, the surface of the carbon steel test specimens were covered in a black substance which had a smudge-like appearance. This was an iron carbide network left behind as a result of preferential dissolution of the ferrite structure. The SEM image provided in Figure 7.22(a) indicates the presence of the iron carbide layer on the sample surface after exposure. The network was fragile and visibly more structured than that observed in static conditions. It was possible to remove it through wiping the surface with a cotton pad and after cleaning the surface with Clarke's solution [173], images of the surface under the network could be captured (Figure 7.22(b)), revealing signs of pit propagation, believed to be related to Fe_3C as suggested by Crolet et al. [26].

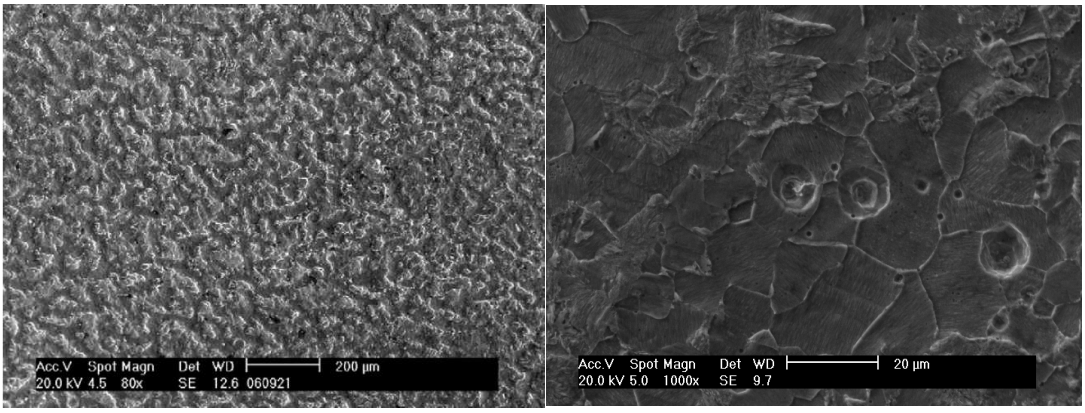

(a) (b)

Figure 7.22: SEM image of carbon steel after exposure to 7 m/s flow in blank conditions (a) Fe_3C revealed itself on the surface (b) areas under the network showed signs of pitting, potentially as a result of Fe_3C presence

Fe_3C is known to act as an electronic conductor where the reduction of hydrogen ions takes place following the intermediate reactions at the interface [26, 188]. Many researchers, including Crolet et al. [26] and Lopez et al. [65, 189] have shown that the dissolution of ferrite can leave behind a cementite network which forms preferential cathodic sites with a lower overpotential, favouring hydrogen evolution. These authors believed that this process creates microgalvanic cells between the Fe_3C and the ferrite phases, resulting in accelerated dissolution of the ferrite, influencing the corrosion kinetics through a galvanic effect.

Iron carbide supports the cathodic reaction, with electrons being supplied from the anodic pit [37]. The production of metal ions attracts anions, particularly Cl^-, into the pit and the soluble chlorides formed hydrolyse, reacting with water to produce hydrochloric acid, increasing the local pH which can increase material dissolution further [25]. A schematic of this scenario is provided in Figure 7.23.

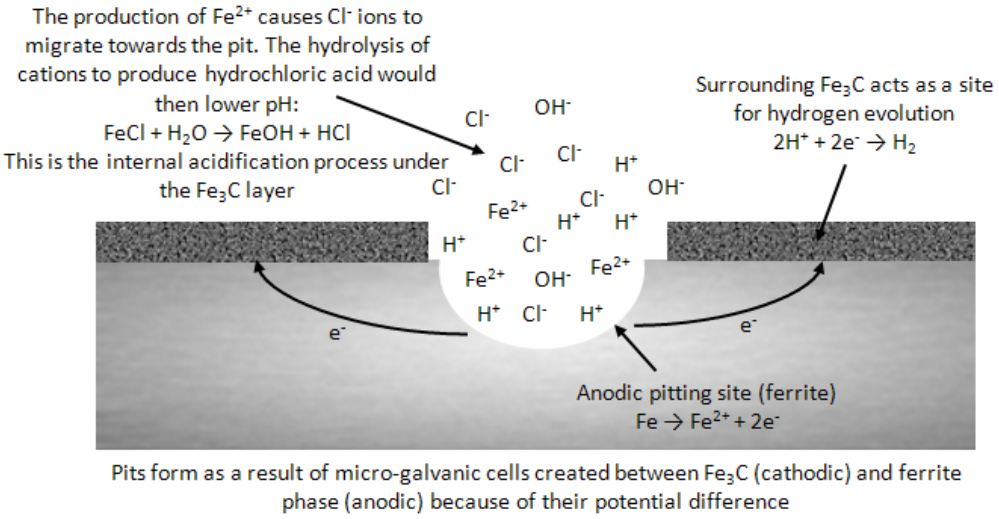

Figure 7.23: Schematic diagram of pitting corrosion where a large cathodic Fe_3C area stimulates the metal dissolution within a pit

Fe_3C has been shown to significantly affect the corrosion kinetics and has been shown to increase corrosion rate by a factor of 3 to 10 in some specific environments [1, 190]. Kermani and Morshed [1] and Crolet et al. [26] have shown that Fe_3C can play a number of roles as well as galvanic coupling, including local acidification, Fe^{2+} enrichment and film anchoring. The effect of cathodic regions of cementite is believed by Farelas et al. [188] to become influential at carbon contents of above 0.1 wt.%. With carbon content of the steel considered in this research above 0.12 wt.%, this research agrees with this statement. Likewise,

Gulbrandsen et al. [174] observed an increase in corrosion rate for St52 steel (0.13 wt.% carbon) which was attributed to the presence of cementite.

7.4.2 Examination of Inductive Behaviour in Impedance Plots

The experimental impedance plots in Figure 7.20 show the presence, and ultimately the disappearance of an inductive loop over time. Li et al. [191] witnessed a similar desertion in the inductive loop for tests conducted with carbon steel in 0.5 M H_2SO_4. However, for these tests, Li et al. [191] found that applying impedance measurements at increasing levels of anodic potential from E_{corr} to 1600 mV ultimately resulted in the evolution of the inductive loop into a capacitance loop. Although impedance measurements were conducted at only E_{corr} in this work, some interesting comparisons can be drawn.

The detailed mechanisms for corrosion in the active dissolution region may involve a network of reactions. However, Li et al. [191] believed that Reactions (7.5) to (7.7) (initially suggested by Bockris et al. [50]) were sufficient to explain the impedance observations witnessed for their experiments with carbon steel in H_2SO_4:

$$\mathrm{Fe} + \mathrm{H_2O} \leftrightarrow \mathrm{FeOH_{ad}} + \mathrm{H^+} + \mathrm{e^-} \tag{7.5}$$

$$\mathrm{FeOH_{ad}} \rightarrow \mathrm{FeOH^+_{sol}} + \mathrm{e^-} \tag{7.6}$$

$$\mathrm{FeOH^+_{sol}} + \mathrm{H^+} \leftrightarrow \mathrm{Fe^{2+}_{sol}} + \mathrm{H_2O} \tag{7.7}$$

Li et al. [192] suggested that at potentials close to E_{corr} for the carbon steel in H_2SO_4, (where metal dissolution is moderate), most of the $FeOH_{ad}$ formed is consumed by Reaction (7.6) (which was believed to create the inductive behaviour) and that the adverse effects of its coverage do not affect Reaction (7.5). Increasing the applied anodic potential of the AC measurements resulted in accelerated metal dissolution and the accumulation of $FeOH_{ad}$ on the surface, which shifts the equilibrium of Reaction (7.5). The adverse effects of adsorption resulted in the disappearance of the inductive loop and the evolution of a low frequency capacitive loop instead.

A comparison of the results discussed by Li et al. [192] against those presented both here (Figure 7.20) and by Farelas et al. [188] (Figure 7.21) in CO_2-saturated environments depict the disappearance of the inductive loop. However, as opposed to the loop disappearing with increased applied anodic potential with Li et al. [191],

the low frequency loop disappears over time on its own accord in this work (Figure 7.20) and the work of Farelas et al. [188] (Figure 7.21). Based on the analysis provided by Li et al. [191], similar adsorption mechanisms can be used to explain the presence and disappearance of the inductive loop in both Figure 7.20 and Figure 7.21, which are in a CO_2-saturated environments. Note in this case that Fe_L refers to the ligand Fe-CO_2 as proposed by Nesic et al. [191].

$$Fe_L + H_2O \leftrightarrow Fe_LOH_{ad} + H^+ + e^- \quad (7.8)$$

$$Fe_LOH_{ad} \rightarrow Fe_LOH^+_{sol} + e^- \quad (7.9)$$

$$Fe_LOH^+_{sol} + H^+ \leftrightarrow Fe^{2+}_{sol} + CO_2 + H_2O \quad (7.10)$$

$$2H^+ + 2e^- \rightarrow H_2 \quad (7.11)$$

Instead of the increasing anodic potential of the impedance measurements applied by Li et al. [191], it is the gradual formation of Fe_3C in these experiments which accelerates the dissolution process through the creation of more favourable cathodic sites for the hydrogen evolution. The increase in the rate of metal dissolution results in the accumulation of $Fe(OH)_{ad}$ on the surface. As the adsorption of the intermediate product becomes more significant, the inductive loop begins to disappear. This process has been proposed by both Farelas et al. [188] and Zhang and Cheng [193, 194] who have witnessed inductive behaviour in CO_2-saturated environments.

7.4.3 Equivalent Circuit Modelling of Impedance Plots

The mechanism leading to the evolution of the interface in the blank solution is represented by the equivalent circuit in Figure 7.24 which has been proposed by numerous authors [188, 195-197]. This model has been widely used to simulate a steel-CO_2 interface involving an adsorbed intermediate product.

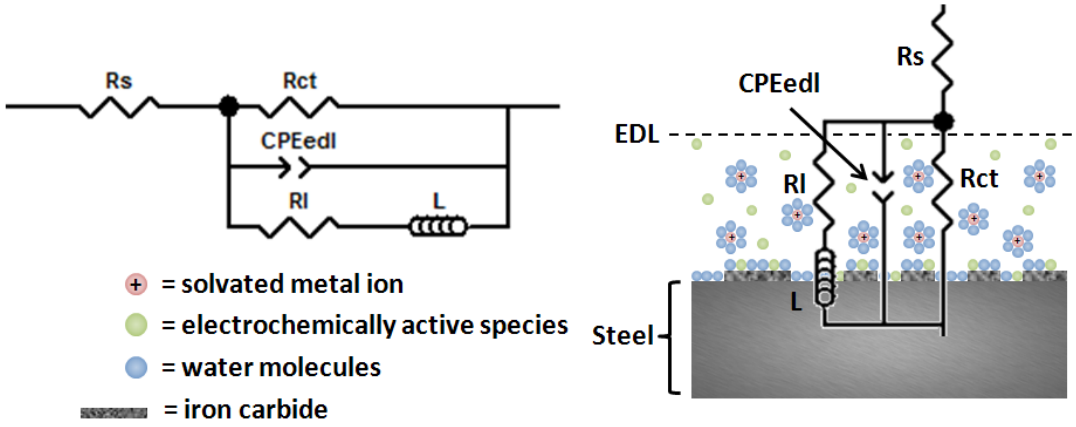

Figure 7.24: Equivalent circuit used for modelling AC impedance data in blank solution at 7 m/s; R_s is the solution resistance, CPE_{edl} is a constant phase element representing the capacitance of the electric double layer, R_l is the inductive resistance, L is the inductance and R_{ct} is the charge transfer resistance

Figure 7.25 provides an interpretation of the level of agreement between the proposed model in Figure 7.24 and one example of the experimental data. Fitting using the Zview™ software produced an average error of 3.65%.

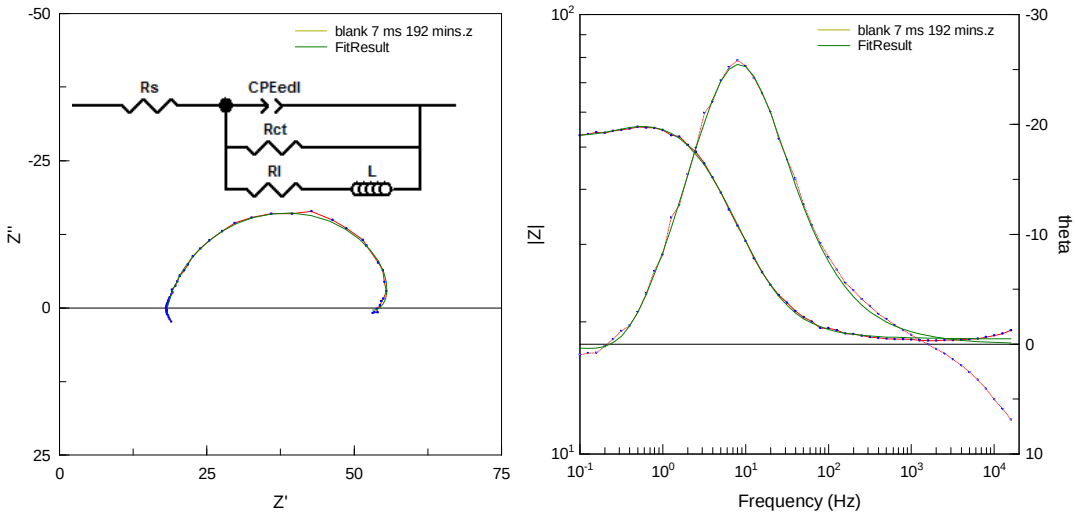

(a) (b)

Figure 7.25: (a) Nyquist plot and (b) Bode/Bode phase plot for carbon steel in blank solution indicating the fit of the model (green line) to the experimental data (red line). Test conditions were: 7 m/s, 45°C and CO_2-saturated at 1 bar

Values for the electrical parameters in the equivalent circuit in Figure 7.24 which represent the behaviour in the blank solution are provided in Table 7.2 following data fitting using Zview^{TM} software. An increase in capacitance is observed with time due to the physical-electrical properties of iron carbide [188].

Table 7.2: Values of the elements of the equivalent circuit in Figure 7.24, representing the electrochemical process occurring on a carbon steel surface in the blank solution.

Time (mins)	R_s ($\Omega \cdot cm^2$)	CPE_{edl} ($\mu F cm^{-2} s^{n-1}$)	n	R_l ($\Omega \cdot cm^2$)	R_{ct} ($\Omega \cdot cm^2$)
0	17.9(±0.2)	860(±36)	0.82(±0.02)	182.2(±25.1)	57.1(±2.7)
48	18.0(±0.1)	970(±41)	0.83(±0.02)	175.8(±39.9)	51.4(±1.9)
96	18.1(±0.2)	1110(±39)	0.84(±0.01)	144.7(±27.4)	48.6(±1.7)
144	18.1(±0.1)	1304(±109)	0.83(±0.02)	227.1(±45.6)	42.4(±2.2)
192	18.0(±0.2)	1493(±103)	0.86(±0.03)	236.9(±69.8)	40.4(±2.1)

The magnitude of capacitance was believed by Farelas et al. [188] to be proportional to the number of sites available for hydrogen evolution i.e. it is influenced by the area of Fe_3C, which is an electronic conductor [188]. By considering Figure 7.26, it is evident that the relationship between capacitance and charge-transfer resistance is similar for this work and that of Farelas et al. [188]. Although the values of charge-transfer and capacitance differ as a result of the disparity in solution chemistry and carbon steel composition, the charge-transfer resistance decreases (i.e. corrosion rate increases) as capacitance values increase (i.e. the area of Fe_3C increases) [188].

Both results indicate that a limiting, minimum charge-transfer resistance is being reached as the capacitance increases. This is likely to be attributed to the fact that the anodic regions of the surface are beginning to reach a limiting rate of dissolution once the surface becomes saturated with $FeOH_{ad}$ [188].

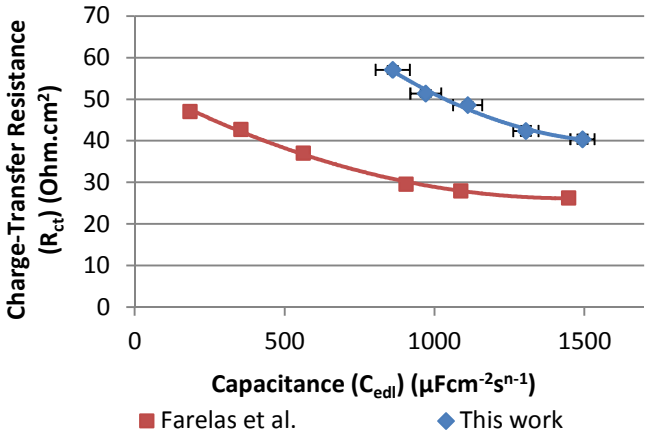

Figure 7.26: Relationship between charge-transfer resistance and EDL capacitance for this work and that of Farelas et al. [188] which both involve the revealing of iron carbide on a mild steel surface in uninhibited solutions. Test conditions for this work were: 7 m/s, 45°C and CO_2-saturated at 1 bar. Test conditions for Farelas et al. [188] were: C1018 steel, 3 wt.% NaCl solution, 0.5 m/s, 80°C and CO_2-saturated at 1 bar.

All AC impedance plots in Figure 7.20 express a depressed semi-circular shape in the Nyquist plot with the centre under the real axis. This is typical behaviour for solid metal electrodes that show frequency dispersion of the AC impedance data [198]. This anomaly has generally been attributed to different physical phenomena such as surface roughness [199-203], inhomogeneities at the electrode surface [199, 204], impurities [199, 201, 205], grain boundaries [199, 201] and distribution of the surface active sites [201, 206, 207]. To take into account the non-ideal frequency response of the experimental data in Figure 7.20, a constant phase element (CPE_{edl}) was used instead of an ideal capacitor. The impedance function of a CPE (Z_{CPE}) is defined by the mathematical expression given below:

$$Z_{CPE} = \frac{1}{(Qi\omega)^n} \qquad (7.12)$$

where Q is a proportional factor, ω is 2πf, i is √-1 and n is an empirical exponent between 0 and 1 which measures the deviation from ideal capacitor behaviour [208]. The value of 'n' can also be a measure of surface inhomogeneity i.e. values closer to 1 represent a more homogenous surface [208].

After analysing the impedance data in Table 7.2, it is obvious that the charge-transfer resistance R_{ct} decreases with time from 57.1 to 40.4 Ohm.cm^2, signifying an increase in corrosion rate throughout the experiment [188]. The value of 'n' also increases marginally throughout the duration of the test from 0.82 to 0.86. Past

authors have attributed the increase in n to a reduction in surface roughness as the polishing marks on the sample are removed during the dissolution process [208]. However, this factor can be discounted here as roughness measurements performed using contact profilometry indicated an increase in surface roughness of the sample from 40±15 nm up to 180±24 nm. Another possible explanation is that the increase in 'n' is attributed to an increase in surface homogeneity as a result of the revealing of the Fe_3C film as seen in the study by Farelas et al. [188].

7.4.4 Estimating Corrosion Rate in Blank Solution at 7 m/s

Rapid and accurate methods for measuring corrosion rates are of tremendous importance for corrosion engineers, especially for these types of practical applications. Direct analysis methods such as weight loss or solution analysis can require long exposure times. Moreover, these techniques cannot provide an appreciation for changes in corrosion rates over time [209].

The nature of electrochemical processes allows different electrochemical techniques to be employed to corroding systems in order to quantify degradation rates [209]. All electrochemical techniques are based on Faraday's Law and they present great advantages in that they have a short measuring time, high accuracy and can provide continuous corrosion monitoring [209]. On the other hand, these techniques involve perturbing the system through external polarisation which can lead to changes in the system-specific properties [209].

DC techniques are traditionally implemented for corrosion measurements, especially using the linear polarisation resistance technique. However, since the early work of Epelboin et al. [210] in the 1970's with iron in H_2SO_4 with propargylic alcohol, interest in the technique was stimulated and its application has grown increasingly quickly because of its ability to provide an insight into the corrosion mechanisms as well as rates of material loss.

Regrettably, AC impedance has demonstrated that some uncertainties have been created regarding interpreting corrosion rates when the plots become complicated and exhibit additional capacitive or inductive loops [210].

For the situation where inductive behaviour is present (such as those shown in Figure 7.20 for the blank system), certain authors [210, 211] believe that the charge-transfer resistance (R_{ct}) of the circuit (shown in Figure 7.27 and presented in Table 7.2) provides a more accurate interpretation of corrosion rate, as opposed to the resistance value determined when the inductive loop is extrapolated to the x-

axis by simulating the behaviour down to zero frequency (termed 'R_p' and also shown in Figure 7.27). The charge-transfer resistance, R_{ct}, can be extracted directly from the circuit model, whilst the polarisation resistance, R_p, can be determined by the application of the following equation proposed by a number of authors [209, 212, 213] which effectively involves modelling the behaviour down to zero frequency and deducting the solution resistance from the value obtained:

$$R_p = \lim_{\omega \to 0} Z - R_s \qquad (7.13)$$

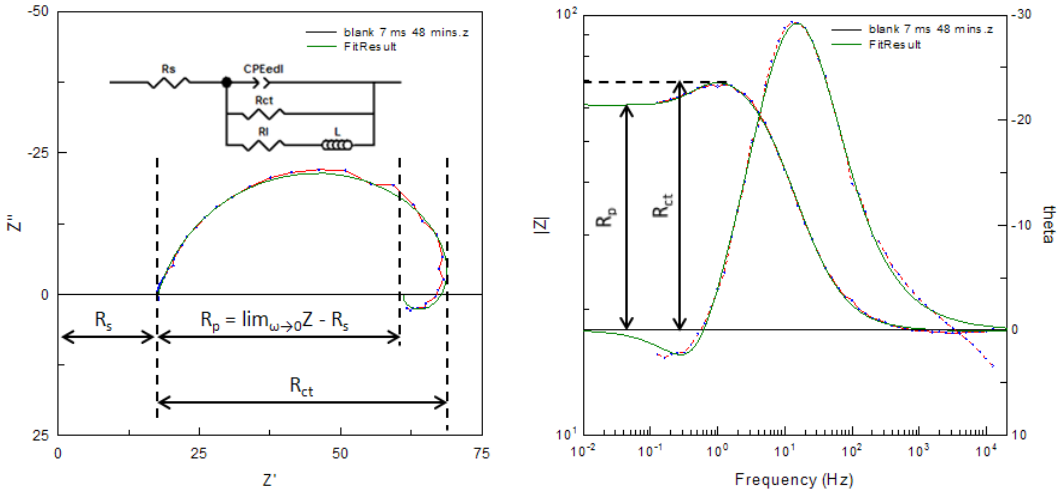

Figure 7.27: Model showing where R_p and R_{ct} are recorded for Nyquist plots when inductive loops are present

Epelboin and co-workers [210] interpreted corrosion rates for iron in H_2SO_4 with propargylic alcohol in terms of the charge-transfer resistance (R_{ct}) from AC impedance measurements. By comparing the inhibitor efficiency calculated from R_{ct} with that of weight loss data, Epelboin et al. [210] concluded that the two values closely correlated with judgement being made predominantly at high concentrations of inhibitor. At lower concentrations, the corrosion rates determined through weight loss, R_p and R_{ct} were very similar, which presented ambiguity over which technique was most appropriate.

In 1981, Lorenz and Mansfeld [209] indicated that the results of Epelboin et al. [210] were doubtful, by showing unequivocally through the use of atomic adsorption that corrosion rate is correlated to electrochemical DC data and to the extrapolated value of the inductive loop of AC impedance measurements down to low frequency (shown in Figure 7.28). These tests were conducted with and without the

application of triphenylbenzylphosphonium-cholride ($TPBP^+$) in 0.5 M H_2SO_4 and 1M HCl.

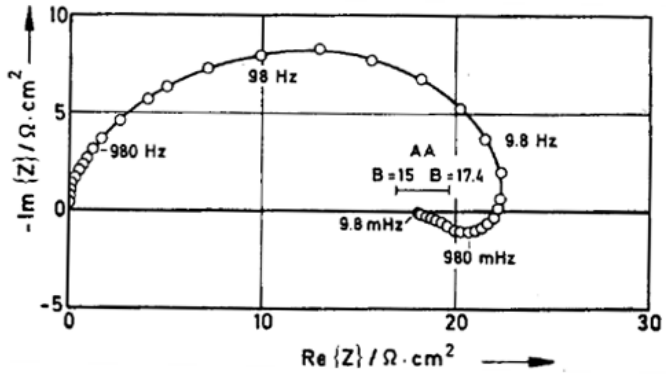

Figure 7.28: AC impedance diagram for iron in aerated 0.5 M H_2SO_4. AA represents the solution analysis through atomic adsorption – from Lorenz and Mansfeld [209]

When considering the significance of R_{ct} and the correlation with i_{corr}, it must be considered that R_{ct} is only determined by the Faradaic process of charge-transfer-controlled corrosion reactions [210, 211, 214]. In most corrosion systems, the impedance diagrams can contain additional capacitance and inductance loops which influence the corrosion process. Only when one capacitive semicircle is present in the impedance plot will R_{ct} be equal to R_p. For all other instances, the method proposed by Silverman [212], Aksüt et al. [213] and Lorenz et al. [209] should be followed. They stated that in the limit of zero frequency, the impedance approaches the DC resistance. Therefore the polarisation resistance from the fitted curve was estimated for the data presented here by applying '$R_p = \lim_{\omega \to 0} Z - R_s$' to the model after simulating the behaviour to lower frequencies. Using the value of R_{ct} neglects the effects of bulk and surface diffusion processes and adsorption processes, which can influence corrosion rates dramatically. These processes are particularly common in inhibition systems or under the formation of protective iron carbonate scales.

Both R_{ct} and R_p values were determined from the AC impedance plots of the blank solution as a function of time and are compared in Table 7.3 along with R_p values from the linear polarisation resistance technique. The R_p values from LPR agreed much more closely with the values determined using the zero frequency approach, as expected.

Table 7.3: Charge-transfer and polarisation resistance according to AC and DC measurements for tests conducted in the blank solution as a function of time.

Time (mins)	R_{ct} ($\Omega \cdot cm^2$)	$R_p = \lim_{\omega \to 0} Z - R_s$ ($\Omega \cdot cm^2$)	R_p from LPR (minus R_s) ($\Omega \cdot cm^2$)
0	57.1(±2.7)	43.7(±1.9)	45.1(±2.3)
48	51.4(±1.9)	40.5(±1.7)	42.1(±3.7)
96	48.6(±1.7)	37.5(±2.3)	39.4(±3.5)
144	42.4(±2.2)	36.9(±2.1)	36.4(±1.5)
192	40.4(±2.1)	36.5(±1.2)	34.1(±1.9)

A Tafel plot created at the end of the blank test is provided in Figure 7.29(a). Tafel extrapolation of the anodic and cathodic branches produced a corrosion rate of 11.9 mm/year at the end of the test. For the final measured value of R_p in the test before the Tafel plot (34.1 $\Omega \cdot cm^2$), this corresponds to a Stern-Geary coefficient of 34.9.

Gravimetric results produced an *average* corrosion rate of 9.8±0.7 mm/year. Based on the average value of R_p over the test (39.1 $\Omega \cdot cm^2$), a Stern-Geary coefficient of 33.1±2.3 was calculated.

Determining the Stern-Geary coefficient from the Tafel slope values themselves was not possible given the nature of the anodic Tafel slope in Figure 7.29(a). Therefore the plot of corrosion rate as a function of time is based on the Stern-Geary coefficient calculated from mass loss measurements and average R_p values, with the upper and lower error bars corresponding to predictions based on the lowest (30.8) and highest (35.4) Stern-Geary coefficients recorded. These results are presented for values of R_p (from both AC and DC techniques) and R_{ct} (from AC impedance only).

The plot in Figure 7.29(b) indicates that failure to compensate for the inductive loop can result in a difference in estimation of corrosion rate by over 2 mm/year in some cases. The graph also shows that the extrapolation of the Tafel slope can provide a reasonable approximation of the carbon steel corrosion rate, although this technique only determines the *in-situ* corrosion rate at the end of the test, whilst the mass loss measurements determine the average material loss rate over the entire test. Figure 7.29(b) also shows signs of convergence between R_p and R_{ct} throughout the test as the inductive loop begins to disappear in the Nyquist plot.

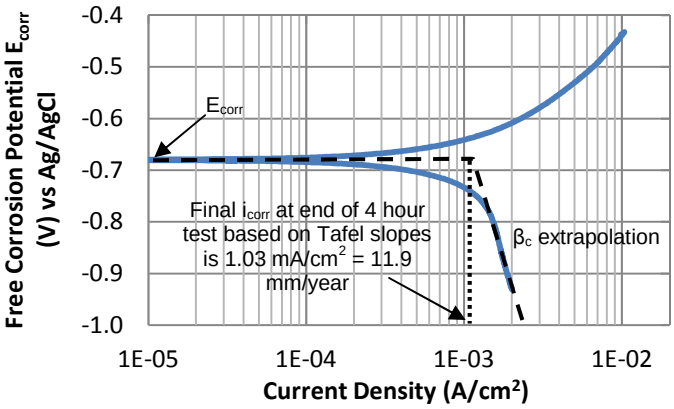

(a)

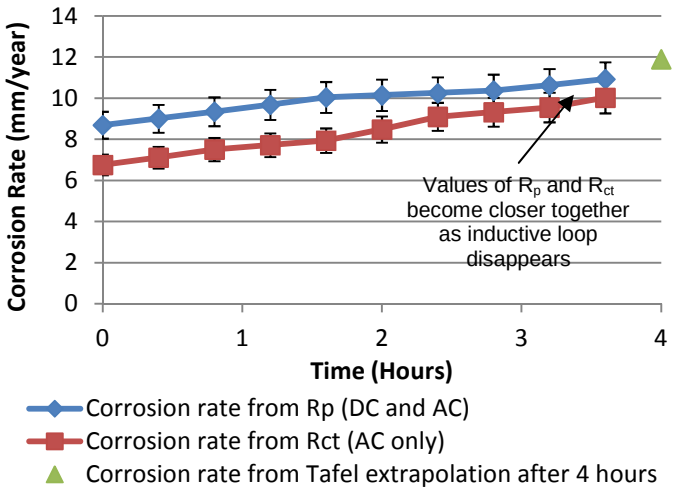

(b)

Figure 7.29: (a) Tafel plot for carbon steel after 4 hours and (b) Corrosion rate as a function of time based on values of polarisation resistance (R_p) from AC and DC techniques and values of charge-transfer resistance (R_{ct}) from AC impedance. Test conditions were: 7 m/s, 45°C and CO_2-saturated at 1 bar

7.5 Varying Inhibitor A Concentration – Inhibition at 0 Hours

7.5.1 AC Impedance Plots

Initial inhibition tests were conducted by adding Inhibitor A to the system at the start of the experiment and measuring *in-situ* corrosion rate as a function of time for an impingement velocity of 7 m/s. All inhibitors considered in this section took effect rapidly, reaching a plateau within the first 15 minutes of the test. At the end of each 4 hour test, a final AC impedance measurement was taken which was used to review the performance of the inhibitor in the system. The AC impedance measurements conducted at the end of each 4 hour test are provided in Figure 7.30 for concentrations of 10, 25, 50, 75 and 100 ppm. The plots show that an increase

in concentration of Inhibitor A increases the diameter of the semi-circle, signifying a reduction in corrosion rate of the carbon steel [207]. The Nyquist plots also indicate that the addition of the inhibitor created a significant amount of inductive behaviour, considerably more than that seen in the blank solution. The adsorption or desorption processes of corrosion inhibitors/intermediates on a metal surface has been attributed to induction on Nyquist plots [38].

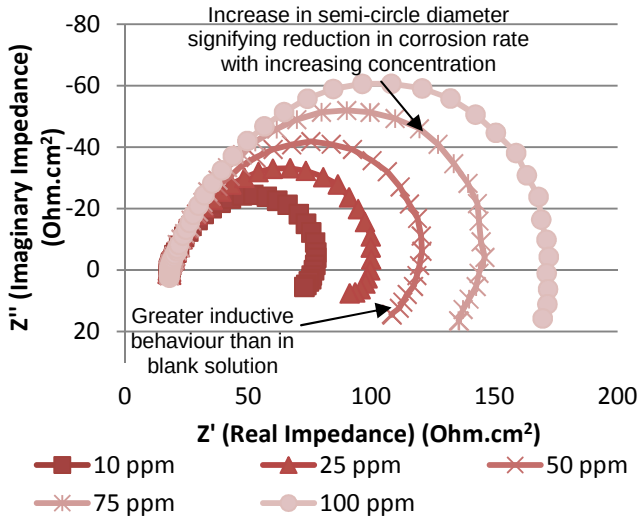

(a)

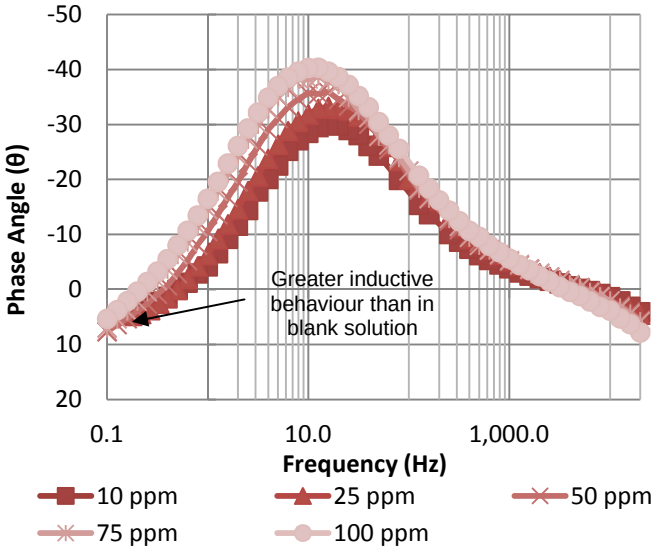

(b)

Figure 7.30: (a) Nyquist plot and (b) Bode phase plot after 4 hours for various concentrations of Inhibitor A. Test conditions were: 7 m/s, 45°C and CO_2-saturated at 1 bar

7.5.2 Equivalent Circuit and Corrosion Rate Prediction

It was important to be able to determine the correct values of R_p to enable corrosion rates to be established for the inhibited system. The Nyquist and Bode phase plots in Figure 7.30 were fitted to the equivalent circuit shown in Figure 7.31, which, incidentally, is the same circuit used for the blank system.

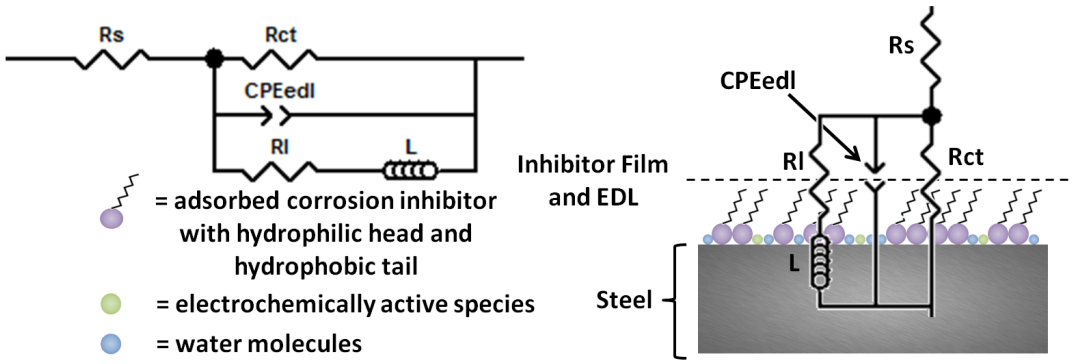

Figure 7.31: Equivalent circuit used to model AC impedance data for Inhibitor A added to the system from the start of the test at 7 m/s; R_s is the solution resistance, CPE_{edl} is a constant phase element representing the capacitance of the electric double layer, R_l is the inductive resistance, L is the inductance and R_{ct} is the charge transfer resistance

As with tests in the blank solution, the presence of inductance necessitated that the Nyquist plots were simulated down to lower frequencies using the appropriate model to determine values of R_p at zero frequency (i.e. using '$R_p = \lim_{\omega \to 0} Z - R_s$') as shown in Figure 7.32. These tests produced significantly larger inductive loops and therefore, the discrepancy between values of R_{ct} and R_p were even greater than those observed in the blank system, producing a greater percentage discrepancy in corrosion rate approximation, as will be shown later.

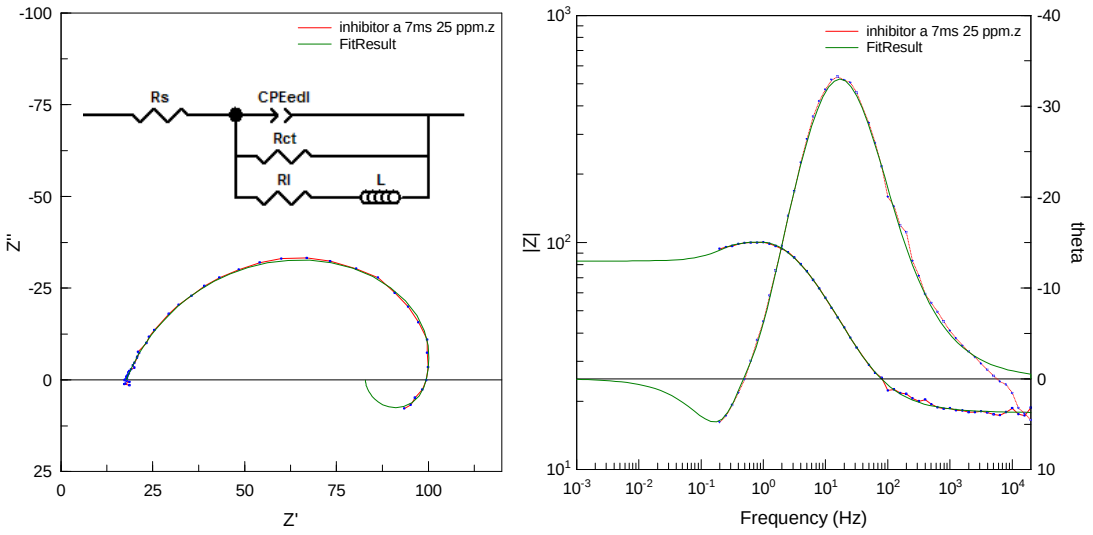

(a) (b)

Figure 7.32: (a) Nyquist plot and (b) Bode/Bode phase plot for carbon steel with 25 ppm Inhibitor A indicating the fit of the model (green line) to the experimental data (red line). Test conditions were: 7 m/s, 45°C and CO_2-saturated at 1 bar

To clarify the approximation of R_p from the impedance results, linear polarisation measurements were performed after each AC measurement. Interestingly, upon studying the Tafel plots, it was found that the polarisation curves were discontinuous in the vicinity of E_{corr}. An example of the Tafel plot is provided in Figure 7.33 for the inhibited system at 100 ppm Inhibitor A in comparison to the blank solution. It is worth noting that E_{corr} was stable upon the point of making these measurements. Figure 7.33 demonstrates that the carbon steel in the presence of Inhibitor A expresses sensitivity to polarisation in the anodic range. In this environment, the degree of coverage of the electrode with the inhibiting species decreases sharply with increasing anodic potential until it appears to fully desorb from the surface. DC measurements were possible for the evaluation of R_p at E_{corr} as the desorption behaviour was only observed over anodic potentials. However, systems sensitive to polarisation often appear to exhibit inductive behaviour [209]. Examples include tests with triphenylbenzylphosphonium-cholride ($TPBP^+$) [209] and propargylic alcohol (PA) [209, 210].

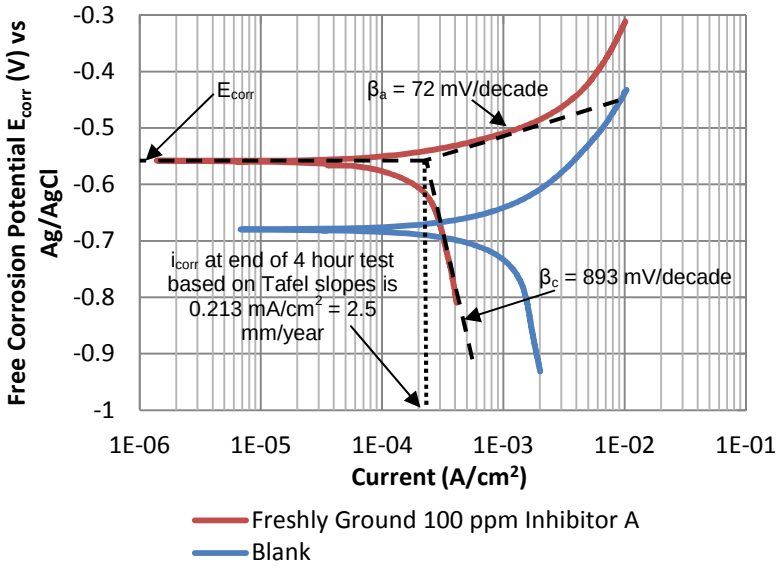

Figure 7.33: Plot indicating discontinuous polarisation curve in the vicinity of E_{corr} under steady state conditions for Inhibitor A in comparison to blank solution. Test conditions were: 7 m/s, 45°C and CO_2-saturated at 1 bar

Both Aksüt et al. [213] and Lorenz and Mansfeld [209] showed that the application of propargylic alcohol and allyl alcohol to inhibit the corrosion of iron in aerated 0.5 M H_2SO_4 produced inductive behaviour. Figure 7.34(a) shows the sensitivity of propargylic alcohol to small DC voltage perturbations. For these systems, DC measurements were unable to estimate R_p because of the strong adsorption and desorption processes in the vicinity of E_{corr}. The difficult anodic and cathodic behaviour of the system in the presence of propargylic alcohol also created problems when conducting AC impedance measurements at E_{corr}. The strong desorption of propargylic alcohol in the vicinity of E_{corr} led to high depolarisation in the anodic part of the sinusoidal signal depending on the AC amplitude. Figure 7.34(b) shows the influence of the AC voltage amplitude on the form of the Nyquist plot. Therefore, the R_p value obtained by extrapolation of the inductive loop could not be correlated with the inductive loop for the tests performed by Lorenz and Mansfeld.

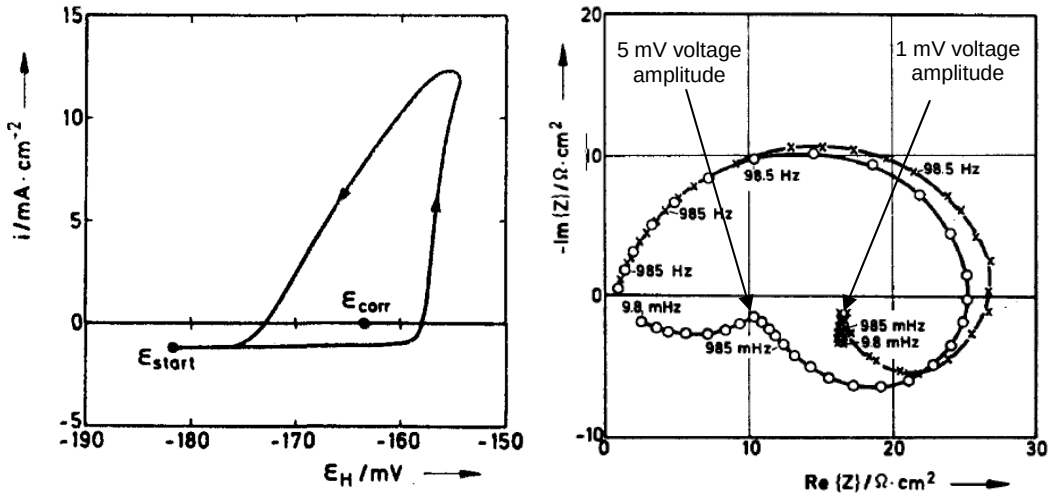

(a) (b)

Figure 7.34: (a) Cyclic voltammetric current density current density-potential curves in the vicinity of E_{corr} (0.3 mV/s scan rate) and (b) Nyquist plot showing the dependence of inductive behaviour on the AC signal amplitude. Test conditions were: Iron electrode, 0.5 M H_2SO_4 aerated solution, 360 rpm rotation, 25°C and 20 mM propargylic alcohol - from Lorenz and Mansfeld [209]

Conversely, tests also performed by Lorenz and Mansfeld [209] using $TPBP^+$ as an inhibitor for iron in 0.5 M H_2SO_4 showed that desorption of the inhibitor also occurred at anodic potentials (Figure 7.35), but the behaviour was such that R_p measurements were possible using DC and AC measurements (as is the case here). A quantitative comparison between different experimental results obtained by DC and AC measurements, as well as solution analysis in the presence of $TPBP^+$ showed that all techniques were excellent at predicting corrosion rates. The results from the application of these techniques can be seen in Figure 7.36. All the values predicted by the different techniques determined resistance values less than the charge-transfer resistance [210]. More so, the extrapolated inductive loop of the Nyquist plot agreed well with this data, as shown in Figure 7.36. These results clearly show that the corrosion rate of the system can be unequivocally correlated to R_p if the inductive behaviour is *not* sensitive to the AC voltage perturbations.

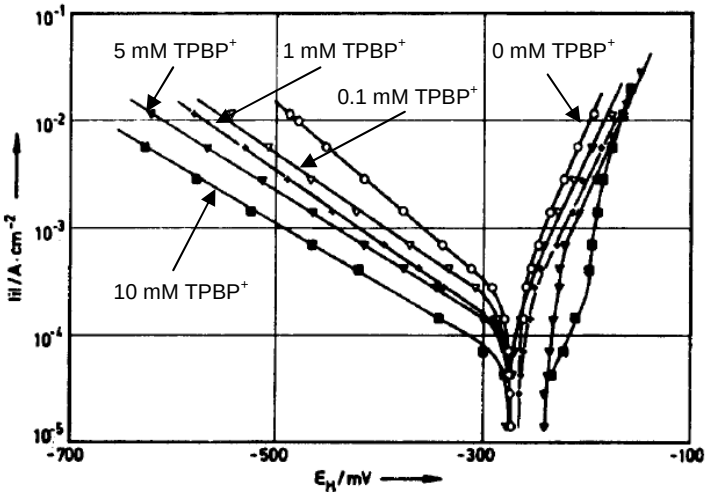

Figure 7.35: Steady state galvanostatic current density-potential curves for various concentrations of $TPBP^+$. Test conditions were: Iron electrode, 0.5 M H_2SO_4 aerated solution, 270 rpm rotation and 25°C - from Lorenz and Mansfeld [209]

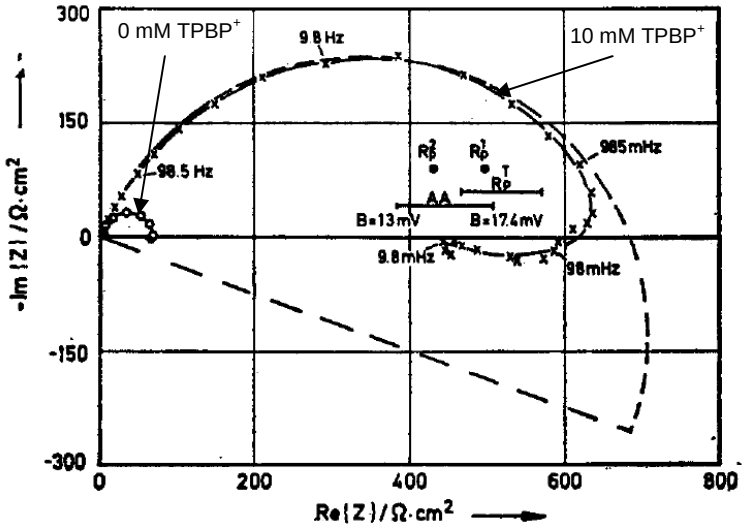

Figure 7.36: Nyquist plot for application of 0 and 10 mM $TPBP^+$, where R_p^T is from cyclic voltammetry, R_p^1 is from steady state galvanostatic curves, R_p^2 is from steady state potentiostatic curves and AA is from solution analysis through atomic adsorption. Test conditions were: Iron electrode, 0.5 M H_2SO_4 aerated solution, 270 rpm rotation, and 25°C - from Lorenz and Mansfeld [209]

Based on the findings of Lorenz and Mansfeld [209], the carbon steel electrode under the application of 25 ppm Inhibitor A was subjected to a lower amplitude of AC voltage to determine if the inductive behaviour was influenced by the voltage perturbations. Results in Figure 7.37 show that the inductive behaviour was independent of voltage amplitude, suggesting that the extrapolated inductive loop

should provide a valid representation of corrosion rate, just as those determined by Lorenz and Mansfeld for the application of $TPBP^+$ [209].

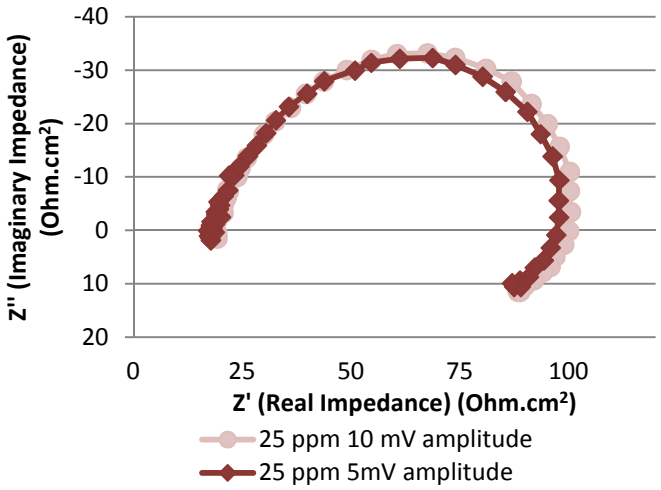

Figure 7.37: Nyquist plot showing the lack of dependence of inductive behaviour on the AC signal amplitude. Test conditions were: 7 m/s, 45°C and CO_2-saturated at 1 bar

R_p values predicted from AC and DC techniques are provided in Table 7.4. Both R_p values from AC and DC measurements agree well with each other, predicting values lower than the charge-transfer resistance used by Epelboin et al. [210] to determine corrosion rate.

Table 7.4: Charge-transfer and polarisation resistance according to AC and DC measurements for tests conducted in the presence of Inhibitor A

Conc. (ppm)	R_{ct} ($\Omega \cdot cm^2$)	$R_p = \lim_{\omega \to 0} Z - R_s$ ($\Omega \cdot cm^2$)	R_p from LPR (minus R_s) ($\Omega \cdot cm^2$)
10	65.4(±9.1)	48.7(±5.1)	49.9(±3.2)
25	91.8(±14.2)	63.1(±5.3)	63.8(±4.1)
50	117.0(±8.9)	78.4(±9.8)	79.4(±3.9)
75	145.6(±9.3)	101.1(±7.7)	105.2(±7.4)
100	170.9(±10.7)	135.1(±7.1)	138.3(±9.2)

Measurement of Tafel slopes shown previously in Figure 7.33(a) produced a Stern-Geary coefficient of 28.9 with the application of 100 ppm Inhibitor A. Using this coefficient and values of R_p and R_{ct} from Table 7.4, it was possible to compare values of corrosion rates estimated by AC and DC techniques as well as those

through Tafel extrapolation and gravimetric measurement. Figure 7.38 strongly suggests that the extrapolation of the inductive loop for AC impedance plots provides a much more accurate interpretation of corrosion rate as opposed to the Faradaic charge-transfer resistance. These findings agree with the work of numerous previous authors [195, 209, 213].

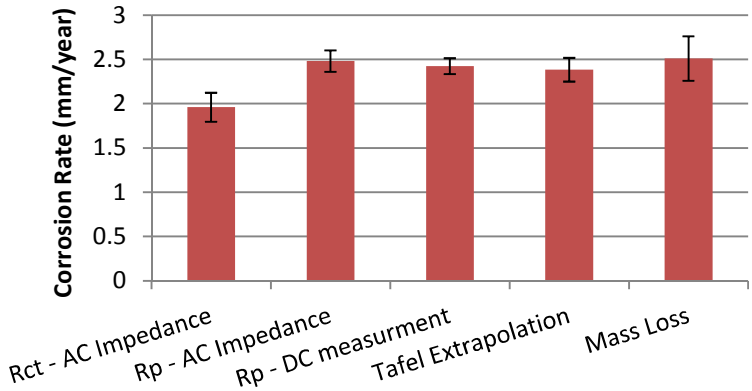

Figure 7.38: Comparison of corrosion rates predicted by AC and DC techniques as well as Tafel extrapolation and gravimetric analysis in the presence of 100 ppm Inhibitor A

Using the combined values of R_p predicted from both DC and AC techniques along with the Stern-Geary coefficient, it was possible to estimate the corrosion rates of the carbon steel in the presence of 10, 25, 50 and 75 ppm and also compare them to the gravimetric analysis. Figure 7.39 shows that the application of *in-situ* electrochemistry is able to predict the corrosion rate of the sample at concentrations of 50 ppm and higher. At concentrations below 50 ppm, a slight discrepancy between the values begins to emerge.

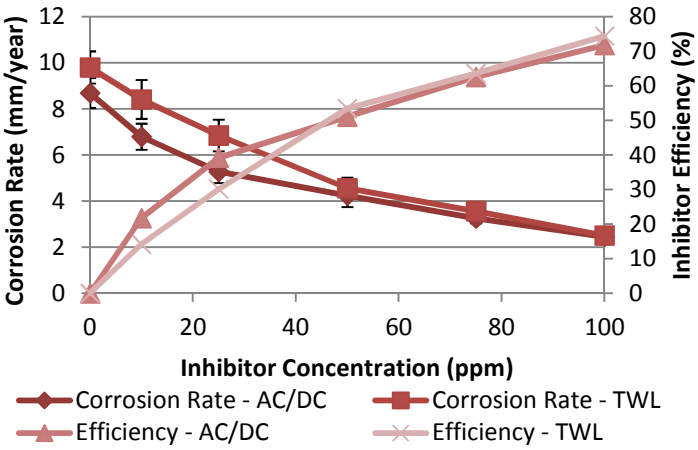

Figure 7.39: Comparison of corrosion rate and efficiency of Inhibitor A based on *in-situ* electrochemistry and gravimetric analysis

7.5.3 Analysis of Equivalent Circuit Parameters

Table 7.5 provides the equivalent circuit parameter values used to model the processes occurring on the carbon steel electrode in the presence of Inhibitor A using the circuit provided in Figure 7.31. Interestingly, the circuit fit used suggests that only one capacitive time constant (CPE_{edl}) can be distinguished from the impedance plots.

Table 7.5: Values of the elements of the equivalent circuit in Figure 7.31, representing the electrochemical process occurring on a carbon steel surface in the presence of Inhibitor A.

Conc. (ppm)	R_s ($\Omega \cdot cm^2$)	CPE_{edl} ($\mu F cm^2 s^{n-1}$)	n	R_l ($\Omega \cdot cm^2$)	R_{ct} ($\Omega \cdot cm^2$)
10	18.0(±0.1)	795(±32)	0.81(±0.01)	194.8(±32.1)	65.4(±9.1)
25	17.9(±0.2)	750(±42)	0.78(±0.02)	208.0(±45.8)	91.8(±14.2)
50	17.9(±0.2)	689(±39)	0.76(±0.03)	255.3(±54.8)	117.0(±8.9)
75	18.0(±0.1)	676(±12)	0.77(±0.03)	339.0(±72.3)	145.6(±9.3)
100	18.0(±0.2)	654(±42)	0.77(±0.02)	392.1(±76.0)	170.9(±10.7)

Numerous researchers have reported the existence of two capacitive loops for inhibited carbon steel in CO_2-saturated solutions [38, 163, 198, 215, 216]; one corresponding to a protective film on the surface, and the other to the EDL. However, a selection of authors [196, 215, 216] have also found that one capacitive loop is able to characterise the whole system depending upon the inhibiting molecule, as is the situation for the addition of Inhibitor A in these results. Some notable work published by Lopez et al. [198], shown in Figure 7.40, reported the presence of one capacitive loop for the circuit representing the inhibition of carbon steel in the presence of 100 ppm aminopropylimidazol.

The appearance of solely one capacitive loop for circuits representing inhibited carbon steel has been justified by a number of authors [196, 215, 216]. Reasons explaining the presence of a single time constant tend to focus on suggestions that AC impedance is unable to register inhibitor films which comprise of monolayers [216, 217] or are porous [216, 217] and consequently offer low levels of inhibition preventing them from establishing a capacitive loop. Both these factors were suggested by Chen et al. [217] and Ozcan et al. [216] as reasons why the AC impedance measurements would fail to detect a time constant associated with a protective film.

It could be considered that in situations where the inhibitor offers little protection or merely blocks active sites on the metal surface, the inhibitor film resistance will be much smaller than the charge-transfer resistance [216]. The semi-circle representing the protective film could effectively merge with the charge-transfer loop as seen in other studies [198, 216]. Hence, the EIS spectra for the inhibited test can be described using one capacitor in the electrical equivalent circuit.

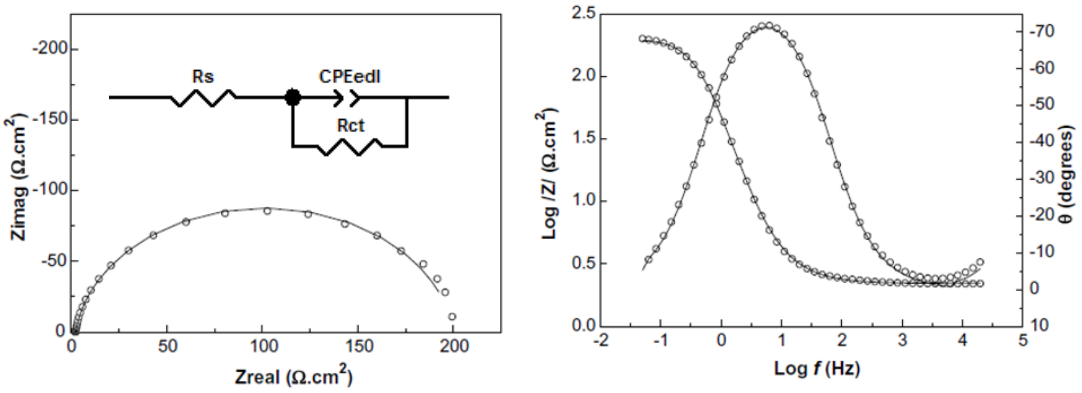

(a) (b)

Figure 7.40: (a) Nyquist and (b) Bode and phase plot at 72 hours for carbon steel in the presence of 100 ppm aminopropylimidazol. Points indicate experimental data and lines indicate fitting model. Test conditions were: 5% NaCl solution, 100 rpm rotation, 40°C and CO_2-saturated at 1 bar - from Lopez et al. [198]

It is believed that time constants must be separated by at least one order of magnitude in order to avoid overlap in an EIS spectrum [38]. It is theoretically possible that one time constant can encapsulate both processes if they both occur at similar frequencies [38]. The individual time constant witnessed by Lopez [198] in Figure 7.40 was attributed to the potential dominance in charge-transfer resistance over the film resistance. The occurrence of these mechanisms at similar frequencies was believed to result in the data effectively merging into one loop [38]. By studying Figure 7.40 closely, there appear to be signs of a second time constant appearing in the low frequency range of the Nyquist plot. However, this behaviour is not apparent on the Bode or Bode phase plots.

Authors conducting AC impedance measurement [218] have also found that the 'blocking' effect of chemicals on the surface of samples tends to result in a reduction of capacitance of the EDL, such as that observed in this study as shown in Table 7.5. Increasing Inhibitor A concentration from 10 to 100 ppm reduces the capacitance from 795 to 654 μFcm^2s^{n-1}. As the concentration of Inhibitor A is increased, the level of adsorption increases. The adsorption of the inhibitor onto the carbon steel decreases the EDL electrical capacity by displacing water molecules and other ions which were originally adsorbed on the surface [208].

7.6 Varying Inhibitor B Concentration – Inhibition at 0 Hours

7.6.1 AC Impedance Plots

AC impedance plots recorded at the end of 4 hour tests for the inhibition of carbon steel at 7 m/s flow velocity using Inhibitor B are provided in Figure 7.41.

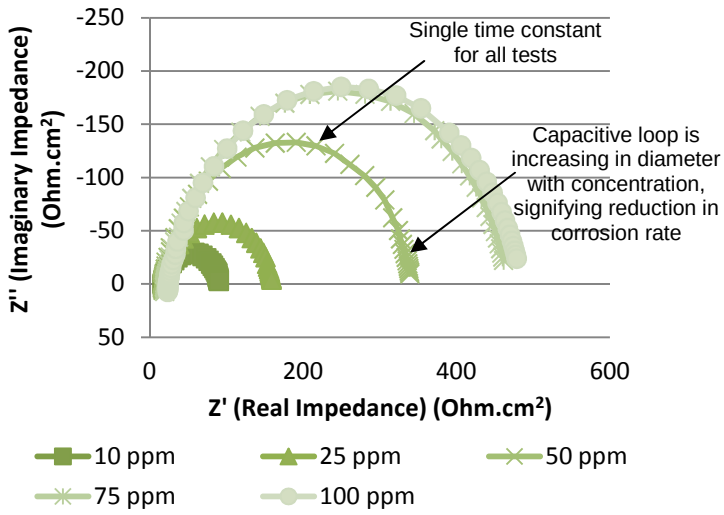

(a)

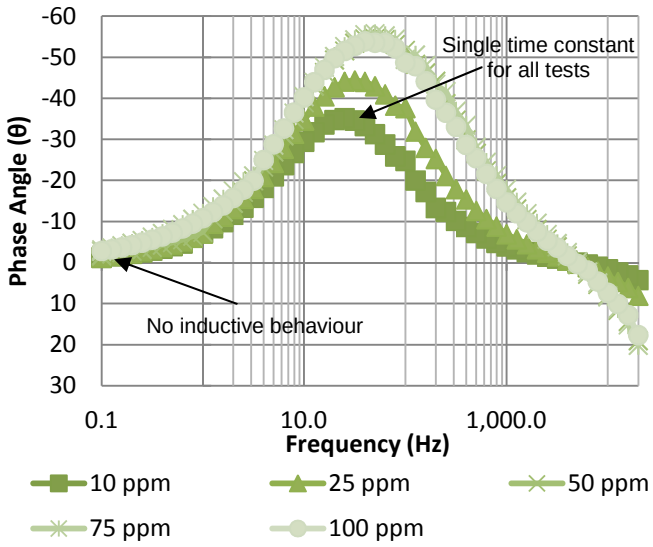

(b)

Figure 7.41: (a) Nyquist plot and (b) Bode phase plot after 4 hours for various concentrations of Inhibitor B. Test conditions were: 7 m/s, 45°C and CO_2-saturated at 1 bar

The Nyquist plots indicate that an increase in concentration of Inhibitor B promotes an increase in the semi-circle diameter, signifying a reduction in corrosion rate.

7.6.2 Equivalent Circuit and Corrosion Rate Prediction

The impedance plots in Figure 7.41 show that no inductive behaviour was observed with the application of Inhibitor B at the concentrations considered. The plots indicate that the creation of the inhibitor film fails to register in the impedance measurements as only one capacitive loop is visible. As stated previously, this is either attributed to the formation of a monolayer on the surface of the specimen, the porosity of the surface film or the dominance of the charge-transfer resistance in relation to the film resistance [216, 217].

The equivalent circuit proposed for the system comprises of the simple circuit shown in Figure 7.42. Figure 7.43 indicates the fit of the proposed circuit to the experimental data.

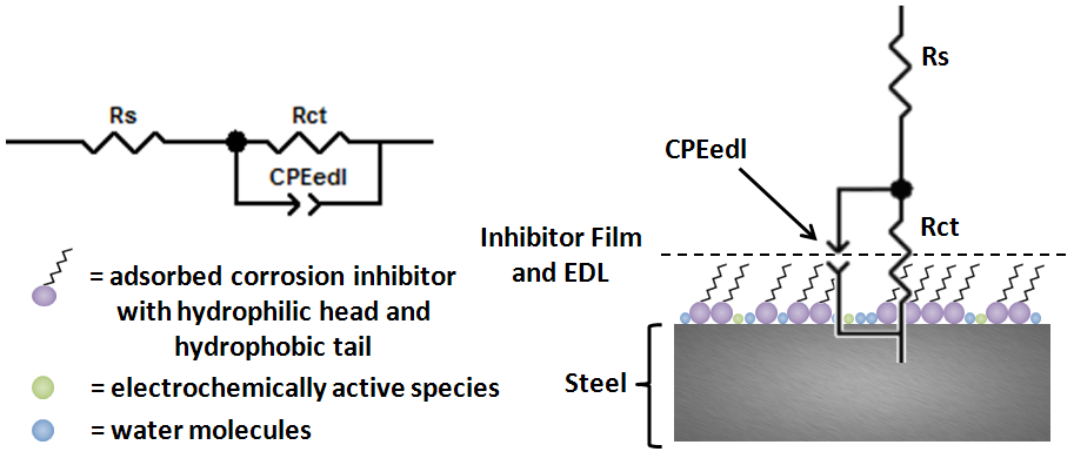

Figure 7.42: Equivalent circuit used to model AC impedance data for Inhibitor B added to the system from the start of the test at 7 m/s; R_s is the solution resistance, CPE_{edl} is a constant phase element representing the capacitance of the electric double layer and R_{ct} is the charge-transfer resistance

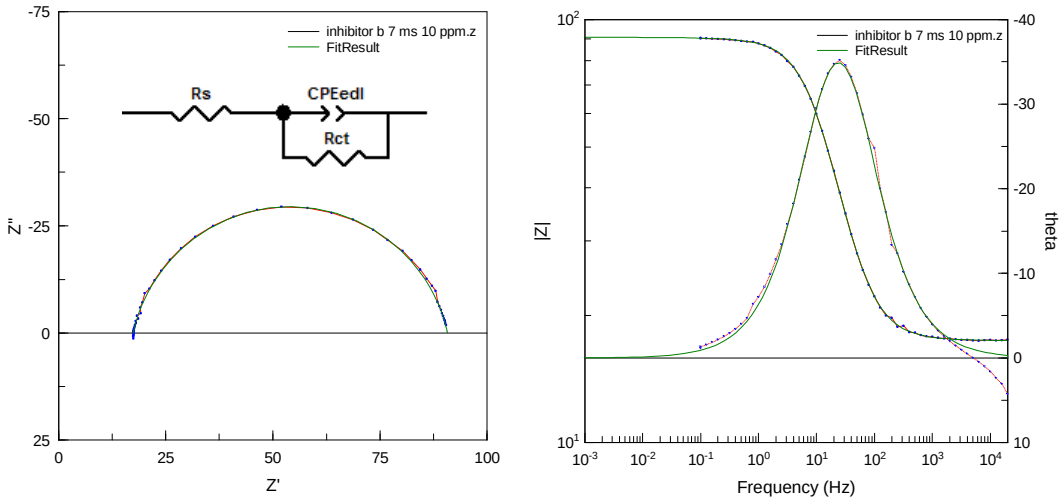

(a) (b)

Figure 7.43: (a) Nyquist plot and (b) Bode/ Bode phase plot for carbon steel with 10 ppm Inhibitor B indicating the fit of the model (green line) to the experimental data (red line). Test conditions were: 7 m/s, 45°C and CO_2-saturated at 1 bar

A comparison of the predicted R_p values from both AC and DC techniques is provided in Table 7.6 along with values of charger-transfer resistance (R_{ct}) from the equivalent circuit. In this scenario, because of the simplicity of the circuit fit, a special case is adopted whereby the charge-transfer resistance equals the polarisation resistance. This only occurs when one time constant is observed in the system as highlighted by Epelboin et al. [210, 211].

Table 7.6: Charge-transfer and polarisation resistance according to AC and DC measurements for tests conducted in the presence of Inhibitor B

Conc. (ppm)	R_{ct} ($\Omega \cdot cm^2$)	$R_p = \lim_{\omega \to 0} Z - R_s$ ($\Omega \cdot cm^2$)	R_p from LPR (minus R_s) ($\Omega \cdot cm^2$)
10	73.3(±5.1)	73.2(±5.5)	75.4(±6.7)
25	141.9(±8.9)	142.3(±9.1)	145.1(±8.9)
50	321.2(±15.8)	324.4(±18.5)	354.2(±16.3)
75	440.0(±20.8)	438.2(±22.1)	445.5(±34.2)
100	455.3(±15.3)	449.4(±16.2)	463.9(±23.1)

When considering the Tafel plots of carbon steel in the presence of 100 ppm Inhibitor B in Figure 7.44, determining the cathodic Tafel value was not possible due to the non-linear nature of the curve. Consequently, it was not possible to determine the Stern-Geary coefficient through Tafel slope measurement alone. As an alternative, the Tafel slope of the anodic branch (which exhibited much stronger activation controlled behaviour) was extrapolated back to E_{corr} to estimate i_{corr}. This produced a corrosion rate of 0.46 mm/year, which agreed well with 0.42 mm/year predicted through gravimetric analysis. Based on these two corrosion rates and the R_p value at 100 ppm, it was possible to determine a Stern-Geary coefficient of 17.9.

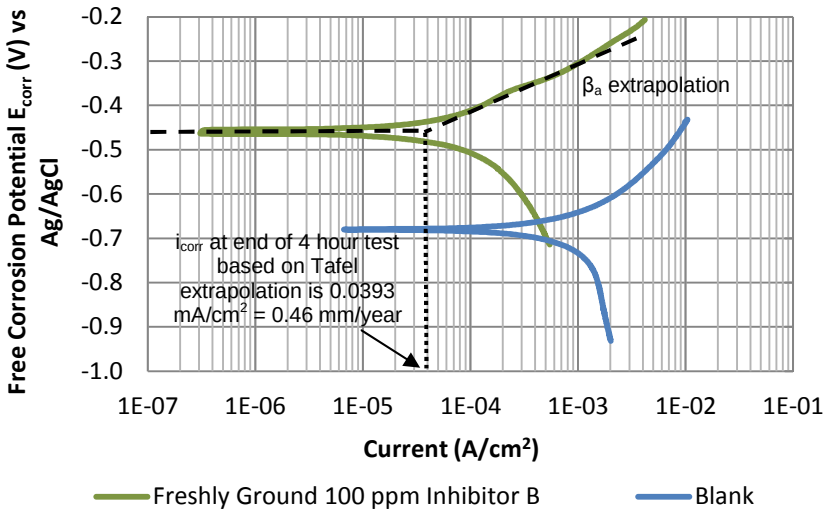

Figure 7.44: Tafel plot in flow-induced corrosion conditions after addition of 100 ppm Inhibitor B for freshly ground and pre-corroded samples (Anodic and cathodic curves were constructed from separate samples). Test conditions were: 7 m/s, 45°C and CO_2-saturated at 1 bar

Using the values of R_p measured from both DC and AC techniques, corrosion rates of the carbon steel were estimated in the presence of 10, 25, 50 and 75 ppm Inhibitor B and compared to the gravimetric measurements. Figure 7.45 shows that the application of *in-situ* electrochemistry is capable of predicting the *in-situ* corrosion rate accurately, especially at concentrations of 50 ppm and above.

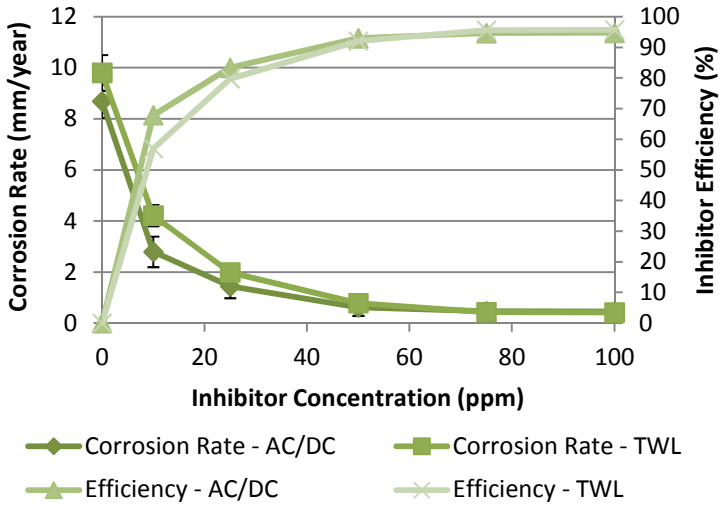

Figure 7.45: Comparison of corrosion rate and efficiency of Inhibitor B based on *in-situ* electrochemistry and gravimetric analysis

7.6.3 Analysis of Equivalent Circuit Parameters

The parameters obtained following the fitting of the impedance experimental results for the application of Inhibitor B are listed in Table 7.7. An increase in Inhibitor B concentration causes a decrease in the capacitance of the EDL. The capacitance of the EDL can be described using the following Helmholtz model [192, 208, 219, 220]:

$$C_{edl} = \varepsilon_r \varepsilon_0 \frac{A}{d} \tag{7.14}$$

where A is the area of the sample in direct contact with the electrolyte (i.e. regions not covered by an inhibitor film), d is the thickness of the double layer, ε_0 is the electrical permittivity of the electrolyte and ε_r is the dielectric constant.

As the inhibitor is adsorbed onto the surface, the area of carbon steel in direct contact with the electrolyte will undoubtedly decrease as the inhibitor film acts as an insulator by blocking active sites on the material surface. The reduction in the area of the steel in direct contact with the electrolyte causes a decrease in capacitance of the EDL.

Epelboin [210] and Lagrenee et al. [221] stated that one method of determining inhibitor efficiency is by considering the percentage reduction in capacitance of the EDL as this parameter is believed to be directly proportional to the area of carbon steel in contact with the electrolyte. Likewise, the percentage increase in R_p can be used as this is inversely proportional to the corrosion rate. Both resistance and capacitance values of the blank and inhibited systems can allow inhibitor efficiencies to be estimated using the following equations [210, 221]:

$$\mathrm{IE}_{\mathrm{R_p}}\ (\%) = 100\ \mathrm{x}\left(1 - \frac{\mathrm{R_{p,blank}}}{\mathrm{R_{p,inhibited}}}\right) \tag{7.15}$$

$$\mathrm{IE}_{\mathrm{C_{edl}}}\ (\%) = 100\ \mathrm{x}\left(1 - \frac{\mathrm{C_{edl,inhibited}}}{\mathrm{C_{edl,blank}}}\right) \tag{7.16}$$

A number of authors [220, 222] have reported that the capacitance of the EDL can offer a reasonable indication of inhibitor efficiency. However, most authors find that the use of the resistance values to approximate the corrosion inhibitor efficiency is a more common and robust approach [222-227]. It must be considered that the use of both these techniques possess limitations. The use of resistance values to estimate inhibitor efficiency only holds under the precondition that the Tafel slopes (and hence the Stern-Geary coefficient) are not influenced by the presence of inhibiting molecules. Additionally, for the implementation of Equation (7.16), using capacitance values will only offer a reasonable prediction of inhibitor efficiency if the chemical properties of the EDL are not significantly affected by inhibitor presence.

Table 7.7: Values of the elements of the equivalent circuit in Figure 7.42 when fitting to the impedance spectra of Figure 7.41, representing the electrochemical process occurring on a carbon steel surface in the presence of Inhibitor B.

Conc. (ppm)	R_s ($\Omega \cdot cm^2$)	CPE_{edl} ($\mu F cm^{-2} s^{n-1}$)	n	R_{ct} ($\Omega \cdot cm^2$)
10	18.0(±0.1)	409(±42)	0.86(±0.03)	73.3(±5.1)
25	17.9(±0.2)	208(±23)	0.87(±0.02)	141.9(±8.9)
50	17.9(±0.2)	100(±12)	0.88(±0.01)	321.2(±15.8)
75	17.8(±0.2)	76(±6)	0.90(±0.02)	440.0(±20.8)
100	18.0(±0.1)	75(±5)	0.90(±0.02)	455.3(±15.3)

The introduction of an inhibitor into the EDL undoubtedly changes its composition and structure [219]. The inhibitor molecules on the metal surface affect the EDL by

causing a change in the dielectric properties of the water [222]. If the dielectric constant is sufficiently changed, it can have implications on the use of capacitance to determine inhibitor efficiency. An example for this system with the application of Inhibitor B is provided in Figure 7.46 where the inhibitor efficiencies are calculated based on resistance and capacitance values and are compared with those determined from gravimetric analysis. The results clearly highlight that the use of R_p and C_{edl} provide reasonable approximations for the inhibitor efficiencies, but they do underestimate the efficiency and this is possibly because of the aforementioned reasons.

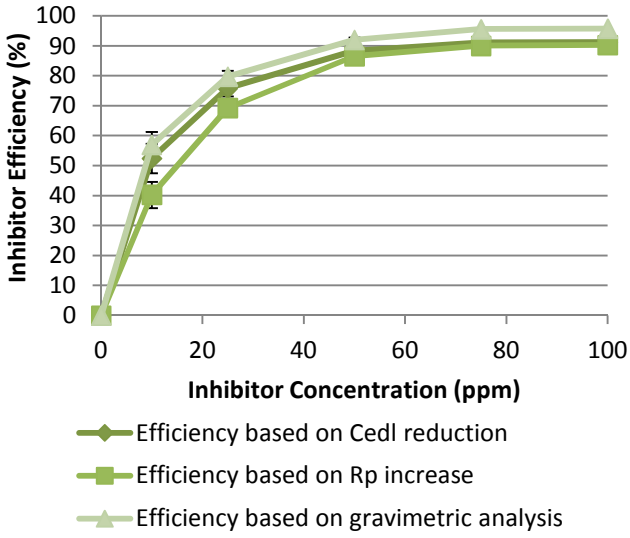

Figure 7.46: Efficiency of Inhibitor B based on the reduction in EDL capacitance, the increase in polarisation resistance and gravimetric analysis

Finally, Table 7.7 indicates that the value of 'n' increases with Inhibitor B concentration. A possible explanation for this observation could be the increase in surface homogeneity as a result of the increased coverage of the inhibitor film [208]. Seeing as the value of 'n' begins to stabilise with the corrosion rate, this feature adds further credence to the argument.

7.7 Varying Inhibitor C Concentration – Inhibition at 0 Hours

7.7.1 AC Impedance Plots

The AC impedance plots at the end of 4 hours tests for the addition of various concentrations of Inhibitor C at 7 m/s flow velocity are provided in Figure 7.57. The Nyquist plot at 10 ppm shows the presence of inductive behaviour at low frequencies. In this scenario, the inductive behaviour may be related to the stability of the film as suggested by Neville et al. [165]. The diameter of the semi-circle at 10

ppm is smaller than that observed in the blank solution which suggests that the low concentration of inhibitor is capable of potentially increasing the corrosion kinetics. However, we will see that this is not the case in due course.

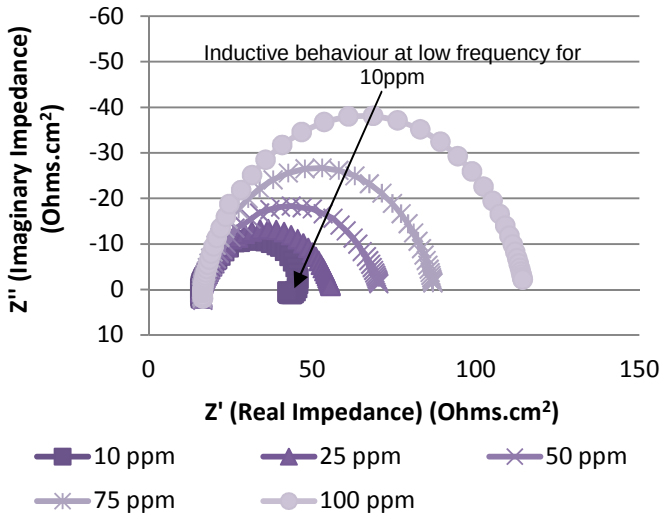

(a)

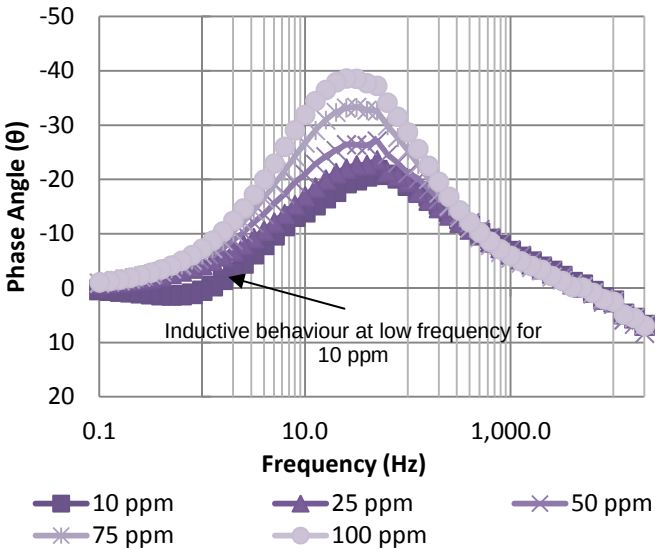

(b)

Figure 7.47: (a) Nyquist plot and (b) Phase plot after 4 hours for various concentrations of Inhibitor C. Test conditions were: 7 m/s, 45°C and CO_2-saturated at 1 bar

7.7.2 Equivalent Circuit and Corrosion Rate Prediction

The presence of inductive behaviour at 10 ppm and its subsequent disappearance at higher concentrations necessitated the use of two equivalent circuits to model the

behaviour over the range of concentrations. The equivalent circuit provided in Figure 7.48 was used to model the system at 10 ppm, whilst the circuit in Figure 7.49 represents the processes occurring at the carbon steel interface for concentrations of 25 ppm and above.

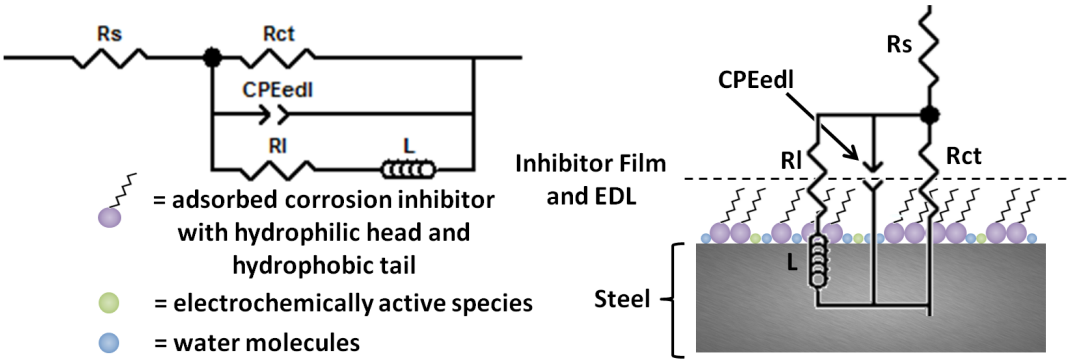

Figure 7.48: Equivalent circuit used to model AC impedance data for Inhibitor C added to the system from the start of the test at 7 m/s (10 ppm only); R_s is the solution resistance, CPE_{edl} is a constant phase element representing the capacitance of the electric double layer, R_l is the inductive resistance, L is the inductance and R_{ct} is the charge transfer resistance

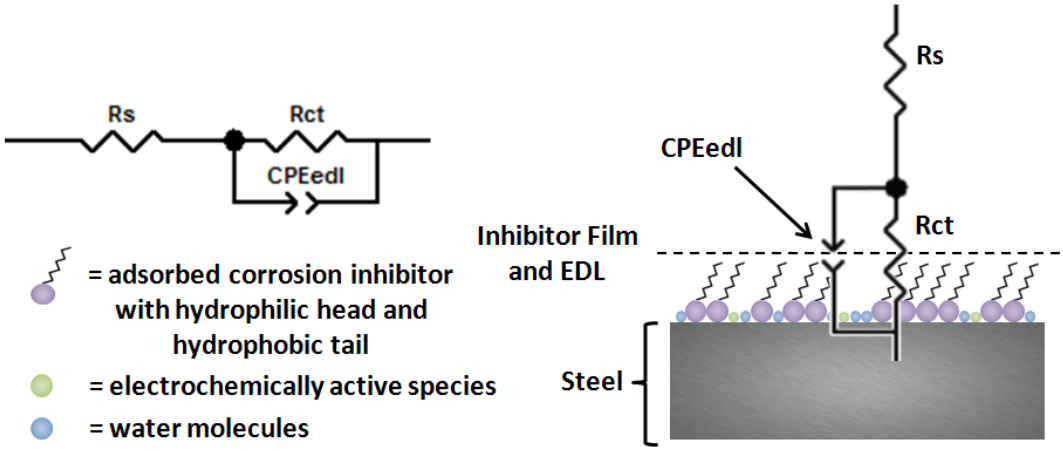

Figure 7.49: Equivalent circuit used to model AC impedance data for Inhibitor C added to the system from the start of the test at 7 m/s (25, 50, 75 and 100 ppm); R_s is the solution resistance, CPE_{edl} is a constant phase element representing the capacitance of the electric double layer and R_{ct} is the charge transfer resistance

Figure 7.50 and Figure 7.51 demonstrate the high level of fit between the proposed model and the experimental data for 10 ppm with inductive behaviour and 50 ppm without the inductive loop.

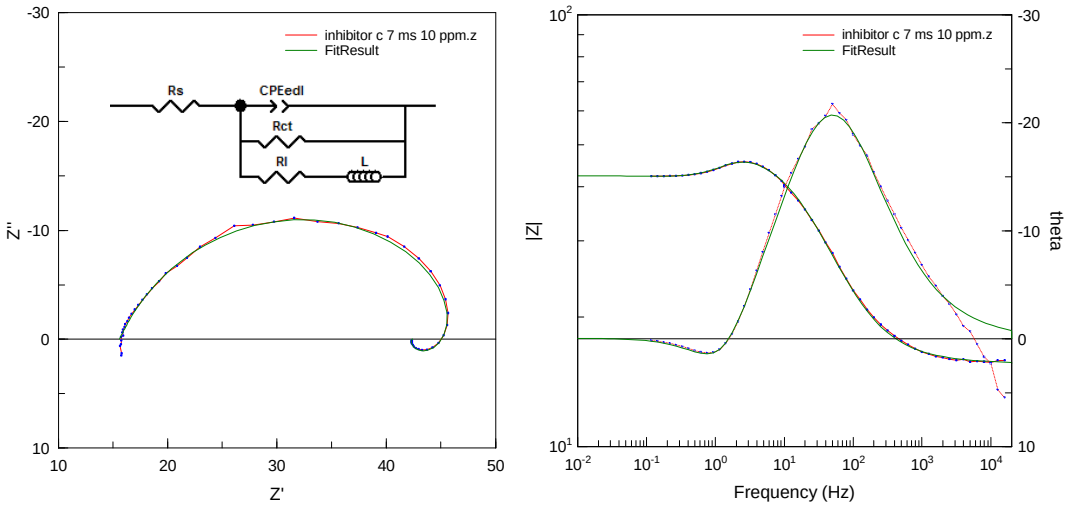

(a) (b)

Figure 7.50: (a) Nyquist plot and (b) Bode/Bode phase plot for carbon steel with 10 ppm Inhibitor C indicating the fit of the model (green line) to the experimental data (red line). Test conditions were: 7 m/s, 45°C and CO_2-saturated at 1 bar

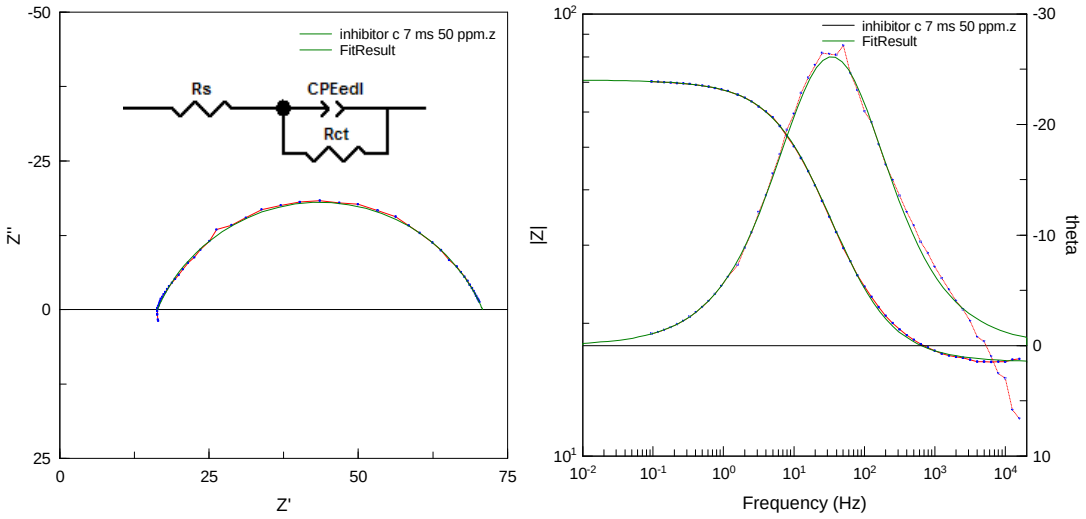

(a) (b)

Figure 7.51: (a) Nyquist plot and (b) Bode/Bode phase plot for carbon steel with 50 ppm Inhibitor C indicating the fit of the model (green line) to the experimental data (red line). Test conditions were: 7 m/s, 45°C and CO_2-saturated at 1 bar

Comparison between the predicted R_p values using both AC and DC techniques is provided in Table 7.6 along with the values of charge-transfer resistance. Again, a strong correlation is seen between the two sets of polarisation resistance values. Charge-transfer resistance values closely matched those from the AC impedance R_p values, except for the concentration of 10 ppm because of the inductive loop

presence at low frequencies, as expected from previous results in the blank system and with Inhibitor A.

Table 7.8: Charge-transfer and polarisation resistance according to AC and DC measurements for tests conducted in the presence of Inhibitor C

Conc. (ppm)	R_{ct} ($\Omega \cdot cm^2$)	$R_p = \lim_{\omega \to 0} Z - R_s$ ($\Omega \cdot cm^2$)	R_p from LPR (minus R_s) ($\Omega \cdot cm^2$)
10	33.15(±2.4)	27.59(±2.1)	29.98(±2.9)
25	39.13(±3.6)	40.57(±5.1)	43.59(±4.7)
50	53.03(±6.1)	55.87(±3.8)	59.17(±3.4)
75	71.17(±1.2)	73.73(±2.0)	80.48(±7.3)
100	98.57(±13.4)	101.52(±12.4)	109.12(±8.9)

Extrapolation of the anodic Tafel slope in Figure 7.52 produced a corrosion rate of 1.75 mm/year, closely agreeing with the value of 1.58 mm/year calculated from weight loss measurements. Based on these corrosion measurements and the value of R_p, a Stern-Geary coefficient of 17.8 was calculated (very similar to Inhibitor B).

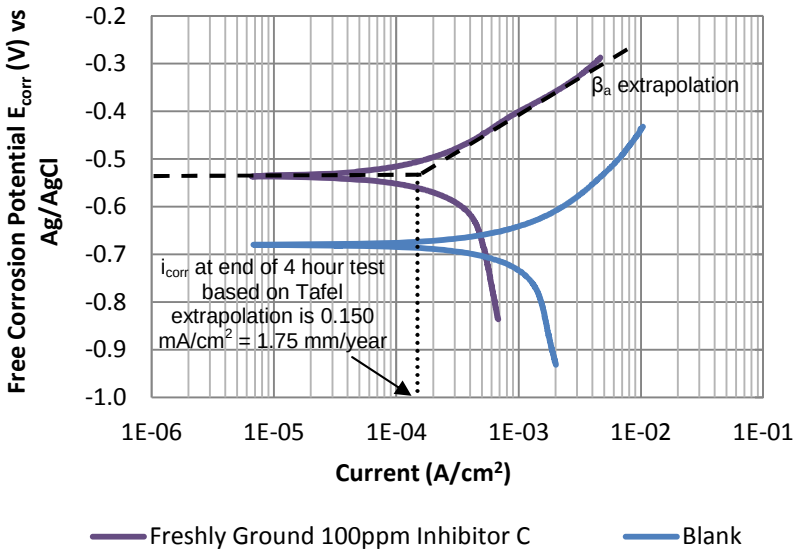

Figure 7.52: Tafel plot in flow-induced corrosion conditions after addition of 100 ppm Inhibitor C (Anodic and cathodic curves were constructed from separate samples). Test conditions were: 7 m/s, 45°C and CO_2-saturated at 1 bar

Predicted values of R_p combined with the Stern-Geary coefficient allowed the corrosion rate to be estimated as a function of inhibitor concentration. These corrosion rates from electrochemistry could subsequently be compared to

gravimetric measurements in Figure 7.53. A strong agreement between the AC/DC polarisation results and the gravimetric analysis are evident after taking into account the change in the Stern-Geary coefficient.

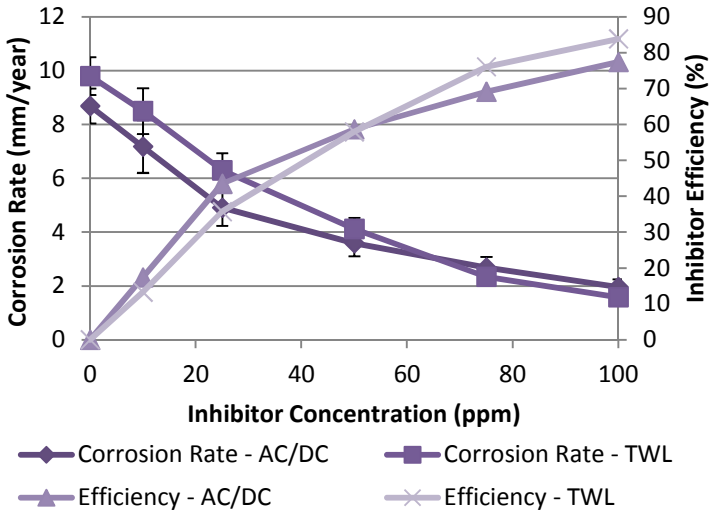

Figure 7.53: Comparison of corrosion rate and efficiency of Inhibitor C based on *in-situ* electrochemistry and gravimetric analysis

7.7.3 Analysis of Equivalent Circuit Parameters

The parameters obtained following the fitting of the impedance experimental results for the application of Inhibitor C are provided in Table 7.9 using circuits in Figure 7.48 for 10 ppm and Figure 7.49 for 25 ppm and greater. Similar to Inhibitor B, a reduction in capacitance is observed with increasing inhibitor concentration as the inhibitor film begins to reduce the area of carbon steel in direct contact with the electrolyte.

Under the application of Inhibitor B it was shown that the percentage reduction in capacitance and percentage increase in R_p calculated using Equations (7.15) and (7.16) respectively can provide a reasonable indication of efficiency.

Table 7.9: Values of the elements of the equivalent circuit in Figure 7.57(a) for Inhibitor C

Conc. (ppm)	R_s ($\Omega \cdot cm^2$)	CPE_{edl} ($\mu F cm^{-2} s^{n-1}$)	n	R_l ($\Omega \cdot cm^2$)	R_{ct} ($\Omega \cdot cm^2$)
10	18.1(±0.1)	754(±64)	0.75(±0.02)	129.6(±31.3)	33.15(±2.4)
25	17.9(±0.2)	651(±39)	0.78(±0.02)	N/A	39.13(±3.6)
50	17.9(±0.2)	535(±34)	0.78(±0.02)	N/A	53.03(±6.1)
75	18.1(±0.2)	402(±61)	0.82(±0.01)	N/A	71.17(±1.2)
100	18.0(±0.1)	312(±24)	0.84(±0.02)	N/A	98.57(±13.4)

The efficiency results determined from the capacitance, resistance and gravimetric analysis are provided in Figure 7.54. These results demonstrate that determining the inhibitor efficiency using solely resistance values, or solely capacitance values can fail to represent the true efficiency of the inhibitor.

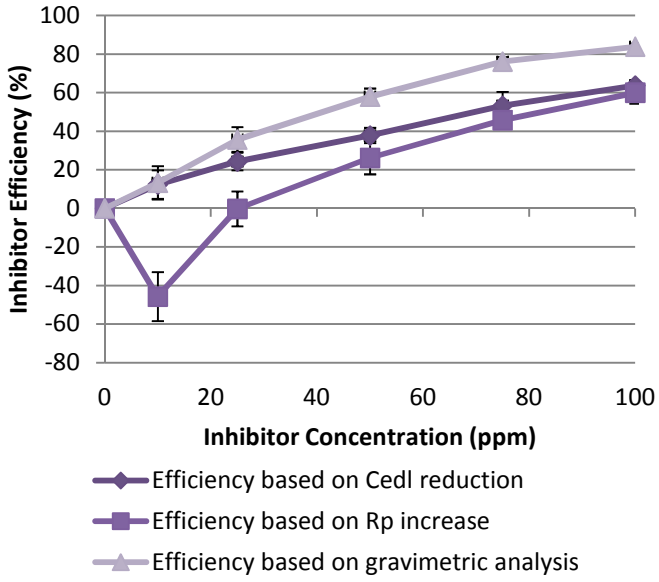

Figure 7.54: Efficiency of Inhibitor C based on the reduction in EDL capacitance, the increase in polarisation resistance and gravimetric analysis

In this situation, the addition of the components within Inhibitor C have had an influence over the capacitance level of the EDL by affecting the dielectric constant. The capacitance does reduce in the system as inhibitor concentration is increased, but not in a manner which is solely indicative of the level of surface coverage (and hence corrosion rate) of the sample. It is evident that the dielectric constant of the electrolyte within the EDL has been affected, causing the capacitance within the

system to change, preventing a true reflection of the inhibitor efficiency. Poor correlation between inhibitor efficiency calculated from mass loss and capacitance values has been recorded by both Epelboin et al. [210] for the application of propargylic alcohol to inhibit mild steel in 0.5 M H_2SO_4 solutions as well as Mahdavian and Ashhari [222] for the application of 2-mercaptobenzimidazole and 2-mercaptobenzoxazole in the protection of mild steel in HCl solutions and Mernari et al. [224] for the application of 3,5-bis(n-pyridyl)-4-amino-1,2,4-triazoles in the inhibition on mild steel in 1 M HCl.

Interestingly, the efficiency determined based on the increase in R_p produces an even worse approximation of inhibitor efficiency. The reason behind this discrepancy lies in the fact that the percentage increase in R_p neglects the change in Stern-Geary coefficient as a result of inhibitor addition. Although both Inhibitor B and C reduced the Stern-Geary coefficient from 33.1 to values of 17.9 and 17.8 respectively, the effect of underestimating efficiency was more pronounced for Inhibitor C. The reason behind this lies in the fact that for large R_p values (such as with high concentrations of Inhibitor B and Inhibitor C), a change in the Stern-Geary coefficient produces a much smaller change in corrosion rate and hence, a small change in the efficiency. For small values of R_p (as with low concentrations of Inhibitor B), the estimation of the Stern-Geary coefficient becomes critical in determining the correct corrosion rate. Small changes in the coefficient can influence the magnitude of corrosion and the efficiency dramatically.

Table 7.10 indicates the importance of considering changes in the Stern-Geary coefficient, especially at low concentrations. For high values of resistance such as Inhibitor B at 100 ppm, failure to compensate for the change in coefficient results in an underestimate of corrosion rate by 0.39 mm/year (a difference of 4.5% in efficiency calculation). Conversely, at lower values of R_p (100 ppm Inhibitor C), failure to change the coefficient results in an underestimate of corrosion by 1.62 mm/year and a difference of 18.8% in efficiency.

Table 7.10: Example of how accounting for the changes in the Stern-Geary coefficient can influence the efficiency determined by linear polarisation measurements for 'small' and 'large' values of polarisation resistance

Conditions	R_p ($\Omega.cm^2$)	Stern-Geary Coefficient	Corrosion Rate (mm/year)	Efficiency (%)	
Blank	43.7	33.1	8.69	N/A	N/A
100 ppm Inhibitor B	449.4	33.1	0.85	90.2	Difference of 0.39 mm/year and 4.5%
100 ppm Inhibitor B	449.4	17.9	0.46	94.7	
100 ppm Inhibitor C	109.1	33.1	3.52	59.5	Difference of 1.62 mm/year and 18.8 %
100 ppm Inhibitor C	109.1	17.8	1.89	78.3	

It is clear that as the R_p values become increasingly larger, the effect of the Stern-Geary coefficient on the inhibitor efficiency lessens. However, it is important to note that in cases where corrosion rates are very high, determining this coefficient is crucial in order to estimate inhibitor efficiency accurately. Researchers need to be aware that using solely resistance values to determine efficiency is not ideal when the inhibitor effects are small.

7.8 Influence of Pre-Corrosion for Inhibitors

In laboratory tests, inhibitors are often evaluated on their adsorption to freshly ground surfaces as in the previous sections of this research. Laboratory experience has indicated that inhibitors tend to perform differently on corroded surfaces than on freshly ground surfaces [174, 185].

The internal surface of a pipeline tends to be covered with different kinds of corrosion products such as mill scale and rust from storage and pipeline testing [185]. Additionally, a pipeline may have been in operation for a number of years before an increase in water cut necessitates the use of inhibition. In this case, the metal surface may be covered with different types of scale, iron carbonate or uncorroded iron carbide, significantly altering the inhibitor efficiency. It is believed that some inhibitors are capable of incorporating into the corrosion product and providing a protective barrier against the corrosive medium [198]. On the other hand, some inhibitors under-perform in the presence of corrosion products as they are restricted from accessing the active sites on the metal surface [174].

The purpose of this section is to establish the effect of pre-corrosion on the performance of the inhibitors in the jet impingement system. The samples were pre-corroded in the blank environment for 2 hours before inhibitor was added to the SIJ. Final AC impedance measurements were then performed after 4 hours of inhibition.

7.8.1 AC Impedance Plots

The Nyquist plots for Inhibitors A, B and C on freshly ground and pre-corroded surfaces are provided in Figure 7.55, Figure 7.56 and Figure 7.57, respectively. The application of each inhibitor to the pre-corroded carbon steel specimen resulted in remarkably similar behaviour between three chemical blends. By considering the three Figures (Figure 7.55(b), Figure 7.56(b) and Figure 7.57(b)) it is evident that low concentrations (25 ppm and below) results in a single time constant system with no inductive behaviour. As the concentration of the inhibitor is increased, the size of the semi-circle increases and a second time constant emerges at very low frequencies. This second semi-circle also appears to grow with increasing concentration of each chemical, especially in the case of the application of Inhibitor B at 100 ppm (Figure 7.56(b)) where a distinct second capacitive loop is visible.

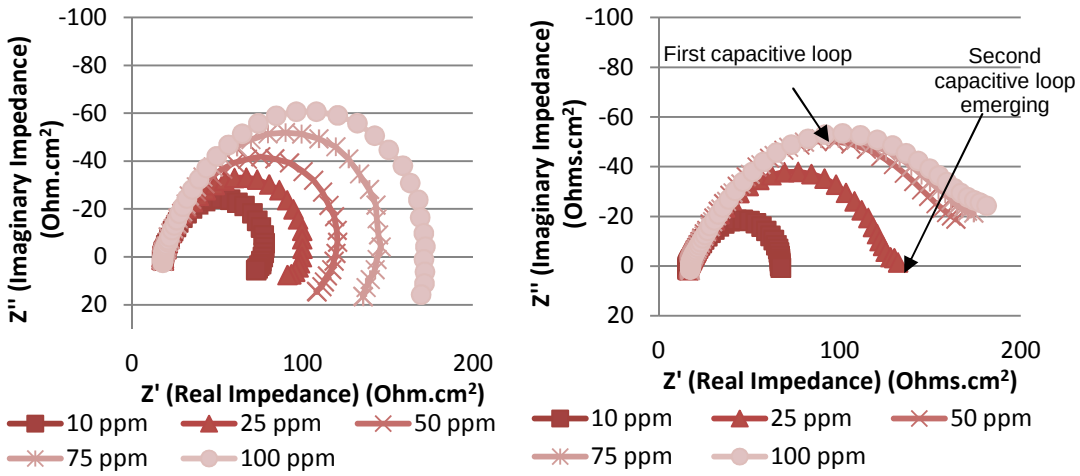

(a) (b)

Figure 7.55: Nyquist plots (a) after 4 hours of inhibition (b) after 6 hours (with 2 hours of initial pre-corrosion) for various concentrations of Inhibitor A. Test conditions were: 7 m/s, 45°C and CO_2-saturated at 1 bar

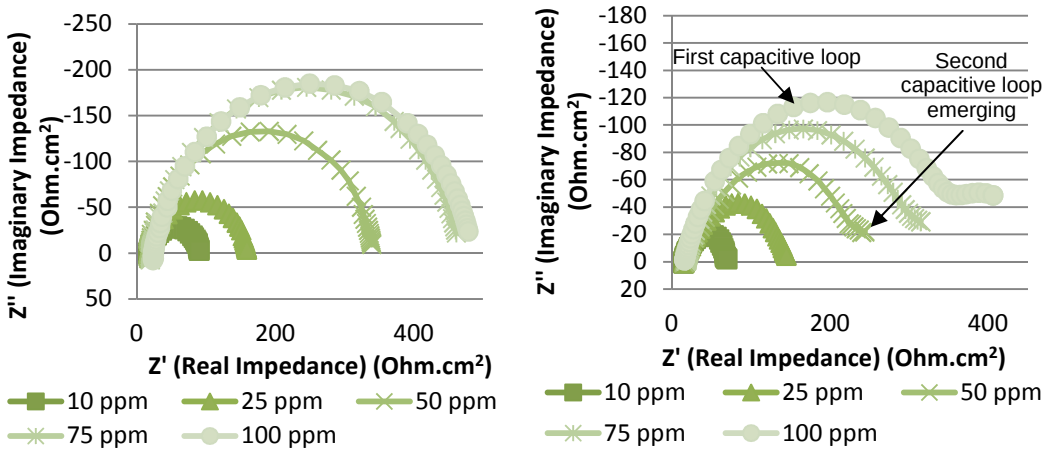

(a) (b)

Figure 7.56: Nyquist plots (a) after 4 hours of inhibition (b) after 6 hours (with 2 hours of initial pre-corrosion) for various concentrations of Inhibitor B. Test conditions were: 7 m/s, 45°C and CO_2-saturated at 1 bar

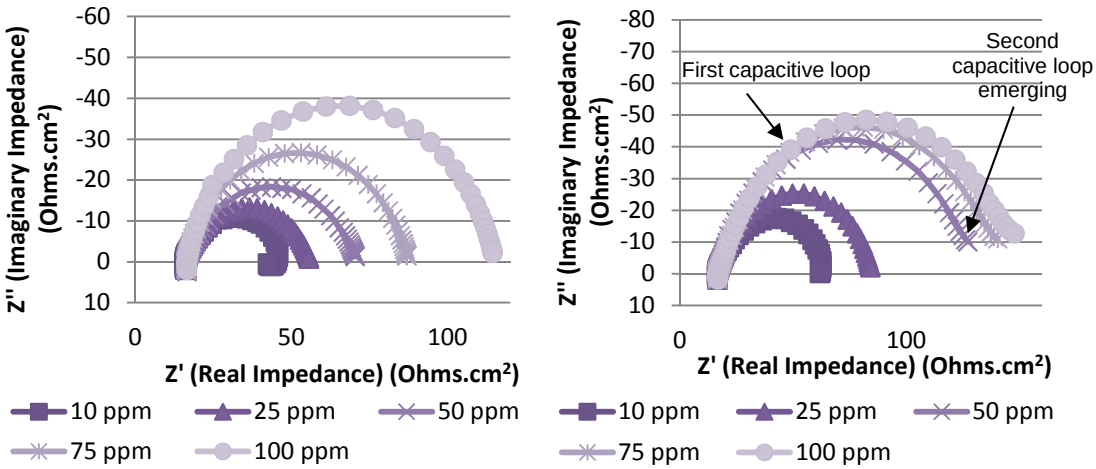

(a) (b)

Figure 7.57: Nyquist plots (a) after 4 hours of inhibition (b) after 6 hours (with 2 hours of initial pre-corrosion) for various concentrations of Inhibitor C. Test conditions were: 7 m/s, 45°C and CO_2-saturated at 1 bar

7.8.2 Equivalent Circuits and Analysis of Circuit Parameters

The behaviour of the system at low concentrations of Inhibitors A, B and C was modelled using a single time constant system shown previously in Figure 7.49. This was applied to concentrations of 10 and 25 ppm for each chemical. For concentrations greater than 25 ppm, two time constants were used by applying the circuit provided in Figure 7.58, in order model the second feature seen at low frequencies.

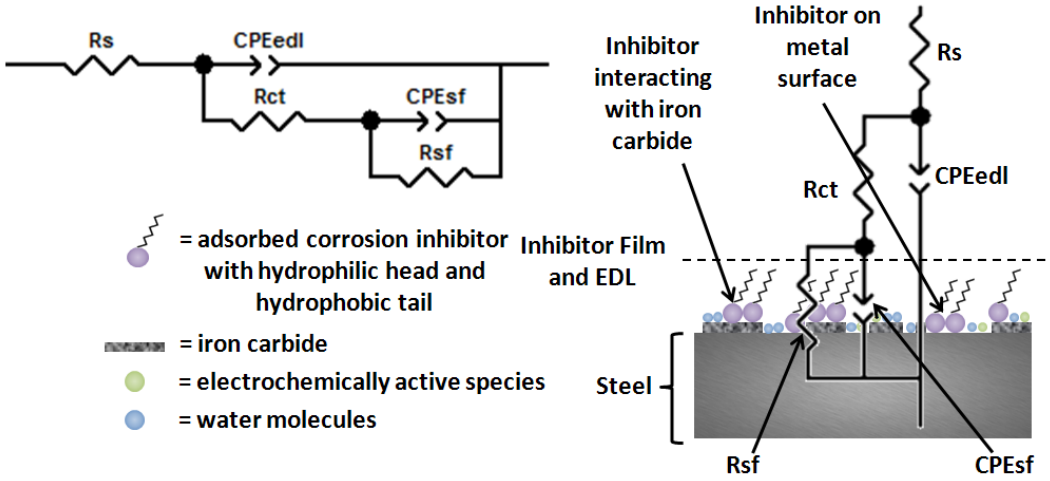

Figure 7.58: Equivalent circuit used to model AC impedance data for Inhibitor A at 50, 75 and 100 ppm after 2 hours pre-corrosions at 7 m/s; R_s is the solution resistance, CPE_{edl} is a constant phase element representing the capacitance of the electric double layer, R_{ct} is the charge transfer resistance, CPE_{sf} and R_{sf} are the capacitance and resistance of the second feature in the AC impedance spectra

In order to show the fitting quality with the proposed equivalent circuit, the Nyquist plots for Inhibitors B and C at 100 ppm are presented in Figure 7.59.

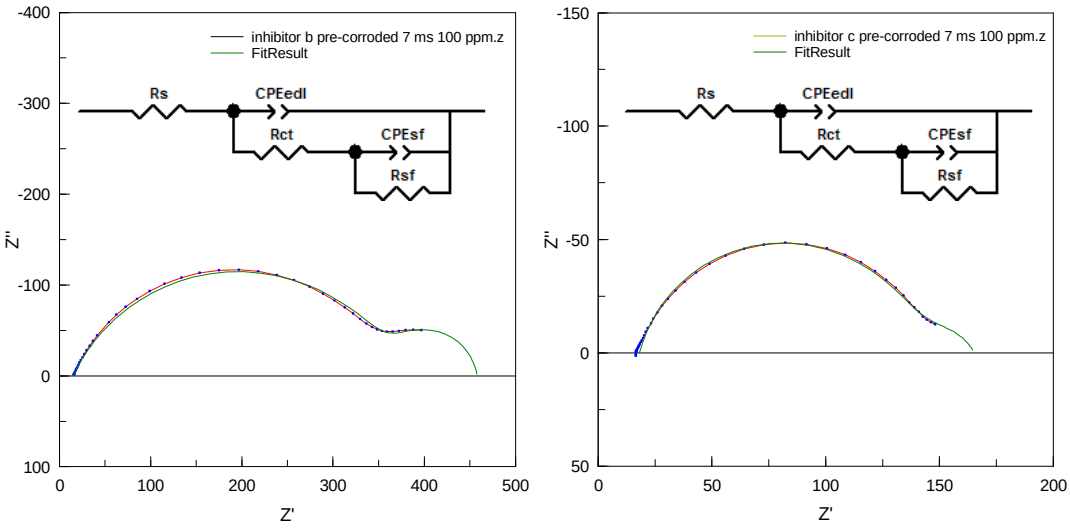

(a) (b)

Figure 7.59: Nyquist plots for carbon steel with (a) 100 ppm Inhibitor B and (b) 100 ppm Inhibitor C indicating the fit of the model (green line) to the experimental data (red line). Test conditions were: 7 m/s, 45°C and CO_2-saturated at 1 bar, with 2 hours pre-corrosion

The equivalent circuit parameters associated with Inhibitors A, B and C in the pre-corrosion experiments are provided in Table 7.11, Table 7.12 and Table 7.13. The

behaviour of the EDL is similar to what has been observed before for the three chemicals. As the concentration of each inhibitor increases the capacitive loop associated with the EDL increases i.e. R_{ct} increases, and the size of the capacitance values (CPE_{edl}) reduce. The order of magnitude of the capacitance values are what would be expected given the previous tests conducted without pre-corrosion.

Table 7.11: Values of the elements of the equivalent circuit in Figure 7.55

Conc. (ppm)	R_s ($\Omega \cdot cm^2$)	R_{ct} ($\Omega \cdot cm^2$)	CPE_{edl} ($\mu Fcm^{-2}s^{n-1}$)	n	R_{sf} ($\Omega \cdot cm^2$)	CPE_{sf} ($mFcm^{-2}s^{n-1}$)	n	$R_p = \lim_{\omega \to 0} Z$ ($\Omega \cdot cm^2$)
10	17.9	53.3	968	0.74	-	-	-	54.6
25	18.0	116.5	963	0.72	-	-	-	117.8
50	17.9	135.1	799	0.76	33.61	309	0.67	166.4
75	17.9	150.2	650	0.75	45.2	555	0.70	193.1
100	17.9	159.8	614	0.75	64.8	495	0.71	222.3

Table 7.12: Values of the elements of the equivalent circuit in Figure 7.56 for Inhibitor B

Conc. (ppm)	R_s ($\Omega \cdot cm^2$)	R_{ct} ($\Omega \cdot cm^2$)	CPE_{edl} ($\mu Fcm^{-2}s^{n-1}$)	n	R_{sf} ($\Omega \cdot cm^2$)	CPE_{sf} ($mFcm^{-2}s^{n-1}$)	n	$R_p = \lim_{\omega \to 0} Z$ ($\Omega \cdot cm^2$)
10	17.9	55.2	502	0.79	-	-	-	55.3
25	17.9	133.0	461	0.70	-	-	-	133.4
50	18.0	218.1	303	0.73	35.2	512	0.75	252.6
75	17.9	290.4	250	0.75	50.1	454	0.78	340.8
100	18.0	360.9	165	0.72	82.5	246	0.95	440.4

Table 7.13: Values of the elements of the equivalent circuit in Figure 7.57 for Inhibitor C

Conc. (ppm)	R_s ($\Omega \cdot cm^2$)	R_{ct} ($\Omega \cdot cm^2$)	CPE_{edl} ($\mu Fcm^{-2}s^{n-1}$)	n	R_{sf} ($\Omega \cdot cm^2$)	CPE_{sf} ($mFcm^{-2}s^{n-1}$)	n	$R_p = lim_{\omega \to 0} Z$ ($\Omega \cdot cm^2$)
10	17.9	46.12	796	0.80	-	-	-	47.33
25	17.8	68.17	690	0.79	-	-	-	69.03
50	18.0	108.4	676	0.82	10.12	682	0.67	118.4
75	17.9	116.4	636	0.84	16.2	510	0.70	132.9
100	17.9	121.6	586	0.84	25.3	871	0.70	146.7

The interesting point to note from these tables is that the presence of three inhibitors above 25 ppm promotes the formation of a second capacitive loop which possesses very high values of capacitance of the order of 100 $mFcm^{-2}s^{n-1}$.

Based on previous measurements coupled with the SEM analysis and visual inspection, it has been established that Fe_3C reveals itself on the surface of the sample during the pre-corrosion period.

It is suggested that at high concentrations of inhibitor, the chemical is able to interact with Fe_3C as well as the metal surface, which ultimately creates the secondary time constant. Lopez [198] demonstrated that various imidazoline derivatives work by blocking active cathodic sites on Fe_3C and/or acting as a physical barrier to prevent the transport of corrosive species to the surface.

Many of the components in Inhibitors A, B and C contain hydrocarbon chains which may generate interactions amongst certain molecules in the form of van der Waals forces and act as diffusion barriers to aggressive ions from the bulk solution by effectively blocking pores in the cementite network by aggregating together.

It is possible that the adsorption of the inhibitor onto the cementite surface could indeed lead to the blockage of active sites, but also the formation of occlusion cells or stagnant areas due to the interaction among the hydrophilic tails of the molecules in the pores of Fe_3C. In areas such as these, the dissolved ferrite could result in a localised concentration of Fe^{2+}. The hydrophilic nature of the 'net' created from the molecule tails would cause carbonate and bicarbonate ions to migrate to these regions and form $FeCO_3$. Additionally, it has been shown that pearlite and ferrite

structures (such as the one considered here) provide better sites for the anchoring of $FeCO_3$ because of the laminar structure of Fe_3C [26]. The adsorption of the inhibitor onto the Fe_3C network or the potential for $FeCO_3$ to form may be what manifests itself as the new capacitive loop visible at concentrations above 50 ppm.

The magnitude of the capacitance of the second capacitive loops and a comparison with similar impedance plots in literature may help to shed some light into the electrochemical process which is responsible for the generation of this secondary loop.

Mora-Mendoza and Turgoose [228] produced very similar impedance plots to those observed in this work with long duration tests in uninhibited conditions for mild steel at a pH of 3.8 (Figure 7.60). The formation of a small capacitive loop was attributed to the diffusion barrier created from the precipitation of $FeCO_3$ based on the analysis of cross-sectional SEM images and the magnitude of capacitance, which reached the order of 100 $mFcm^{-2}s^{n-1}$, just like those observed in this study.

Other researchers [38, 229] have also shown that the creation of a diffusion barrier can introduce additional time constants in the system. These tend to occur predominantly at low frequency ranges (below 1 Hz) and tend to possess very high capacitance values (greater than 100 milliFarads).

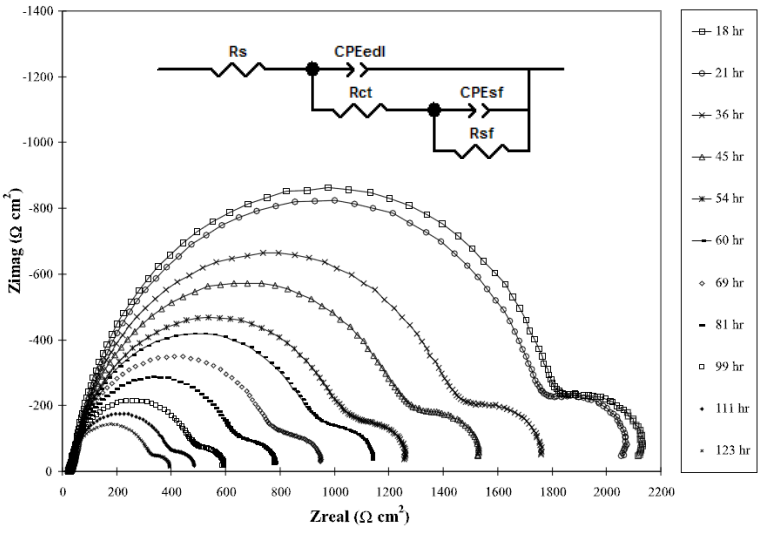

Figure 7.60: Nyquist plot recorded between 18 and 123 hours for mild steel in CO_2 solutions, pH 3.8, 1000 rpm – from Mora-Mendoza et al. [228]

Farelas et al. [188] also witnessed capacitance loops at low frequencies which were attributed to the formation of $FeCO_3$ under an Fe_3C layer. However, the capacitance

values associated with this low frequency process were not disclosed in the publication. Park and MacDonald [229] conducted impedance measurements to evaluate the growth of a porous magnetite film on carbon steel in a NaCl solution. They found that the film restricted the transport of active electrochemical species (creating a 'pore resistance' termed R_{pore}) to the surface, resulting in a low frequency response with capacitance values of the order of 100's of $mFcm^{-2}s^{n-1}$.

The assignment of the capacitance loops to particular processes in impedance plots tends to be performed based on the magnitude of capacitance associate with each mechanism and the frequency ranges at which they occur [207]. Tait [38] and Bentiss et al. [207] stated that the charge-transfer corrosion process (i.e. the EDL behaviour) tends to manifest itself at 'high to medium' frequencies which is what is observed in this particular scenario. Behaviour associated with inhibitor films and coatings tend to occur at frequencies even higher than that of the corrosion process [38] and diffusion mechanisms tend to be observed at very low frequencies [38]. A number of authors [38, 188, 228], have demonstrated that capacitance values of the order of milliFarads at low frequencies are typically associated with diffusion processes as a result of corrosion products or films which act as diffusion barriers to electrochemically active species. Loops at higher frequency above those expected for the EDL tend to be assigned to coatings and protective films [38].

With the second capacitive loop (CPE_{sf}) having such a high capacitance, this adds further credence to the suggestions that there is an interaction between the inhibitor and Fe_3C on the surface which promotes the formation of a diffusion barrier.

7.8.2.1 Inhibitor Efficiency of Freshly Ground vs. Pre-Corroded

Based on the electrochemical measurements, values of R_p were extracted from the AC impedance plots for Inhibitors A-C. Values of R_p were used to determine the efficiency as a function of inhibitor concentration for the three different chemicals. Results in Figure 7.61 indicate that Inhibitors A and C produced higher efficiencies as a result of the pre-corrosion, where as Inhibitor B produced almost identical behaviour.

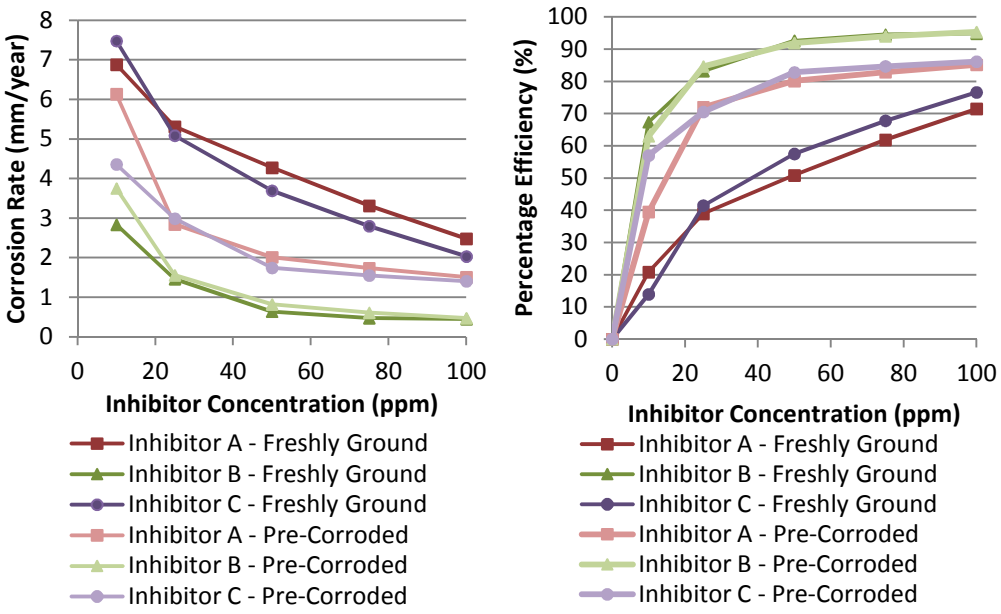

(a) (b)

Figure 7.61: (a) Corrosion rates and (b) inhibitor efficiencies of freshly ground and pre-corroded specimens in flow-induced corrosion tests at 7 m/s for three inhibitors after 4 hours

7.9 Erosion-Corrosion using Submerged Impinging Jet (SIJ)

A much more severe form of degradation is apparent in oil and gas production when sand particles are present in the production fluid, resulting in a process termed 'erosion-corrosion'. The transition from a flow-induced corrosion regime to that of erosion-corrosion as a result of sand production can occur very early in the life of an asset [3]. However, in the majority of cases, estimates tend to show that wells will only begin to start producing sand a number of years into their life, after pressure declines and water production commences [4].

The configuration of the oil-sand slurry produced from wells, combined with the presence of water, CO_2 and salts containing Cl^-, HCO_3^- and SO_4^- ions create an exceptionally aggressive environment for pipelines and equipment used to transport these fluids. The corrosive degradation experienced by these transportation lines is accelerated by the erosive mechanism attributed to the sand impingement from the moving slurry, resulting in the synergistic effect of erosion-corrosion [230].

Previous studies at Leeds University [117, 118, 163, 164] showed that performance of inhibitors can become adversely affected by the presence of sand through either:

- removal of protective films by sand particle impacts, or

- the consumption of the inhibitor by sand particles, reducing the residual concentration in the bulk solution

The final aspect of the inhibitor evaluation was to consider these two aspects and evaluate the inhibitors through both gravimetric analysis and *in-situ* electrochemistry when sand was present in the system. Tests were conducted in the same manner as the flow-induced corrosion tests (at 7 m/s), but with the addition of 100 mg/L and 500 mg/L of sand.

As discussed previously, the erosion-corrosion degradation process can be divided into four components as follows:

$$\mathrm{TML} = \mathrm{E} + \mathrm{C} + \mathrm{dE_C} + \mathrm{dC_E} \tag{7.17}$$

where TML is the total mass loss, E is pure erosion in the absence of any corrosion and C is the corrosion in the absence of any erosion. dC_E is the effect of erosion on corrosion (often referred to as the additive effect) and dE_C is the effect of corrosion on erosion (usually termed synergistic effect) [118].

The application of *in-situ* electrochemistry provides information on the contribution of corrosion processes (C + dC_E), whilst the total mass loss determines the rate of the overall degradation process. Both sets of information are provided in Figure 7.62. The *in-situ* response in the flow-induced corrosion tests are omitted for clarity in Figure 7.62.

For the blank tests in Figure 7.62 (blue graphs), only a marginal increase in mass loss is observed over the 4 hour test as a result of introducing sand. The introduction of 500 mg/L sand increases the degradation rate from 9.8 mm/year to 10.4 mm/year. It is obvious that corrosion is the dominant mechanism in this environment. For tests at 7 m/s with 500 mg/L sand, the *in-situ* corrosion measurement comprises just under 95% of the total damage. In comparison to tests performed by Neville and Wang [118] at 20 m/s and 50°C with 500 mg/L sand onto carbon steel samples in a blank brine solution, the contribution of (C + dC_E) only amounted to 30% because of the severity of the erosion component and the total degradation rate exceeded 20 mm/year.

The *in-situ* corrosion rate in the blank solution fails to change significantly when sand is added to the system. It may be expected that sand would fail to influence the *in-situ* corrosion rate as test have shown earlier in this Chapter that no

protective film forms on the surface in the uninhibited environment. For these blank tests, the total mass loss would therefore be expected to comprise entirely of pure electrochemical corrosion (C) and pure erosion (E), the sum of the synergistic effects (dC_E and dE_C) appear to be very small.

Application of the three inhibitors successfully reduced the level of degradation in the flow-induced corrosion and erosion-corrosion environments. The addition of sand to the system had the greatest adverse effect on the efficiency of Inhibitor A, with the addition of 500 mg/L increasing the total degradation rate from 2.5 to 3.6 mm/year (a reduction in inhibitor efficiency of 10%). By considering the electrochemical response (C + dC_E) for Inhibitor A in Figure 7.62, it is evident that the sand increased the *in-situ* corrosion rate. As discussed earlier, this is attributed to either a reduction in the bulk concentration of inhibitor through adsorption onto sand particles, or more likely, the removal of the inhibitor film as a result of continuous particle impingement. The increase in *in-situ* corrosion rate was from 2.5 to 3.3 mm/year based on the average readings for the application of Inhibitor A.

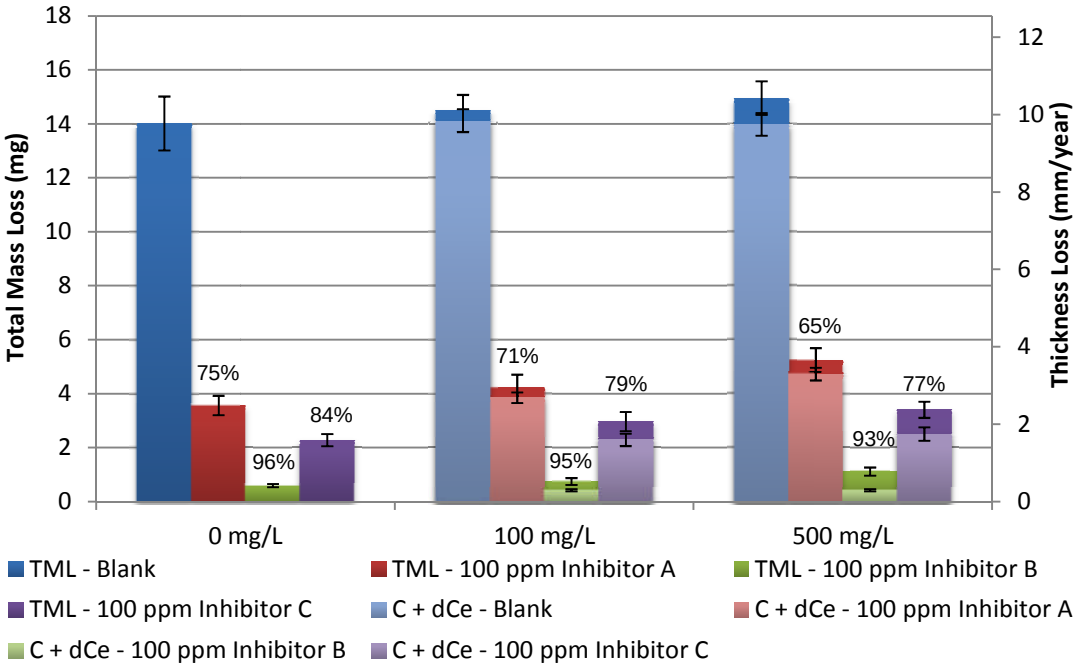

Figure 7.62: Total mass loss and *in-situ* corrosion rate measurements highlighting the effect of sand concentration on inhibitor performance at 100 ppm. Test conditions were: 7 m/s, 45°C, 500 mg/L sand and CO_2-saturated at 1 bar

In addition to Inhibitor A, Inhibitor C displayed an increase in *in-situ* corrosion rate from 1.6 to 1.8 mm/year as a result of introducing 500 mg/L sand into the system. This indicates that this chemical was not as adversely affected by sand particle

impingement in terms of film disruption or reduction in residual concentration through adsorption onto sand.

Finally, Inhibitor B was the most efficient chemical tested in these conditions, producing an efficiency of 93% even in the presence of 500 mg/L sand. Interestingly, there was no significant change to the *in-situ* corrosion rate of the carbon steel suggesting that the inhibitor film was either resistant to particle impingement or regenerated quickly enough to prevent significant dissolution of the steel.

It is often assumed that an inhibited rate of 0.1 mm/year is the desired target for most oil and gas companies, although there appears to be no real rationale behind this. However, given the severity of the conditions (7 m/s and 500mg/L sand concentration), the reduction of degradation rate down to 0.7 mm/year can still be regarded as excellent, especially when compared to the current inhibitor used on the facility (Inhibitor A) which proved to be the least effective chemical evaluated.

7.9.1 Evaluation of Erosion and Corrosion Through SEM

Based on a previous CFD analysis of the jet impingement system [116], it was evident that three distinct regions existed on the surface of the sample, which were exposed to different regimes. Zone I (located less than 2 mm radially from the centre of impingement) is subjected to a large amount of plastic deformation and high angle particle impingement in erosion-corrosion conditions. Zone II (3 to 6 mm radially) is exposed to low particle impact angles and this region experiences a lot of material removal as a result of cutting, as well as material dissolution. In Zone III (greater than 7 mm radially from the centre of the sample), far fewer particle impacts occur and they are at much lower angles.

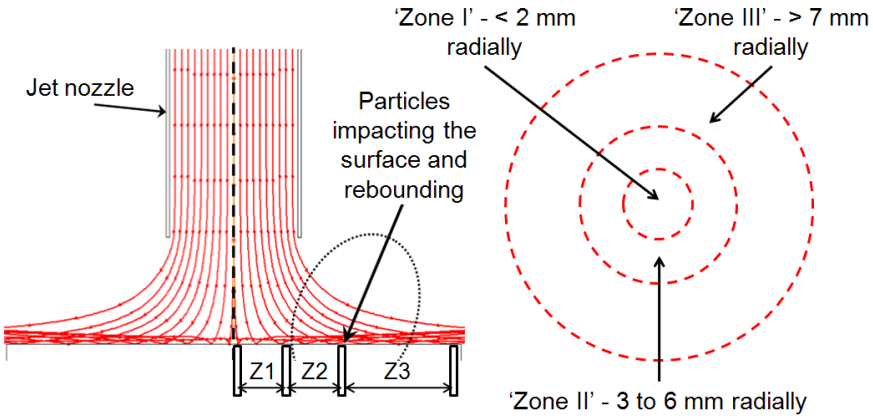

Figure 7.63: Different regions of attack on carbon steel surface

Although the inhibitors have been evaluated through the reduction in mass loss and *in-situ* electrochemistry, it is important to assess the performance based on microscopic studies and visual inspection of the corrosion attack. This is an indispensible form of evaluation as certain inhibitors may effectively inhibit homogeneous corrosion, but help to promote pitting or mesa attack.

Images of tests at 7 m/s with and without 500mg/L of sand are provided in Figure 7.64(a)-(g). Figure 7.64(a) shows the centre of the sample (Zone I) subjected to erosion-corrosion in blank conditions, indicating plastic deformation as a result of sand particle impingement. This image is typical for all the erosion-corrosion samples analysed in this region. In contrast, towards the outside of the sample in Zone III (Figure 7.64(b)), the material removal mechanism shows more signs of corrosion damage through selective dissolution of the ferrite phase.

Although Inhibitor A significantly reduced mass loss for the carbon steel, inspection under SEM revealed a number of areas where localised attack had occurred on the sample (Figure 7.64(c)). These regions of attack appeared to be aligned in the direction of the specimen polishing marks and act as initiation points for localised attack. Pacheco et al. [231] stated that from their laboratory experience, pitting tended to initiate in the troughs of machining marks on specimens. It could be postulated that the localised attack has caused the inductive behaviour witnessed in the AC impedance plots as induction has been linked to this form of attack as well as pitting by other authors in the past [38]. Additionally, some of the damaged areas as a result of particle impingement may have also acted as initiation points for localised attack, which would explain the increase in the corrosion rate of the sample in the presence of sand.

Inhibitor B was the most efficient chemical and this is reflected in the SEM images. The original polishing marks on the surface of the sample are visible in flow-induced corrosion (Figure 7.64(d)) and erosion-corrosion tests with 500 mg/l sand (Figure 7.64(e)). The presence of polishing marks on the surface of the sample indicates that the regime is indeed erosion-corrosion, albeit the corrosion damage is very dominant based on the gravimetric analysis and in-situ corrosion rates displayed earlier in Figure 7.62.

For the application of Inhibitor C, no localised attack could be seen on the samples (Figure 7.64(f)). The level of corrosion was very low and uniform, resulting in a

clean surface and a small reduction in the visibility of the polishing marks on the surface.

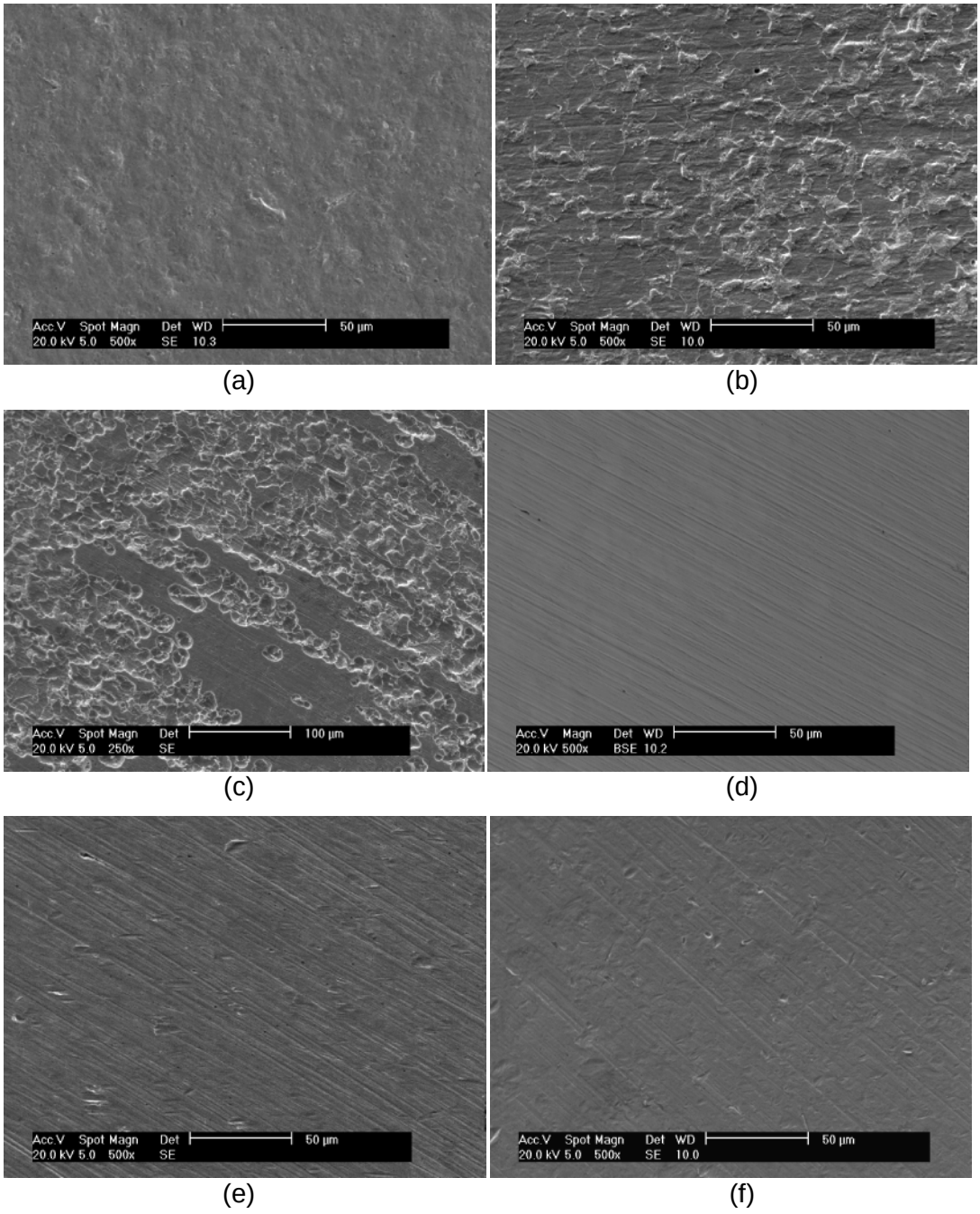

Figure 7.64: SEM images of (a) Erosion-corrosion blank sample, Zone I; (b) Erosion-corrosion blank sample, Zone II; (c) Erosion-corrosion with 100 ppm Inhibitor A, Zone II; (d) Flow-induced corrosion with 100 ppm Inhibitor B, Zone II; (e) Erosion-corrosion with 100 ppm Inhibitor B, Zone II; (f) Erosion-corrosion with 100 ppm Inhibitor C, Zone II; (g) Erosion-corrosion with 100 ppm Inhibitor D, Zone II

Unfortunately, the limitation of the jet impingement system at Leeds is that it cannot be conducted for long periods of time making it difficult to identify whether localised

corrosion would be a potential failure mechanism with these inhibitors. Although signs of mesa-attack were apparent under some SEM images, ideally longer tests are required in order determine the severity of localised attack on carbon steel and whether the inhibitors would pose a problem from this respect.

7.9.2 Corrosion Inhibitor Evaluation Using Leeds Empirical Model

The traditional approach to evaluate a corrosion inhibitor combines an assessment of cost, efficiency and availability [232]. In terms of corrosion allowance for pipelines, two of the most dominant criteria are corrosion modelling and corrosion inhibitor availability [233, 234].

Inhibitor efficiency is generally calculated based on the percentage reduction in corrosion rate. The problem with this approach is that while inhibitors may be 99% efficient in laboratory tests, long term field monitoring reflects much lower efficiencies [233, 235]. One of the contributing reasons behind this is that there will be periods in the field when corrosion inhibitor is not injected. Likely reasons for this can relate to pump failures and logistic issues [233].

This leads to the concept of inhibitor availability in which the field performance is determined based on the assumption that lines are not inhibited 100% of the time. For example, 95% corrosion inhibitor availability would mean that the inhibited corrosion rate is assumed for 95% of the time and uninhibited corrosion rate for 5% of the time [233].

Inhibitor availability was also incorporated into the model. The underlying assumptions with this method being integrated into the model are that the formation of any corrosion products during periods without inhibition do not affect the performance of the inhibitor in the system when injection restarts. Figure 7.65 shows the predicted thickness loss on the facility between 2005 and 2010 according to the Leeds Empirical Model. The model also provides the predicted behaviour had 50 ppm Inhibitor B (most efficient chemical at most cost effective concentration) been used after the line replacement in 2005, along with varying levels of inhibitor availability.

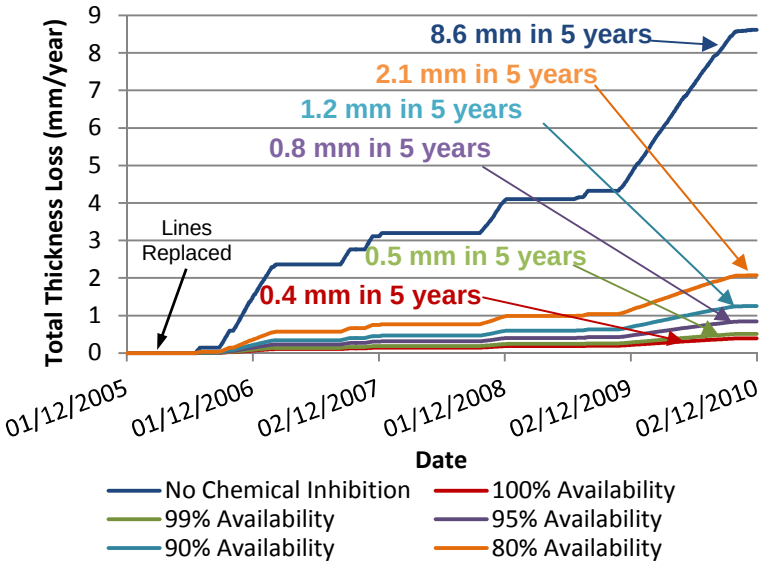

Figure 7.65: Predicted thickness loss as a function of time on the offshore facility had 50 ppm Inhibitor B been used. The graph also displays different levels of inhibitor availability

7.10 Conclusions

- There is significant contrast in inhibitor performance between static and dynamic conditions. The research within this Chapter demonstrates how misleading quantification of inhibitor performance in static conditions can be for a system such as the one considered here, which can ultimately lead to the selection of the wrong inhibitor at the inappropriate concentration.

- The research has highlighted the potential for the SIJ to not only be a useful tool to predict corrosion rate in dynamic systems, but it also shows that the system can produce much more severe conditions than in static conditions, testing the inhibitor performance to the limit and ensuring the best inhibitor is chosen for a particular environment.

- AC impedance measurements were used to understand the dissolution behaviour of carbon steel in dynamic conditions at 7 m/s impingement without inhibition. The implementation of this form of electrochemistry was shown to be a practical technique for identifying and understanding the corrosion mechanisms. This was achieved by modelling the dissolution process using equivalent circuits and relating the observed behaviour to the changes in electrochemical parameters in the circuit.

- The preferential dissolution of ferrite during the corrosion process resulted in the revealing of Fe_3C which subsequently caused an increase in the rate of dissolution by acting as a cathodic site with lower overpotential for the hydrogen evolution reaction. The revealing of Fe_3C was also believed to have caused pitting on the surface of the material as well as accelerating the corrosion kinetics.

- Inductive behaviour was present in the AC impedance plots for the blank system and was attributed to the adsorption of intermediate products in the corrosion mechanism. It was shown that extrapolation of the inductive loop to the real axis produced a polarisation resistance value which provided a more accurate interpretation of corrosion rate compared to the charge-transfer resistance extracted from the equivalent circuit.

- The AC impedance technique was also shown to be a practical technique for evaluating inhibitor film formation as well as performance. The AC data was used to calculate corrosion related electrochemical parameters through the use of electrical equivalent circuit models and was shown to be a useful tool for studying inhibitor mechanisms. The technique can measure electrochemical related parameters such as the resistance and capacitances associated with the EDL as well as the overall polarisation resistance to help determine *in-situ* corrosion rates.

- The percentage reduction in the EDL capacitance and the percentage increase in the polarisation resistance from impedance measurements were shown to be two methods which can be used to estimate inhibitor efficiency.

- However, these two techniques were shown to possess limitations when the inhibitor either changes the dielectric properties of water in the EDL, or the inhibitor significantly changes the Stern-Geary coefficient by altering the Tafel slopes. The limitations of this process were particularly evident when inhibitor efficiency was low and the resulting corrosion rate was high.

- A more accurate form of measurement was achieved by determining efficiency using the polarisation resistance values combined with the measured value of Stern-Geary coefficient. This method produced an excellent interpretation of corrosion rate when compared with gravimetric analysis.

- Impedance measurements in inhibited environments for samples which were pre-corroded highlighted that the inhibitors possessed another means of reducing corrosion as well as blocking active sites through adsorption onto the material surface. The low frequency response of the impedance measurements indicated that the inhibitors are capable of interacting with iron carbide to create a diffusion barrier to aggressive species involved in the corrosion reactions. Interestingly, this interaction of the inhibitor with Fe_3C helped to improve inhibitor performance for all three chemical evaluated.

- Erosion-corrosion tests showed that in some cases, the introduction of sand into the system can increase the *in-situ* corrosion rate of carbon steel either through disruption to the protective film or by reduction in the residual concentration of inhibitors in the bulk solution through adsorption of active components onto the surface of sand particles.

Chapter 8 -
Erosion-Corrosion Mitigation in Extreme Environments Through Chemical Inhibition

8.1 Introduction and Chapter Outline

Sand production has established itself as a major concern in the operation of oil and gas facilities with its occurrence becoming increasingly prevalent, particularly in aging assets. The erosion of carbon steel pipework attributed to particle impingement, coupled with the electrochemical corrosion processes in CO_2-saturated environments can create exceptionally high degradation rates which can be to both difficult predict and mitigate.

8.1.1 Causes of Sand Production

As reservoir pressure declines throughout the producing life of a well, some of the supporting overlying rock is removed and increased stress is placed on the formation sand itself. At some point, the formation sand grains break free from their matrix and can be produced along with the process fluid [236].

An increase in the water cut of produced fluids is a common observation in aging wells. For a typical water-wet sandstone formation, some grain-to-grain cohesiveness is provided by the connate water surrounding each sand grain [236]. The onset of water production can cause the connate water to cohere to the produced water, resulting in a decrease in surface tension forces and a subsequent decline in grain-to-grain cohesiveness, promoting the loosening of sand particles from their matrix, allowing them to enter the well bore [236].

The production of reservoir fluids creates a pressure differential at the well bore along with drag forces which can combine to exceed the formation compressive strength. Many operators find that a critical flow rate exists for wells, below which pressure differential and frictional drag forces do not exceed those required to cause sand production [236]. However, the demand for production often necessitates flow rates above this threshold, inevitably leading to sand presence in the process fluid.

All the factors formerly mentioned can promote the onset or an increase in sand production which ultimately threatens asset integrity, particularly in environments which are also corrosive. The removal of material through both mechanical (particle impingement) and electrochemical (CO_2 corrosion) processes is known collectively as ‘erosion-corrosion’.

8.2 Understanding and Mitigating the Effects of Erosion-Corrosion

Although erosion by solid particle impingement is known to occur in the oil and gas industry, its interaction with corrosion to create an erosion-corrosion regime is generally not fully understood in CO_2 environments [143]. An appreciation for the relations between erosion and corrosion and the contribution of each process towards degradation rate is essential when it comes to determining how to mitigate the damage effectively.

One promising method towards reducing solely CO_2 corrosion is through the application of adsorption inhibitors. Research in the mid-1940s highlighted that long-chain polar compounds possessed inhibition properties [118]. This discovery dramatically altered inhibitor practices in oil and gas production and facilitated the operation of wells with high corrosivity and water content. Over the last decade, significant advancements in chemical inhibition have enabled operators to use carbon steel pipework in oil and gas facilities where sand production is a concern. The ability of these chemicals to control degradation in an environment which consists of both erosion and corrosion material removal mechanisms is well documented [159, 163, 237], but the underlying processes of inhibition have not been the topic of considerable discussion.

Erosion-corrosion experiments performed in Chapter 7 produced small levels of erosion at 7 m/s and failed to significantly increase the degradation rate of the material from that of a flow-induced corrosion environment. The question is posed as to whether these chemicals would be able to withstand more severe hydrodynamic conditions and higher velocity sand particle impingement. It would be interesting to observe whether the chemical packages are capable of reducing the erosion component of damage, or merely reduce the electrochemical processes at the surface, as observed by other authors [6, 166].

This Chapter considers carbon steel degradation in extreme conditions (high velocity, sand-containing and non-scale ($FeCO_3$) forming). The objectives are to understand the synergistic effect which occurs between erosion and corrosion when both processes are occurring simultaneously, assess the feasibility of chemicals to control erosion-corrosion and understand the various mechanisms by which this is achieved. In comparison to the previous Chapter, which focused on performing tests in conditions which simulated those on the offshore facility, this section of the

thesis seeks to understand the behaviour in much more severe conditions, beyond those which an inhibitor may be expected to perform acceptably.

Four inhibitors are reviewed in their ability to control erosion-corrosion through a combination of gravimetric measurements, *in-situ* electrochemistry (AC and DC) and surface profilometry. The three previously reviewed chemicals are assessed, along with one high shear resistant chemical package (Inhibitor D).

Being able to understand the interactions of these degradation processes and the inhibitor behaviour in these environments will undoubtedly allow for better control of erosion-corrosion and help in the development of chemicals for the oil and gas industry.

It is worth noting that the primary study is not to assess the detailed surface chemistry – it is more an assessment of the feasibility of chemicals to significantly control erosion-corrosion and develop and initial understanding of how this is facilitated. The outline of this Chapter is provided in Figure 8.1.

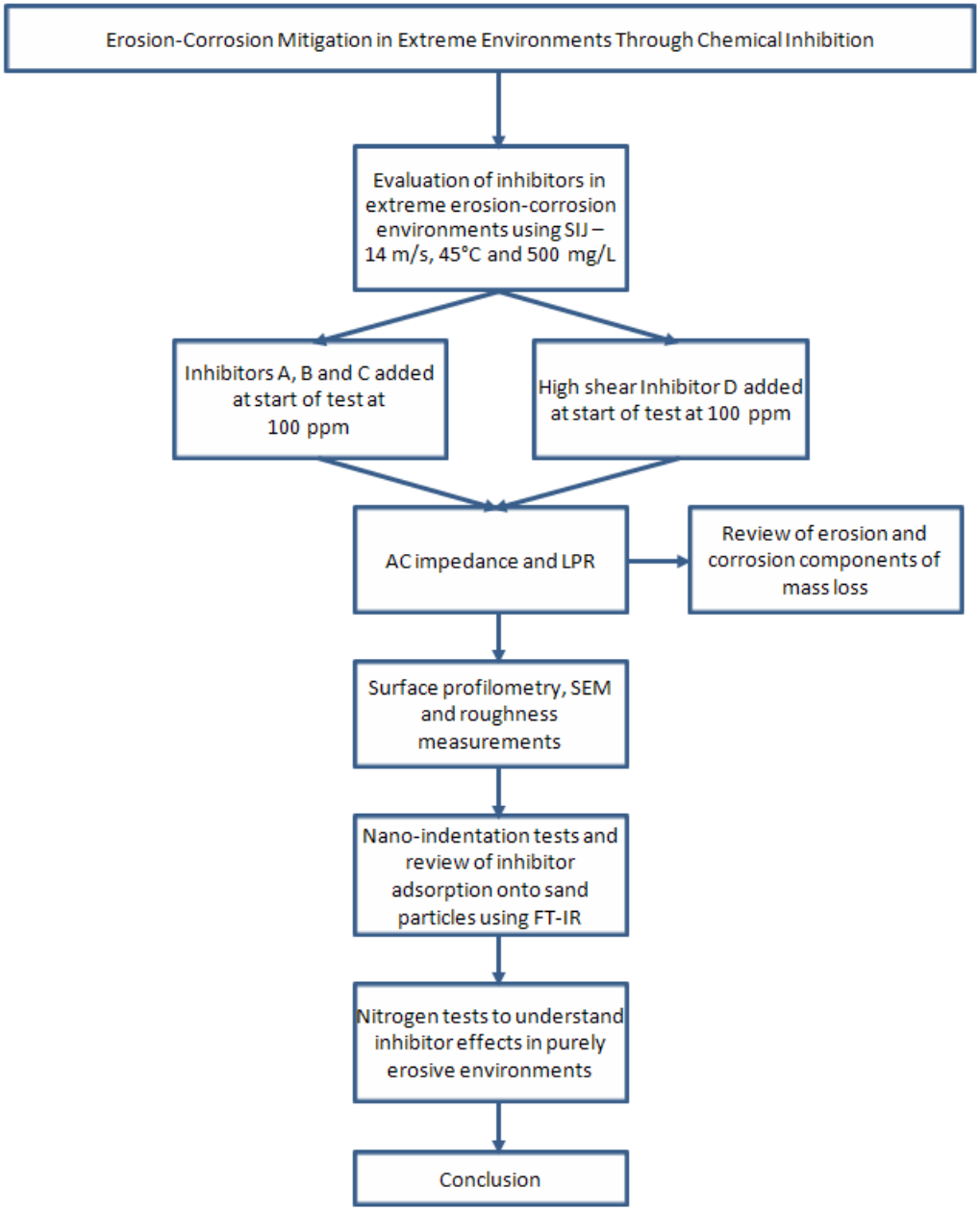

Figure 8.1: Outline of Chapter 8

8.3 Experimental Erosion-Corrosion Setup and Test Procedure

Erosion-corrosion experiments were conducted using the submerged impinging jet (SIJ) setup which is described in Section 7.3.1. Inhibitors A to C were once again used in this Chapter at concentrations of 100 ppm. In addition to these chemicals, a high shear resistant chemical was introduced (Inhibitor D). The composition of this inhibitor is provided in Table 8.1 and is known to possess strong film-forming characteristics.

Table 8.1: Composition/information on chemical components of Inhibitor D

Chemical Name	Inhibitor D
Alkyl Benzenes	(1-5%)
Amide/Imidazolines	(10-30%)
Maleated Tall Oil	(10-30%)
Methanol	(30-60%)
Propan-2-ol	(1-5%)
Quaternary Ammonium Compound	(5-10%)
2-Mercaptoethanol	(1-5%)

The same brine composition, temperature (45°C), sand concentration (500 mg/L) and partial pressure (fully CO_2-saturated at 1 bar) were used for experiments in this Chapter as in the previous Chapter. The flow velocity was the only parameter changed, which was increased to 14 m/s.

8.3.1 *In-Situ* Corrosion Test Procedure

Two identical carbon steel samples were used in the jet impingement rigs, with one sample being placed under each of the two nozzles. One sample was used for gravimetric analysis and the other specimen was used to assess the electrochemical response of the material to erosion-corrosion. Therefore, *in-situ* here refers to corrosion measurements being made under erosion-corrosion conditions (in contrast to static conditions which would produce very different behaviour).

Weight loss measurements were made to an accuracy of 0.01 mg before and after the test after cleaning the surface with Clarke's solution [173].

In-situ measurements were achieved by connecting an electrical wire to the back of one of the samples via a soldering process and mounting the material in a non-conducting resin using a standard embedding procedure. Samples were wet-ground up to 1200 silicon carbide abrasive paper, degreased with acetone, rinsed with distilled water and dried before fixing them into the rig and starting the test. The embedded sample formed the working electrode within a three electrode cell which also comprised of a Ag/AgCl reference electrode and a platinum auxiliary electrode. Corrosion measurements were performed on the specimen through the implementation of a combination of DC linear polarisation and AC impedance

measurements over three and half hours, with the remaining half hour being used for potentiodynamic sweeps. Solution resistance (R_s) was measured for each test using AC impedance and was subsequently subtracted from the linear polarisation resistance to determine the correct resistance value.

AC impedance was chosen as the electrochemical method to determine corrosion rate in the system as this approach was capable of providing a further insight into the dissolution and inhibitor mechanisms as well as the *in-situ* corrosion rates. The impedance measurements were performed using a Solartron 1280 potentiostat which applied an oscillating potential to the working electrode of 10 mV about E_{corr} using a frequency range of 20 kHz to 100 mHz with 10 points per decade. Scans were performed approximately every 20 minutes and the Nyquist, Bode and Bode phase plots were analysed using Zview^{TM} software.

Exactly 10 linear polarisation and 10 AC impedance measurements were performed over the duration of each test. The sample potential was scanned from 15 mV more negative than E_{corr} to 15 mV more positive than E_{corr}, at a scan rate of 0.25 mV/s. At the end of the experiment, potentiodynamic sweeps were conducted. Cathodic and anodic sweeps were performed by starting from E_{corr} and finishing at either ±250 mV from E_{corr}. Only one sweep (either anodic or cathodic) was performed for a single working electrode at the end of the test.

Tafel slope values were used in conjunction with the measured values of polarisation resistance (R_p) from both AC and DC measurements to determine i_{corr} using Stern-Geary theory [41] and hence the corrosion rate in mm/year with the use of Faraday's law.

As highlighted by Neville et al. [118] the total mass loss attributed to erosion-corrosion can be divided into four components as shown in the following equation:

$$\mathrm{TML} = \mathrm{E} + \mathrm{C} + \mathrm{dE_C} + \mathrm{dC_E} \tag{8.1}$$

where TML is the total mass loss, E is pure erosion in the absence of any corrosion and C is the corrosion in the absence of any erosion. dC_E is the effect of erosion on corrosion and dE_C is the effect of corrosion on erosion [118].

By implementing this methodology it is possible to determine the contribution of the corrosion component (C + dC_E) through the application of *in-situ* electrochemistry

and use it in conjunction with the total mass loss measurements to determine the erosion component ($E + dE_C$).

8.4 Erosion-Corrosion Gravimetric Results

Total mass loss (TML) measurements in Figure 8.2 for tests performed at 14 m/s impingement with 500 mg/L sand indicate that three of the four inhibitors are capable of reducing the degradation rate from that in the uninhibited environment. The maximum inhibitor efficiency recorded was 82%, achieved with 100 ppm of Inhibitor D, which reduced the mass loss from 30.4 mg to 5.5 mg. Inhibitor A produced an increase in the mass loss of carbon steel from 30.4 mg to 39.4 mg at 14 m/s, while in static conditions this inhibitor exceeded 98% efficiency. The increase in degradation rate observed in Figure 8.2 will be discussed in due course based on the *in-situ* electrochemical response of the material in this environment.

Under such severe conditions, it is perhaps surprising to observe such large reductions in mass loss. However, SIJ tests conducted by Neville and Wang [118] at 20 m/s with 500 mg/L sand on carbon steel in CO_2 environments also showed that the third generation of corrosion inhibitors are capable of significantly reducing the level of degradation by well over 50%. Considering that results presented here are for the same sand concentration and a lower test velocity, a reduction of 80% seems comparatively realistic.

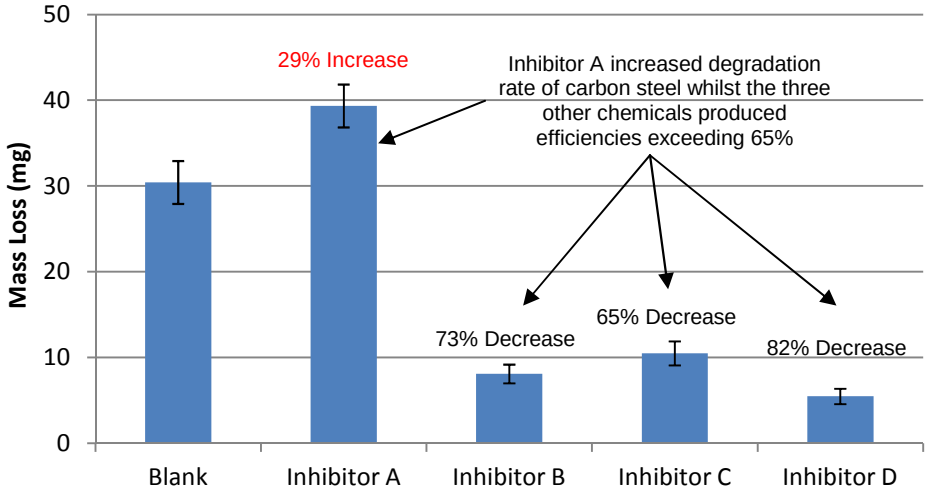

Figure 8.2: Mass loss results for four inhibitors after SIJ tests. Test conditions were: 14 m/s, 45°C, 500mg/L sand and CO_2-saturated at 1 bar

The erosion-corrosion degradation mechanism is obviously far more severe at 14 m/s with 500 mg/L sand than tests in static solutions and those performed at 7 m/s

in Chapter 7. The pure erosion within the system will undoubtedly contribute significantly to the degradation rate as a result of increased impingement velocity. In this situation, the damage caused to the surface is considerably more than purely an electrochemical process at the surface. An inhibitor is required that is able to mitigate the mechanical damage as well as the dissolution of the material if degradation rates are to be reduced to an acceptable level.

8.5 *In-Situ* Corrosion Assessment

8.5.1 Blank Tests

The Nyquist plot in Figure 8.3 represents that of carbon steel exposed to the blank solution at 14 m/s with 500 mg/L sand. The corrosion rate in the system remained stable throughout the 4 hour test and consequently, only one plot is displayed in the Figure 8.3 for clarity due to the similarity between each impedance plot.

Flow-induced corrosion tests in the blank solution at 7 m/s displayed both capacitance and inductance in the Nyquist plots, with the inductive loop being linked with the presence of Fe_3C on the sample surface. Interestingly, in erosion-corrosion tests at 14 m/s, there was no inductive behaviour present in the Nyquist or Phase plots. The impedance plots could therefore be modelled using the single time constant circuit depicted in Figure 8.3.

When the carbon steel specimens were removed from the SIJ, visual inspection revealed that the black substance identified as iron carbide in tests at 7 m/s was no longer present. It is suggested that any undissolved iron carbide remaining after the preferential dissolution of ferrite was detached from the surface through the high level of shear and/or sand particle impingement. This process would be classed under the mechanism of corrosion enhanced erosion or 'dE_c' as referred to in Equation (8.1).

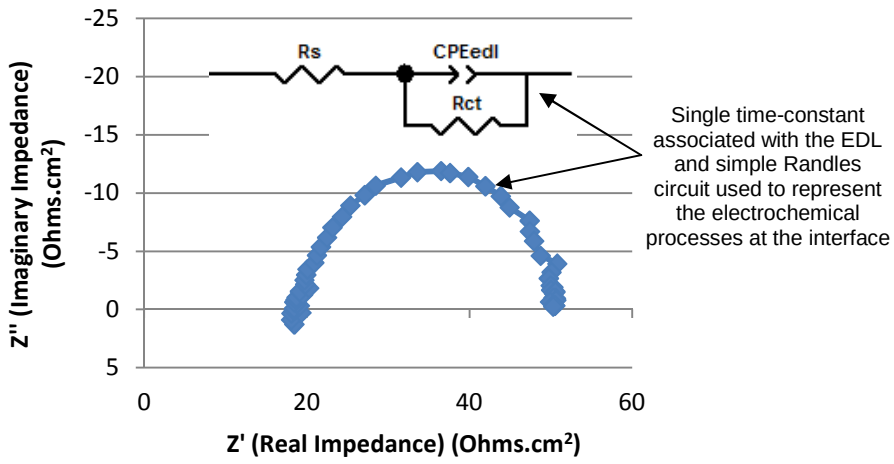

(a)

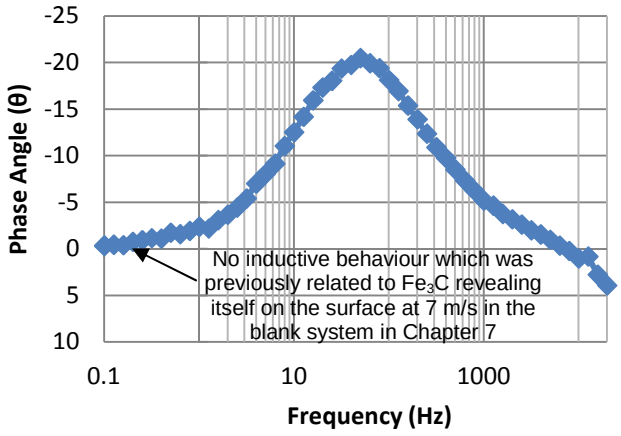

(b)

Figure 8.3: (a) Nyquist Plots and (b) Bode phase plots of the impedance spectra for the blank test using the SIJ along with equivalent circuit used to model the data. Test conditions were: 14 m/s, 45°C, 500 mg/L sand and CO_2-saturated at 1 bar

SEM images of the specimen surface are provided in Figure 8.4. These indicate signs of plastic deformation at the centre of the sample because of the high angles of impact (Figure 8.4(a)). Outside of this central region, a significant amount of cutting occurred on the surface, caused by much lower angles of impingement. In contrast to images at 7 m/s where dissolution of the material surface was clearly visible and few signs of particle impingement were seen, the surface in Figure 8.4 shows a distinct increase in the contribution of erosion. Both images indicate signs of surface roughening, although it is difficult to elucidate whether this is attributed to either the erosion or corrosion process.

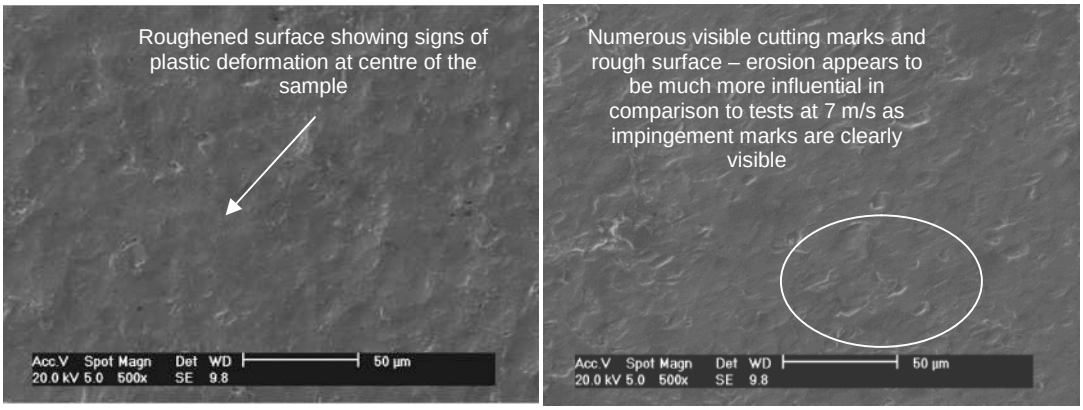

Figure 8.4: SEM images of SIJ sample in blank (a) Zone I - indicating 'light' plastic deformation at the centre of the sample and (b) Zone II – indicating material removal via cutting

The *in-situ* corrosion rates measured by both LPR and AC impedance are provided in Figure 8.5, along with values of resistance calculated by each method and E_{corr} as a function of time. Figure 8.5(a) indicates that the corrosion rate remained relatively stable throughout the test at a value of approximately 14 mm/year. Flow-induced corrosion tests at 7 m/s in Chapter 7 produced an increase in corrosion rate and potential as a result of the presence of Fe_3C. This trend was not apparent in these tests at 14 m/s, suggesting that the severity of the environment prevented the revealing of a Fe_3C network on the specimen surface, agreeing with the visual inspection of the sample which indicated there was no black network on the surface of the sample upon removal from the rig.

Considering Figure 8.5(b), values of corrosion rate determined from LPR and AC impedance agree well with each other, with the LPR technique providing a lower estimate of corrosion rate based on average values. R_p values used to determine corrosion rate were taken from the LPR measurements after subtracting the solution resistance (R_s) measured using AC impedance. The resistance from AC impedance was calculated by taking the approach suggested by Silverman [212], Aksüt et al. [213] and Lorenz et al. [209] as discussed in Chapter 7. They stated that in the limit of zero frequency, the impedance approaches the DC resistance. Therefore the polarisation resistance (R_p) from the fitted curve was estimated by applying the equation '$R_p = \lim_{\omega \to 0} Z - R_s$' to the model after simulating the behaviour to lower frequencies.

Values of R_p were used along with recorded Tafel slope readings to determine the corrosion rate through the application of Faraday's Law, in exactly the same manner as in Chapter 7.

The difference in corrosion rate between the two methods of approximately 0.5 mm/year shown in Figure 8.5(b) is minor considering that small values of R_p are being measured in this environment. For low values of resistance, only slight changes in R_p are required to cause large changes in corrosion rate because of its inverse relationship with corrosion rate. In these situations, compensating for solution resistance (R_s) is critical.

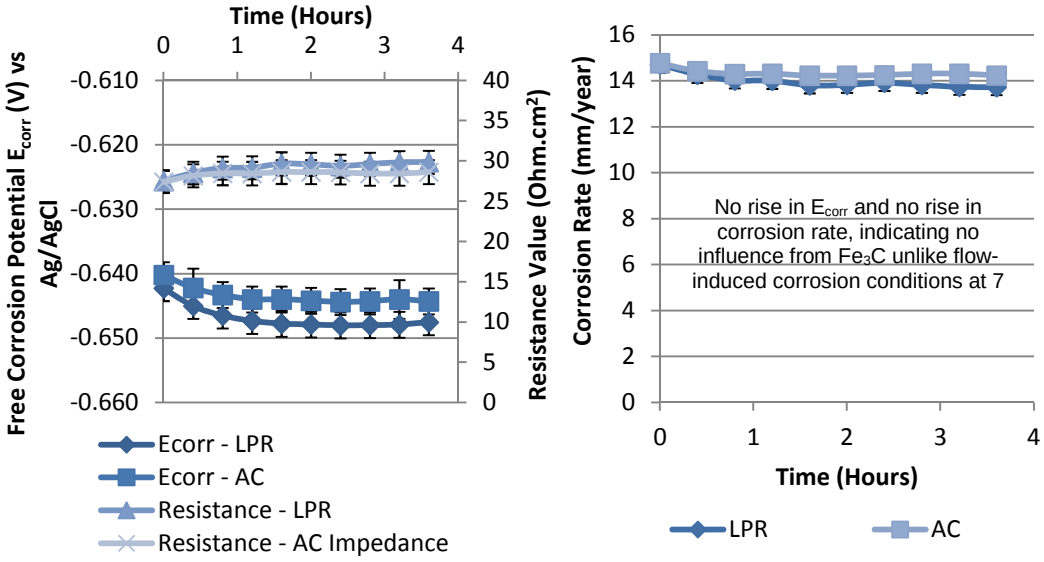

(a) (b)

Figure 8.5: (a) Free corrosion potential and resistance measurements and (b) corrosion rates as a function of time from AC impedance and LPR techniques for the blank test using the SIJ. Test conditions were: 14 m/s, 45°C, 500 mg/L sand and CO_2-saturated at 1 bar

Values of capacitance for the system in Figure 8.6 extracted from the AC impedance measurements remained stable throughout the duration of the test suggesting the composition of the EDL remains unchanged over the 4 hour test, and agreeing with the fact that no Fe_3C network revealed itself on the surface of the material. Experiments at 7 m/s in Chapter 7 showed an increase in capacitance associated with the revealing of a Fe_3C network and this change in capacitance was not observed for the system at 14 m/s impingement.

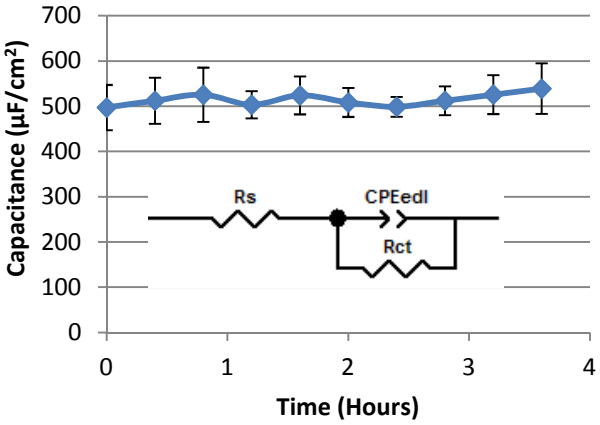

Figure 8.6: CPE_{edl} values from AC impedance for blank test in SIJ. Test conditions were: 14 m/s, 45°C, 500 mg/L sand and CO_2-saturated at 1 bar

The *in-situ* electrochemical analysis combined with SEM images of carbon steel in the blank environment identified that no protective $FeCO_3$ film, nor a Fe_3C network form on the surface of the sample within the four hour period.

In the past, previous authors [138-141, 149, 166] have directed the majority of their attention towards erosion-corrosion environments under scale forming conditions. The research presented in this thesis focuses on non-scale forming conditions and its inhibition due to the low pH and low temperature in which the tests were conducted. In these environments, the synergy which exists between erosion and corrosion is not as significant compared to that witnessed in the presence of a protective iron carbonate film subjected to sand particle impingement [149]. However, in these situations, the steel surface is constantly susceptible to erosion attack as it is not alleviated through the presence of a thick iron carbonate film as seen in previous studies where $FeCO_3$ was found to reduce the mechanical damage to the substrate [8, 149]. The inhibition of the degradation process can consequently be particularly challenging as the inhibitor does not have a corrosion product to assist in mitigating any of the degradation mechanisms.

Ramachandran et al. [159] highlighted that certain inhibitors were able to interact with corrosion products in order to reduce erosion and corrosion processes. Obviously, in this situation this property of the chemical in not available and it is the responsibility of the inhibitor alone to reduce degradation rates to an acceptable level.

8.5.2 Inhibitor A

Gravimetric measurements indicated that the addition of 100 ppm Inhibitor A increased the degradation rate of carbon steel in the erosion-corrosion environment at 14 m/s. In previous studies, the application of this inhibitor at 7 m/s without sand managed to effectively mitigate general degradation, although the chemical did induce localised corrosion on the surface of the sample.

Selected AC impedance measurements for the system as a function of time are provided in Figure 8.7. Nyquist and Bode plots indicate the presence of induction, which is much more pronounced than that observed for the application of Inhibitor A at 7 m/s. It is likely that the inductive behaviour is linked to the instability of the inhibitor film as observed by Neville et al. [118] who suggested that the adsorption/desorption process of the chemical may be linked to inductive loops.

The equivalent circuit used to model the AC impedance data for this system is provided in Figure 8.7(a). The same circuit was adopted for tests performed at 7 m/s using this chemical, which contains two time constants consisting of one capacitive and one inductive loop.

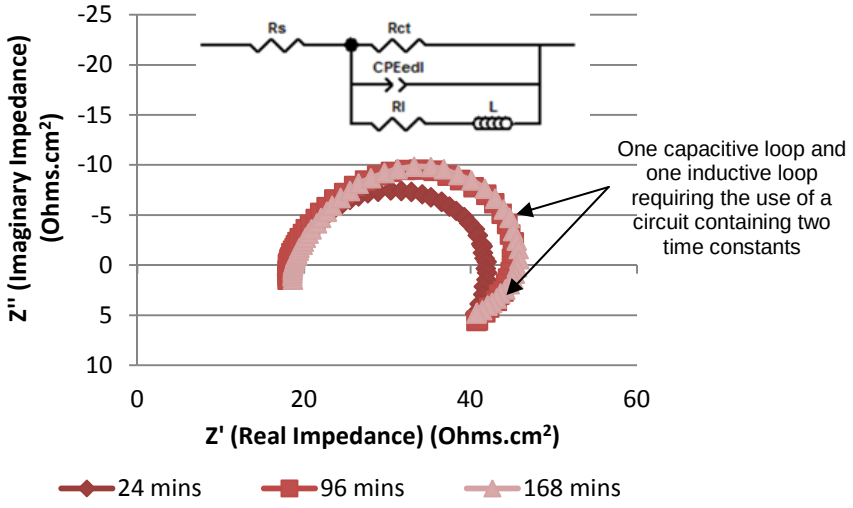

(a)

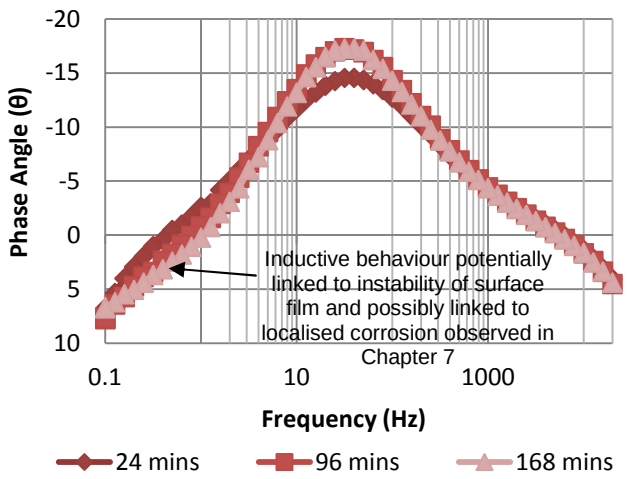

(b)

Figure 8.7: (a) Nyquist Plots and (b) Bode phase plots of the impedance spectra for the addition of 100 ppm Inhibitor A using the SIJ along with equivalent circuit used to model the data. Test conditions were: 14 m/s, 45°C, 500 mg/L sand and CO_2-saturated at 1 bar

Values of R_p from the AC measurements were determined by simulating the frequency response down to zero using the Zview™ software as demonstrated in Figure 8.8. The solution resistance was subtracted from these resistance values and subsequently used to determine the corrosion rate in conjunction with measured Tafel slope values.

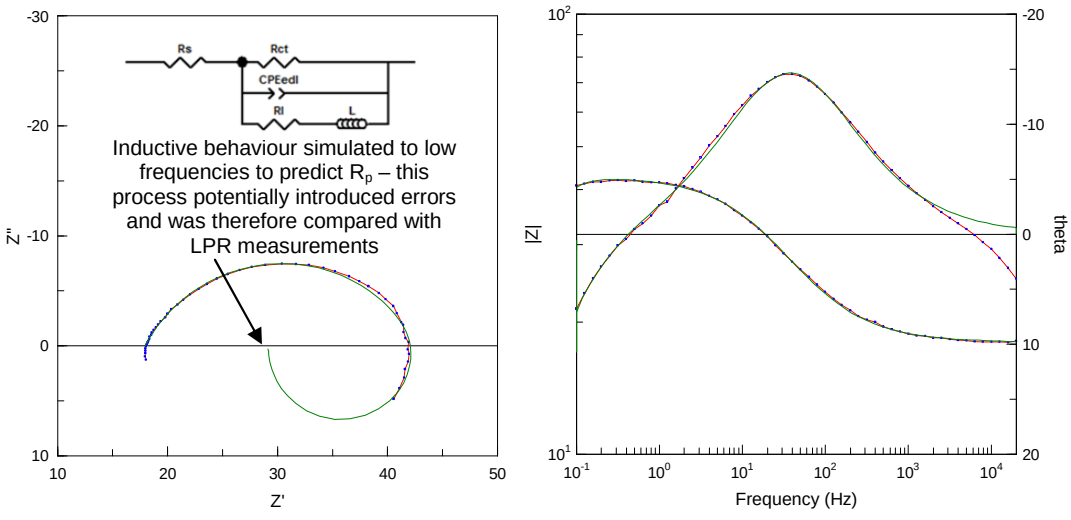

Figure 8.8: Example of simulated data overlaying the Nyquist, Phase and Bode plots down to low frequencies to predict R_p; data corresponds to a measurement taken at 24 minutes

The *in-situ* corrosion rates measured by AC impedance and LPR provided in Figure 8.9 show that the inhibitor increases the corrosion kinetics at the surface of the sample as tests in the blank solution only measured corrosion rates of 14 mm/year. Interestingly, a certain degree of disagreement existed between AC and DC techniques in terms of R_p measurement which led to differences in the magnitude of corrosion rate (Figure 8.9(b)). Although the difference in R_p between the two techniques was never greater than 4 Ohms·cm^2 (Figure 8.9(a)), this still had large implications on the difference in corrosion rate because of the size of the values measured. Hence, a difference in 5-7 mm/year was recorded between the two techniques.

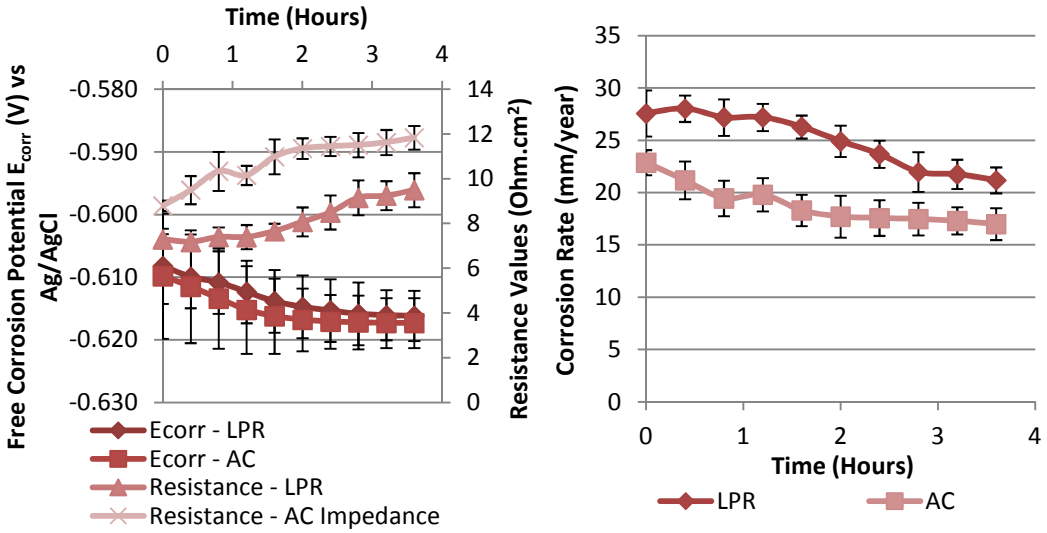

(a) (b)

Figure 8.9: (a) Free corrosion potential and resistance measurements and (b) corrosion rates as a function of time from AC impedance and LPR techniques for the addition of 100 ppm Inhibitor A in the SIJ. Test conditions were: 14 m/s, 45°C, 500 mg/L sand and CO_2-saturated at 1 bar

The presence of induction in the Nyquist plot is believed to contribute to the discrepancy between the LPR and AC impedance measurements. Data was simulated to lower frequencies in order to determine where the Nyquist plot intersects the real axis and hence determine the value of R_p to correlate with the LPR readings. The use of this technique will have undoubtedly introduced errors into the resistance value used to determine corrosion rate. Caution needs to be exercised when using this AC technique in these situations and needs to be compared with another electrochemical or gravimetric method, as in this case.

Addition of Inhibitor A at the start of the test produced a large value of the EDL capacitance (C_{edl}) as shown in Figure 8.10 which has also been observed in inhibition tests by Salasi et. al [218] who attributed the behaviour to an initial reduction in the double layer thickness. Over the duration of the experiment the capacitance value of the EDL decreases to a steady state value. The stabilisation of capacitance coincides with the constant corrosion rate from the AC impedance measurements.

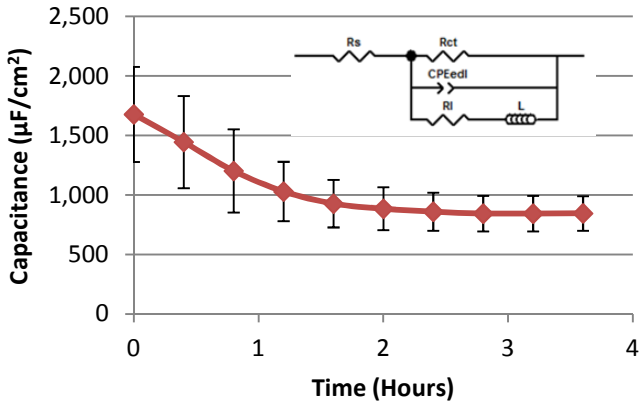

Figure 8.10: CPE_{edl} values from AC impedance for addition of 100 ppm Inhibitor A in SIJ. Test conditions were: 14 m/s, 45°C, 500 mg/L sand and CO_2-saturated at 1 bar

Analysis of the surface using SEM (Figure 8.11) revealed what appeared to be a very rough surface, potentially caused by the high corrosion rate of the sample. There were few signs of particle impingement on the surface of the material, suggesting that corrosion was the dominant material removal mechanism.

Magnussen [153] stated that corrosion inhibitors were capable of having adverse effects on corrosion rate if the chemicals undergo a complex-forming reaction with the surface. According to Donahue et al. [238], the acceleration of corrosion in the presence of organic compounds is related to the oxidative tendency of the surface chelates. If charge transfer occurs with the desorption of a complex ion according to the reaction:

$$[(\mathrm{FeOH}) \bullet \mathrm{Inh_n}]_{\mathrm{ads}} = [(\mathrm{FeOH}) \bullet \mathrm{Inh_n}]^{+}_{\mathrm{sol}} + \mathrm{e}^{-} \qquad (8.2)$$

the additive will undoubtedly act as a stimulator. Tests conducted by Babic-Samardzija et al. [239] indicated an increase in corrosion rate with the application of 4-nitropyrazole (NOP). The formation of a soluble $[FeCl_x\text{-}(OH)_y(NOP)_z]_n$ complex could easily be removed from the surface. The removal of the soluble complex was

clearly detrimental to the surface and perhaps the inductive behaviour observed in this study is related to the desorption process occurring.

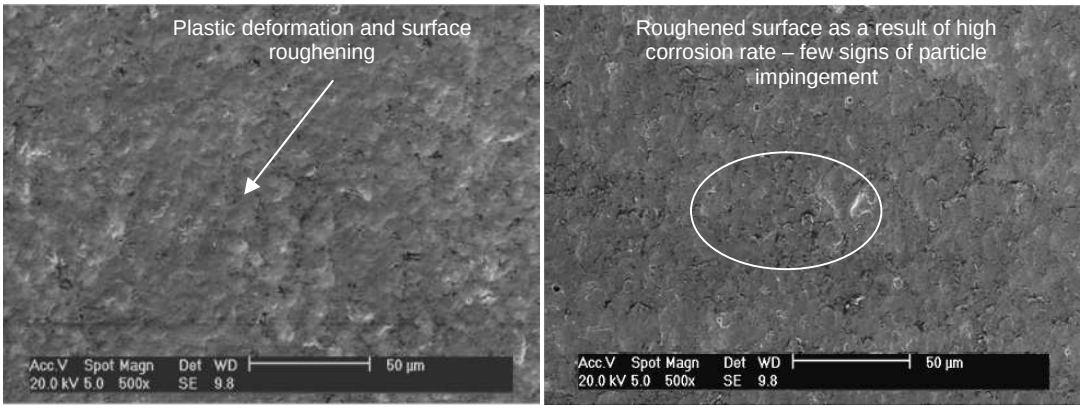

(a) (b)

Figure 8.11: SEM images of SIJ sample using Inhibitor A in (a) Zone I - indicating plastic deformation at the centre of the sample as well as surface roughening and (b) Zone II – indicating a roughened surface, but few signs of erosion on the surface of the sample

8.5.3 Inhibitor B

A typical Nyquist plot for the application of 100 ppm Inhibitor B is provided in Figure 8.12. The plot expresses one clear capacitive loop corresponding to the EDL. The size of the semi-circle is significantly greater than that of the blank solution, indicating a sizeable reduction in the corrosion rate of the carbon steel.

The Nyquist plot for the impedance measurements were represented using a single time constant model as shown in Figure 8.13 which indicates the value of capacitance as a function of time.

Numerous researchers report the existence of two capacitive loops for inhibited carbon steel in CO_2-saturated solutions [38, 163, 198, 215, 216]; one loop corresponding to a protective film on the surface, and the other to the EDL. However, a selection of authors [196, 215, 216] have also found that one capacitive loop is able to characterise the whole system, depending upon the inhibiting molecule, as is the situation for the addition of Inhibitor B.

The appearance of this individual capacitive loop could result from the possibility that in this environment, the inhibitor is only capable of forming a monolayer/bilayer on the surface, and/or the high rate of wall shear stress from the turbulent flow or

particle impingement makes the inhibitor film porous, preventing it from establishing a capacitive loop [216, 217].

It could also be considered that the inhibitor film resistance is much smaller than the charge-transfer resistance [216]. The semi-circle representing the inhibitor film could effectively merge with the charge transfer loop as seen in other studies [198, 216]. Hence, the impedance spectra for the inhibited test can be described using one capacitor in the electrical equivalent circuit.

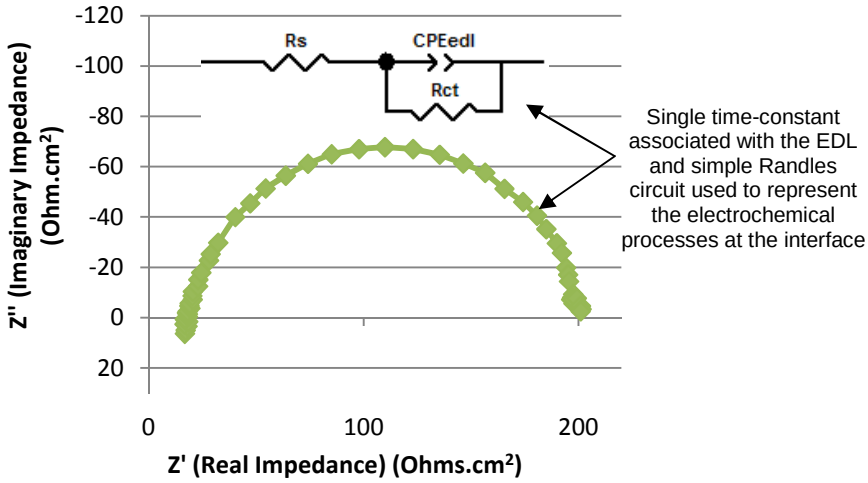

(a)

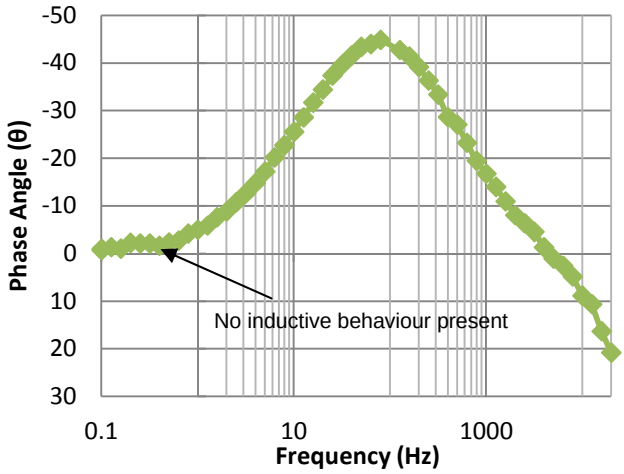

(b)

Figure 8.12: (a) Nyquist Plots and (b) Bode phase plots of the impedance spectra for the addition of 100 ppm Inhibitor B using the SIJ along with equivalent circuit used to model the data. Test conditions were: 14 m/s, 45°C, 500 mg/L sand and CO_2-saturated at 1 bar

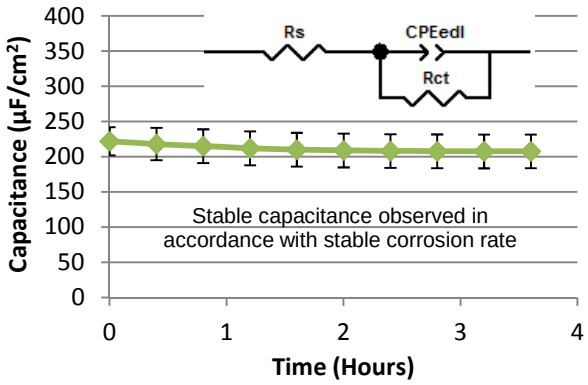

Figure 8.13: CPE_{edl} values from AC impedance for addition of 100 ppm Inhibitor B in SIJ. Test conditions were: 14 m/s, 45°C, 500 mg/L sand and CO_2-saturated at 1 bar

AC impedance and LPR measurements showed a strong correlation with each other as shown in Figure 8.14(a), producing *in-situ* corrosion rates of approximately 1 mm/year which are reflected in Figure 8.14(b).

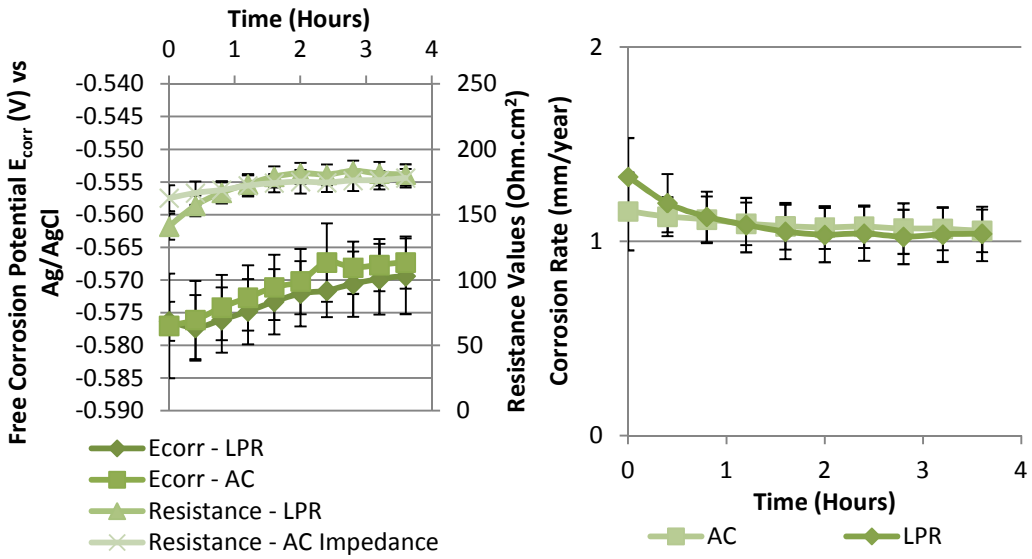

(a) (b)

Figure 8.14: (a) Free corrosion potential and resistance measurements and (b) corrosion rates as a function of time from AC impedance and LPR techniques for the addition of 100 ppm Inhibitor B in the SIJ. Test conditions were: 14 m/s, 45°C, 500 mg/l sand and CO_2-saturated at 1 bar

SEM images (Figure 8.15) of the surface indicated plastic deformation at the centre of the sample. Towards the outer edge of the material surface, the original polishing marks could still be clearly identified. Signs of particle impingement were visible and no corrosion or localised attack could be seen. The microscope observations gave

the impression that the degradation process was dominated by erosion in this regime, which is likely given the large reduction in *in-situ* corrosion rate observed.

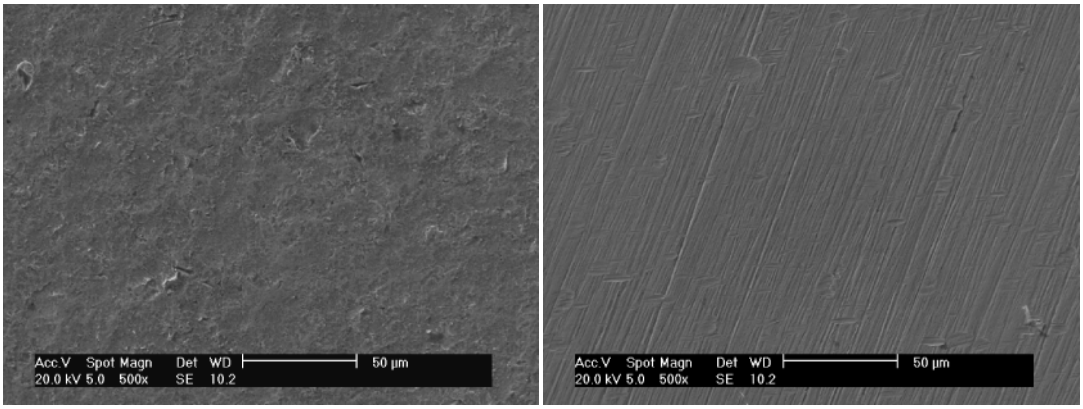

(a) (b)

Figure 8.15: SEM images of SIJ sample using Inhibitor B in (a) Zone I - indicating plastic deformation at the centre of the sample and (b) Zone II – no indication of corrosion on the surface but distinct signs of particle impingement

8.5.4 Inhibitor C

Inhibitor C presented similar *in-situ* electrochemical behaviour to Inhibitor B in that it could be represented by the same equivalent circuit, possessing only a single time-constant as shown in Figure 8.16. Capacitance values reduced marginally throughout the test in conjunction with the corrosion rate (Figure 8.17).

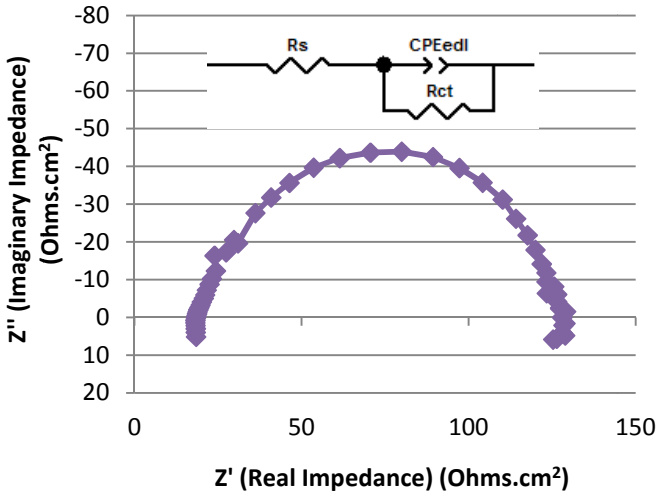

(a)

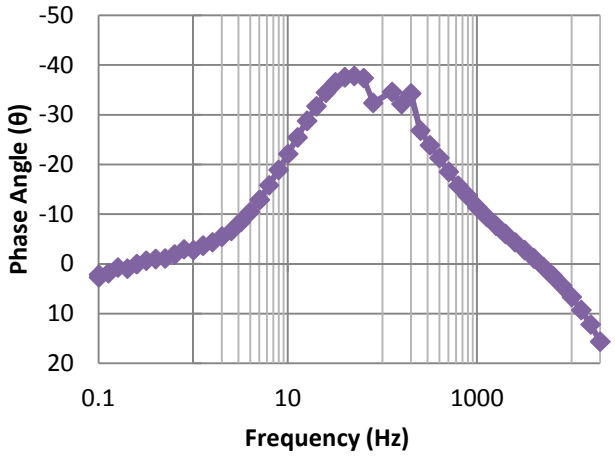

(b)

Figure 8.16: (a) Nyquist Plots and (b) Bode phase plots of the impedance spectra for the addition of 100 ppm Inhibitor C using the SIJ along with equivalent circuit used to model the data. Test conditions were: 14 m/s, 45°C, 500 mg/L sand and CO_2-saturated at 1 bar

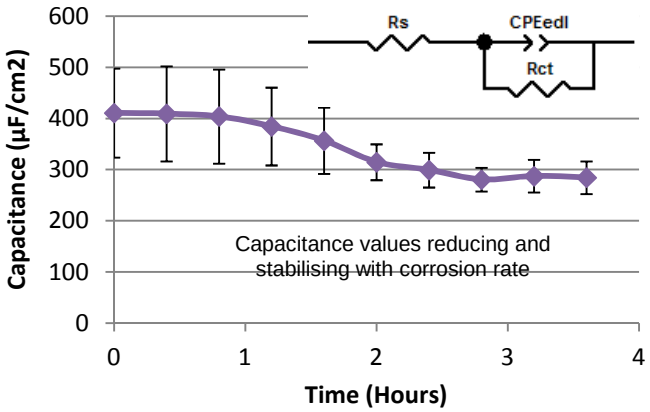

Figure 8.17: CPE_{edl} values from AC impedance for addition of 100 ppm Inhibitor C in SIJ. Test conditions were: 14 m/s, 45°C, 500 mg/L sand and CO_2-saturated at 1 bar

Figure 8.18(a) indicates that Inhibitor C immediately ennobles the potential of the carbon steel sample to around -0.57 V. The potential gradually rises over the test by around 15 to 20 mV, representing similar behaviour to Inhibitor B. Corrosion rates were reduced to below 3 mm/year by the end of the experiment.

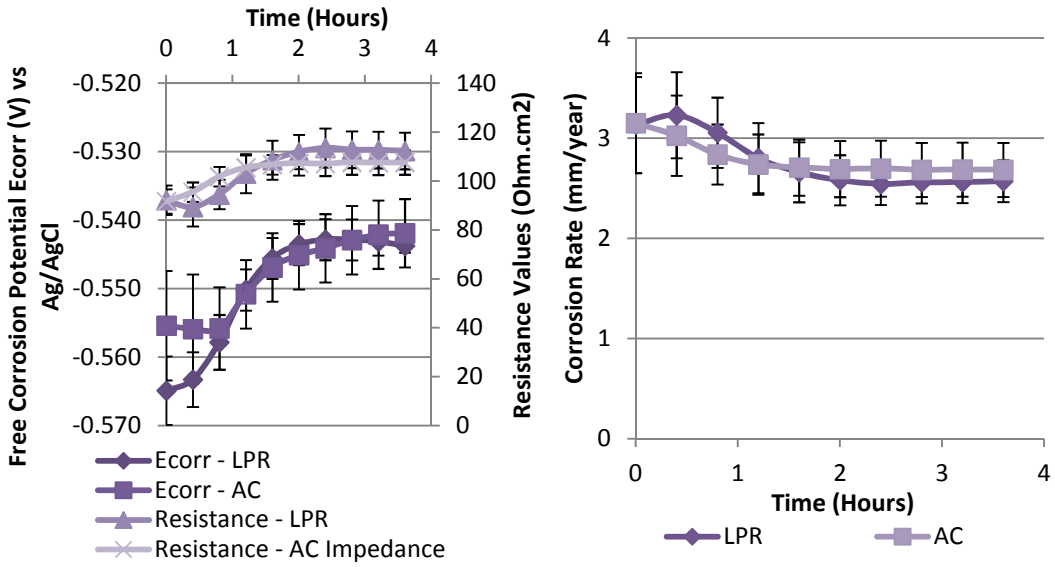

(a) (b)

Figure 8.18: (a) Free corrosion potential and resistance measurements and (b) corrosion rates as a function of time from AC impedance and LPR techniques for the addition of 100 ppm Inhibitor C in the SIJ. Test conditions were: 14 m/s, 45°C, 500 mg/l sand and CO_2-saturated at 1 bar

Inhibitors C also produced SEM pictures comparable to that of Inhibitor B as shown in Figure 8.19. However, the higher *in-situ* corrosion rate resulted in the disappearance of the polishing marks on the specimen surface.

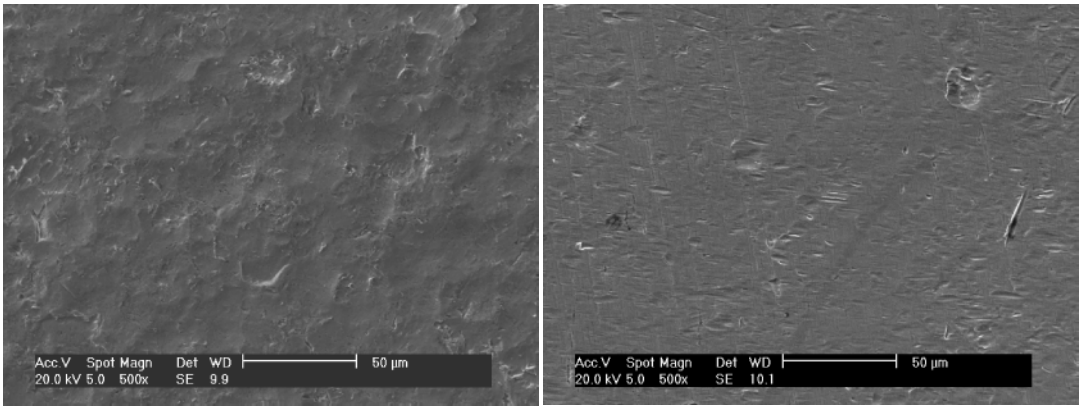

Figure 8.19: SEM images of SIJ sample using Inhibitor C in (a) Zone I - indicating plastic deformation at the centre of the sample and (b) Zone II – distinct signs of particle impingement and reduction in visibility of polishing marks due to corrosion

8.5.5 Inhibitor D – High Shear Resistant Inhibitor

E_{corr} and R_p values as a function of time for the application of Inhibitor D are provided in Figure 8.20. In contrast to Inhibitors B and C, this chemical produced a

very high initial corrosion rate which reduced throughout the first 30 minutes of the test.

The high initial corrosion rate could be attributed to the slow adsorption process of the inhibitor, or possibly be as a result of the reaction between the chemical and the surface which induces the formation of an inhibitor film, but also promotes a high initial corrosion rate [239]. This type of behaviour has been shown to occur with chemicals that form a complex with the metal surface in acidic solutions [239].

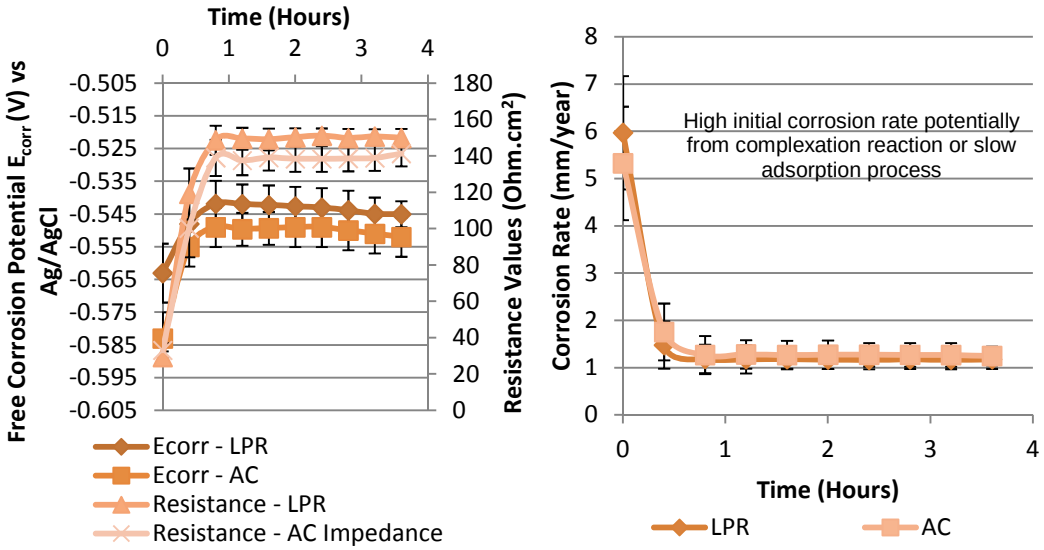

(a) (b)

Figure 8.20: (a) Free corrosion potential and resistance measurements and (b) corrosion rates as a function of time from AC impedance and LPR techniques for the addition of 100 ppm Inhibitor D in the SIJ. Test conditions were: 14 m/s, 45°C, 500 mg/l sand and CO_2-saturated at 1 bar

AC impedance measurements in Figure 8.21 revealed two clear time constants in the Nyquist plots which were visible from the start of the test and became more pronounced throughout the experiment. Figure 8.21 indicates that the progressive separation between the two time constants ultimately becomes very distinct. The behaviour witnessed necessitated the use of an electrical equivalent circuit containing two time constants provided in Figure 8.21(a).

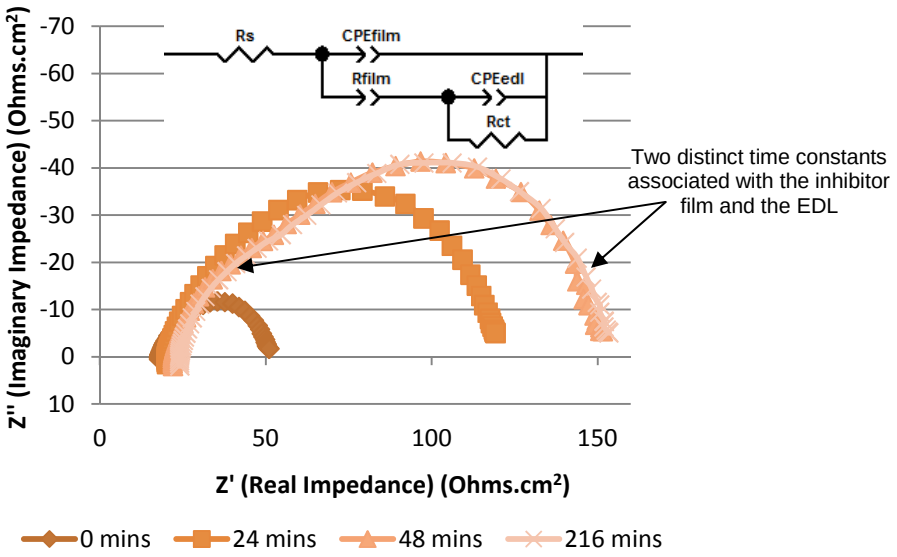

(a)

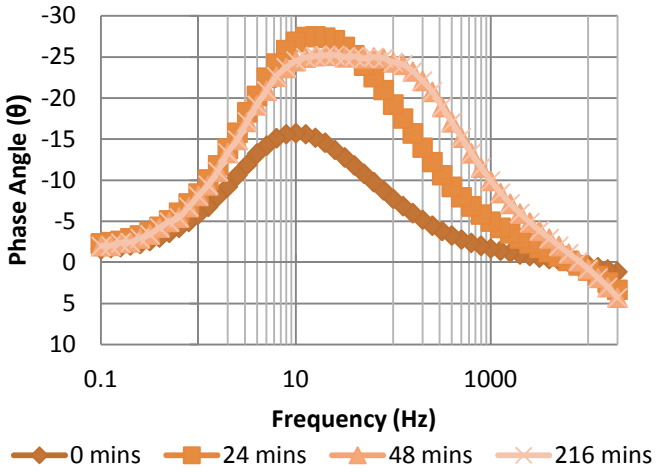

(b)

Figure 8.21: (a) Nyquist Plots and (b) Bode phase plots of the impedance spectra for the addition of 100 ppm Inhibitor D using the SIJ along with equivalent circuit used to model the data. Test conditions were: 14 m/s, 45°C, 500 mg/L sand and CO_2-saturated at 1 bar

The plots provided in Figure 8.22 indicate the goodness of fit of the model proposed and show the presence of the two time constants more clearly.

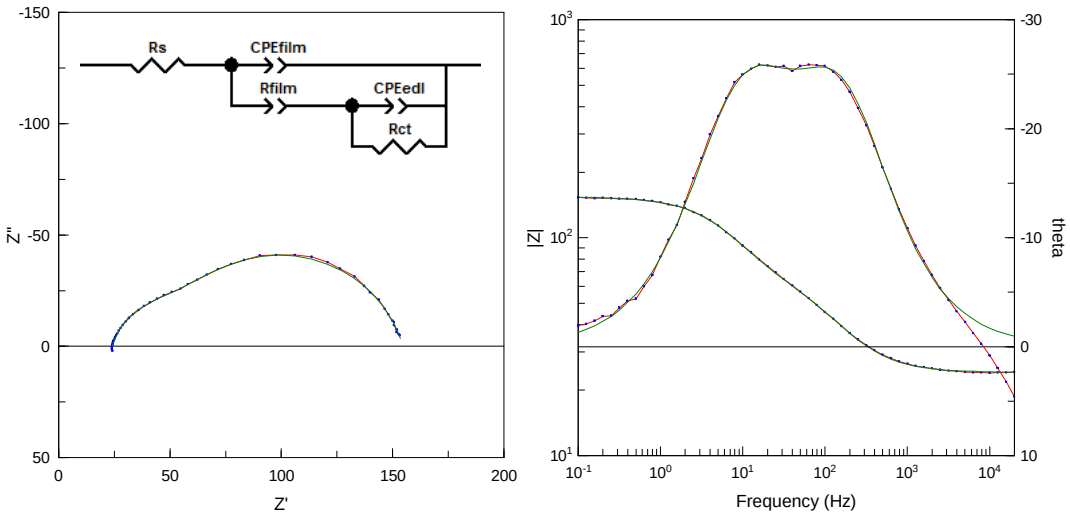

Figure 8.22: Example of fitted data overlaying a Nyquist plot for 100 ppm Inhibitor D; data corresponds to a measurement taken at 216 minutes. Test conditions were: 14 m/s, 45°C, 500 mg/L sand and CO_2-saturated at 1 bar

Corrosion, coating and diffusion processes are not always associated with the same frequency range in Nyquist plots. By considering the capacitance values of each loop and their frequency positions, it was possible to identify the mechanisms corresponding to each part of the impedance plot.

The lower frequency loop in Figure 8.21 is the larger of the two semi-circles, possessing a capacitance of approximately 500 µF/cm^2. Values of this order of magnitude tend to be more closely related to the EDL when surface adsorption occurs in conjunction with corrosion [38]. Interestingly, the higher frequency capacitive loop produces an even lower capacitance of 140 µF/cm^2. Based on the concept by Tait [38] that inhibitor filming/coating processes usually occur at higher frequencies than corrosion processes and considering that this inhibitor is renowned for its film forming characteristics, it is reasonable to assume that the high frequency loop represents the inhibitor film properties and the low frequency loop corresponds to the EDL behaviour (the corrosion process). Additionally, it has been reported that the dielectric constant of organic coatings is significantly less than that of water. Constants for inhibitor coatings have been reported as being between 4 and 8 [240], whilst water at 45°C is just below 70 [241], suggesting that a lower capacitance of the inhibitor film compared to the EDL would be expected in light of the fact that the capacitance value is directly proportional to the dielectric constant.

Capacitance values for the EDL and inhibitor films recorded as a function of time are provided in Figure 8.23(a). A sharp decrease in capacitance of the EDL (CPE_{edl}) is observed in the first hour in Figure 8.23(a). This can be attributed to the reduction in sample area in direct contact with the electrolyte as the inhibitor film forms [198, 242]. Conversely, the inhibitor film increases its active area over the first hour resulting in an increase in film capacitance (CPE_{film}). This initial increase is followed by a small decline in film capacitance over the remaining 3 hours of the test. An explanation for this was offered by Bommersbach et al. [242], who attributed the decline of capacitance in their readings to an increase in the film thickness over the experiment. It is important to note that there is a continual increase in the film resistance (R_{film}) throughout the duration of the test. Therefore the reduction in film capacitance is most likely not attributed to a reduction in surface coverage of the inhibitor, as this would promote a decrease in the film resistance.

Interestingly, throughout the AC impedance measurements, it was observed that there was an increase in solution resistance (R_s) from approximately 18 to 25 $Ohms.cm^2$. This increase (presented in Figure 8.23(b)) was not witnessed with the application of Inhibitors A to C. Magnussen [153] explained that inhibition may be partially caused by the presence of Ohmic potential drops because of the formation of poorly conducting films on the surface of the substrate. This helps to reinforce the theory of the formation of a protective film on the metal surface.

Additionally, AC impedance studies by Park et al. [229] indicated that the growth of a porous magnetite film on the surface of carbon steel in high temperature chloride solutions produced an increase in solution resistance.

However, it must be considered that another explanation for the increase in solution resistance is that the inhibitor works partly by removing aggressive ions from the environment which would also reduce the solution conductivity [153].

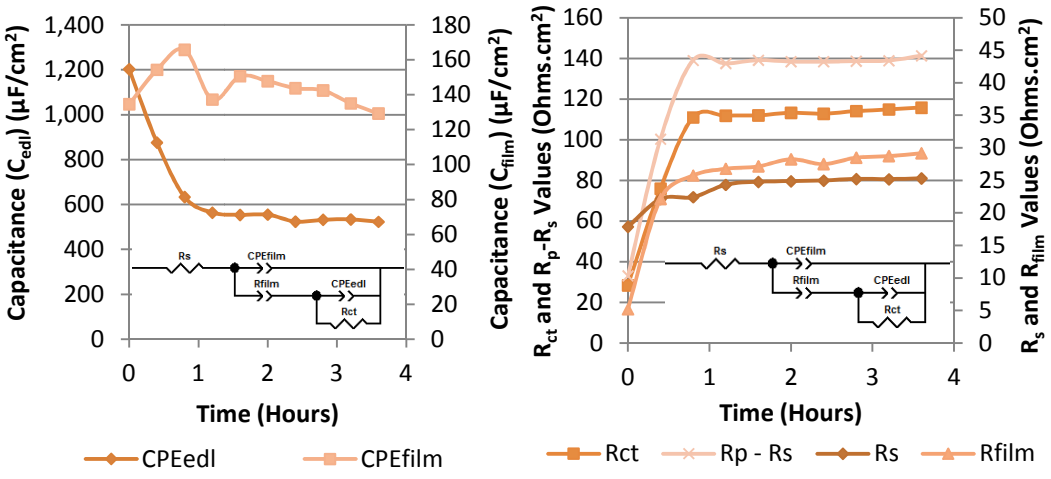

(a) (b)

Figure 8.23: (a) Capacitance values of EDL and inhibitor film from AC impedance for addition of 100 ppm Inhibitor D in SIJ (b) Resistance values for the EDL, inhibitor film, polarisation resistance and solution resistance, all from impedance measurements. Test conditions were: 14 m/s, 45°C, 500 mg/L sand and CO_2-saturated at 1 bar

The application of Inhibitor D produced distinct signs of film formation by producing an almost clear orange/brown film on the material surface. Upon inspection of the sample under SEM, there were signs of light plastic deformation at the centre of the test specimen (Figure 8.24(a)). Outside of this region, signs of particle impingement were very difficult to locate (Figure 8.24(b)).

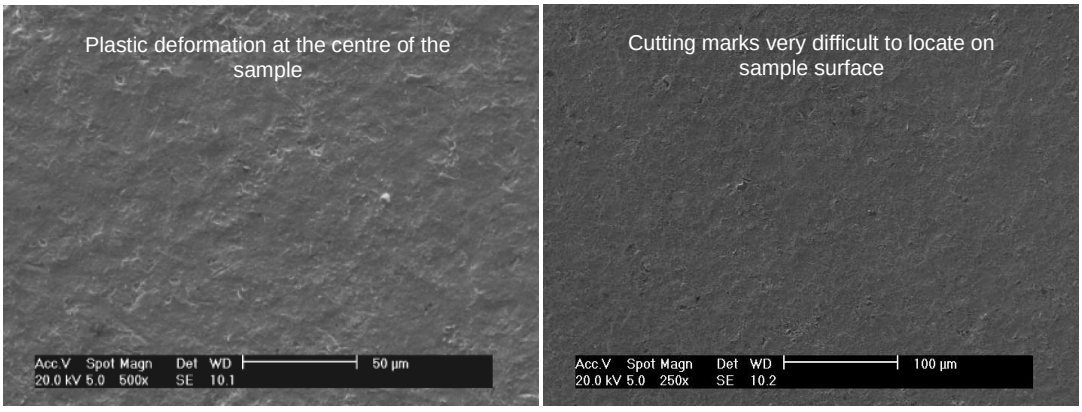

Figure 8.24: SEM image of SIJ sample using Inhibitor D in (a) Zone I – plastic deformation at the centre of the sample and (b) Zone II – very little indication of erosion damage toward outer edge of the surface

8.6 Erosion and Corrosion Components of Mass Loss

By recording both the total mass loss and the corrosion rate from *in-situ* electrochemical measurements, it is possible to examine the contribution of erosion

components (E + dE_C) and corrosion components (C + dC_E) towards the total degradation rate as shown in Figure 8.25.

All inhibitors reduced the *in-situ* corrosion rate by over 75% with the exception of Inhibitor A which caused an increase in corrosion rate. Based on the average values obtained, all inhibitors were able to reduce the damage attributed to erosion. However, when considering the error bars, only Inhibitor D was able to conclusively reduce the contribution of erosion damage. This is perhaps counter intuitive as it may be expected that a corrosion inhibitor would work by reducing the 'C' or 'dC_E' components of damage.

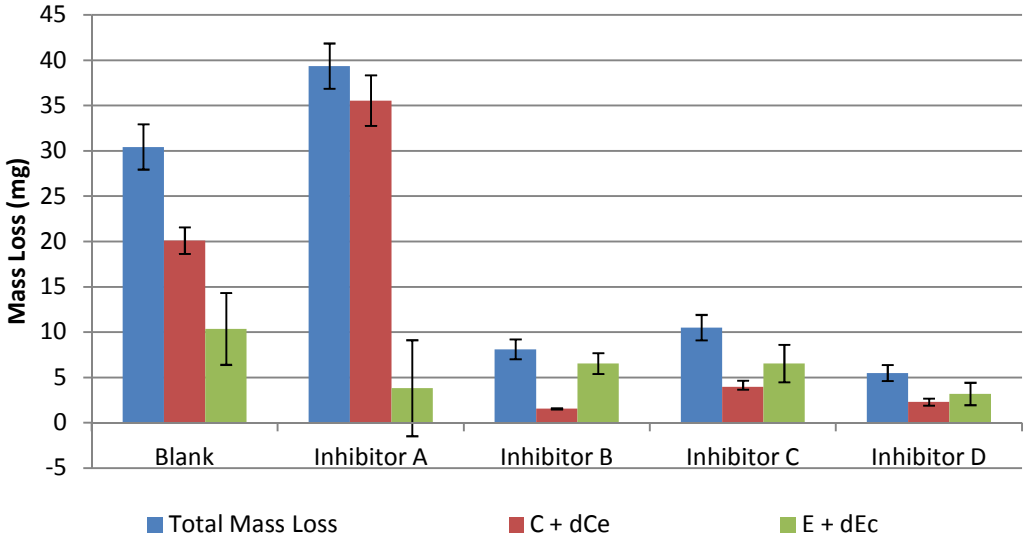

Figure 8.25: Influence of Inhibitors A to D on total mass loss, erosion component (E + dE_C) and corrosion component (C + dC_E). Test conditions were: 14 m/s, 45°C, 500 mg/L sand and CO_2-saturated at 1 bar

The ratios of erosion to corrosion damage in Figure 8.26 indicate that the blank system and the addition of Inhibitor A produce a corrosion dominant environment, while carbon steel in the presence of Inhibitors B to D comprised of 60-80% erosion because of the suppression of the corrosion process.

Reviewing the relative contributions of erosion and corrosion in this manner for the blank environment is important. Determining the dominant mechanism in the system can help to identify the best approach towards mitigating the effects. If the degradation mechanism were dominated by erosion, perhaps selecting a more erosion resistant material would be a better approach as opposed to the use of corrosion inhibition.

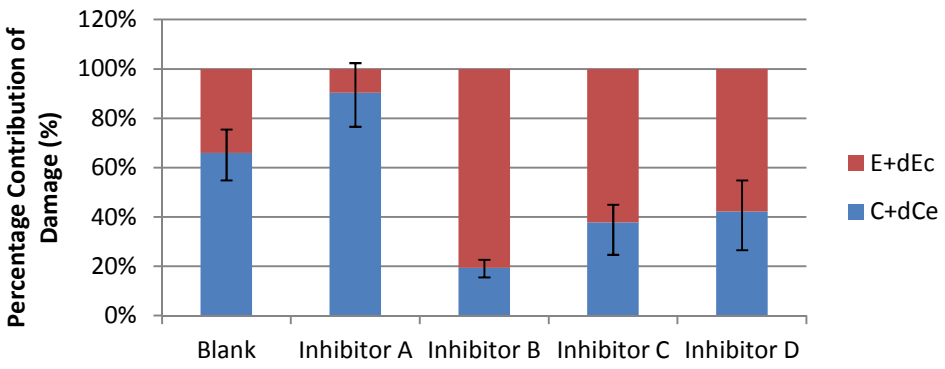

Figure 8.26: Percentage contribution of corrosion and erosion in jet impingement tests. Test conditions were: 14 m/s, 45°C, 500 mg/l sand and CO_2-saturated at 1 bar

8.7 Surface Profilometry using Talysurf

Surface profilometry of the carbon steel samples exposed to 14 m/s flow in the presence of 500 mg/L sand was conducted using a Talysurf 120L. 3-D profiles of the samples were taken and three examples are provided in Figure 8.27(a) – (c) for the blank system and the application of Inhibitors A and B, respectively.

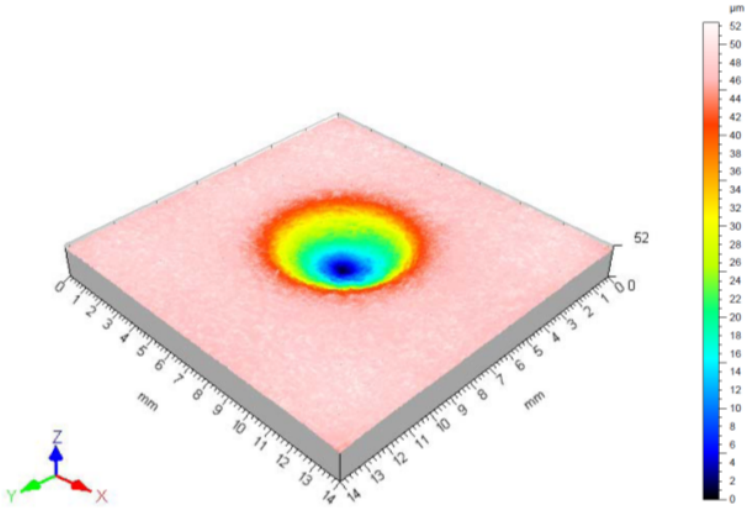

(a)

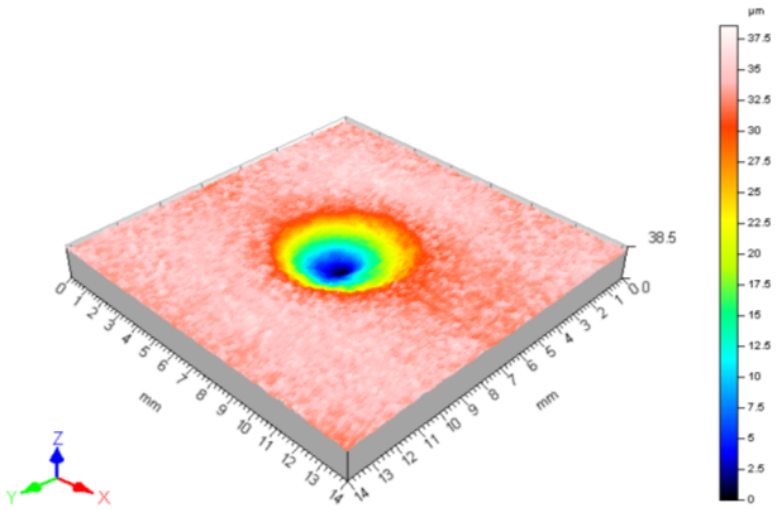

(b)

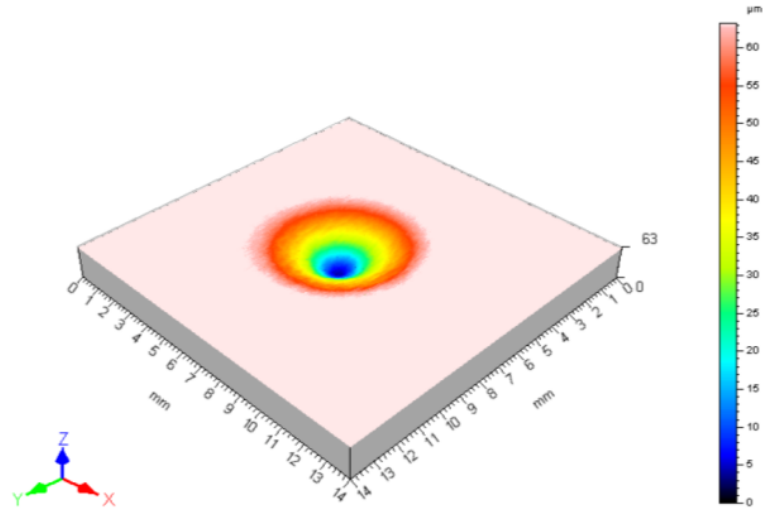

(c)

Figure 8.27: Example of a 3-D profile of the carbon steel sample exposed to SIJ in the presence of (a) No Inhibitor (b) Inhibitor A (c) Inhibitor B. Test conditions were: 14 m/s, 45°C, 500 mg/l sand and CO_2-saturated at 1 bar

Surface profilometry results indicated quite a dramatic difference in the texture of the outer region of the wear scar. Inhibitors B to D appeared smoother on the profilometry images (extremely similar to Figure 8.27(c)). Inhibitor A produced a visibly rougher surface than in the blank solution (Figure 8.27(a)-(b)).

To confirm these observations, roughness measurements were extracted from the profilometry data outside of the wear scar. The roughness measurements are indicated in Figure 8.28 and interestingly, they correlate well with the observed *in-*

situ corrosion rates. This data suggests that the reduction in corrosion rate may be at least partly attributed to the ability of the inhibitor to reduce surface roughness or maintain a low surface roughness. The role of a smooth surface in reducing turbulent intensity of the local flow is a feature of inhibitors which has been previously highlighted. Schmitt [243] showed that the drag reducing properties of corrosion inhibitors can be derived from surface roughness. Similar to the well known fact that the length and height amplitude of sand waves at the sea shore corresponds to the size and turbulence of the waves, it can be assumed that the roughness pattern of a metal surface under flow-induced corrosion or erosion-corrosion should correspond to the size of turbulent eddies and vortices in the near-wall flow region [243].

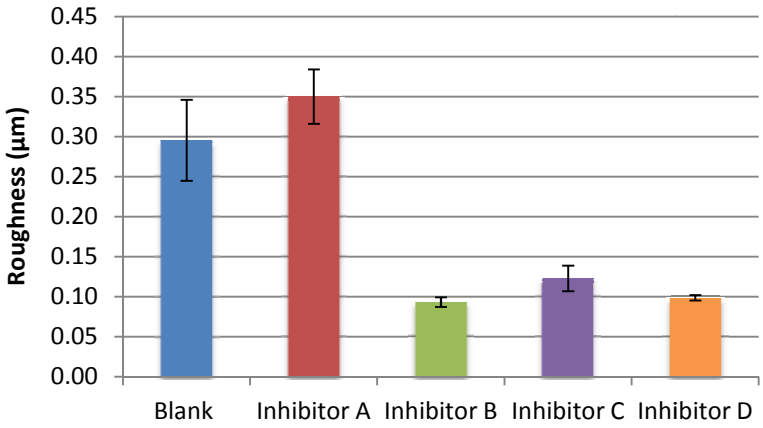

Figure 8.28: Surface roughness measurements of Zone (III) with different inhibitors

To ensure comparability between all roughness measurements, a Gaussian filter was applied to the data with a 0.8 mm cut off (Figure 8.29). Two examples of the roughness profile extracted from the sample are provided in Figure 8.30.

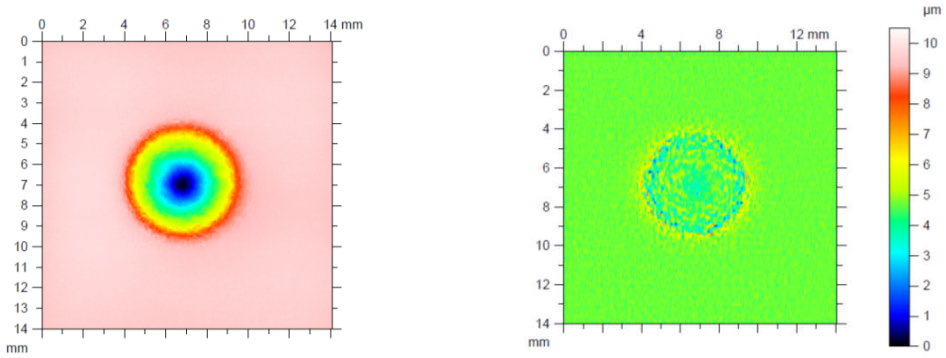

(a) (b)

Figure 8.29: Specimen profile (a) before and (b) after the application of a Gaussian filter with 0.8 mm cut off for Inhibitor C

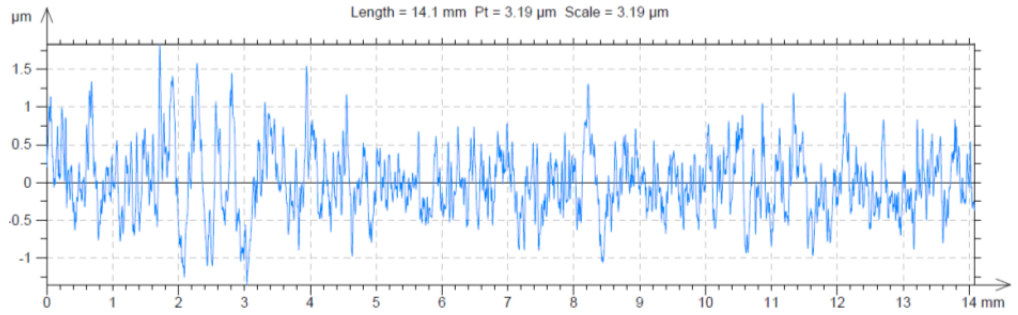

(a)

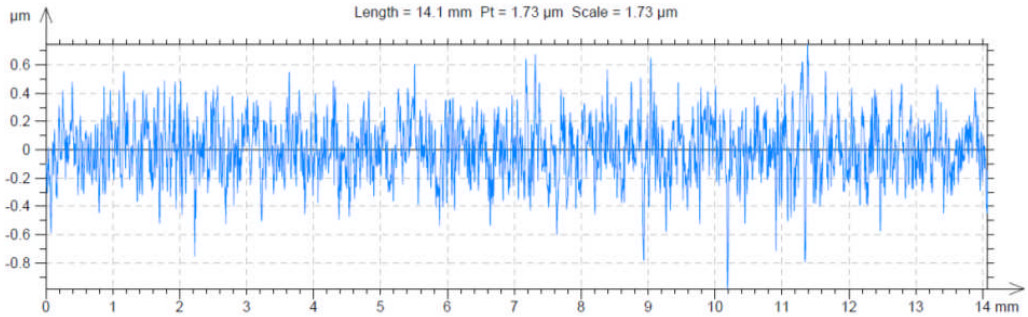

(b)

Figure 8.30: Roughness profile extracted from the surface of the sample for (a) Inhibitor A and (b) Inhibitor C

3D profilometry produced a cross-sectional image for each specimen consisting of a worn inner region and a flat outer region degraded from predominantly flow-induced corrosion with a small degree of particle impingement. These defined regions have previously been characterised [165]. It was possible to extract 2D profiles from the 3D images to observe the cross-section of the samples.

Figure 8.31 is a schematic representation of the surface cross-section showing that the gravimetric measurements comprise mass loss from a general thickness loss shown in the red hatched area plus the groove created predominantly by the impinging sand (blue hatched area). The mass loss attributed to the blue hatched area is measured post-test by contact profilometry where a volume loss divided by a density gives the equivalent mass loss. The difference between this and the gravimetric mass loss is the general thickness loss. Whether the inhibitors reduce the general thickness loss of the material or the impact zone volume enables their mechanisms to be better understood. The penetration depth for each profile was also measured with respect to the height of the outer region after the jet impingement test using the profilometry software. The mass loss data enables the general thickness and hence, the total penetration depth to be determined as indicated in Figure 8.31. The penetration depths are shown in the 2D profiles provided in Figure 8.32 which account for the general thickness loss.

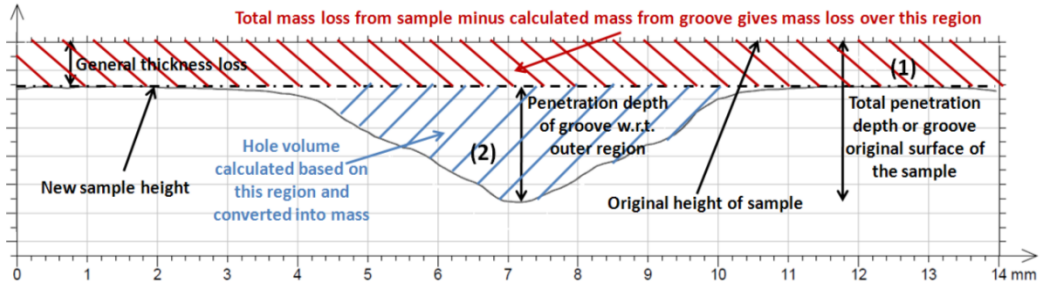

Figure 8.31: 2-D schematic representation of sample cross-section indicating depths and regions of general thickness loss and groove caused by impinging sand

The ability of Inhibitor D to reduce the erosion component is reflected not only in the mass loss results, but also in the 2D profile. By comparing the profiles in Figure 8.32, it is clear that Inhibitor D is capable of significantly reducing the total penetration depth of the sample, promoting a decrease from approximately 57 µm to 27 µm, a reduction of 52%. Although Inhibitor A was able to reduce the penetration depth, it came at the expense of a very high *in-situ* corrosion rate (discussed later). Inhibitors B and C produced profiles which interestingly appeared to increase the penetration depth of the sample from the blank condition on average. The average depths recorded, along with the range of errors associated with each measurement are highlighted in Figure 8.33. These results suggest that the application of Inhibitors B and C do not conclusively increase the penetration depth of the test specimen, however, an average increase is observed when using these chemicals.

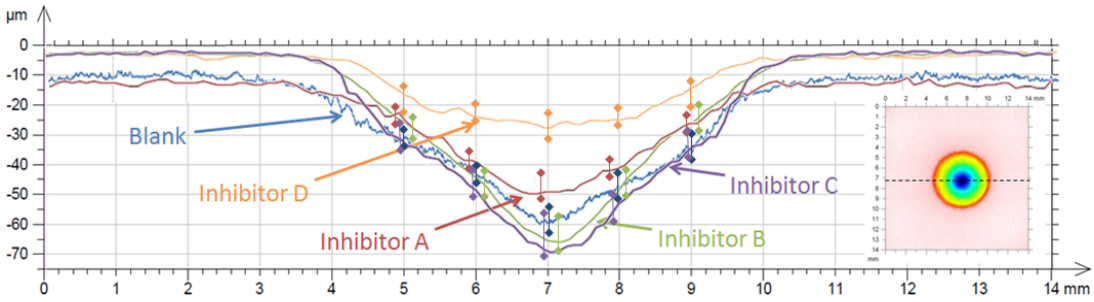

Figure 8.32: 2D profiles extracted from the 3D images of test specimens under the application of Inhibitors A-D. Test conditions were: 14 m/s, 45°C, 500 mg/l sand and CO_2-saturated at 1 bar

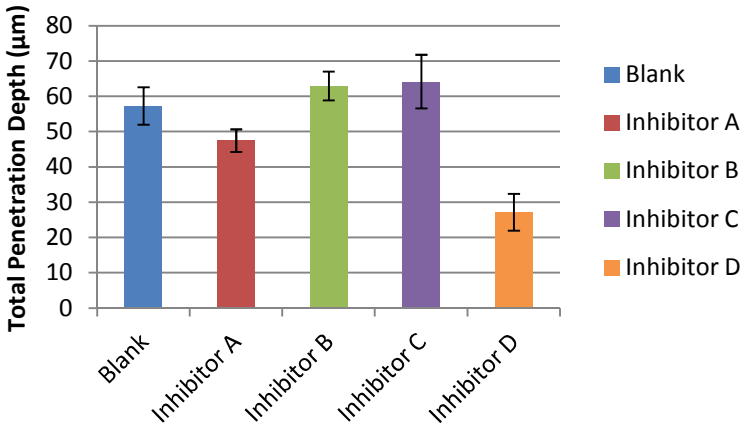

Figure 8.33: Total penetration depth of wear scar on carbon steel samples from SIJ tests under the application of Inhibitors A-D. Test conditions were: 14 m/s, 45°C, 500 mg/L sand and CO_2-saturated at 1 bar

8.8 Review of Inhibitor Efficiencies

Figure 8.34 presents a review of the efficiencies of each inhibitor, considering how effectively they were able to reduce the total penetration depth, the total mass loss and the *in-situ* corrosion rate.

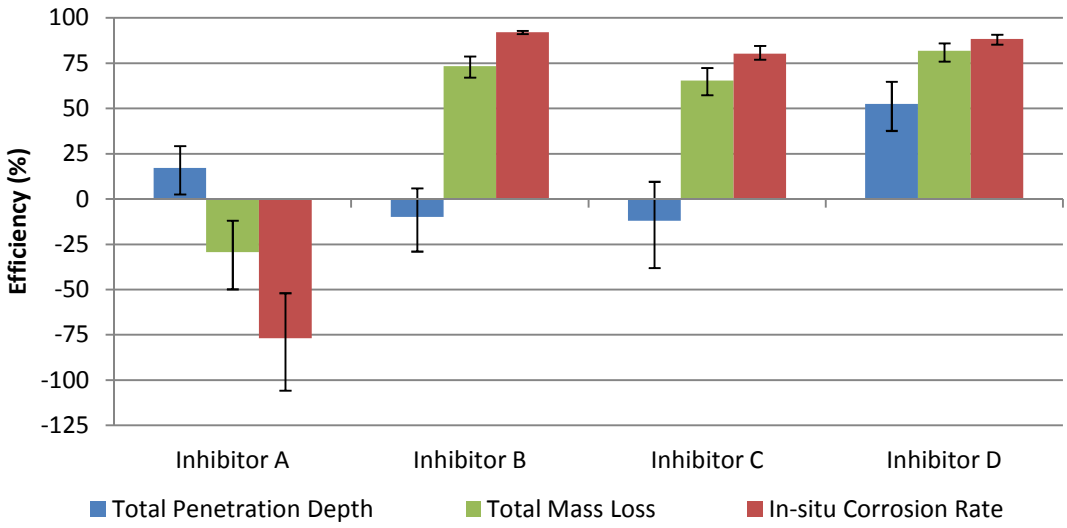

Figure 8.34: Efficiencies of Inhibitors A to D based on reduction (or increase) in total depth, general thickness and total mass loss

Based on the information collated, Inhibitor A reduced the penetration depth but resulted in an increase in the corrosion kinetics at the surface of the sample. The application of Inhibitor B prevented the sample from corroding the most effectively, producing a clean surface after the test. Inhibitor B also took effect very quickly, producing a low corrosion rate from the very start of the test. This suggests that even if the inhibitor film is disrupted by particle impingement, it regenerates quickly afterward, minimising the effects of corrosion attributed to erosion (dC_E).

The penetration depth of the sample appeared to increase with the application of Inhibitors B and C from that of the blank solution, although this increase was not significant on the whole. A possible explanation as to why an increase in penetration depth was observed could be a result of the effective corrosion inhibition properties of the two chemicals combined with their inability to reduce pure erosion. Levy [104, 105] stated that a certain amount of 'conditioning' (plastic deformation and creation of lips etc.) is required before material is removed from the surface of samples. It is plausible that the continual high corrosion rate at the centre of the sample in the blank environment is reducing the extent of conditioning on the surface of the sample and reducing the level of material removal as a result of the formation of lips etc. which are subsequently removed through further impingement.

The reduction in corrosion rate at the centre of the sample for the application of Inhibitors B and C would theoretically leave the material exposed to more plastic deformation, and hence a greater profile depth.

One of the most important observations is that the total mass loss bares no correlation with total penetration depth. In a scenario whereby the performance of these chemicals is validated through gravimetric measurement, Inhibitor B would be one of the most efficient chemicals. Additionally, the implementation of electrochemistry in this environment would also suggest that Inhibitor B would be a suitable candidate.

It must be noted that the penetration rates will ultimately determine when failure of pipework would occur in these tests. It is plausible than a situation could develop in an oil and gas system whereby a semi-protective $FeCO_3$ film is unable to form on the surface because of increased severity of hydrodynamic conditions or successive particle impingement. It is then the responsibility of the inhibitor to offer protection to the exposed, bare surface of the steel from erosion-corrosion. This behaviour has been seen in flow loop tests performed on a carbon steel elbow within a flow loop by Shadley et al. [139], whereby tests with 4.0 wt.% sand at above 5 m/s caused complete removal of any protective film on the surface.

An inhibitor is needed that will create a film on the surface which is able to minimise the damage attributed to particle impingement. Based on the results of this research, Inhibitor D controls the degradation most effectively.

Schmitt [243] stated that certain inhibitors are capable of interacting with the active sites of crystal growth during corrosion product formation, yielding scales with smaller crystal sizes, lower porosities and higher fracture stresses and strains. This ultimately makes the steel surface more resistant to high shear and sand particle impingement. Research has also indicated that inhibitors can incorporate into the corrosion product layer and form a protective barrier against erosion [244]. However, there is no formation of corrosion product ($FeCO_3$) in this particular environment for the inhibitor to interact with. It is therefore the responsibility of the film generated by Inhibitor D to withstand the erosion subjected to the surface.

It is clear that further work is required to determine the properties and thickness of the inhibitor film formed on the surface, however, this study has highlighted the feasibility for certain chemicals to be able to mitigate the effects of erosion as well as corrosion.

8.9 Surface Hardness Measurements

To understand the effect of particle impingement on the surface, hardness measurements were conducted inside and outside the wear scar for tests in blank conditions and in inhibited tests with Inhibitors B and D. According to Hutchings [89], material at the eroded surface can strain hardened by the repetitive impact of sand particles. As a result of the strain hardening, the deformed surface can be significantly harder than that of the bulk material.

Figure 8.35 shows the effect of strain hardening for specimens subjected to erosion-corrosion conditions inside and outside of the wear scar. The box plots provided show the results from 50 indentations performed both inside and outside the worn region.

Hardness measurements performed on the outer edge of the specimen showed similar results irrespective of the inhibitor applied. Measurements performed on the wear scar indicated that the hardness of the surface in this region exceeded that of the outer region on average for all three samples.

Inhibitors B and D were examined in this section because they produced the most interesting results. Inhibitor B failed to reduce the erosion component of damage significantly, but was the most efficient chemical in terms of reducing the *in-situ* corrosion rate. In contrast, Inhibitor D was the most efficient chemical at reducing the erosion component of damage.

The level of hardness can be related to the degree of work hardening on the surface of the material. However, in this environment, a corrosion process is also occurring at the interface of the material which needs to be considered. As discussed previously, Inhibitor B produced a large penetration depth and also exhibits the highest hardness within the wear scar, which is to be expected considering the fact that the material corrosion rate is low, leaving it more susceptible to plastic deformation. The lowest hardness values within the wear scar were measured for the application of Inhibitor D, which produced mean values of hardness only slightly higher than that recorded outside of the wear scar. Values for the hardness of the specimen in the blank environment fell half way between that of the two inhibitors. The results indicate that the level of corrosion in the blank system reduced the level of plastic deformation at the centre of the sample. The high plastic deformation seen at the centre of the Inhibitor B sample is a result of almost no corrosion occurring on the surface of the sample, allowing the material to be subjected to significant plastic deformation. The box plots also highlight that the film

formed from the addition of Inhibitor D is able to reduce the level of plastic deformation at the centre of the sample. It can be postulated that this film is capable of adsorbing the impact energy of the sand particles and alleviating the mechanical damage caused to the substrate.

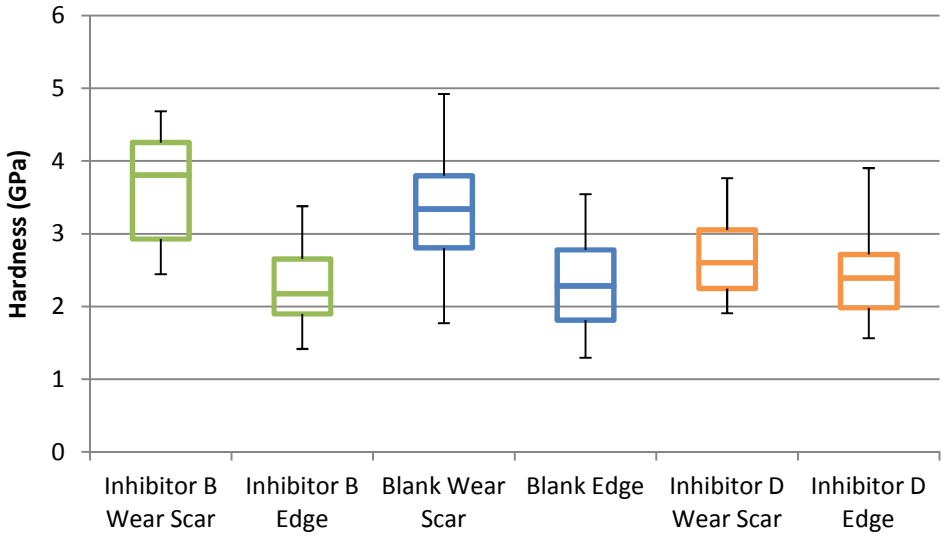

Figure 8.35: Hardness measurements performed inside an outside of the wear scar for erosion-corrosion specimens with the application of Inhibitor B and D in comparison to the blank environment

8.10 Inhibitor Adsorption onto Sand

The loss of corrosion inhibitor through adsorption onto the sand surface is believed to be a potential risk for certain chemicals [112]. This process results in a depletion of inhibitor from the liquid phase and as the quantity and surface area of sand in pipeline systems increases, there is an increasing removal of inhibitor from the process fluid, which presents the possibility of a detrimental reduction in inhibitor performance [112, 245].

However, the adsorption of sand particles onto the surface of samples can potentially have beneficial effects. Both Hassani et al. [170] and Neville and Wang [118] suggested that certain inhibitors are capable of adsorbing onto the surface of sand particles, changing their path movement in pipework flow, thus affecting the dynamics of impact and potentially reducing erosion rates.

McMahon et al. [246] examined the effects of sand and interfacial adsorption loss on corrosion inhibitor efficiency. Three inhibitor chemistries were studied and were all found to have reduced performance in the presence of sand, although the chemistries were commercially sensitive.

Ramachandran et al. [157] used optical microscopy to take a depth profile of a grain of silica sand. The results indicated that the profile was more irregular than expected from a sphere or octahedron. They concluded that the irregular shape of sand particles produced a surface area 2.6 and 1.8 times greater than that of a sphere or octahedron, respectively, indicating the potential for large reductions in bulk inhibitor concentration if the active chemicals possessed a strong affinity for the sand surface.

These findings prompted an investigation as to whether Inhibitors A to D adsorb onto the surface of sand particles, which may suggest another mechanisms by which these chemicals reduce the degradation attributed to erosion-corrosion.

Sand was removed from the rig at the end of erosion-corrosion tests by sieving the solution. The particles were rinsed thoroughly with distilled water, allowed to dry and analysed under the FT-IR spectrometer.

The neat chemicals were also scanned under the spectrometer and the resulting spectra are provided in Figure 8.36. Commercial sensitivity prevented that the exact chemistry of these compounds from being known, making it impossible to identify which peaks are attributed to each molecule. However, the peaks seen at 2925 (stretching) and 2855 (bending) cm^{-1} are typical of CH_2 stretching [247, 248].

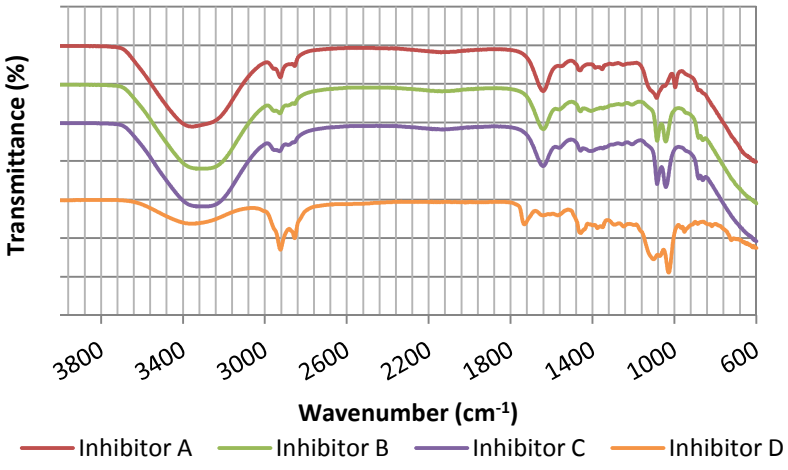

2925 cm^{-1}	CH_2 asymmetrical stretching	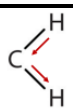	[247, 248]
2855 cm^{-1}	CH_2 symmetrical stretching	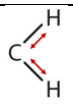	[247, 248]

Figure 8.36: FT-IR spectra for neat Inhibitors A to D along with assigned vibration bonds of interest

Five spectra for the sand surfaces are provided in Figure 8.37. Two of the four inhibitors (A and D) were detected on the surface of the sand through the CH_2 vibration frequencies. Inhibitors B and C produced no trace on particles and these readings were reproducible in three scans performed on the particles.

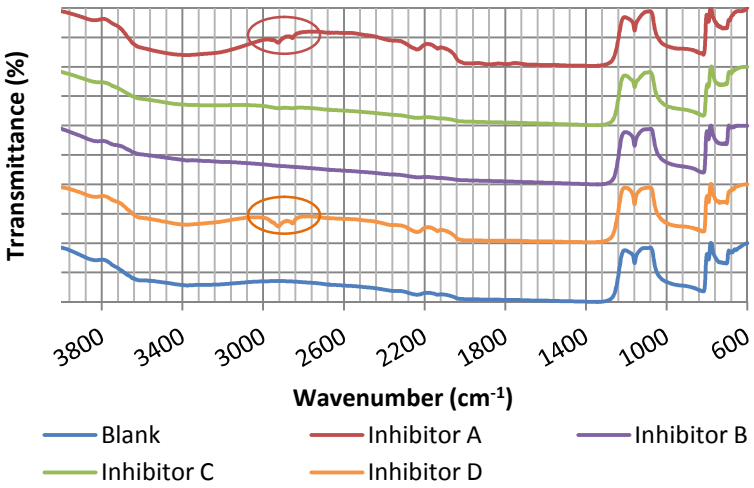

2925 cm^{-1}	CH_2 asymmetrical stretching	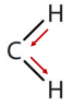	[247, 248]
2855 cm^{-1}	CH_2 symmetrical stretching	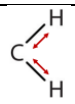	[247, 248]
1160 cm^{-1}	SiO stretching		[249, 250]
794 cm^{-1}	SiO bending		[249, 250]

Figure 8.37: FT-IR spectra for sand particles taken from erosion-corrosion tests along with assigned vibration bonds of interest

To determine whether the inhibitors were capable of reducing the effects of pure erosion, tests were conducted in a N_2-saturated solution at 14 m/s with 500 mg/l sand and 100 ppm inhibitor. Results in Figure 8.38 indicate that only Inhibitors A and D were capable of reducing the erosion damage when error bars are taken into account. Either the formation on the inhibitor film on the surface of the sample, the adsorption of the chemical onto the sand or a combination of these factors has allowed these two inhibitors to reduce pure erosion.

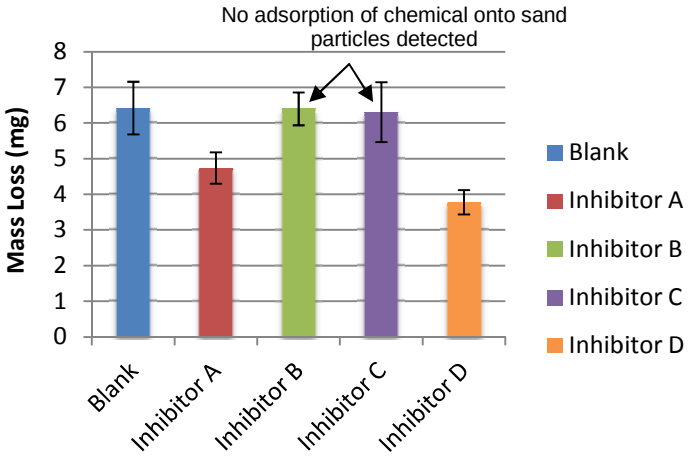

Figure 8.38: Influence of inhibitor on pure erosion in N_2-saturated solution; Test conditions were 14 m/s, 500 mg/l sand and 100 ppm inhibitor

It is worth noting that by saturating the solution with nitrogen, the environmental conditions are changed dramatically from that of a CO_2 environment. Therefore the reduction of pure erosion seen here may not be representative of the real system at lower pH. The tests performed here, however, show it is possible for some chemicals to not only reduce corrosion, but the effects of pure erosion as well.

Small variations in pH can easily influence the efficiency of the inhibitor and its film-forming capabilities. Firstly, the inhibiting species often exhibit pH-dependant solubility. In addition, the structure of the film and morphology may also depend on the pH. Secondly, deprotonation of organic inhibitors is a frequent occurrence in adsorption and film-forming processes which results in comparable pH effects.

8.11 Conclusions

A series of jet impingement tests have been conducted on carbon steel in an erosion-corrosion environment to evaluate the performance of four commercially available inhibitors in controlling the level of degradation. Gravimetric measurements, *in-situ* electrochemistry and surface profilometry were applied to understand the various mechanisms by which inhibitors reduce degradation in erosion-corrosion environments. Based on the research conducted, the following conclusions can be made:

- The application of *in-situ* electrochemistry can allow the contribution of erosion and corrosion components to be determined for systems in which both phenomena occur. Developing an understanding of the level of contribution and being able to quantify the contribution of each component is

important to help operators determine how to mitigate degradation rates effectively.

- The application of AC impedance is a useful tool for identifying the film forming characteristics of corrosion inhibitors, as well as the *in-situ* corrosion rate in the system

- By examining the contributions of erosion and corrosion towards the total degradation rate, this research has highlighted the capability of certain chemicals to reduce not only the corrosion processes in erosion-corrosion, but the influence of the erosion component as well.

- Surface profilometry of specimens is an important aspect of inhibitor evaluation in erosion-corrosion environments when the erosion component of damage is considerably large. Results here have indicated that gravimetric measurements and the application of *in-situ* electrochemistry can potentially be misleading when determining chemical efficiencies.

- Results indicated that certain chemicals may be able to reduce the pure erosion component of damage significantly through film formation.

- The adsorption of corrosion inhibitors onto sand particles was detected through FT-IR measurements. This process could potentially help in the reduction of erosion damage by absorbing a proportion of the impact energy of the sand particles when they impinge onto the carbon steel surface, or by altering the path of the particles in the flow. However, this process also has the negative effect of reducing the bulk concentration of the chemical, and potentially the corrosion inhibition efficiency.

Chapter 9 - Understanding Components of Corrosion Inhibitors and Developing Residual Analysis Techniques

9.1 Introduction and Chapter Outline

Practical inhibitor formulations tend to combine a variety of different components which tend to be a mixture of cathodic and anodic species. The simultaneous use of various inhibitors often results in more efficient inhibition than the individual effects of the components, resulting in what can be termed as ‘synergistic effects’.

These effects depend strongly on not only the types of chemicals combined, but also on the ratio. The positive synergy indicates chemical interactions between the different inhibitors, such as co-operative adsorption, or bulk chemical reactions between the species, leading to the formation of protective layers [153].

In this Chapter, the components of Inhibitor B are reviewed in an effort to understand the synergistic effect occurring within corrosion inhibitor blends and to determine which components are the most influential in the inhibition process in a particular environment.

Based on the mass loss results obtained from a systematic experimental matrix, the main synergist and most active chemical in the blend is determined. The adsorption process of this particular ‘active ingredient’ is elucidated through the implementation of adsorption isotherms and the attachment mechanism of the molecule to carbon steel is identified using a combination of surface analysis techniques and information from existing literature.

A colorimetric technique is tailored for residual analysis purposes and used in conjunction with *in-situ* corrosion rate measurements in static conditions. The technique is tested to verify whether it can monitor residual inhibitor concentration in saline solutions with dissolved CO_2 present, and if the detection technique works in the presence of the other chemical components found in Inhibitor B.

Finally, tests are performed with and without the presence of sand in the system to identify whether or not the active ingredient adsorbs onto the surface of sand particles and if it influences the residual concentration and *in-situ* corrosion rate.

An outline of this Chapter is provided in Figure 9.1.

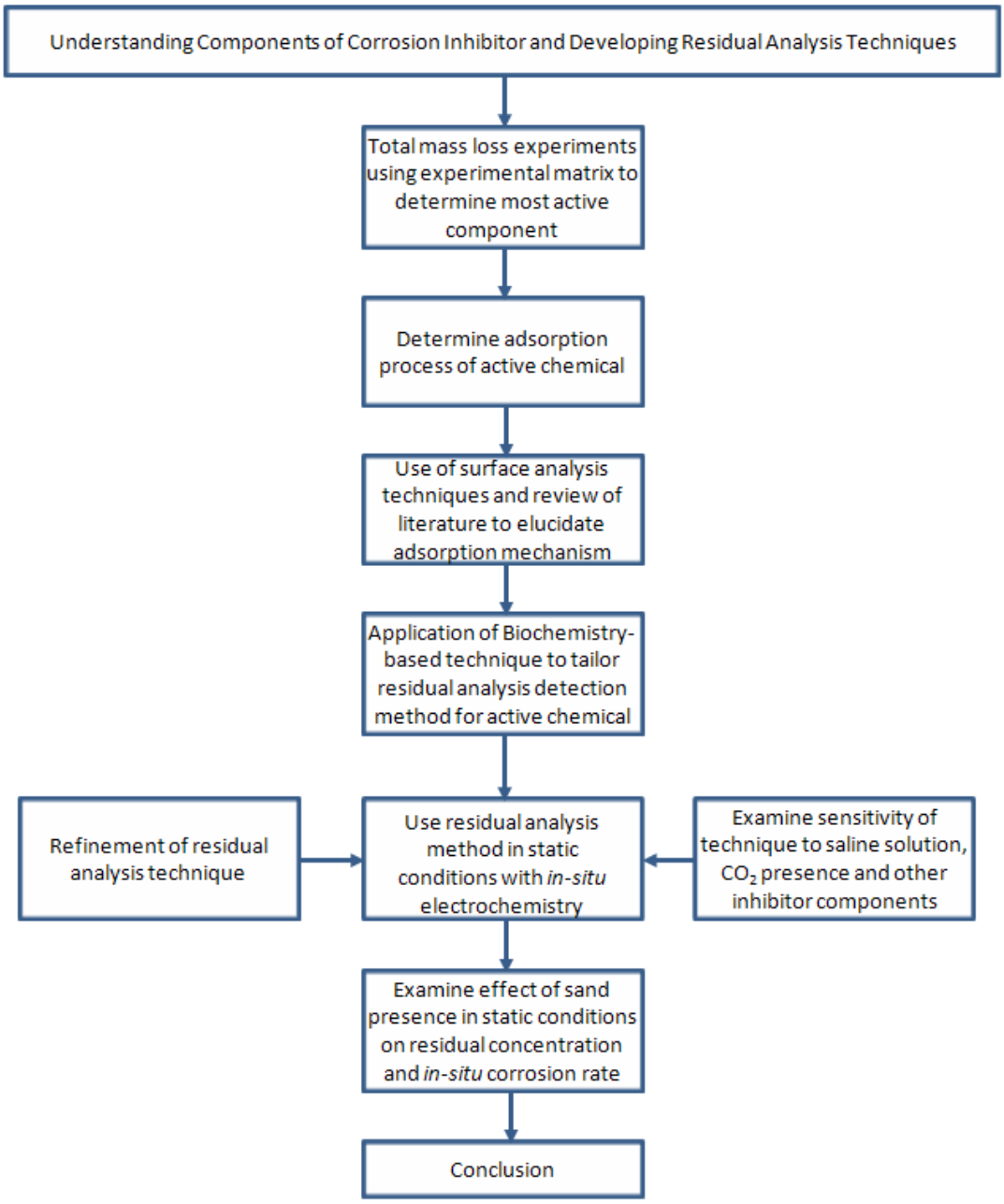

Figure 9.1: Outline of Chapter 9

9.2 Common Organic Oil and Gas Corrosion Inhibitors

An organic corrosion inhibitor can be classified as anodic, cathodic, or both (ambiodic) depending on how they influence metal potential and reaction processes. The chemical structure of the inhibitor molecules is one of the governing factors, determining how effectively a compound will inhibit a system [154]. Combining structures can create a chemical which is more effective than either chemical alone. The adsorption of organic inhibitors on metal surfaces is often

associated with heteroatoms such as nitrogen, oxygen, sulphur and phosphorous within the structure of the molecule [251, 252].

Oil and gas corrosion inhibitors generally have a surfactant molecular structure comprising a charged polar 'head' joined to a long chained alkyl group (e.g. C_{16}-C_{18}) [253]. The charged polar head of the molecule attaches itself to the anodic/cathodic sites on the corroding steel surface. The hydrophobic 'tail' then extends out into the solution which can reduce the corrosion of the steel and lend itself to the co-adsorption of oil, producing a hydrophobic film. Solubility is considered to be one of the most important properties of the inhibitor, allowing the chemical to be effective at very small concentrations [248].

In light of the fact that Inhibitor B proved to be the most efficient chemical blend evaluated in Chapter 7, a selection of its components were considered for individual evaluation.

Although the formulation is commercially sensitive, the generic structure of the components in Inhibitor B which were considered are provided in Table 9.1, along with a summary from literature about their adsorption behaviour.

Table 9.1: Generic constituents of Inhibitor B

Carboxylic Acids and Anhydrides	
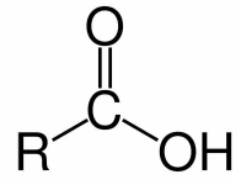 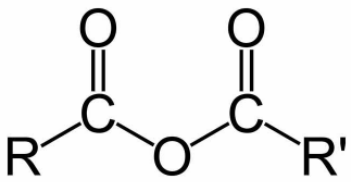	Research has shown that carboxylate compounds are effective corrosion inhibitors in aqueous solutions through the formation of an organic film [152]. The carboxyl group in the compounds can easily bond with Fe^{2+} on the steel surface through a complexation reaction. These organic compounds can adhere to the surface through a coordination bond. Carboxylate and carboxylic acids undergo chemisorption and tend to be mainly anodic type inhibitors [254].
It has been suggested that the inhibition process of succinic anhydrides occurs through a 'salt-like' incorporation of the inhibitor into the carbonate/bicarbonate corrosion product [253]. Durnie et al. [253] believed that succinic anhydrides hydrolyse to a dicarboxylic acid when added to acidic brines. They then react at the surface with Fe^{2+}	

and/or Fe^{3+} produced at the anodic sites to form iron carboxylate compounds [253].

Quaternary Ammonium Salts

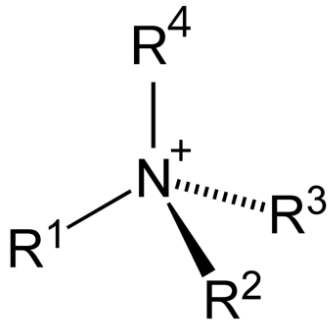

Quaternary ammonium salts which possess long hydrocarbon chains are typical cationic surfactants which possess a high solubility in oil. The nitrogen atom typically collects with four carbon atoms to carry a positive charge [251].

Zvauya and Dawson [255] investigated the effects of benzyl dimethyl-n-hexadecylammonium chloride (BHDC) in CO_2-saturated NaCl solution.

The data obtained fitted the Frumkin isotherm and it was found that the chemical mainly inhibits the anodic process, producing an enthalpy change of -10.6 kJ/mol. It was proposed that the mechanism of adsorption involved charge sharing and that BHDC was adsorbed both through the positively charged nitrogen atom and the electrons in the benzene ring [255]. It has been reported that the adsorption via the π-electrons predominated over the adsorption via the positively charged cation [255].

Zvauya and Dawson [255] stated that when the molecules are orientated perpendicularly to the surface with the alkyl chain protruding into the solution they form a close-packed layer which is made possible by the attractive forces between the negatively charged benzene ring and the positive charge on the methyl groups on adjacent molecules. This attraction, coupled with the van de Waals forces between the long alkyl groups, results in attractive forces between adjacent adsorbed molecules and consequently necessitated the use of the Frumkin isotherm which accounts for lateral interactions between adsorbed molecules [255].

Imidazoline

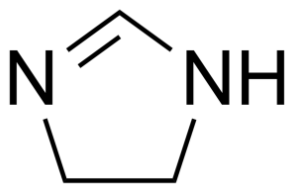

Imidazolines and their salts are a popular choice in the oil and gas industry. Filming amines are also used to neutralise acids to form inhibitive films on metals [155]. Research by Ai et al. [251] proved that a synergistic effect occurs between an imidazoline derivative and KI (Potassium Iodide) for inhibiting galvanic corrosion.

It was shown that the inorganic anion I^- was capable of changing the excess charge of carbon steel significantly and that changes in the surface charge influenced the adsorption of the organic inhibitor onto the surface dramatically [251]. Nitrogenous compounds can undergo adsorption through the formation of an iron-nitrogen coordinate bond or π-electron interaction between compounds with aromatic character and the iron surface. Durnie et al. [256, 257] determined negative values of free energy ($\Delta_{ad}G^o$) for tests using various nitrogenous-based compounds. $\Delta_{ad}G^o$ was found to become more negative with increasing temperature and chain length. This information suggested the favourability of longer chains to adsorb more readily at higher temperatures. The thermodynamic favourability of adsorption was also found to decrease along with the average charge density at the head group [256, 257].

It has been extensively reported that the imidazoline head group plays the critical role in the adsorption process [258]. The role of the hydrocarbon chain in an imidazoline monolayer is to provide a barrier to water and chloride ingress [258].

Thiol Compounds

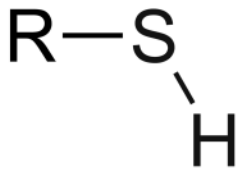

Sulphur-containing organic compounds have been identified as better electron donors than compounds which contain oxygen and nitrogen. Few noticeable studies have been performed on these compounds in a CO_2-saturated environment [155].

9.3 Synergistic Effects of Corrosion Inhibitor Components

The simultaneous use of different inhibitors often results in more efficient inhibition than the individual effect of the components. This phenomena, referred to as a 'synergistic effect' is not only depend upon the chemicals themselves, but also the ratio of the different compounds and their environment [153]. Positive synergy tends to manifest itself as a result of chemical interactions between the different inhibitors, such as co-operative adsorption, chemical reactions between the species in the bulk electrolyte or surface catalysed reactions which lead to the formation of protective layers [153].

In order to determine the synergy between compounds, a matrix of experiments was devised to test four of the components from Inhibitor B at a set of relative concentrations recommended by the service company, utilising all possible

combinations. Four components were selected for analysis. These were an anhydride/polyamine reaction product, an imidazoline derivative, a quaternary ammonium salt and 2-mercaptoethanol. The matrix consisted of 16 individual experiments, summarised in Table 9.2, which assessed the performance of the chemicals either individually, in groups of 2 or 3, or all together. The concentration of the chemical components was 20 ppm, except for the imidazoline derivative which was applied at 40 ppm. These concentrations were suggested by the chemical vendor.

The influence of each of these compounds on reducing corrosion rate could then be further understood by applying this systematic approach. The tests were conducted in a SIJ for 4 hours at 7 m/s without the presence of sand and gravimetric measurements were used to assess inhibitor performance.

Table 9.2: Test matrix used to assess inhibitor component synergy in submerged impinging jet; APRP = anhydride/polyamine reaction product, ID = imidazoline derivative, QAS = quaternary ammonium salt and ME = 2-mercaptoethanol

	All Components	1-1	1-2	1-3	1-4	2-1	2-2	2-3	2-4	2-5	2-6	3-1	3-2	3-3	3-4
20 ppm APRP	✓	✓				✓	✓	✓				✓	✓		✓
40 ppm ID	✓		✓			✓			✓	✓		✓		✓	✓
20 ppm QAS	✓			✓			✓		✓		✓	✓	✓	✓	
20 ppm ME	✓				✓			✓		✓	✓		✓	✓	✓

Gravimetric results from the matrix of submerged impinging jet tests in Table 9.2 are provided in Figure 9.2. Four versions of the same dataset are presented in Figure 9.2 to highlight the effect of the different components in the system.

As an example, all white filled bars with red borders in Figure 9.2(a) depict tests in which the anhydride/polyamine reaction product is present in the blend of chemicals administered to the rig, irrespective of the presence of other chemicals. Similarly, all white bars with green borders in Figure 9.2(b) contain the imidazoline derivative, and so on.

From first analysis of the data, there is a clear indication that the presence of 2-mercaptoethanol (ME) in the system provides a significant level of protection for

carbon steel against CO_2 corrosion and appears to be the most effective chemical, whether that be the chemical on its own, or with the addition of other components.

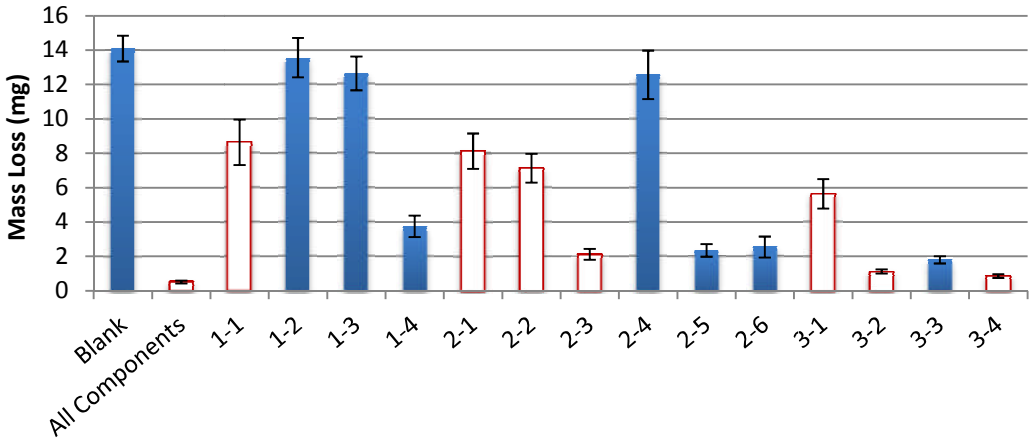

(a)

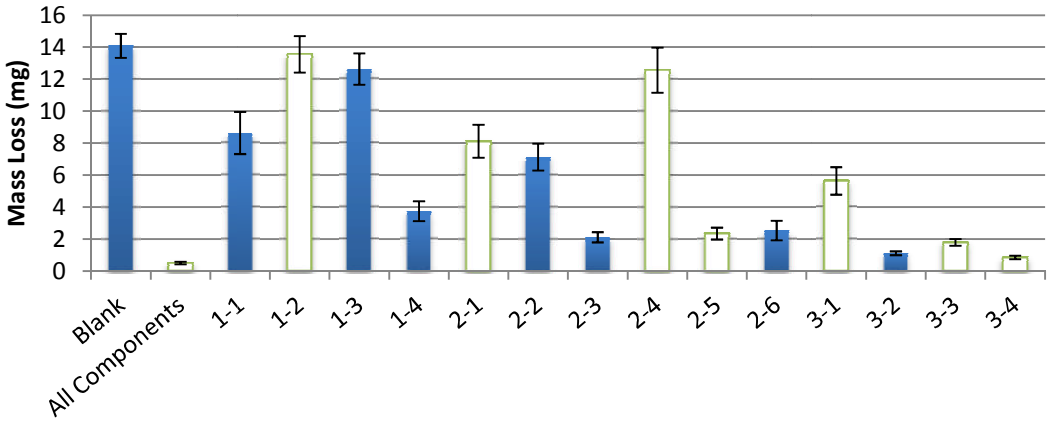

(b)

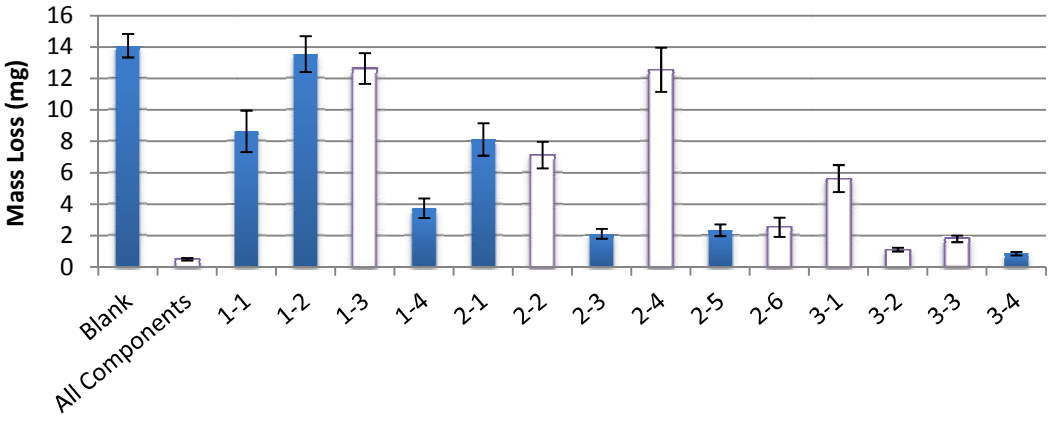

(c)

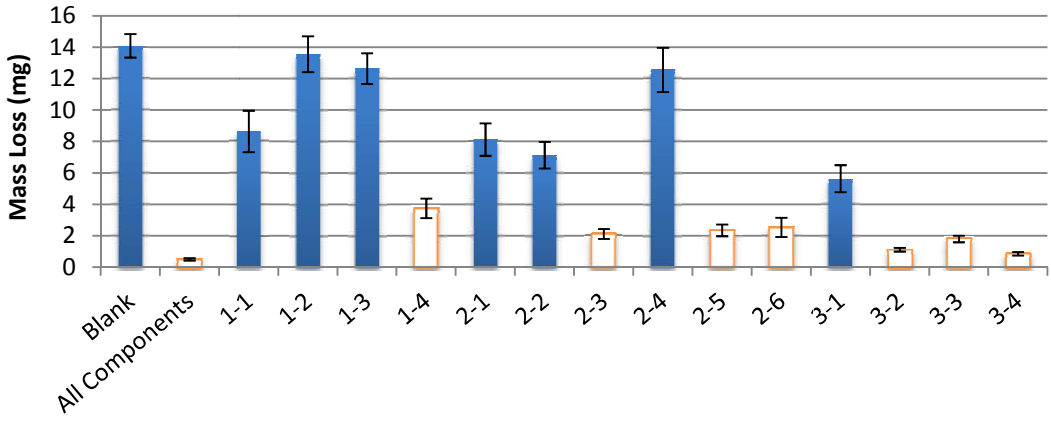

(d)

Figure 9.2: Efficiency of Inhibitor B components in various combinations; (a) blends containing the anhydride/polyamine reaction product are in red (b) blends containing the imidazoline derivative are in green (c) blends containing the quaternary ammonium salt are in purple (d) blends containing 2-mercaptoethanol are in orange

ME dictates a significant proportion of the corrosion inhibition properties for the blend of chemicals in this specific environment. With ME present in the system, the recorded mass loss never rose above 3.75 mg, irrespective of the other chemicals added, representing an efficiency of 73% or greater.

Table 9.3 ranks the component blends in order of efficiency. It is clear that the top 8 blends all contain ME, once again highlighting its importance as a component of the corrosion inhibitor, helping to reinforce the statement that ME is the most influential component in reducing corrosion rates in this particular environment.

Table 9.3: Corrosion component blends ranked in order of efficiency

Rank	Test Number	Mass Loss (mg)	20 ppm APRP	40 ppm ID	20 ppm QAS	20 ppm ME
1	All Components	0.51	✓	✓	✓	✓
2	3-4	0.86	✓	✓		✓
3	3-2	1.12	✓		✓	✓
4	3-3	1.8		✓	✓	✓
5	2-3	2.12	✓			✓
6	2-5	2.35		✓		✓
7	2-6	2.54			✓	✓
8	1-4	3.75				✓
9	3-1	5.64	✓	✓	✓	
10	2-2	7.13	✓		✓	
11	2-1	8.12	✓	✓		
12	1-1	8.64	✓			
13	2-4	12.56		✓	✓	
14	1-3	12.64			✓	
15	1-2	13.56		✓		
16	Blank	14.09				

A key property of inhibitor components is their ability to operate together and produce a ‘synergistic effect’. Figure 9.3 demonstrates the influence that each inhibitor component has on increasing efficiency within the different chemical blends. For example, in Figure 9.3(a), tests were conducted with and without the anhydride/polyamine reaction product (APRP). Each bar in blue represents the efficiency obtained when the chemicals listed underneath each bar are added to the brine solution. The additional white bars on top of the blue bars in Figure 9.3(a) represent the increase in efficiency as a result of conducting the same test again, but with the inclusion of the APRP.

In terms of increasing the efficiency of the chemical blends, ME proved to be the most influential, followed by the APRP. The imidazoline derivative and quaternary ammonium salt produced little further reduction in the corrosion rate of the carbon steel. The APRP increased the efficiency of the 8 tests in Figure 9.3(a) by 26%, whilst the addition of ME increased efficiency by nearly 60% on average.

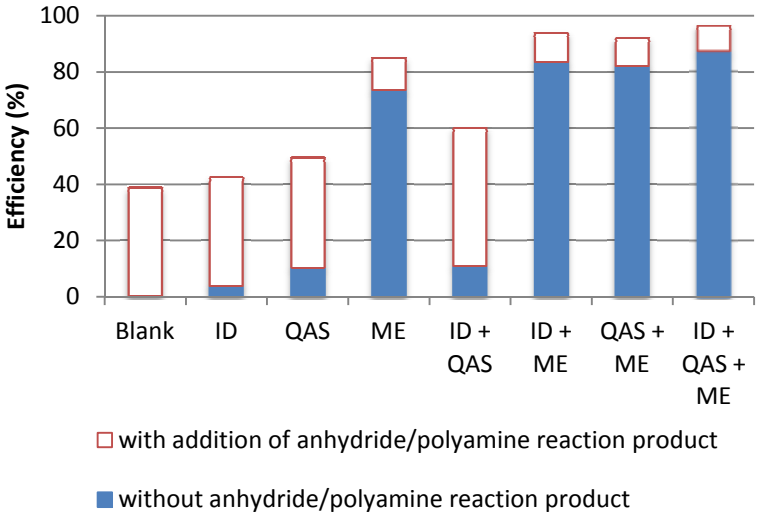
Efficiency (%)
100
80
60
40
20
0
Blank
ID
QAS
ME
ID + QAS
ID + ME
QAS + ME
ID + QAS + ME
with addition of anhydride/polyamine reaction product
without anhydride/polyamine reaction product

(a)

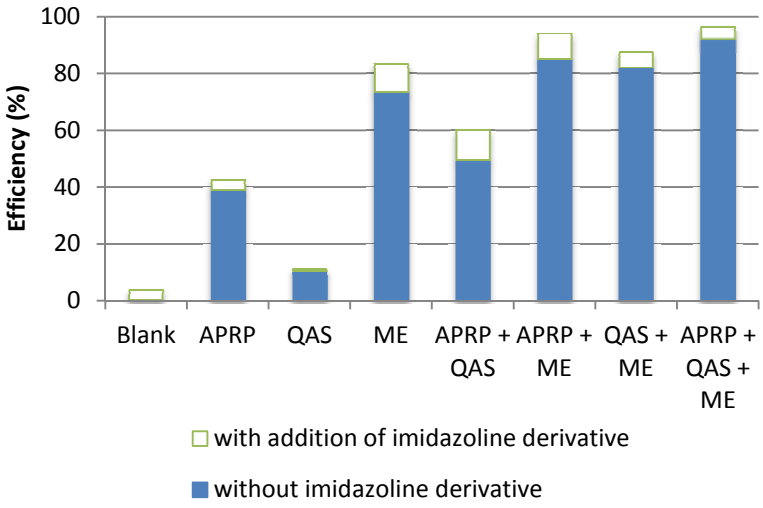
Efficiency (%)
100
80
60
40
20
0
Blank
APRP
QAS
ME
APRP + QAS
APRP + ME
QAS + ME
APRP + QAS + ME
with addition of imidazoline derivative
without imidazoline derivative

(b)

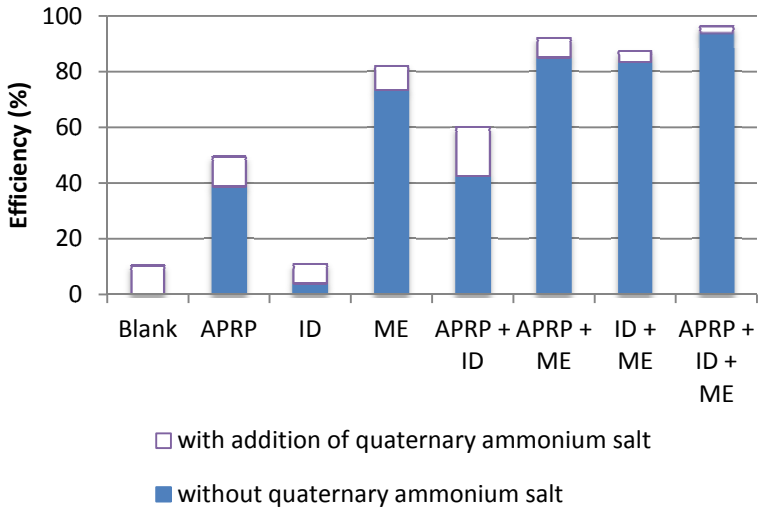
Efficiency (%)
100
80
60
40
20
0
Blank
APRP
ID
ME
APRP + ID
APRP + ME
ID + ME
APRP + ID + ME
with addition of quaternary ammonium salt
without quaternary ammonium salt

(c)

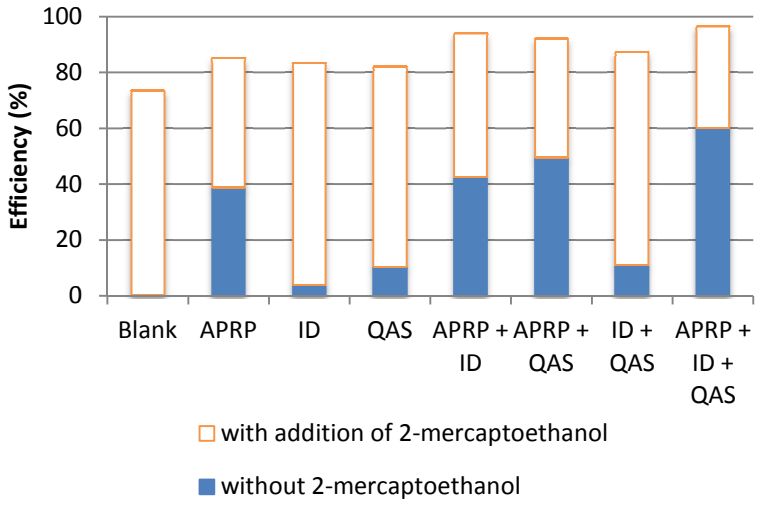

(d)

Figure 9.3: Inhibition efficiencies with an without the addition of (a) anhydride/polyamine reaction product, (b) imidazoline derivative, (c) quaternary ammonium salt and (d) 2-mercaptoethanol

9.4 Adsorption Characteristics of 2-mecaptoethanol

Selecting an appropriate corrosion inhibitor for a particular system requires consideration of not only the electrolyte, metal, amount and type of corrosion product, temperature, type of oil etc., but also the structural-chemical properties and adsorption characteristics of the inhibitor molecule [259]. The design and selection of corrosion inhibitors has traditionally involved an empirical process based on extensive laboratory and field testing. The development of theories to explain how these chemicals behave in different environments has grown in popularity over recent years and can help influence the design and selection process [248].

Despite the development of a number of quantitative structure/activity relationships, the most significant criterion is the efficiency of the inhibitor under conditions representative of those in the field [248].

One method of determining the effectiveness of corrosion inhibitors is through the implementation of adsorption isotherms [248]. By empirically developing adsorption models, it is possible to accurately predict inhibitor performance based on thermodynamic parameters and calculations. It is widely acknowledged that adsorption isotherms provide a valuable insight into corrosion inhibition mechanisms [248].

By using the methodology adopted by Durnie et al. [196, 215, 248, 253, 256, 257, 260, 261] as a basis, this section of the Chapter aims to determine the adsorption

characteristics of ME and the method by which corrosion inhibition is achieved by the chemical. This particular chemical was selected because of its high efficiency and the fact it was the most active chemical tested in the previous section of this Chapter.

Before implementing the methodology, it is important to highlight the theory and assumptions behind the construction of adsorption isotherms.

9.5 Methodology for Constructing Adsorption Isotherms

9.5.1 Theory

When organic compounds are adsorbed at an electrolyte/electrode interface, they may be considered to displace water at the inner Helmholtz plane of the EDL via the following reaction:

$$Org_{(aq)} + nH_2O_{(ads)} \leftrightarrow Org_{(abs)} + nH_2O_{(aq)} \quad (9.1)$$

Assuming that the steel electrode corrodes uniformly over the surface, the corrosion rate is related to the total number of corroding sites. When an inhibitor is present in the system, the corrosion rate is then proportional to the number of remaining corrosion sites after chemicals have adsorbed onto the steel surface [253]. The fundamental assumption of constructing the adsorption isotherm is that this electrochemical information can be used to define the fractional surface coverage (θ) of the material:

$$\theta = \frac{i_{corr\ (blank)} - i_{corr\ (inhibited)}}{i_{corr\ (blank)}} \quad (9.2)$$

where $i_{corr\ (blank)}$ is the corrosion current density in the blank solution and $i_{corr\ (inhibited)}$ is the corrosion current density in the presence of inhibitor.

9.5.2 Isotherm Selection

When fitting the behaviour of inhibitor adsorption to models it is necessary to empirically determine which isotherm best fits the surface coverage data. The models proposed by Durnie et al. [253] are all considered here as potential fits to the adsorption behaviour:

Temkin isotherm

$$K_{ad}C = e^{f\theta} \quad (9.3)$$

Langmuir isotherm

$$K_{ad}C = \frac{\theta}{1-\theta} \tag{9.4}$$

Freundlich isotherm

$$K_{ad}C^{1/n} = \theta \tag{9.5}$$

Frumkin isotherm

$$K_{ad}C = \frac{\theta}{1-\theta}e^{f\theta} \tag{9.6}$$

where θ is the surface coverage, C is the concentration (molal), K_{ad} is the adsorption equilibrium constant and f is the molecular interaction constant.

Once a suitable adsorption isotherm has been selected, corrosion rate measurements can be used to determine thermodynamic data relating to inhibitor adsorption.

Durnie et al. [253] demonstrated that the isosteric enthalpy of adsorption (i.e. $\Delta_{ad}H$) can be determined through differentiation of the logarithmic form of the aforementioned adsorption isotherms, assuming a constant value of θ.

$$\left(\frac{\partial \ln C}{\partial T}\right)_{\theta=\text{constant}} = -\left(\frac{\partial \ln K_{ad}}{\partial T}\right)_{\theta=\text{constant}} \tag{9.7}$$

Substituting the van't Hoff equation into Equation (9.7) yields the following expression:

$$\left(\frac{\partial \ln C}{\partial T}\right)_{\theta=\text{constant}} = -\frac{\Delta_{ad}H^o}{RT^2} \tag{9.8}$$

Integrating Equation (9.8) produces an equation which allows $\Delta_{ad}H^o$ to be determined by measuring the inhibitor concentrations required to achieve a constant surface coverage over a suitable temperature range:

$$\ln C = -\frac{\Delta_{ad}H^o}{RT} + \text{constant} \tag{9.9}$$

Using this approach, the calculated values of $\Delta_{ad}H^o$ and K_{ad} can be used to determine other important thermodynamic properties such as the change in Gibbs free energy ($\Delta_{ad}G^o$) and the change in entropy ($\Delta_{ad}S^o$):

$$\Delta_{ad}G^{o} = -RT\ln(K_{ad}) \quad (9.10)$$

$$\Delta_{ad}S^{o} = \frac{\Delta_{ad}H^{o} - \Delta_{ad}G^{o}}{T} \quad (9.11)$$

By considering the thermodynamics of adsorption, valuable information can be aquired relating to the corrosion inhibitor mechanism. For example, a negative value of $\Delta_{ad}H^{o}$ represents an exothermic reaction, signifying either a physi- or chemisorption process [253, 256, 259]. However, an endothermic process is attributed unequivocally to chemisorption [253, 256, 259]. The value of $\Delta_{ad}G^{o}$ will provide information on the spontaneity of the reaction and if $\Delta_{ad}S^{o} < 0$, there is a reduction in the number of degrees of freedom as a result of the adsorption process [253, 256, 259].

Durnie and Gough [256] adopted a semi-empirical method, involving correlating quantum mechanical properties of imidazolines molecules with their inhibition performance. By using the form of the Hansch equation it was possible to determine a relationship between some key quantum mechanical properties and adopt them to model thermodynamic data. Some of the properties considered were the average charge density at the head group, the molecular volume and the dipole moment. The correlation shown between theoretical (using quantum mechanical data) and experimental (using Temkin adsorption isotherms) for $\Delta_{ad}G^{o}$ and $\Delta_{ad}S^{o}$ are provided in Figure 9.4(a) and (b), respectively. The strong correlation observed helps to reinforce the validity of the adsorption isotherm technique adopted in this study.

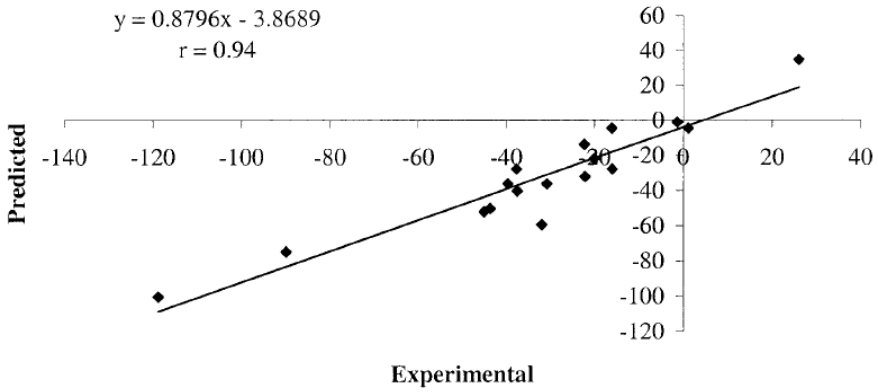

(a)

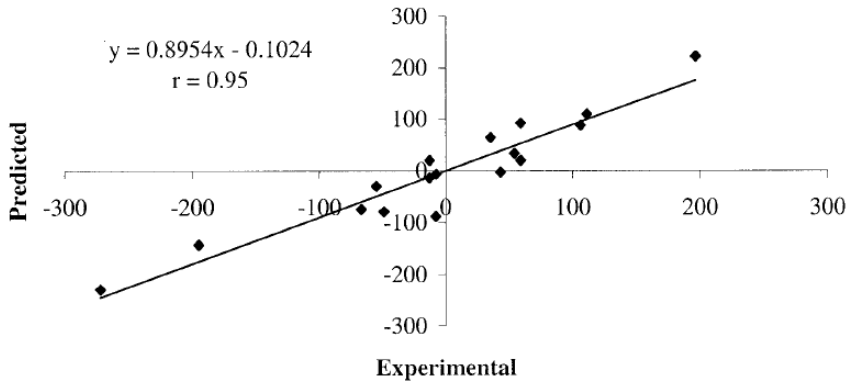

(b)

Figure 9.4: Correlation between experimental (relating to Temkin adsorption isotherms) and predicted (from quantum mechanical modelling) (a) enthalpies and (b) entropies of adsorption [256]

9.5.3 Methodology and Electrochemical Measurements

Static experiments comprising of a three-electrode cell were used to monitor corrosion rate and are described fully in Section 7.2.1. Solution composition remained identical to previous tests and the brine was saturated with CO_2 at atmospheric pressure.

The corrosion process was studied by means of the DC linear polarisation technique using a computer controlled ACM Gill 8 potentiostat. Measurements were conducted between -15 and +15 mV against E_{corr} using a scan rate of 0.25 mV/s. Readings were taken at intervals of 10 minutes over a 2 hour period with the final three readings being averaged and used as the steady-state corrosion rate.

After inhibitor was added to the system, the test continued for a further 4 hours with continuous LPR measurements to allow the corrosion rate to stabilise. Again, the final three measurements were averaged to obtain the inhibited rate. This technique followed the same methodology adopted by Durnie et al. [196, 256, 260]. The percentage reduction (inhibitor efficiency) enabled the surface coverage to be estimated for a number of different temperatures and various concentrations of ME.

9.6 Constructing and Fitting Adsorption Isotherm for 2-Mercaptoethanol

Tests were conducted at three temperatures (30, 40 and 50°C) to construct the adsorption isotherm. These temperatures were purposely selected below the scaling temperature to prevent the formation of $FeCO_3$ from interfering with

measurements during pre-corrosion. Using lower temperatures ensured that the pre-corrosion readings remained relatively stable and that the reduction in corrosion rate after the application of inhibitor was from the adsorption process and not the blocking of active sites on the steel surface as a result of the formation of $FeCO_3$.

Concentrations of ME were varied to produce a range of inhibitor efficiencies between 20 and 80% to ensure that the data was recorded over a suitable enough range to fit to the adsorption isotherms. To achieve these efficiencies ranges, tests had to be conducted at very low concentrations. Examples of the linear polarisation data collected are provided in Figure 9.5 for the three different temperatures and indicate that concentrations were of the order of 10's of ppb.

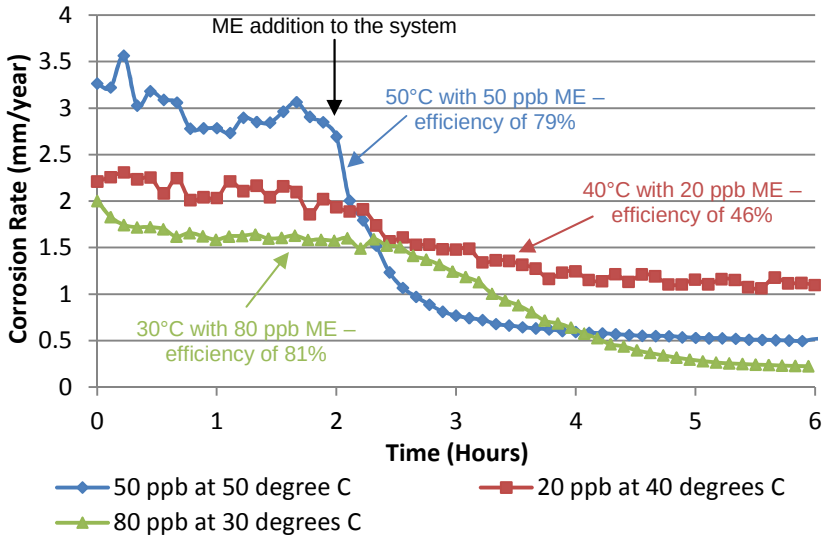

Figure 9.5: Examples of corrosion rates vs. time from linear polarisation measurements which helped in the modelling of the adsorption isotherm

9.6.1 Fitting to Adsorption Isotherms

Based on the results gathered, it was possible to empirically determine which adsorption isotherm best fitted the surface coverage data. Numerous experiments were required to provide a statistically significant regression fit to the correct isotherm. For a reliable and linear isotherm plot, the surface coverage must fall in the linear window of inhibitor adsorption i.e. $\theta = 0.2\text{-}0.8$.

Two of the four isotherms considered provided strong correlations between ME concentration and surface coverage; the Langmuir and Frumkin isotherms. Examples of the correlations obtained at 50°C are provided in Figure 9.6.

Both the Langmuir and Frumkin isotherms are based on monolayer chemisorption onto the surface of the material [206, 262]. Not surprisingly, both models produce strong correlations as the Frumkin isotherm is an extension of that of the Langmuir and accounts for the interactions between adsorbed species on the surface of the sample [253].

Elayyachy et al. [206] reviewed the performance of a number of sulphur-containing compounds as inhibitors for the corrosion of steel in a 1 M HCl solution. They determined that the Langmuir isotherm provided the best fit to the data, however, other isotherms considered in the fitting process were not referred to, so it was unclear whether the Frumkin isotherm was considered. The sulphur compounds studied were determined to adsorb on the steel surface through a chemisorption process based on the change in Gibbs free energy [206].

The strong correlation of the Frumkin isotherm (R^2 = 0.9636) in Figure 9.6 not only confirms the validity of the approach used extensively by Durnie et al. [196, 215, 248, 253, 256, 257, 260, 261], but it also suggests that ME chemisorbs onto the surface of the carbon steel and the molecules interact with each other on the surface [253].

Previous work by Nešić et al. [186] has also demonstrated the validity of this approach in which the adsorption behaviour of both an amine and imidazoline based corrosion inhibitor were correlated with the Frumkin isotherm. The polarisation behaviour observed by Nešić et al. [186] for the application of the amine and imidazoline chemicals in CO_2-saturated solutions suggested that lateral interaction between the long polymer chains of the inhibiting molecules hindered the transport of cathodic species to the surface of the material and reducing the rate of the cathodic reaction. It could be suggested that the lateral interactions between the molecules played a decisive role in the selection of the Frumkin isotherm as opposed to the Langmuir isotherm for both the work performed by Nešić et al. [186] and that conducted in this research.

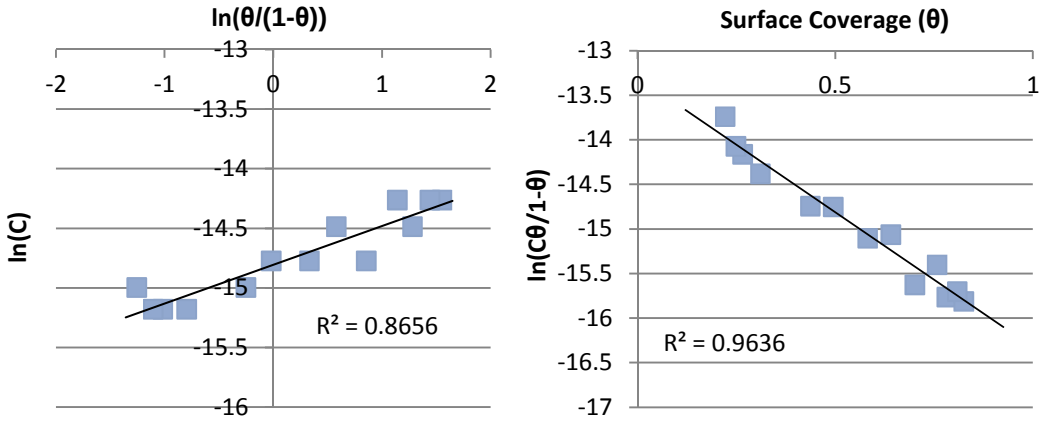

(a) (b)

Figure 9.6: Plot for (a) Langmuir and (b) Frumkin adsorption isotherms of 2-mercaptoethanol at 50°C

Frumkin isotherm plots were also constructed for temperatures of 30 and 40°C. Using each of these plots, it was possible to determine the concentration at which 50% surface coverage occurs (θ=0.5) for each temperature as shown in Table 9.4. By purely considering the information in this table, it is evident that the adsorption process is chemisorption. The concentration required to reach 50% surface coverage decreases with increasing temperature. This demonstrates that the efficiency of the inhibitor improves with temperature, which is a feature of an endothermic process. Referring back to Figure 9.5, it is possible to observe the effect of temperature on the reaction process. For the test performed at 30°C it is clear that a much higher relative concentration (80 ppb) is required to produce the same efficiency as the test at 50°C with the application of 50 ppb, indicating that an increase in temperature favours the adsorption process.

Table 9.4: Concentration of 2-mercaptoethanol required to achieve 50% surface coverage on a carbon steel electrode in a CO_2-saturated environment at temperatures of 30, 40 and 50°C

Temperature (K)	1/T (K^{-1} x 10^{-3})	Concentration required for θ=0.5 (ppb)	Molal concentration for θ=0.5	Natural log of molal concentration (ln(C))
303	3.30	68.9	$8.8x10^{-7}$	-13.94
313	3.19	40.0	$5.1x10^{-7}$	-14.49
323	3.10	28.8	$3.7x10^{-7}$	-14.81

If the process is endothermic, then the adsorption mechanism is unequivocally attributed to chemisorption [253]. To confirm the assumptions derived from the results in Table 9.4, the isosteric enthalpy of adsorption (enthalpy at constant surface coverage) was calculated.

By extracting the concentration required at each temperature to produce 50% surface coverage from Table 9.4, it was possible to construct a van't Hoff plot for ME. Selecting the values at a constant surface coverage of 50% ensured that the extrapolated concentration was located within the linear portion of the isotherm, reducing subsequent calculation errors.

Figure 9.7 presents the van't Hoff plot for ME. Based on the positive gradient of the line, it is evident that this compound gives rise to an endothermic adsorption process.

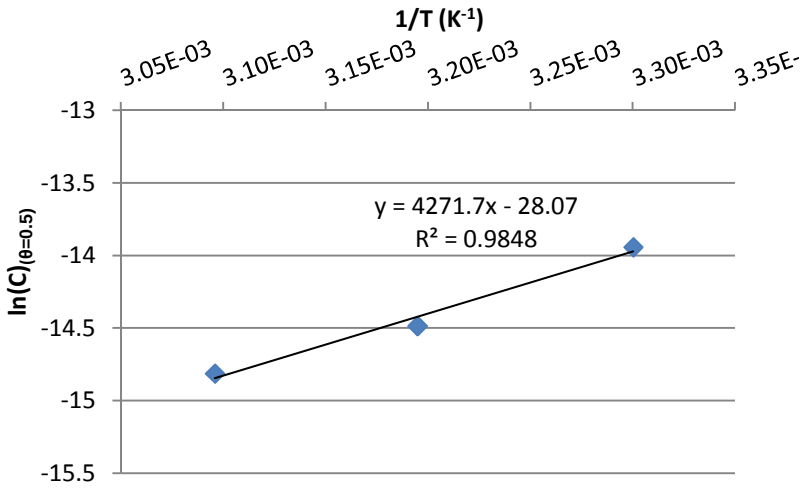

Figure 9.7: Van't Hoff plot for 2-mercaptoethanol in the temperature range of 30-50°C

Through the application of Equation (9.9), the isosteric enthalpy of adsorption, $\Delta_{ad}H^{o}$ is calculated by taking the gradient of the van't Hoff plot in Figure 9.7 and multiplying by the gas constant. The thermodynamic parameters pertaining to $\Delta_{ad}G^{o}$ and $\Delta_{ad}S^{o}$ can then be calculated using Equations (9.10) and (9.11). These thermodynamic properties are displayed in Table 9.5 for conditions at 30, 40 and 50°C.

Table 9.5: Fundamental adsorption constants for 2-mercaptoethanol

Temperature (K)	$\Delta_{ad}H^o$ (kJ mol^{-1})	$\Delta_{ad}G^o$ (kJ mol^{-1})	$\Delta_{ad}S^o$ (J K^{-1} mol^{-1})
303		-28.9	210.4
313	34.8	-32.7	222.9
323		-33.6	226.1

As expected, ME displays a negative value of $\Delta_{ad}G^o$, indicative of spontaneous adsorption at the surface. The free energy becomes more negative with increasing temperature suggesting that the thermodynamic favourability of adsorption increases with temperature [259].

Adsorption at a surface generally produces a reduction in the number of degrees of freedom i.e. negative values of $\Delta_{ad}S^o$. However, Durnie et al. [259] and Shaw [263] demonstrated adsorption from a solution onto a metal does not necessarily follow this trend. The reason behind this is that a certain amount of destructuring (desolvation) is associated with the adsorption process [259]. Durnie et al. [259] and Shaw [263] believed a possible explanation for positive entropy (as seen with 2-mercaptoethanol) was attributed to the fact that the system undergoes an entropy increase as the adsorbed surface water molecules are being substituted or replaced by inhibitor molecules.

9.6.2 FT-IR Analysis

A number of organic sulphur-containing compounds are known to be effective corrosion inhibitors in acidic solutions [264, 265]. Some of these compounds, such as benzenethiol and phenylmethanethiol, react at the metal interface and their reaction products are adsorbed onto the surface, resulting in excellent inhibition [265].

ME can theoretically adsorb in three ways; through formation of a sulphonium ion ($HO\text{-}CH_2CH_2\text{-}SH_2^+$) which adsorbs through electrostatic attraction, the chemical adsorption of the molecule by the formation of a σ-bond between the sulphur and an iron atom, or the interaction via the hydroxyl group could also be a possible adsorption mechanism if this group dissociates [265]. Uehara et al. [265] believed that molecules such a ME, which act as extremely weak bases, were unlikely to undergo electrostatic adsorption of the sulphonium ion and be of minor importance.

Figure 9.8 shows the FT-IR spectrum of ME in the liquid state. Strong bands for the FT-IR spectrum of neat ME are shown at 2933 and 2873 cm^{-1}, typical of CH_2 stretching [266, 267], 1009 cm^{-1}, which is associated with out-of-phase C-C-O stretching and at 663 and 723 cm^{-1}, which have previously been assigned to C-S stretching [266-269]. The v(C-S) band at the lower wavenumber (663 cm^{-1}) has been attributed to the gauche conformation of the S-C-C chain [266, 269]. The v(C-S) band at the higher wavenumber (723 cm^{-1}) is characteristic of the anti conformation [266, 269]. The FT-IR scan of the polished surface is provided in Figure 9.9.

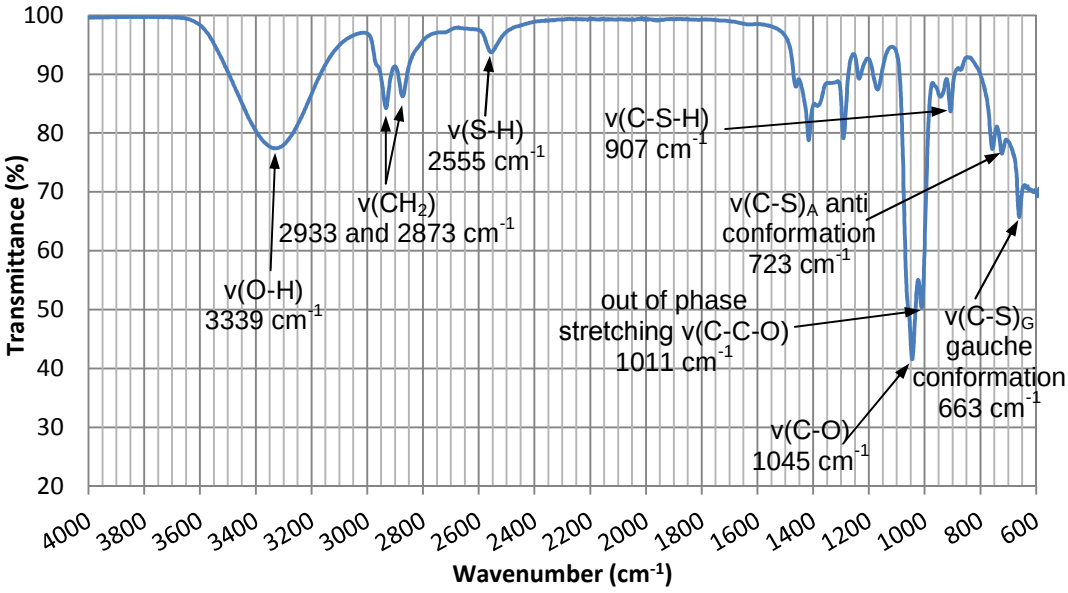

Figure 9.8: Infrared spectrum for neat 2-mercaptoethanol

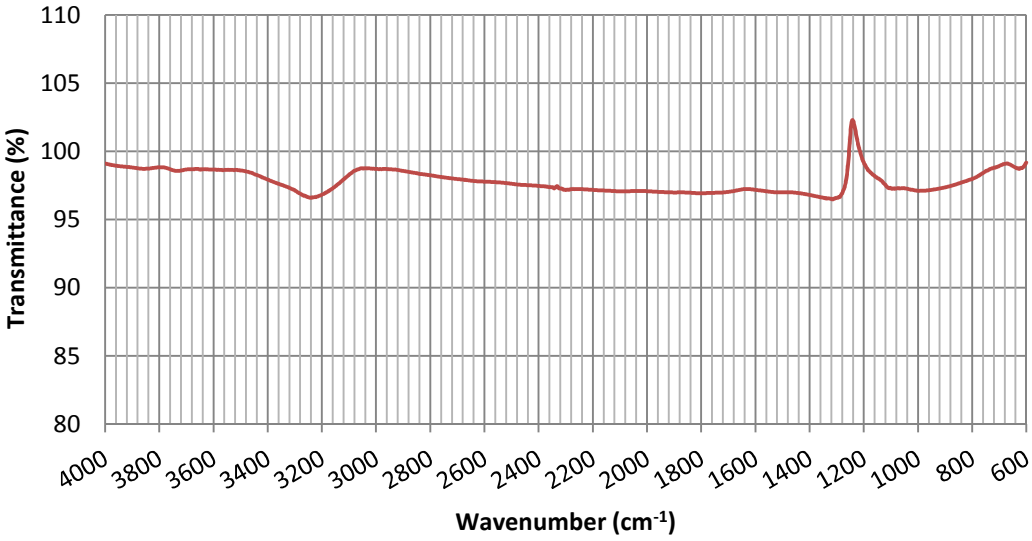

Figure 9.9: Infrared spectrum of a polished specimen

Figure 9.10 shows the spectrum of the adsorbed ME film at the carbon steel surface. The film was formed through immersion of the metal substrate in a 20 ppm static solution for 4 hours at 45°C. The missing S-H stretching band around 2555 cm^{-1} suggests the covalent bonding between the sulphur atoms and the metal surface was the adopted adsorption mechanism as has been previously reported on gold samples by Kudelski et al. [266].

Regrettably, a number of other bands are not visible on the FT-IR spectra relating to the C-O and C-C-O stretching frequencies around 1000 cm^{-1} which makes it difficult to prove conclusively that this covalent bond occurs, despite it being the most likely form of attachment to the surface [265]. The reason for these bands disappearance from the spectra is unknown.

However, one of the peaks clearly visible within the adsorbed layer spectrum is the band relating to the gauche conformation of C-S at 668 cm^{-1}. The band corresponding to the anti conformation was not detected at 723 cm^{-1} and has been reported to have been missing in other spectra [266]. This has been attributed to its weak intensity and the large intensity ratio of the gauche to anti v(C-S) bands [266].

Kudelski et al. [266] found that the ratio of these two intensities changed significantly depending on the material ME adsorbed onto and suggesting that the orientation of the molecule differs depending on the substrate. These experiments considered the adsorption of ME onto copper, gold and silver. Tarabara et al. [269] also presented similar findings, determining that the gauche isomer prevails at low bulk concentrations of 2-mercaptoethanol (around 0.2 ppm) when chemisorbing onto silver hydrosol. A densely packed monolayer (97% anti-isomers) was found to form as the concentration began to increase. This was attributed to the ordering processes at the metal surface caused by the formation of the monolayer. It was stated that the molecule orientated in the gauche conformation occupies more ‘surface space’ than in the anti conformation, and as a result, the ratio of anti to gauche intensity depends on the number of adsorbed molecules, that is, the density of the ME layer. Kudelski et al. [266] observed a chemisorption process onto gold which took place in less than 5 minutes, reaching an anti-gauche equilibrium which was defined from the bulk concentration and not the incubation time [269].

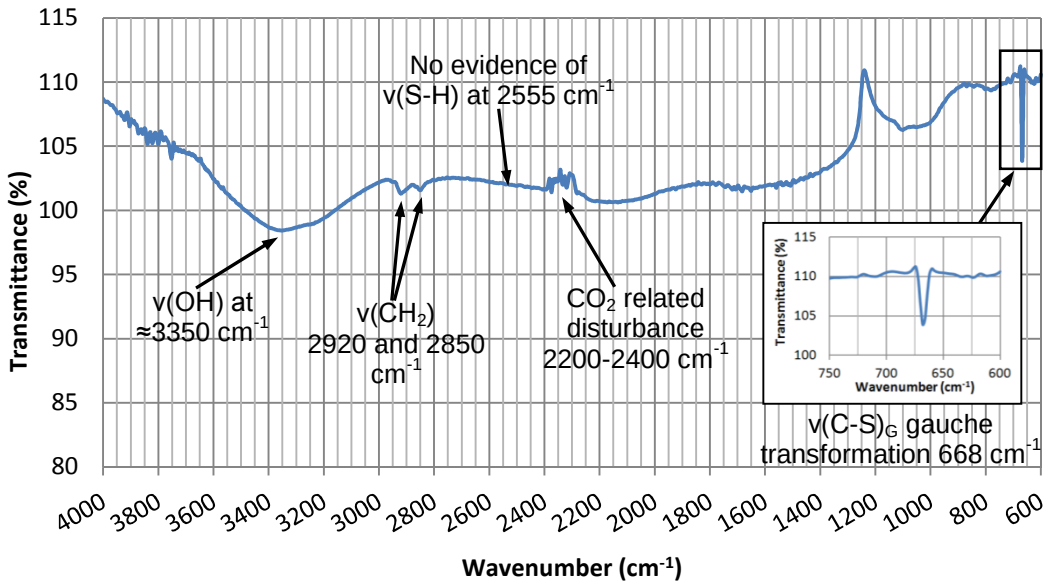

Figure 9.10: Infrared spectrum for 2-mercaptoethanol layer formed on carbon steel in CO_2-saturated solutions at 20 ppm in a static solution after 4 hours

The intense $v(C\text{-}S)_G$ band and the disappearance of the $v(C\text{-}S)_T$ band observed in the FT-IR spectrum provide evidence for the predominance of gauche isomers on the surface of the carbon steel material. This conformation behaviour can be depicted in Figure 9.11 and Figure 9.12 if it is assumed that ME interacts with the steel surface through a Fe-S covalent bond.

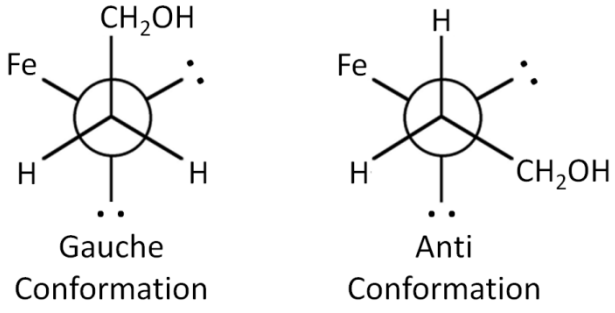

Figure 9.11: Gauche and anti conformational isomers of ME when bonded to the metal surface (view from above onto the surface)

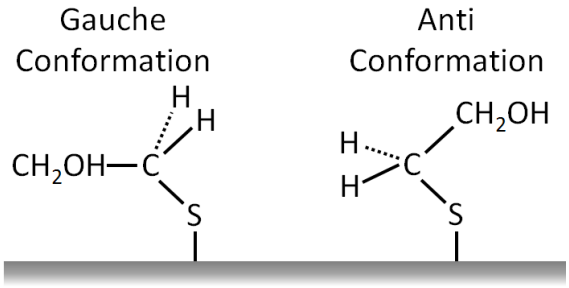

Figure 9.12: Gauche and anti conformational isomers of 2-mercaptoethanol when bonded to the metal surface

Although the FT-IR measurements suggest the predominance of the gauche conformation, the analysis performed is *ex-situ*, unlike the *in-situ* analysis performed by Kudelski et al. [266]. It is possible that the rinsing of the sample with distilled water prior to examination under the FT-IR may promote a change in the film structure and conversion of ME orientation from the anti-conformation to the gauche conformation.

From the FT-IR analysis, it is possible that the adsorption of ME in CO_2 conditions adopts the same adsorption characteristics as those proposed by Ohno, Uehara and Aramaki on other metal surfaces [264, 265]. They determined that thiol molecules either dissociate at the interface to form thiolate anions or are reduced by cathodic reactions. Therefore, the following two processes are proposed here:

$$\mathrm{HOCH_2CH_2SH \rightarrow HOCH_2CH_2S{:}^- + H^+} \tag{9.12}$$

$$\mathrm{HOCH_2CH_2SH + e^- \rightarrow HOCH_2CH_2S{:}^- + H^+_{(ads)}} \tag{9.13}$$

The anions formed would then be able to chemisorb onto the iron surface by forming and Fe-S σ-bond, i.e.

$$\mathrm{HOCH_2CH_2S{:}^- \rightarrow HOCH_2CH_2S{:}\,Fe} \tag{9.14}$$

9.7 Residual Analysis of Corrosion Inhibitors

The residual analysis of corrosion inhibitors is an important concept in the oil and gas industry. The ability to monitor chemical additives and accurately analyse process fluids on-site can help operators ensure asset integrity and detect flow assurance and process problems early [270]. Unfortunately, the multifarious nature of oilfield process fluids introduces complexity and poses challenges to the detection and monitoring of chemical species.

Analysis techniques implemented in the oil and gas industry can include gas chromatography (GC) [271], electrospray mass spectrometry (ES-MS) [272], high performance liquid chromatography (HPLC) [272], inductively coupled plasma optical emission spectrometry (ICP-OES) [273, 274], and fluorescence/turbidometry techniques [275]. Regrettably, most of these techniques are not suited for offshore application because the procedures required are time-consuming and complicated. The processes also tend to require specially trained lab staff and sensitive, expensive equipment which is often not robust enough to withstand the offshore environment [270]. These issues make on-site analysis difficult and therefore oilfield samples are usually sent to onshore laboratories for analysis. The whole procedure can prove to be very time consuming and increase the risk of sample contamination/chemical changes during transportation, inevitably introducing uncertainty in the results. Additionally, while operators are waiting for an analysis of the sample, there are risks associated with production which could potentially be solved on the same day through the implementation of a real-time analysis technique [270]. If preventative action can be taken much more rapidly, the risk of production loss can be minimised, saving oil and gas companies a considerable amount of time and money.

9.7.1 Application of Biochemistry-based Techniques in Oilfield Corrosion

Recent studies have indicated that inspiration can be taken from biological systems to solve detection problems for oilfield produced fluids. Some of the most notable work has been performed by Fuller et al. [270, 276], who developed colorimetric detection reagents for the analysis of both methanol and monoethylene glycol.

On first consideration, it may not be apparent that biological detection methods could be applied to oilfield fluid analysis. However, biological fluids such as blood are complex mixtures of liquids with solid components, much like the system experienced in oilfield production. Decades of research in healthcare have provided analysis techniques capable of fast and accurate detection. Translating this approach to the oil and gas industry for the monitoring of oilfield fluids could provide service companies with simple methods which generate real-time measurements [276].

Biochemistry-based techniques (particularly the use of spectrophotometric measurements) often involve inexpensive equipment and have shown potential as residual analysis methods [270, 276]. Since the spectrophotometric techniques

involve the addition of reagents to samples, background readings can be taken beforehand to remove potential interferences [270]. These attributes allow simple, rapid and sensitive assays to be developed for use on-site. By providing a real-time analysis technique, operators can make timely, informed decisions when time is critical and delays occur which result in lost revenue [270].

Assays developed in biological sciences often work by exploiting the strong inter-molecular forces (e.g. hydrogen bonding, electrostatic interactions, hydrophobic interactions, van de Waals forces) found between particular molecules. The detection reagent and chemical possess a high affinity for each other, with the reagent being designed so that when it comes into contact with the complementary chemical it produces fluorescence or change in absorbance that can be measured photometrically. The signal strength is proportional to the chemical concentration and can be determined by initial calibration.

The analysis of chemical residual concentrations can be used to help optimise chemical dosing regimes, which can prevent production upsets and interventions by ensuring the levels of protective chemical are at or above the minimum inhibitory concentration, without being unnecessarily high [276].

9.7.2 Residual Analysis Technique for 2-mercaptoethanol

In terms of determining alkylthiols concentrations, gas chromatography tends to be the most widely used technique. Unfortunately, users tend to face considerable difficulty when storing and analysing alkylthiol samples because of their reactivity and strong adsorption properties onto solid surfaces [277]. Traces of alkylthiols have been known to disappear during gas chromatography analysis [277]. Furthermore, isolating the compound of interest is difficult when the sample is complex and contains numerous interfering organic substances.

One specific disulphide, known as 5,5’-dithiobis(2-nitrobenzoic acid) or DTNB has been used in the past for the spectrophotometric determination of thiol groups in a variety of biological samples. This section seeks to determine whether the same principal can be applied to measure ME residual concentrations throughout corrosion studies.

DTNB (see Figure 9.13) is a versatile water-soluble compound and produces a measureable yellow-coloured product when it reacts with sulphydryls. Ellman’s Reagent, as it is commonly known, is very useful as a sulphydryl assay reagent

because it specifically targets –SH groups, and posesses a high molar extinction coefficient and short reaction time.

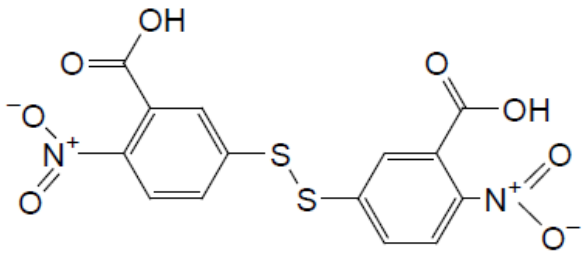

Figure 9.13: Structure of 5,5'-dithio-bis-(2-nitrobenzoic acid) (DTNB)

DTNB reacts with a free sulphydryl group to produce a mixed disulphide and 2-nitro-5-thiobenzoic acid by targeting the conjugate base ($R\text{-}S^-$) of a free sulphydryl group. TNB is produced from the reaction (Figure 9.14) which is effectively the 'coloured' species as it has a high molecular extinction coefficient in the visible range. Studies have shown that the molar extinction coefficient is approximately $14{,}150 M^{-1}cm^{-1}$ at 412 nm and pH 8.0 [278].

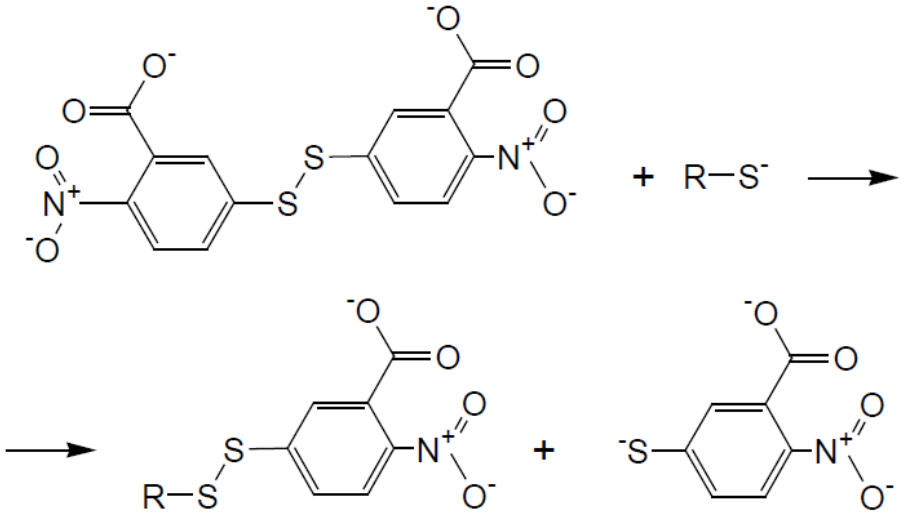

Figure 9.14: Reduction of $DTNB^{2-}$ with a free sulphydryl group to form a mixed disulphide and TNB^{2-}

Initially, a calibration curve was create using known concentrations to establish the relationship between absorbance and concentration for ME.

Ellman's Reagent solution was prepared by dissolving 4 mg of DTNB in 1 ml of 0.1 M tris(hydroxymethyl)aminomethane (Tris) reaction buffer. 50 µl of Ellman's Reagent was then added to a 1000 µl of 0.1 M Tris. For each concentration, 100 µl

of sample tested was mixed with 27.5 µl of the diluted Ellman's Reagent in a well on a 96 well plate. The solutions were left for at least 15 minutes and the level of absorbance was measured using a spectrophotometer set to 410 nm.

Concentrations of 2-mercaptoethanol were tested between 0 and 40 ppm in distilled water. The resulting calibration curve is depicted in Figure 9.15 and provides an extremely strong correlation between absorbance and ME concentration.

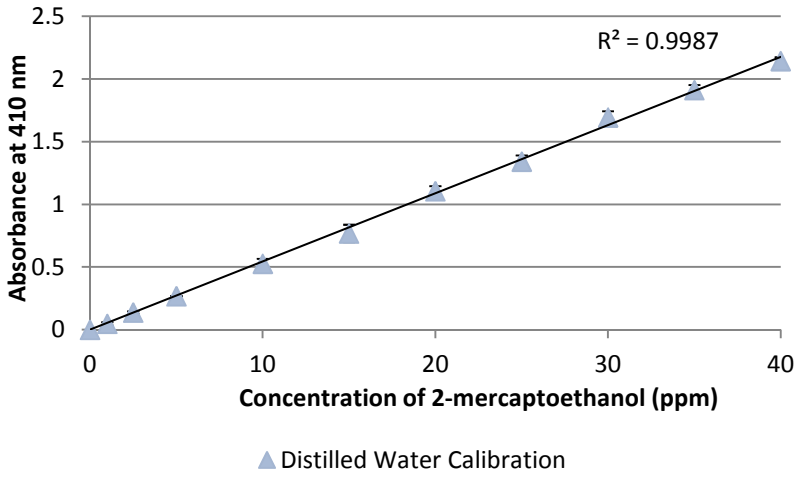

Figure 9.15: Measured absorbance levels at 410 nm when 2-mercaptoethanol is derivatised by DTNB at concentrations between 0 and 40 ppm (values of absorbance for the sample prior to the addition of the reagent have been subtracted from initial values)

The next stage of the process was to determine whether the calibration would be independent of salt concentration and CO_2 presence and if it could be detected within a blend of Inhibitor B components. Figure 9.16 indicates that the presence of the saline solution and the introduction of the other components of Inhibitor B failed to disrupt the absorbance measurements.

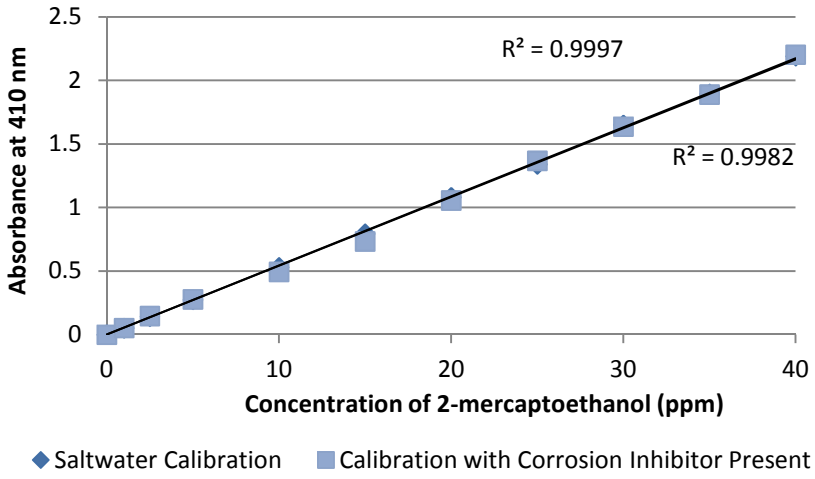

Figure 9.16: Measured absorbance levels at 410 nm when 2-mercaptoethanol is derivatised by DTNB at concentrations between 0 and 40 ppm (values of absorbance for the sample prior to the addition of the reagent have been subtracted from initial values)

9.7.3 Static Tests with 2-mercaptoethanol – *In-situ* Residual Analysis

9.7.3.1 20 ppm 2-mercaptoethanol

To demonstrate how this technique can be used in conjunction with electrochemical measurements, the performance of ME was reviewed in static conditions and samples of the solution were removed from the vessel throughout the test for analysis.

Static tests were performed on carbon steel samples in CO_2-saturated brine at 45ºC for 8 hours in conditions identical to those described in Section 7.2.4. One litre of the brine solution was used in each static experiment, with the working electrode being allowed to pre-corrode for 2 hours before ME was introduced to the system.

Tests were also performed with selected components from Inhibitor B (anhydride/polyamine reaction product, quaternary ammonium salt and imidazoline derivative) which contained 20 ppm of ME to demonstrate that the concentration could be determine when incorporated into a mixture of various other chemicals.

The corrosion rates of the samples were measured by polarising the sample from 15 mV below E_{corr} to 15 mV above E_{corr}. The polarisation resistance was calculated from the potential-current relationship and converted to a corrosion rate based on measured values of β_a and β_c recorded from the end of the test.

ME was added after 2 hours of pre-corrosion and the residual concentration of the solution was monitored every hour. The corrosion rate and residual concentration of ME as a function of time are provided in Figure 9.17.

ME was able to reduce the corrosion rate to approximately 0.08 mm/year, which represents a reduction in corrosion rate of 97%. Taking into account the small error associated with the residual measurements, there was no significant change in the concentration of the chemical over the test duration.

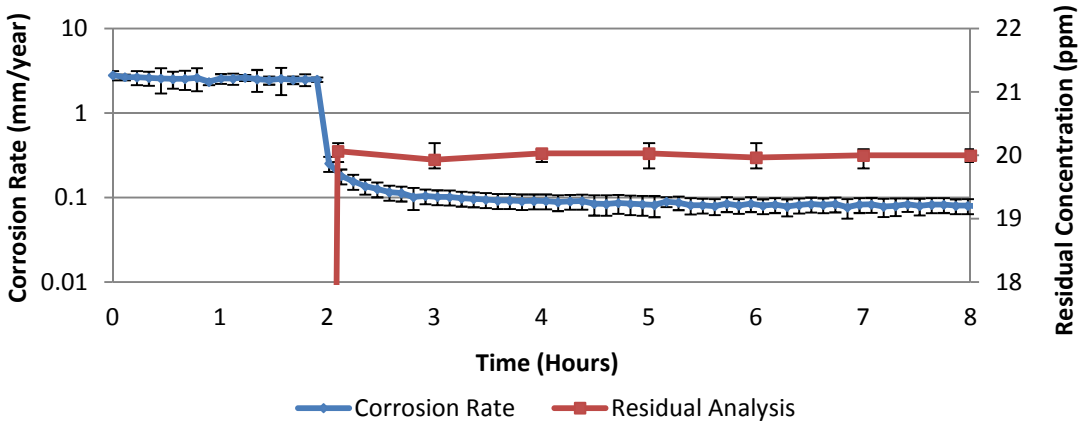

Figure 9.17: Corrosion rates and residual analysis of carbon steel as a function of time for the application of 20 ppm 2-mercaptoethanol in static solutions with chemical addition after 2 hours. Test conditions were: static, 45°C and CO_2-saturated at 1 bar

9.7.3.2 20 ppm 2-mercaptoethanol in 100 ppm Corrosion Inhibitor

Results for the application of 100 ppm of corrosion inhibitor containing 20 ppm ME in static conditions is provided in Figure 9.18 along with the residual ME concentration measurements. Again, no noticeable change in ME was detected, which is to be expected due to the small surface area of metal (1 cm^2) exposed to the solution. The measured corrosion rate was reduced further to 0.03 mm/year because of the presence of other chemicals to complement ME.

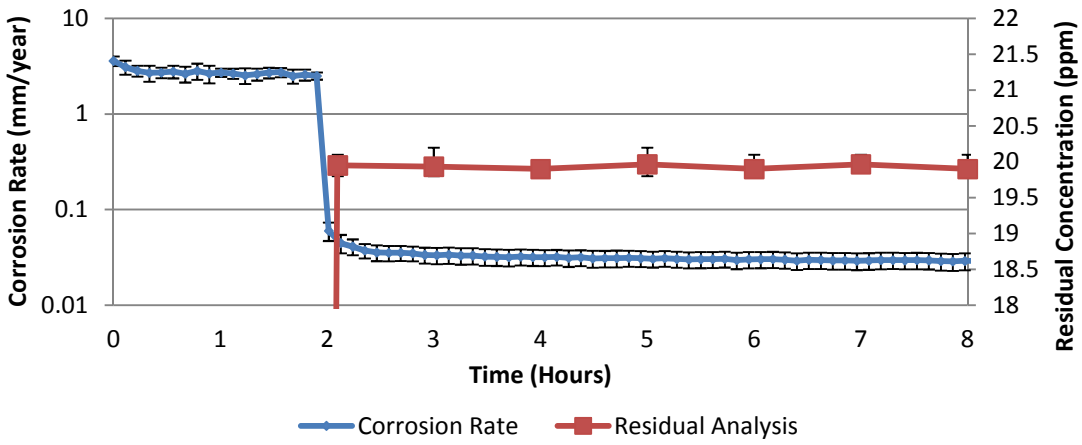

Figure 9.18: Corrosion rates and residual analysis of carbon steel as a function of time for the application of 100 ppm corrosion inhibitor containing 20 ppm 2-mercaptoethanol in static solutions with chemical addition after 2 hours. Test conditions were: static, 45°C and CO_2-saturated at 1 bar

9.8 Effect of Sand Presence on Inhibitor Performance and Residual Inhibitor Concentrations

McMahon et al. [246] examined the effect of produced sand on the efficiency of a number of commercially available CO_2 corrosion inhibitors. The formulations and chemistries of the inhibitors were commercially sensitive, but the results indicated that these chemicals were capable of adsorbing onto the surface of sand particles and reducing the residual concentration in the bulk solution. McMahon and co-workers noticed a distinct increase in carbon steel corrosion rate with increasing sand concentration. However, no residual analysis measurements of the chemicals in the system were performed. Instead, McMahon [246] produced a calibration curve of corrosion rates against concentrations for inhibited systems without sand in static conditions. Tests were then repeated in the presence of sand for a given concentration and the increase in corrosion rate was used to approximate the reduction in residual concentration.

This section of work focuses on implementing the ME assay to determine the influence of sand presence on residual concentration. Tests were repeated in static conditions with the addition of 1000 and 10000 mg/L sand. The sample was pre-corroded for 2 hours before inhibition. The residual concentration of ME was recorded every hour, as in tests for the previous section.

To allow the inhibitor to adsorb onto the sand particles, two beakers were set up for each test. The first beaker was used for pre-corrosion and the second beaker contained the same brine solution with sand particles and inhibitor, which has been

stirred in the test solution for 1 hour. When pre-corrosion of the sample had finished, the working electrode, reference and counter were transferred over to the second beaker and polarisation measurements were continued. This is similar to the approach adopted by McMahon et al. [246], but the implementation of two beakers for one test ensured that the pre-corroded sample could be transferred back into the test solution immediately, significantly reducing the chances of the surface being contaminated.

Despite the introduction of sand into the system, Figure 9.19 clearly shows that no significant reduction of ME could be detected in the bulk solution as a result of the sand presence using the colorimetric technique. There was also no change in the corrosion rates despite the large quantity of sand being introduced. These results suggest that the adsorption (if any) of ME onto sand particles is negligible in the given conditions.

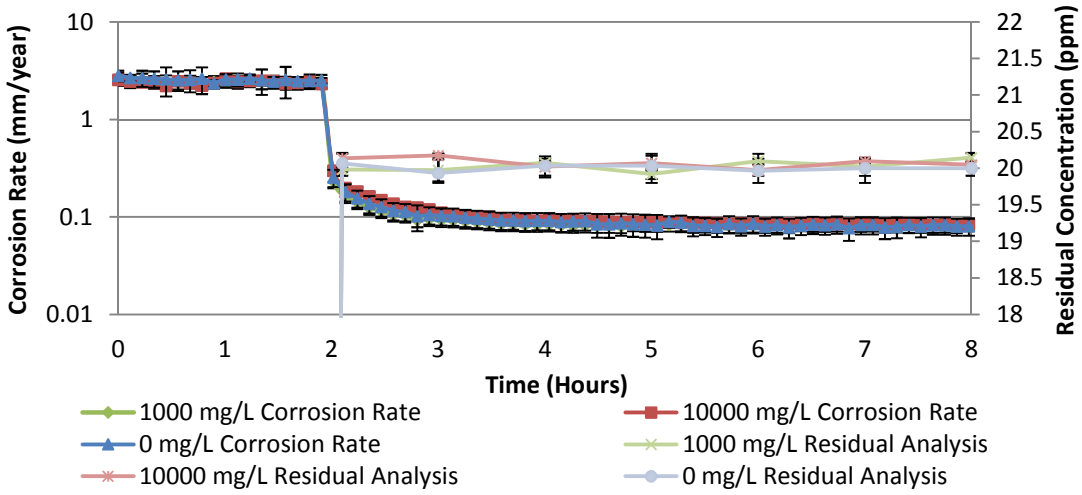

Figure 9.19: Corrosion rates of carbon steel as a function of time for the application of 2-mercaptoethanol at 20 ppm in static solutions with addition after 2 hours. Residual concentration of the chemical is also provided. Test conditions were: static, 45°C, CO_2-saturated at 1 bar with the addition of 1000 or 10000 mg/L sand

Tests performed with the addition of 20 ppm ME within 100 ppm of Inhibitor components (shown in Figure 9.20) also indicated no distinct change in ME residual concentration throughout the test. However, an interesting change in inhibitor adsorption was evident when considering the corrosion rate as a function of time.

Although the introduction of sand to the system may not have significantly affected the corrosion rate at the end of the test (unlike test performed by McMahon et al.

[246]), there is a distinct difference in the rate of decrease in the corrosion rate of the carbon steel.

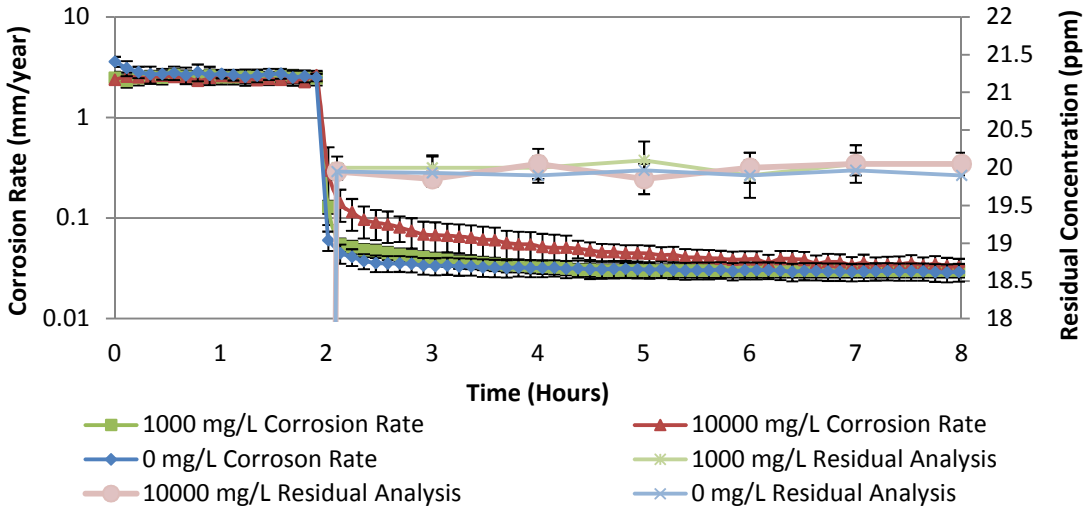

Figure 9.20: Corrosion rates of carbon steel as a function of time for the application of 100 ppm corrosion inhibitor (containing 20 ppm 2-mercaptoethanol) in static solutions with addition after 2 hours Residual concentration of the chemical is also provided. Test conditions were: static, 45°C, CO_2-saturated at 1 bar with the addition of 500, 1000 or 10000 mg/L sand

McMahon et al. [246] determined that the adsorption of chemicals onto sand particles only became significant for the chemicals studied at high concentrations of sand (>1000mg/L). The findings presented here tend to agree with their study in that 1000 mg/L of sand appears to cause a very slight (but not significant) change in the rate decline in corrosion rate, suggesting that the minimum sand concentration required to cause noticeable adsorption effects is close to this concentration.

As mentioned, no significant reduction in ME concentration could be detected using the colorimetric technique. This suggests that the slower rate of corrosion decline is attributed to the adsorption of one of the other inhibiting components onto the sand particles i.e. the anhydride polyamine reaction product, the quaternary ammonium salt or the imidazoline derivative.

It is known that nitrogen-containing compounds can enter into interactions with silicas, some of which are particularly strong [279]. The possible interaction mechanisms of nitrogen-containing compounds such as amines is shown in Figure 9.21. The reported affinity between cationic species and silica may help to explain why an anionic species such as ME failed to interact with the sand particles. This is

an area which will require further study for the exact component(s) to be identified which have adsorbed onto the sand surface.

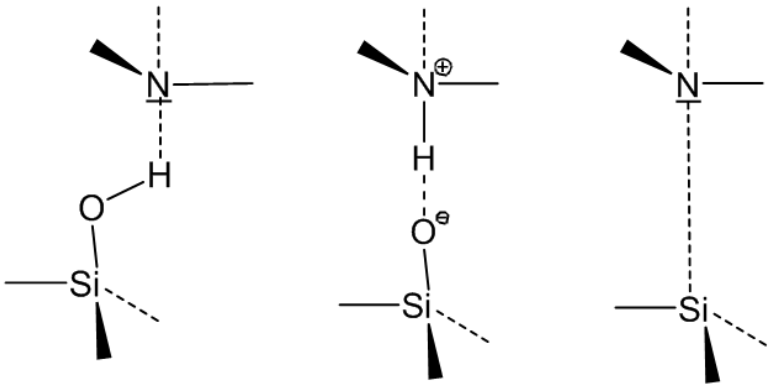

(a) (b) (c)

Figure 9.21: Possible interfacial forms of the interactions between a nitrogen-containing compound and a silica surface: (a) Hydrogen bridge linkage, (b) Brönsted interaction and (c) Lewis-interactions [279, 280]

9.9 Conclusions

This Chapter presented a systematic review of the synergistic effects which occur between four key inhibitor components (anhydride/polyamine reaction product, imidazoline derivative, quaternary ammonium salt and 2-mercaptoethanol) in one particular environment.

- Through the application of a test matrix consisting of 14 jet impingement experiments the level of synergy promoted by each chemical in reducing corrosion rate was quantified.
- The tests indicated that ME was the most active and influential component in reducing corrosion rate of carbon steel in the test environment considered.
- Determination of thermodynamic data through adsorption isotherms allowed a more advanced understanding of the mechanisms associated with how ME interacts with the metal surface. The adsorption process was attributed unequivocally to chemisorption.
- A spectrophotometric technique was presented and employed to determine the concentration of ME in CO_2-saturated saltwater solutions involving a colorimetric reaction using 5,5'-dithio-bis-(2-nitrobenzoic acid) (DTNB).
- The technique was shown to be unaffected by the other inhibiting components tested in this work and was implemented in static corrosion tests which indicated no significant depletion in ME concentration after being administered to the test solution.

- The presence of sand in the system produced no effect on *in-situ* corrosion rate or the residual concentration of ME in static tests when ME was the only inhibiting chemical present.
- A change in *in-situ* corrosion rate was observed when ME was present with other chemicals, but no change in ME residual concentration was observed, suggesting that one of the other chemical components possess an affinity for the surface of sand particles.

Chapter 10 - Final Conclusions and Future Considerations

The thesis presented has established a link between an engineering issue and scientific research for an erosion-corrosion related problem on an oil and gas facility. Based on the findings of this study, the following conclusions can be made, which have been divided into project specific and scientific conclusions:

10.1 Chapter 6 Conclusions

Chapter 6 presented the development of an empirical prediction model for erosion-corrosion degradation rates on an offshore facility.

- **Project Specific Conclusions**
    - By systematically considering the environmental and physical conditions on the facility, it was possible to accurately predict degradation rates on the lines in question between 2005 and 2010 and plot the thickness loss of the pipework as a function of time using the mass loss results from a SIJ.
    - The rates of degradation predicted for the facility agreed closely with the inspection data provided, producing a more accurate interpretation than that of the commercially available CO_2 corrosion models of de Waard and Milliams and Norsok.
    - A review of the current inhibition strategy on the facility was conducted, which was subsequently incorporated into the model. The current inhibitor was found to be under-performing significantly because of the system being under-dosed.
    - A graphical user interface was developed for the empirical model which provides the degradation rate on the facility as a function of time and monitors the total thickness loss of the pipework based on input parameters of sand concentration, flow velocity and inhibitor efficiency.
- **Scientific Conclusions**
    - The use of CFD to model the hydrodynamics of the SIJ indicated that the degradation rates predicted by the SIJ were higher than that predicted by the IFE flow loop (Norsok model) because of differing levels of turbulence in each system which produced markedly different levels of wall shear stress.
    - When accounting for the differences in wall shear stress, the correlation between the two models was greatly improved, indicating that this parameter may be useful when making hydrodynamic comparisons between systems.

10.2 Chapter 7 Conclusions

Chapter 7 reviewed the performance of the current inhibitor used on the oil and gas facility in comparison to two other candidate inhibitors in both static and dynamic conditions at concentrations between 10 and 100 ppm.

- **Project Specific Conclusions**
    - The three inhibitors evaluated behaved considerably differently in static in comparison to dynamic conditions, in particular the current inhibitor on the facility. The fact that the current inhibitor was so sensitive to flow may explain why this chemical may have been recommended at an insufficient concentration. The results highlighted the importance in replicating the hydrodynamic conditions on the facility in the laboratory to prevent the selection of the wrong chemical at an insufficient dose rate.
    - In blank, dynamic conditions at 7 m/s, the formation of Fe_3C on the surface of the material was identified and was shown to act as an accelerant to the cathodic reaction, increasing the rate of anodic dissolution. The revealing of Fe_3C was also believed to have caused pitting on the surface of the material.
    - For short pre-corrosion times, impedance measurements revealed that the inhibitors experienced an increase in efficiency and were capable of interacting with Fe_3C to improve their efficiency.
    - The introduction of sand into the system caused an increase in degradation rate of carbon steel and a decrease in the efficiency of some of the corrosion inhibitors used.
    - An alternative inhibitor was found to the current inhibitor which was capable of reducing degradation rate in erosion-corrosion environments at 7 m/s by over 92%.
- **Scientific Conclusions**
    - AC impedance measurements were conducted to understand the dissolution behaviour of carbon steel in the blank environment under dynamic conditions. The implementation of this form of electrochemistry was shown to be a practical technique for identifying and understanding corrosion mechanisms. This was achieved by modelling the dissolution process using equivalent circuits and relating the observed behaviour to the changes in electrochemical parameters in these circuits.
    - The presence of inductive behaviour in the Nyquist plots from impedance measurements was related to the revealing of a Fe_3C network and the adsorption of intermediate products onto the surface of the sample. Extrapolating the inductive loop to the real axis

provided a resistance value which produced a more accurate assessment of corrosion rate than the charge-transfer resistance extracted from the equivalent circuit.

- AC impedance was demonstrated as being a practical technique when evaluating inhibitor film formation, providing resistance and capacitance values associated with the EDL.

- The percentage reduction in EDL capacitance and the percentage increase in polarisation resistance were shown to be two methods of estimating inhibitor efficiency. However, these techniques possessed limitations, particularly if the inhibitor affected the dielectric constant or the inhibitors influenced the Stern-Geary coefficient. The most accurate form of analysis was provided when polarisation resistance measurements were used in conjunction with measured Tafel slope values.

- Impedance measurements in inhibited environments for pre-corroded samples demonstrated that the inhibitors possessed another means of inhibition in addition to blocking active sites through surface adsorption. The low frequency response of the impedance measurements indicated that the inhibitors are capable of interacting with Fe_3C to create a diffusion barrier to aggressive species involved in the corrosion reactions. Interestingly, this interaction of the inhibitor with Fe_3C helped to improve inhibitor performance for all three chemical evaluated.

- The presence of sand in the system has been shown to cause disruption to the inhibitor film forming process, either through the removal of the protective layer through particle impingement, or by a reduction in the residual concentration of the bulk solution as a result of chemical adsorption onto the surface of sand particles.

10.3 Chapter 8 Conclusions

Chapter 8 evaluated the performance of four commercially available chemicals in extreme erosion-corrosion environments through a combination of gravimetric analysis, *in-situ* electrochemistry and surface profilometry.

- **Project Specific Conclusions**

  - The combination of *in-situ* electrochemistry and gravimetric analysis in erosion-corrosion environments can help quantify the contribution of erosion and corrosion in the system, which is important for identifying the correct measures required to mitigate the degradation effectively.

  - Certain chemicals have indicated that they possess the ability to reduce not only corrosion, but the erosion component of damage attributed to sand particle impingement.

- **Scientific Conclusions**

    - The implementation of surface profilometry is an important aspect of inhibitor evaluation, particularly in erosion-corrosion environments. Results have indicated that gravimetric measurements and *in-situ* electrochemistry can potentially be misleading when determining inhibitor efficiencies when both erosion and corrosion are present.

    - Corrosion inhibitors were found to adsorb onto the surface of sand particles using FT-IR measurements. It was postulated that this process could potentially help in the reduction of erosion damage by adsorbing some of the impact energy of sand particles when they impact the steel surface, or by altering the path of particles within the flow. However, this process would deplete the inhibitor concentration in the bulk solution and potentially affect the inhibitor efficiency.

10.4 Chapter 9 Conclusions

Chapter 9 presented a review of the synergistic effects which occur between four key inhibitor components in a particular set of environments, whilst also tailoring a colorimetric detection technique for the residual analysis of the most active chemical.

- **Project Specific Conclusions**

    - The most active chemical within the components of Inhibitor B tested was 2-mercaptoethanol for the particular environment considered.

    - A spectrophotometric technique was presented which was able to determine the concentration of 2-mercaptoethanol in CO_2-saturated saltwater solutions involving a colorimetric reaction with DTNB.

- **Scientific Conclusions**

    - The use of adsorption isotherms to determine thermodynamic data provided a more advanced understanding of the mechanisms associated with how ME interacts with the metal substrate i.e. through a chemisorption process.

    - The residual analysis technique was shown to be unaffected by the presence of other inhibiting components from Inhibitor B.

    - The analysis technique was implemented in static conditions, which indicated that there was no significant depletion in ME concentration after being administered to the test solution because of the small surface area of the sample.

    - The presence of sand in the system produced no noticeable effect on the *in-situ* corrosion rate or the residual concentration of ME in static tests when ME was administered on its own.

- A change in *in-situ* corrosion rate was observed when ME was present with other components from Inhibitor B, but no change in ME residual concentration was observed, suggesting one of the other components possessed an affinity for the surface of the sand particles.

10.5 Industrial Relevance

- **Chapter 6**
  - the SIJ is a useful tool for assessing the susceptibility of pipeline materials to flow-induced corrosion environments providing that:
    (a) the environmental and physical conditions on the facility are accurately replicated or there is at least an understanding of the effect of changes in certain unknown parameters which can allow for accurate assumptions to be made regarding their effect.
    (b) the SIJ and flow lines are hydro-dynamically characterised to enable a direct comparison of behaviour to be made between the systems using wall shear stress.
- **Chapter 7**
  - The SIJ is capable of producing severe conditions which can test inhibitor performance in extreme conditions, ensuring the best inhibitor is chosen for a particular application.
  - AC impedance has been identified as a useful technique to help understand how inhibitors interact with polished and pre-corroded carbon steel surfaces, as well as helping to determine *in-situ* corrosion rates.
  - The research indicated that changes in the hydrodynamic severity and the presence of sand in the system can have adverse effects on the performance of inhibitors. It is essential to replicate conditions on a facility accurately in the laboratory in order to be able to understand the true efficiency of the chemicals evaluated.
- **Chapter 8**
  - Chapter 8 demonstrated that specific film-forming inhibitors are capable of reducing the effect of pure erosion in erosion-corrosion environments, which can potentially allow carbon steel to be used in environments where there is a low sand concentration, preventing more expensive materials from being used.
  - Corrosion engineers need to be aware that the presence of sand particles in a system can not only increase *in-situ* corrosion rates by causing disruption to inhibitor films and causing pure erosion, but it is also possible for these chemicals to adsorb onto sand particles,

reducing their concentration in the bulk solution, affecting their inhibition efficiency.

- Companies need to be cautious when evaluating inhibitors in erosion-corrosion environments using electrochemistry and mass loss measurements if using a SIJ. Profilometry results indicated that these measurements alone can be misleading, providing an inaccurate interpretation of inhibitor efficiency.

- **Chapter 9**

  - Chapter 9 demonstrated how easily a residual analysis technique can be tailored for a particular inhibitor component. The main issue hindering the development of these techniques for oil and gas residual analysis is that the papers pertaining to these methods are not readily available. Implementing fast monitoring techniques such as these could significantly minimise the risk of production loss, saving oil and gas companies a considerable amount of money and time.

10.6 Future Considerations

Chapter 6 demonstrated the value of shear stress as a parameter to correlate corrosion rates observed in the laboratory with those in the field. To develop the erosion-corrosion model further, it is suggested that changes to the geometry of the specimen are made.

Based on the CFD analysis it was clear that the shear stress distribution was not uniform over the surface of the sample. However, towards the outer edge of the sample, the level of wall shear stress did stabilise. With the value of shear stress being used to relate corrosion rates seen in the laboratory to those witnessed in the field, it would be beneficial to have a constant value over the sample surface.

The introduction of ring shaped samples in the SIJ would subject the carbon steel to a more stable value of shear stress to allow a more accurate correlation of corrosion rate with this parameter, which would inevitably help in determining rates in the field. Additionally, the use of ring shaped samples would ensure a limited range of impact angles for sand particles, enabling focus to be directed towards understanding the erosion mechanisms more clearly, rather than having a range of impact angles from 0° to 90°.

A deeper understanding of the hydrodynamics in the system and the ability to map corrosion rates onto the actual pipework geometry based on the wall shear stress would be beneficial to help target areas where high corrosion rates or localised attack would be expected.

Chapter 7 considered the effects of pre-corrosion on carbon steel and how this affected the AC impedance behaviour. It would be useful to study longer pre-corrosion times to determine how this may affect the AC impedance measurements. Additionally, reviewing the behaviour of this material in higher temperature environments where $FeCO_3$ formation would occur and relating this to the inhibitor performance using the AC impedance technique may yield some interesting results.

Chapter 8 highlighted the potential for inhibitors to be able to reduce the effects of pure erosion. The initial study in this thesis was to determine whether these chemicals conclusively reduced the erosion component of damage. This objective was achieved, however, it is suggested that the properties of the film which has formed on the surface of the sample, together with the adsorption of components onto the sand particles are explored further do develop a complete understanding of how erosion effects are mitigated in the experiments conducted.

Results in Chapter 9 suggested that one of the components other than 2-mercaptoathanol adsorbed onto the surface of sand particles as the *in-situ* corrosion rate was affected. This process could be explored in more detail and the exact component which adsorbs onto the sand particles could be determined. Finally, other detection techniques could be explored for other well-known inhibiting components. Two suggestions based on a review of literature are:

- the technique proposed by Lowry and Tinsley [281] for the determination of free fatty acids. The concentration was determined by monitoring the colour developed using cupric acetate-pyridine and was later improved upon by Kwon and Rhee [282]. This method has potential to be used as a residual analysis technique for long chain fatty acids, which are a common component of corrosion inhibitors [138, 166, 283]. An alternative colorimetric analysis was also provided by Munson and Bilous [284] based on the reaction with 2-nitrophenylhydrazine

- the techniques developed by Slack and Mader [285] for the detection of a number of substituted imidazolines, a compound which has shown a lot of potential in corrosion inhibition [138, 244, 256-258, 286]. The method involves a reaction with sodium nitroprusside in alkalines to produce a violet coloured solution which obeys Beer's law.

References

1. M.B. Kermani and A. Morshed, "Carbon Dioxide Corrosion in Oil and Gas Production - A Compendium", Corrosion Science, 59, 8 (2003): pp. 659-683.
2. C. Wang, *Erosion-Corrosion Mitigation Using Chemicals*, in *School of Mechanical Engineering*. 2007, University of Leeds.
3. M.M. Salama, "Sand Production Management", Journal of Energy Resources Technology, 122, 1 (2000): pp. 29-33.
4. M.M. Salama, "Influence of Sand Production on Design and Operations of Piping Systems", CORROSION 2000, paper no. 80, (Orlando, FL: NACE, 2000).
5. J. Tronvoll, M.B. Dusseault, F. Sanfilippo, and F.J. Santarelli, "The Tools of Sand Management", SPE Annual Technical Conference and Exhibition, (New Orleans, Louisiana, 2001).
6. K. Dave, K.P. Roberts, J.R. Shadley, E.F. Rybicki, S. Ramachandran, and V. Jovancicevic, "Effect of a Corrosion Inhibitor for Oil and Gas Wells when Sand is Produced", CORROSION 2008, paper no. 570, (New Orleans, LA: NACE, 2008).
7. M.M. Stack and G.H. Abdulrahmen, "Mapping Erosion-Corrosion of Carbon Steel in Oil Exploration Conditions: Some New Approaches to Characterizing Mechanisms and Synergies", Tribology International, 43, (2010): pp. 1268-1277.
8. A. Akbar, X. Hu, A. Neville, and C. Wang, "The Influence of Flow Rate And Inhibitor On The Protective Layer Under Erosion-Corrosion Conditions Using Rotating Cylinder Electrode", CORROSION 2011, paper no. 274, (Houston, TX:NACE, 2011).
9. A. Akbar, X. Hu, C. Wang, and A. Neville, "The Influence of Flow Rate, Sand And Inhibitor On Iron Carbonate Scales Under Erosion-Corrosion Conditions Using A Submerged Impingement Jet", CORROSION 2012, paper no. 1396, (Salt Lake City, UT:NACE, 2012).
10. B. Brown and S. Nesic, "CO_2/H_2S Corrosion under Scale Forming Conditions", CORROSION 2005, paper no. 625, (Houston, TX:NACE, 2005).
11. B. Brown, S. Nesic, and S.R. Parakala, "CO_2 Corrosion in the Presence of Trace Amounts of H_2S", CORROSION 2004, paper no. 736, (New Orleans, LA:NACE, 2004).
12. B. Brown, K.-L. Lee, and S. Nesic, "Corrosion in Multiphase Flow Containing Small Amounts of H_2S", CORROSION 2003, paper no. 341, (San Diego, CA:NACE, 2003).
13. S.N. Smith, B. Brown, and W. Sun, "Corrosion At Higher H_2S Concentrations and Moderate Temperatures", CORROSION 2011, paper no. 81, (Houston, TX:NACE, 2011).
14. H. Fang, B. Brown, and S. Nesic, "High Salt Concentration Effects on CO_2 Corrosion and H_2S Corosion", CORROSION 2010 paper no. 276, (San Antonio, TX:NACE, 2010).
15. M. Martinez, K. Alawadhi, M. Robinson, G. Nelson, and A. MacDonald, "Control of Preferential Weld Corrosion of X65 Pipeline Steel In Flowing Brines Containing Carbon Dioxide", CORROSION 2011, paper no. 268, (Houston, TX: NACE, 2011).
16. S.P.V. Mahajanam and M.W. Joosten, "Guidelines for Filler-Material Selection to Minimize Preferential Weld Corrosion in Pipeline Steels", SPE Projects, Facilities & Construction, 6, 1 (2011): pp. 5-12.

17. S.P.V. Mahajanam and M.W. Joosten, "Selection of Filler Materials to Minimize Preferential Weld Corrosion in Pipeline Steels", SPE International Conference on Oilfield Corrosion, (Aberdeen, UK, 2010).
18. N. Bretherton, S. Robb, K.G. Richterova, D. Donaldson, and R.G. Smith, "Impact of Acetic Acid on Weld Corrosion and its Mitigation", CORROSION 2009, paper no. 562, (Atlanta, GA: NACE, 2009).
19. K. Alawadhi, M. Robinson, A. Chalmers, and I.G. Winning, "Inhibition of Weld Corrosion in Flowing Brines Containing Carbon Dioxide", CORROSION 2008, (New Orleans, LA: NACE, 2008).
20. A. Chalmers, S. McNeil, D. McNaughtan, and I.G. Winning, "Laboratory Development of a Corrosion Inhibitor for a North Sea Main Oil Line Offering Enhanced Environmental Properties and Weld Corrosion Protection", CORROSION 2006, paper no. 487, (San Diego, CA: NACE, 2006).
21. S. Turgoose and J.W. Palmer, "Preferential Weld Corrosion of 1% Ni Welds: Effects of Solution Conductivity and Corrosion Inhibitors", CORROSION 2005, paper no. 275, (Houston, TX: NACE, 2005).
22. C.M. Lee and P. Woollin, "Preferential Weld Corrosion: Effects of Weldment Microstructure and Composition", CORROSION 2005, paper no. 277, (Houston TX: NACE, 2005).
23. H. Craddock, B. Daneilsen, A. Mamann, and S. Caird, "Preferential Weld Protection Corrosion Inhibitor for Topsides Gas Producing Facility under High Shear and "Sweet" Condition", CORROSION 2004, paper no. 425, (New Orleans, LA: NACE, 2004).
24. M. Salama and B. Brown, "A Study of Factors Affecting CO_2 Corrosion and Inhibitor Effectiveness using a Multi-phase Flowloop", CORROSION 2009, paper no. 476, (Atlanta, GA:NACE, 2009).
25. G.T. Burstein, C. Liu, R.M. Souto, and S.P. Vines, "Origins of Pitting Corrosion", Corrosion Engineering, Science and Technology, 39, 1 (2004): pp. 25-30.
26. J.L. Crolet, N. Thevenot, and S. Nesic, "Role of Conductive Corrosion Products in the Protectiveness of Corrosion Layers", Corrosion Science, 54, 3 (1998): pp. 194-203.
27. M.B. Kermani and D. Harrop, "The Impact of Corrosion on Oil and Gas Industry", SPE Production & Operations, 11, 3 (1996): pp. 186-190.
28. C.T. Savell and C. Handsy, "How to Extract Corrosion Rates, Cost of Corrosion and Fleet Readiness from Field Data", CORROSION 2003, paper no. 236, (San Diego, CA:NACE, 2003).
29. G.H. Koch, M.P. Brongers, N.G. Thompson, P. Virmani, and J.H. Payer, "Corrosion Cost and Preventative Strategies in the United States", NACE International, (2002).
30. C.J. Cron and G.A. Marsh, "Overview of Economic and Engineering Aspects of Corrosion in Oil and Gas Production", SPE Journal of Petroleum Technology, 35, 6 (1983): pp. 1033-1041.
31. L.H. Bennett, J. Kruger, R.L. Parker, E. Passaglia, C. Reimann, A.W. Ruff, H. Yakowitz, and E.B. Berman, *Economic Effects of Metallic Corrosion in the United States*, in *NBS Special Publication 511-1*. 1978, National Bureau of Standards, Washington.
32. P.R. Roberge, *Handbook of Corrosion Engineering*. 2000, New York; London: McGraw-Hill.
33. E.E. Stansbury and R.A. Buchanan, *Fundamentals of Electrochemical Corrosion*. 2000: ASM International.
34. J.R. Davis, *Corrosion: Understanding the Basics*. 2000, Materials Park, Ohio: ASM International.
35. N. Perez, *Electrochemistry and Corrosion Science*. 2004: Kluwer Academic.

36. X. Hu, *The Corrosion and Erosion-Corrosion Behaviour of High Alloy Stainless Steels*, in *School of Mechanical Engineering*. 2003, University of Leeds.
37. S.A. Bradford, *Corrosion Control*. 2001: CASTI Publications.
38. S.W. Tait, *An Introduction to Electrochemical Corrosion Tesing for Practicing Engineers and Scientists*. 1994, Racine, WI: Pair O Docs Publications.
39. D.R. Crow, *Principles and applications of electrochemistry*. 1994: S. Thornes.
40. J.R. Scully, "Polarization Resistance Method for Determination of Instantaneous Corrosion Rates", Corrosion, 56, 2 (2000): pp. 199-221.
41. M. Stern, "A Method for Determining Corrosion Rates from Linear Polarization Data", Corrosion, 14, (1958).
42. ASTM-G102, "Calculation of Corrosion Rates and Related Information for Electrochemical Measurements", (West Conshohocken, PA: ASTM, 2010).
43. M.E. Orazem, "A Tutorial on Impedance Spectroscopy", CORROSION 98, paper no. 302, (San Diego, CA:NACE, 1998).
44. B. Kermani, K.A. Esaklul, and J.W. Martin, "Materials Design Strategy: Effects of H_2S/CO_2 Corrosion on Materials Selection", CORROSION 2006, paper no. 121, (San Diego, CA,NACE, 2006).
45. S. Nesic, H. Li, J. Huang, and D. Sormaz, "An Open Source Mechanistic Model for CO_2/H_2S Corrosion of Carbon Steel", CORROSION 2009, paper no. 572, (Atlanta, GA, 2009).
46. C. deWaard and D.E. Milliams, "Carbonic Acid Corrosion of Steel", Corrosion Science, 31, 5 (1975): pp. 131-135.
47. B.R. Linter and G.T. Burstein, "Reactions of Pipeline Steels in Carbon Dioxide Solutions", Corrosion Science, 41, 1 (1999): pp. 117-139.
48. S. Nesic, J. Postlethwaite, and S. Olsen, "An Electrochemical Model for Prediction of Corrosion of Mild Steel in Aqueous Carbon Dioxide Solutions", Corrosion Science, 52, 4 (1996): pp. 280-294.
49. S. Nesic, "Key Issues Related to Modelling of Internal Corrosion of Oil and Gas Pipelines - A Review", Corrosion Science, 49, 12 (2007): pp. 4308-4338.
50. J.O.M. Bockris, D. Drazic, and A.R. Despic, "The Electrode Kinetics of the Deposition and Dissolution of Iron", Electrochimica Acta, 4, 2-4 (1961): pp. 325-361.
51. S. Nesic, D. Drazic, N. Thevenot, and J.L. Crolet, "Electrochemical Properties of Iron Dissolution in the Presence of CO_2 - Basics Revisited", CORROSION 96, paper no. 3, (Denver, CO: NACE, 1996).
52. W.H. Durnie and D. Harrop, "Our Water Chemistry Contains Organic Acids: So What Does It Mean?", SPE International Oilfield Corrosion Symposium, (Aberdeen, UK, 2006).
53. E. Gulbrandsen and K. Bilkova, "Solution Chemistry Effects on Corrosion of Carbon Steels in Presence of CO_2 and Acetic Acid", CORROSION 2006, paper no. 364, (San Diego, CA:NACE, 2006).
54. G. Schmitt and M. Horstemeier, "Fundamental Aspects of CO_2 Metal Loss Corrosion - Part II: Influence of Different Parameters on CO_2 Corrosion Mechanisms", CORROSION 2006, paper no. 112, (San Diego, CA:NACE, 2006).
55. A. Dugstad, "Fundamental Aspects of CO_2 Metal Loss Corrosion - Part 1: Mechanism", CORROSION 2006, paper no. 111, (San Diego, CA:NACE, 2006).
56. A. Dugstad, H. Hemmer, and M. Seiersten, "Effect of Steel Microstructure Upon Corrosion Rate and Protective Iron Carbonate Film Formation", CORROSION 2000, paper no. 24, (Orlando, FL:NACE, 2000).

57. A. Dugstad, "Mechanism of Protective Film Formation During CO_2 Corrosion of Carbon Steel", CORROSION 98, paper no. 31, (San Diego, CA:NACE, 1998).
58. C. deWaard, D.E. Milliams, and U. Lotz, "Predictive Model for CO_2 Corrosion Engineering in Wet Natural Gas Pipelines", CORROSION 91, paper no. 577, (Houston, TX: NACE, 1991).
59. C. deWaard and U. Lotz, "Prediction of CO_2 Corrosion of Carbon Steel", CORROSION 93, paper no. 69, (Houston, TX: NACE, 1993).
60. C. deWaard, L. Smith, P. Bartlett, and H. Cunningham, "Modelling Corrosion Rates in Oil Production Tubing", EUROCORR 2001, paper no. 254, (Riva del Garda, Italy, 2001).
61. F. Ayello, W. Robbins, S. Richter, and S. Nesic, "Crude Oil Chemistry Effects on Inhibition of Corrosion and Phase Wetting", CORROSION 2011, paper no. 60, (Houston, TX:NACE, 2011).
62. C. Mendez, S. Hernandez, J.R. Vera, and S. Dupla, "On the Mechanism of Corrosion Inhibition by Crude Oils", CORROSION 2001, paper no. 30, (Houston, TX:NACE, 2001).
63. S. Hernandez, J.G. Luzon, J. Bruzual, and F.L. Linares, "Isolation of Potential Corrosion Inhibiting Compounds in Crude Oils", CORROSION 2003, paper no. 330, (San Diego Ca, 2003).
64. W.P. Jepson, M. Gopal, and S. Bhongale, "Predictive Model for Sweet Corrosion in Horizontal Multiphase Slug Flow", CORROSION 96, paper no. 19, (Denver, CO:NACE, 1996).
65. D.A. López, T. Pérez, and S.N. Simison, "The Influence of Microstructure and Chemical Composition of Carbon and Low Alloy Steels in CO_2 Corrosion. A State-of-the-art Appraisal", Materials & Design, 24, 8 (2003): pp. 561-575.
66. B. Kermani, D. Edmonds, J.C. Gonzales, G. Lopez-Turconi, L. Scoppio, and G. Dicken, "Development of Superior Corrosion Resistance 3%Cr Steels for Downhole Applications", CORROSION 2003, paper no. 116, (San Diego Ca, 2003).
67. D. Clover, B. Kinsella, B. Pejcic, and R. De Marco, "The Influence of Microstructure on the Corrosion Rate of Various Carbon Steels", Journal of Applied Electrochemistry, 35, 2 (2005): pp. 139-149.
68. S. Al-Hassan, B. Mishra, D.L. Olson, and M.M. Salama, "Effect of Microstructure on Corrosion of Steels in Aqueous Solutions Containing Carbon Dioxide", Corrosion, 54, 6 (1998): pp. 480-491.
69. E. Dayalan, J.R. Shadley, E.F. Rybicki, S.A. Shirazi, and F.D. deMoraes, "CO_2 Corrosion Prediction in Pipe Flow Under $FeCO_3$ Scale-Forming Conditions", CORROSION 98, (San Diego, CA:NACE, 1998).
70. M. Nordsveen, S.N.R. Nyborg, and A. Stangeland, "A Mechanistic Model for Carbon Dioxide Corrosion of Mild Steel in the Presence of Protective Iron Carbonate Films Part 1: Theory and Verification", Corrosion, 59, 5 (2003): pp. 443-456.
71. S. Nesic, A. Stangeland, M. Nordsveen, and R. Nyborg, "A Mechanistic Model for Carbon Dioxide Corrosion of Mild Steel in the Presence of Protective Iron Carbonate Films Part 2: A Numerical Experiment", Corrosion, 59, 06 (2003).
72. S. Nesic and K.-L.J. Lee, "A Mechanistic Model for Carbon Dioxide Corrosion of Mild Steel in the Presence of Protective Iron Carbonate Films Part 3: Film Growth Model", Corrosion, 59, 07 (2003).
73. S. Nesic, J. Lee, and V. Ruzic, "A Mechanistic Model of Iron Carbonate Film Growth and the Effect on CO_2 Corrosion of Mild Steel", 2002).
74. C. deWaard and D.E. Milliams, "Prediction of Carbonic Acid Corrosion in Natural-Gas Pipelines", First International Conference Internal and External

Protection of Pipes, BHRH Fluid Engineering, paper no. F1, (Bedford, England, 1975): pp. 1-8.
75. B. Hedges, I. Mohammed, Y. Sun, D. Harrop, and R. Chapman, "A Prophetic CO_2 Corrosion Tool - But When is it to be Believed?", CORROSION 2005, paper no. 552, (Houston, TX:NACE, 2005).
76. S.D. Kapusta, I.J. Rippon, and B.F.M. Pots, "The Application of Corrosion Prediction Models to the Design and Operation of Pipelines", CORROSION 2004, paper no. 633, (New Orleans, LA:NACE, 2004).
77. S. Olsen, R. Nyborg, P.G. Lunde, and A.M. Halvorsen, "CO_2 Corrosion Prediction Model - Basic Principles", CORROSION 2005, paper no. 551, (Houston, TX: NACE, 2005).
78. Norsok Standard M-506, "CO_2 Corrosion Rate Calculation Model", Available: http://www.standard.no/PageFiles/1178/M-506d1r2.pdf, Last accessed 6th September 2011.
79. P. Fosbol, K. Thomsen, and E. Stenby, "Improving Mechanistic CO_2 Corrosion Models", CORROSION 2009, paper no. 561, (Atlanta, GA:NACE, 2009).
80. R.C. Woollam and S. Hernandez, "Assessment and Comparison of CO_2 Corrosion Predicition Models", SPE International Oilfield Corrosion Symposium, (Aberdeen, UK, 2006).
81. A.M. Anderko and R.D. Young, "Simulation of CO_2/H_2S Corrosion Using Thermodynamic and Electrochemical Models", CORROSION 99, paper no. 31, (San Antonio, TX:NACE, 1999).
82. K. George, K. deWaard, and S. Nesic, "Electrochemical Investigation and Modeling of Carbon Dioxide Corrosion of Carbon Steel in the Presence of Acetic Acid", CORROSION 2004, paper no. 379, (New Orleans, La, 2004).
83. S. Turgoose, R. Cottis, and K. Lawson, "Modelling of Electrode Processes and Surface Chemistry in Carbon Dioxide Containing Solutions", Symposium on Computer Modelling of Corrosion, (San Antonio, TX: NACE, 1990).
84. S. Nesic, S. Wang, J. Cai, and Y. Xiao, "Integrated CO_2 Corrosion - Multiphase Flow Model", SPE International Symposium on Oilfield Corrosion, (Aberdeen, United Kingdom, 2004).
85. C. deWaard, U. Lotz, and A. Dugstad, "Influence of Liquid Flow Velocity on CO_2 Corrosion: A Semi-Empirical Model", CORROSION 95, paper no. 28, (Orlando, FL: NACE, 1995).
86. C. deWaard, L. Smith, and B.D. Craig, "The Influence of Crude Oils on Well Tubing Corrosion Rates", CORROSION 2003, paper no. 629, (San Diego, CA: NACE, 2003).
87. A. Dugstad, L. Lunde, and K. Videm, "Parametric Study of CO_2 Corrosion of Carbon Steel", CORROSION 94, (Houston, TX: NACE International, 1994).
88. A.M. Halvorsen and T. Sontvedt, "CO_2 Corrosion Model for Carbon Steel Including Wall Shear Stress Model for Multiphase Flow and Limits for Production Rate to Avoid Mesa Attack", CORROSION 99, paper no. 42, (San Antonio, TX: NACE, 1999).
89. I.M. Hutchings, *Tribology: Friction and Wear of Engineering Materials*. 1992, London: Edward Arnold.
90. H.M. Clark, "Particle Velocity and Size Effects in Laboratory Slurry Erosion Measurements OR... Do You Know What Your Particles are Doing?", Tribology International, 35, 10 (2002): pp. 617-624.
91. J.G.A. Bitter, "A Study of Erosion Phenomena: Part I", Wear, 6, 1 (1963): pp. 5-21.
92. J.G.A. Bitter, "A Study of Erosion Phenomena: Part II", Wear, 6, 3 (1963): pp. 169-190.

93. G.T. Burstein and K. Sasaki, "Effect of Impact Angle on the Slurry Erosion-Corrosion of 304L Stainless Steel", Wear, 240, 1-2 (2000): pp. 80-94.
94. K. Sasaki and G.T. Burstein, "Erosion-Corrosion of Stainless Steel under Impingement by a Fluid Jet", Corrosion Science, 49, 1 (2007): pp. 92-102.
95. H.M. Clark and K.K. Wong, "Impact Angle, Particle Energy and Mass Loss in Erosion by Dilute Slurries", Wear, 186-187, Part 2 (1995): pp. 454-464.
96. X. Chen, B.S. McLaury, and S.A. Shirazi, "Application and Experimental Validation of a Computational Fluid Dynamics (CFD)-based Erosion Prediction Model in Elbows and Plugged Tees", Computers & Fluids, 33, 10 (2004): pp. 1251-1272.
97. J.A.C. Humphrey, "Fundamentals of Fluid Motion in Erosion by Solid Particle Impact", International Journal of Heat and Fluid Flow, 11, 3 (1990): pp. 170-195.
98. H.M. Clark, "The Influence of the Flow Field in Slurry Erosion", Wear, 152, 2 (1992): pp. 223-240.
99. H.M. Clark and R.B. Hartwich, "A Re-examination of the `Particle Size Effect' in Slurry Erosion", Wear, 248, 1-2 (2001): pp. 147-161.
100. H.M. Clark, "On the Impact Rate and Impact Energy of Particles in a Slurry Pot Erosion Tester", Wear, 147, 1 (1991): pp. 165-183.
101. A.V. Levy, "The Abrasion/Erosion and Erosion-Corrosion Characteristics of Steels", Wear, 138, 1-2 (1990): pp. 111-123.
102. I.M. Hutchings, "Wear by Particulates", Chemical Engineering Science, 42, 4 (1987): pp. 869-878.
103. I. Finnie, "Erosion of Surfaces by Solid Particles", Wear, 3, 2 (1960): pp. 87-103.
104. A.V. Levy and G. Hickey, "Liquid-Solid Particle Slurry Erosion of Steels", Wear, 117, 2 (1987): pp. 129-146.
105. A.V. Levy, J. Yan, and V.D. Arora, "Sand-Water Slurry Erosion of Carburized AISI 8620 Steel", Wear, 101, 2 (1985): pp. 117-126.
106. I.M. Hutchings, "Strain Rate Effects in Microparticle Impact", Journal of Physics D: Applied Physics, 10, (1977): pp. pp.179-184.
107. K.G. Jordan, "Erosion in Multiphase Production of Oil & Gas", CORROSION 98, paper no. 58, (San Diego, CA:NACE, 1998).
108. M.M. Salama and E.S. Venkatesh, "Evaluation of API RP 14E Erosional Velocity Limitations for Offshore Gas Wells", Offshore Technology Conference, (Houston, Texas, 1983).
109. B.S. McLaury, E.F. Rybicki, J.R. Shadley, and S.A. Shirazi, "How Operating and Environmental Conditions Affect Erosion", CORROSION 99, (San Antonio, Tx, 1999).
110. B.S. McLaury and S.A. Shirazi, "Generalization of API RP 14E for Erosive Service in Multiphase Production", SPE Annual Technical Conference and Exhibition, (Houston, Texas, 1999).
111. B.S. McLaury and S.A. Shirazi, "An Alternate Method to API RP 14E for Predicting Solids Erosion in Multiphase Flow", Journal of Energy Resources Technology, 122, 3 (2000): pp. 115-122.
112. S. Ramachandran, V. Jovancicevic, M.B. Ward, and K.A. Bartrip, "Inhibition of the Effects of Particle Impingement", CORROSION 2002, paper no. 498, (Denver, CO: NACE, 2002).
113. M.M. Salama, "An Alternative to API 14E Erosional Velocity Limits for Sand-Laden Fluids", Journal of Energy Resources Technology, 122, 2 (2000): pp. 71-77.
114. X. Chen, B.S. McLaury, and S.A. Shirazi, "Numerical and Experimental Investigation of the Relative Erosion Severity Between Plugged Tees and Elbows in Dilute Gas/Solid Two-Phase Flow", Wear, 261, 7-8 (2006): pp. 715-729.

115. Q.H. Mazumder, S.A. Shirazi, B.S. McLaury, J.R. Shadley, and E.F. Rybicki, "Development and Validation of a Mechanistic Model to Predict Solid Particle Erosion in Multiphase Flow", Wear, 259, 1-6 (2005): pp. 203-207.
116. A. Gnanavelu, N. Kapur, A. Neville, and J.F. Flores, "An Integrated Methodology for Predicting Material Wear Rates due to Erosion", Wear, 267, 11 (2009): pp. 1935-1944.
117. A. Neville and C. Wang, "Erosion-Corrosion of Engineering Steels - Can it be Managed by Use of Chemicals?", Wear, 267, 11 (2009): pp. 2018-2026.
118. A. Neville and C. Wang, "Erosion-Corrosion Mitigation by Corrosion Inhibitors - An Assessment of Mechanisms", Wear, 267, 1-4 (2009): pp. 195-203.
119. M.M. Stack and F.H. Stott, "An Approach to Modelling Erosion-Corrosion of Alloys using Erosion-Corrosion Maps", Corrosion Science, 35, 5-8 (1993): pp. 1027-1034.
120. M.M. Stack, S.M. Abdelrahman, and B.D. Jana, "A New Methodology for Modelling Erosion-Corrosion Regimes on Real Surfaces: Gliding Down the Galvanic Series for a Range of Metal-Corrosion Systems", Wear, 268, 3-4 (2010): pp. 533-542.
121. M.M. Stack, N. Corlett, and S. Turgoose, "Some Recent Advances in the Development of Theoretical Approaches for the Construction of Erosion-Corrosion Maps in Aqueous Conditions", Wear, 233-235, (1999): pp. 535-541.
122. M.M. Stack, N. Corlett, and S. Zhou, "Impact Angle Effects on the Transition Boundaries of the Aqueous Erosion-Corrosion Map", Wear, 225-229, Part 1 (1999): pp. 190-198.
123. M.M. Stack, N. Corlett, and S. Zhou, "A Methodology for the Construction of the Erosion-Corrosion Map in Aqueous Environments", Wear, 203-204, (1997): pp. 474-488.
124. M.M. Stack and B.D. Jana, "Modelling Particulate Erosion-Corrosion in Aqueous Slurries: Some Views on the Construction of Erosion-Corrosion Maps for a Range of Pure Metals", Wear, 256, 9-10 (2004): pp. 986-1004.
125. M.M. Stack, S. Lekatos, and F.H. Stott, "Erosion-Corrosion Regimes: Number, Nomenclature and Justification?", Tribology International, 28, 7 (1995): pp. 445-451.
126. M.M. Stack and N. Pungwiwat, "Erosion-Corrosion Mapping of Fe in Aqueous Slurries: Some Views on a New Rationale for Defining the Erosion-Corrosion Interaction", Wear, 256, 5 (2004): pp. 565-576.
127. M.M. Stack, S. Zhou, and R.C. Newman, "Identification of Transitions in Erosion-Corrosion Regimes in Aqueous Environments", Wear, 186-187, Part 2 (1995): pp. 523-532.
128. C.G. Telfer, M. Stack, and B. Jana, "Particle Concentration and Size Effects on the Erosion-Corrosion of Pure Metals in Aqueous Slurries", Tribology International, 53, (2012): pp. 35-44.
129. M. Stack and G. Abdulrahman, "Mapping Erosion-Corrosion of Carbon Steel in Oil-Water Solutions: Effect of Velocity and Applied Potential", Wear, 274-275, (2012): pp. 401-413.
130. G.H. Abdulrahman and M.M. Stack, "Erosion-Corrosion Maps for Carbon Steel in Crude Oil/Water Slurries: Impact Angle and Applied Potential Effects", 11th Mediterranean Petroleum Conference and Exhibition, (Tripoli, Libya, 2010).
131. K. Wilson, M.M. Stack, and S.M. Abdelrahman, "CFD of Erosion-Corrosion of Fe : Comparison between Predictive Models", WEAR (In Press), (2012).
132. X. Hu, K. Alzawai, A. Gnanavelu, A. Neville, C. Wang, A. Crossland, and J. Martin, "Assessing the Effect of Corrosion Inhibitor on Erosion-Corrosion of

API-5L-X65 in Multi-Phase Jet Impingement Conditions", Wear, 271, 9-10 (2011): pp. 1432-1437.
133. R.J.K. Wood and S.P. Hutton, "The Synergistic Effect of Erosion and Corrosion: Trends in Published Results", Wear, 140, 2 (1990): pp. 387-394.
134. A. Neville, M. Reyes, and X. Hu, "Examining Corrosion Effects and Corrosion/Erosion Interactions on Metallic Materials in Aqueous Slurries", Tribology International, 35, 10 (2002): pp. 643-650.
135. Y. Zheng, Z. Yao, X. Wei, and W. Ke, "The Synergistic Effect between Erosion and Corrosion in Acidic Slurry Medium", Wear, 186-187, 1 (1995): pp. 555-561.
136. R.C. Barik, J.A. Wharton, R.J.K. Wood, and K.R. Stokes, "Electro-Mechanical Interactions During Erosion-Corrosion", Wear, 267, 11 (2009): pp. 1900-1908.
137. H. Rincon, E.F. Rybicki, K.P. Roberts, and J.R. Shadley, "Erosion-Corrosion of Carbon Steel in CO2 Saturated Multiphase Flows Containing Sand", CORROSION 2006, (San Diego Ca, 2006).
138. M. Tandon, V. Jovancicevic, S. Ramachandran, J.R. Shadley, K.P. Roberts, and E.F. Rybicki, "Flow Loop Studies of Inhibition of Erosion-Corrosion in CO_2 Environments with Sand", CORROSION 2006, (San Diego Ca, 2006).
139. J.R. Shadley, S.A. Shirazi, E. Dayalan, M. Ismail, and E.F. Rybicki, "Erosion-Corrosion of a Carbon Steel Elbow in a Carbon Dioxide Environment", Corrosion, 52, 9 (1996): pp. 714-723.
140. J.R. Shadley, S.A. Shirazi, E. Dayalan, and E.F. Rybicki, "Using an Inhibitor to Combat Erosion-Corrosion in Carbon Steel Piping - How Much Does it Help?", Offshore Technology Conference, (Houston, Texas, 1996).
141. J.R. Shadley, S.A. Shirazi, E. Dayalan, and E.F. Rybicki, "Prediction of Erosion-Corrosion Penetration Rate in a CO_2 Environment With Sand", CORROSION 98, (San Diego, CA:NACE, 1998).
142. C. Wang, A. Neville, S. Ramachandran, and V. Jovancicevic, "Alleviation of Erosion-Corrosion Damage by Liquid-Sand Impact Through use of Chemicals", Wear, 258, 1-4 (2005): pp. 649-658.
143. X. Hu, A. Neville, J. Wells, and V.D. Souza, "Prediction of Erosion-Corrosion in Oil and Gas - A Systematic Approach", CORROSION 2008, paper no. 540, (New Orleans, LA: NACE, 2008).
144. X. Hu and A. Neville, "CO_2 Erosion-Corrosion of Pipeline Steel (API X65) in Oil and Gas Conditions - A Systematic Approach", Wear, 267, 11 (2009): pp. 2027-2032.
145. S.S. Rajahram, T.J. Harvey, and R.J.K. Wood, "Evaluation of a Semi-Empirical Model in Predicting Erosion-Corrosion", Wear, 267, 11 (2009): pp. 1883-1893.
146. S.S. Rajahram, T.J. Harvey, and R.J.K. Wood, "Erosion-Corrosion Resistance of Engineering Materials in Various Test Conditions", Wear, 267, 1-4 (2009): pp. 244-254.
147. R.J.K. Wood, "Erosion-Corrosion Interactions and their Effect on Marine and Offshore Materials", Wear, 261, 9 (2006): pp. 1012-1023.
148. S.S. Rajahram, T.J. Harvey, and R.J.K. Wood, "Electrochemical Investigation of Erosion-Corrosion using a Slurry Pot Erosion Tester", Tribology International, 44, 3 (2011): pp. 232-240.
149. F.M. Al-Mutahar, K.P. Roberts, S.A. Shirazi, E.F. Rybicki, and J.R. Shadley, "Modeling and Experiments of $FeCO_3$ Scale Growth and Removal for Erosion-Corrosion Conditions", CORROSION 2012, paper no. 132, (Salt Lake City, UT:NACE, 2012).
150. B. Bozzini, M.E. Ricotti, M. Boniardi, and C. Mele, "Evaluation of Erosion-Corrosion in Multiphase Flow via CFD and Experimental Analysis", Wear, 255, 1-6 (2003): pp. 237-245.

151. A. Keating and S. Nesic, "Numerical Prediction of Erosion-Corrosion in Bends", CORROSION 2000, (Orlando, FL: NACE, 2000).
152. V.S. Sastri, *Corrosion Inhibitors: Principles and Applications*. 1998: Wiley.
153. O.M. Magnussen, Corrosion Protection by Inhibition, in Encyclopedia of Electrochemistry. 2007, Wiley-VCH Verlag GmbH & Co. KGaA.
154. C.C. Nathan, ed. Corrosion Inhibitors. 1973, NACE: Houston, Texas.
155. B. Sanyal, "Organic Compounds as Corrosion Inhibitors in Different Environments - A Review", Progress in Organic Coatings, 9, 2 (1981): pp. 165-236.
156. P. Altoé, G. Pimenta, C.F. Moulin, S.L. Díaz, and O.R. Mattos, "Evaluation of Oilfield Corrosion Inhibitors in CO_2 Containing Media: A Kinetic Study", Electrochimica Acta, 41, 7-8 (1995): pp. 1165-1172.
157. S. Ramachandran, V. Jovancicevic, J. Bassett, and Y.S. Ahn, "Further Advances in the Development of Erosion-Corrosion Inhibitors", CORROSION 2005, paper no. 292, (Houston, TX: NACE, 2005).
158. S. Ramachandran and V. Jovancicevic, "Molecular Modeling of the Inhibition of Mild Steel CO2 Corrosion by Imidazolines", CORROSION 98, (San Diego Ca, 1998).
159. S. Ramachandran, S. Campbell, and M.B. Ward, "Interactions and Properties of Corrosion Inhibitors with By-Product Layers", Corrosion Science, 57, 6 (2001): pp. 508-515.
160. S. Ramachandran, K.A. Bartrip, C. Menendez, and S. Coscio, "Preventing Erosion and Erosion Corrosion Using Specialty Chemicals", International Symposium on Oilfield Chemistry, (Houston, TX: SPE International Symposium of Oilfield Chemistry, 2003).
161. R. Jasinski, "Corrosion of Low-Alloy Steel in Crude Oil/Brine/CO_2 Mixtures", Surfaces, Inhibitors and Passivation, 86-87, (1986): pp. 139-148.
162. C. Wang, A. Neville, and S. Ramachandran, "Understanding Inhibitor Action on Components of Erosion, Corrosion and their Interactions in CO_2-Containing Slurries", SPE International Symposium on Oilfield Corrosion, (Aberdeen, United Kingdom, 2004).
163. C. Wang and A. Neville, "Inhibitor Performance on Corrosion and Erosion/Corrosion Under Turbulent Flow With Sand and CO_2 - An AC Impedance Study", SPE Production & Operations, 23, 2 (2008): pp. 215-220.
164. C. Wang and A. Neville, "Study of the Effect of Inhibitors on Erosion-Corrosion in CO_2-Saturated Condition with Sand", SPE Projects, Facilities & Construction, 4, 1 (2009): pp. 1-10.
165. A. Neville, S. Ramachandran, and V. Jovancicevic, "Erosion-Corrosion Mitigation Using Chemicals", CORROSION 2003, (San Diego, CA: NACE, 2003).
166. K.C. Tummala, K.P. Roberts, J.R. Shadley, E.F. Rybicki, and S.A. Shirazi, "Effect of Sand Production and Flow Velocity on Corrosion Inhibition under Scale Forming Conditions", CORROSION 2009, paper no. 474, (Atlanta, GA: NACE, 2009).
167. C. Wang, S. Ramachandran, and A. Neville, "Understanding the Action of Inhibitors in Mitigating Erosion-Corrosion in Impinging Flows", CORROSION 2004, paper no. 658, (New Orleans, LA: NACE, 2004).
168. B. Mishra, S. Al-Hassan, D.L. Olson, and M.M. Salama, "Development of a Predictive Model for Activation-Controlled Corrosion of Steel in Solutions Containing Carbon Dioxide", Corrosion Science, 53, 11 (1997): pp. 852-859.
169. K.D. Efird, J.A. Boros, T.G. Hailey, and E.J. Wright, "Correlation of Steel Corrosion in Pipe Flow with Jet Impingement and Rotating Cylinder Tests", Corrosion, 49, 12 (1993): pp. 992-1003.

170. S. Hassani, K.P. Roberts, S.A. Shirazi, E.F. Rybicki, J.R. Shadley, and C. Joia, "Characterization and Prediction of Chemical Inhibition Performance for Erosion-Corrosion Conditions in Sweet Oil and Gas Production", CORROSION 2012, paper no. 1122, (Salt Lake City, TX: NACE, 2012).
171. B. Hedges and L. McVeigh, "The Role of Acetate in CO2 Corrosion: The Double Whammy", CORROSION 99, (San Antonio, Tx, 1999).
172. NDT Resource Center, ""Basic Principles of Ultrasonic Testing", Available: http://www.ndt-ed.org/EducationResources/CommunityCollege/Ultrasonics/Introduction/description.htm, Last accessed 20th Jan 2012".
173. ASTM-G1-03, "Standard Practice for Preparing, Cleaning and Evaluating Corrosion Test Specimens", (West Conshohocken, PA: ASTM, 2011).
174. E. Gulbrandsen, S. Nesic, S.M. Hesjevik, S. Skjfrve, B. Sundfer, T. Burchardt, and A. Stangeland, "Effect of Pre-Corrosion on the Performance of Inhibitors for CO_2 Corrosion of Carbon Steel", CORROSION 98, paper no. 13, (San Diego, CA: NACE, 1998).
175. K.D. Efird, "Flow Accelerated Corrosion Testing Basics", CORROSION 2006, paper no. 689, (San Diego, CA: NACE, 2006).
176. K.D. Efird, "Jet Impingement Testing for Flow Accelerated Corrosion", CORROSION 2000, paper no. 52, (Orlando, FL: NACE, 2000).
177. D.C. Silverman, "Technical Note: Conditions for Similarity of Mass-Transfer Coefficients and Fluid Shear Stresses between the Rotating Cylinder Electrode and Pipe", Corrosion, 61, 6 (2005): pp. 515-518.
178. D.C. Silverman, "Technical Note: Simplified Equation for Simulating Velocity-Sensitive Corrosion in the Rotating Cylinder Electrode at Higher Reynolds Numbers", Corrosion, 59, 3 (2003): pp. 207-211.
179. D.C. Silverman, "Technical Note: On Estimating Conditions for Simulating Velocity-Sensitive Corrosion in the Rotating Cylinder Electrode", Corrosion, 55, 12 (1999): pp. 1115-1118.
180. J. Tu, G.H. Yeoh, and C. Liu, *Computational Fluid Dynamics: A Practical Approach*. 2008: Butterworth-Heinemann.
181. A. Gnanavelu, *A Geometry Independant Integrated Method to Predict Erosive Wear Rates in a Slurry Environment*, in *School of Mechanical Engineering*. 2010, University of Leeds.
182. M.D. Deshpande and R.N. Vaishnav, "Submerged Laminar Jet Impingement on a Plane", Journal of Fluid Mechanics, 114, (1982): pp. 213-236.
183. F. Giralt and O. Trass, "Mass Transfer from Crystalline Surfaces in a Turbulent Impinging Jet Part I. Transfer by Erosion", The Canadian Journal of Chemical Engineering, 53, 5 (1975): pp. 505-511.
184. F. Giralt, C.-J. Chia, and O. Trass, "Characterization of the Impingement Region in an Axisymmetric Turbulent Jet", Industrial & Engineering Chemistry Fundamentals, 16, 1 (1977): pp. 21-28.
185. E. Gulbrandsen, R. Nyborg, T. Loeland, and K. Nisancioglu, "Effect of Steel Microstructure and Composition on Inhibition of CO_2 Corrosion", CORROSION 2000, (Orlando, FL:NACE, 2000).
186. S. Nesic, W. Wilhelmsen, S. Skjerve, and S. Hesjevik, "Testing of Inhibitors for CO_2 Corrosion Using Electrochemical Techniques", Proceedings of the 8th European Symposium on Corrosion Inhibitors, (Ann. Univ. Ferrara, N.S., Sez. V, Suppl. N. 10, 1995).
187. M. Stern and A.L. Geary, "Electrochemical Polarization: A Theoretical Analysis of the Shape of Polarization Curves", Journal of the Electrochemical Society, 104, 1 (1957): pp. 56-63.
188. F. Farelas, M. Galicia, B. Brown, S. Nesic, and H. Castaneda, "Evolution of Dissolution Processes at the Interface of Carbon Steel Corroding in a CO_2 Environment Studied by EIS", Corrosion Science, 52, 2 (2010): pp. 509-517.

189. D.A. López, W.H. Schreiner, S.R. de Sánchez, and S.N. Simison, "The Influence of Carbon Steel Microstructure on Corrosion Layers: An XPS and SEM Characterization", Applied Surface Science, 207, 1-4 (2003): pp. 69-85.
190. H.J. Cleary and N.D. Greene, "Electrochemical Properties of Fe and Steel", Corrosion Science, 9, 1 (1969): pp. 3-13.
191. P. Li, T.C. Tan, and J.Y. Lee, "Impedance Spectra of the Anodic Dissolution of Mild Steel in Sulfuric Acid", Corrosion Science, 38, 11 (1996): pp. 1935-1955.
192. W. Li, Q. He, C. Pei, and B. Hou, "Experimental and Theoretical Investigation of the Adsorption behaviour of New Triazole Derivatives as Inhibitors for Mild Steel Corrosion in Acid Media", Electrochimica Acta, 52, 22 (2007): pp. 6386-6394.
193. G.A. Zhang and Y.F. Cheng, "Corrosion of X65 Steel in CO_2-saturated Oilfield Formation Water in the Absence and Presence of Acetic Acid", Corrosion Science, 51, 8 (2009): pp. 1589-1595.
194. G.A. Zhang and Y.F. Cheng, "On the Fundamentals of Electrochemical Corrosion of X65 Steel in CO_2-containing Formation Water in the Presence of Acetic Acid in Petroleum Production", Corrosion Science, 51, 1 (2009): pp. 87-94.
195. D.C. Silverman, "Corrosion Rate Estimation from Pseudo-Inductive Electrochemical Impedance Response", Corrosion Science, 45, 10 (1989): pp. 824-830.
196. R. deMarco, A. Jefferson, W. Durnie, A. Crawford, and B. Kinsella, "Persistence of Carbon Dioxide Corrosion Inhibitors", Corrosion, 58, 4 (2002): pp. 354-363.
197. Y.J. Tan, S. Bailey, and B. Kinsella, "An Investigation of the Formation and Destruction of Corrosion Inhibitor Films using Electrochemical Impedance Spectroscopy (EIS)", Corrosion Science, 38, 9 (1996): pp. 1545-1561.
198. D.A. López, S.N. Simison, and S.R. de Sánchez, "Inhibitors Performance in CO_2 Corrosion: EIS Studies on the Interaction between their Molecular Structure and Steel Microstructure", Corrosion Science, 47, 3 (2005): pp. 735-755.
199. J.-B. Jorcin, M.E. Orazem, N. Pebere, and B. Tribollet, "CPE Analysis by Local Electrochemical Impedance Spectroscopy", Electrochimica Acta, 51, 8-9 (2006): pp. 1473-1479.
200. U. Rammelt and G. Reinhard, "The Influence of Surface Roughness on the Impedance Data for Iron Electrodes in Acid Solutions", Corrosion Science, 27, 4 (1987): pp. 373-382.
201. A. Popova, S. Raicheva, E. Sokolova, and M. Christov, "Frequency Dispersion of the Interfacial Impedance at Mild Steel Corrosion in Acid Media in the Presence of Benzimidazole Derivatives", Langmuir, 12, 8 (1996): pp. 2083-2089.
202. R.D. Armstrong and R.A. Burnham, "The Effect of Roughness on the Impedance of the Interface between a Solid Electrolyte and a Blocking Electrode", Journal of Electroanalytical Chemistry and Interfacial Electrochemistry, 72, 3 (1976): pp. 257-266.
203. J. Pang, A. Briceno, and S. Chander, "A Study of Pyrite/Solution Interface by Impedance Spectroscopy", Journal of The Electrochemical Society, 137, 11 (1990): pp. 3447-3455.
204. K. Juttner, "Electrochemical Impedance Spectroscopy (EIS) of Corrosion Processes on Inhomogeneous Surfaces", Electrochimica Acta, 35, 10 (1990): pp. 1501-1508.
205. A. Popova, E. Sokolova, S. Raicheva, and M. Christov, "AC and DC Study of the Temperature Effect on Mild Steel Corrosion in Acid Media in the

Presence of Benzimidazole Derivatives", Corrosion Science, 45, 1 (2003): pp. 33-58.
206. M. Elayyachy, A. El Idrissi, and B. Hammouti, "New Thio-Compounds as Corrosion Inhibitor for Steel in 1M HCl", Corrosion Science, 48, 9 (2006): pp. 2470-2479.
207. F. Bentiss, M. Lebrini, M. Lagrenee, M. Traisnel, A. Elfarouk, and H. Vezin, "The Influence of Some New 2,5-disubstituted 1,3,4-thiadiazoles on the Corrosion Behaviour of Mild Steel in 1M HCl Solution: AC Impedance Study and Theoretical Approach", Electrochimica Acta, 52, 24 (2007): pp. 6865-6872.
208. M. Outirite, M. Lagrenee, M. Lebrini, M. Traisnel, C. Jama, H. Vezin, and F. Bentiss, "AC Impedance, X-ray Photoelectron Spectroscopy and Density Functional Theory Studies of 3,5-bis(n-pyridyl)-1,2,4-oxadiazoles as Efficient Corrosion Inhibitors for Carbon Steel Surface in Hydrochloric Acid Solution", Electrochimica Acta, 55, 5 (2010): pp. 1670-1681.
209. W.J. Lorenz and F. Mansfeld, "Determination of Corrosion Rates by Electrochemical DC and AC Methods", Corrosion Science, 21, 9-10 (1981): pp. 647-672.
210. I. Epelboin, M. Keddam, and H. Takenouti, "Use of Impedance Measurements for the Determination of the Instant Rate of Metal Corrosion", Journal of Applied Electrochemistry, 2, 1 (1972): pp. 71-79.
211. I. Epelboin, M. Keddam, and J.C. Lestrade, "Faradaic Impedances and Intermediates in Electrochemical Reactions", Faraday Discussions of the Chemical Society, 56, (1973): pp. 264-275.
212. Argentum Solutions Inc., "Tutorial on Electrochemical Impedance Spectroscopy", Available: http://www.argentumsolutions.com/tutorials/impedance_tutorialpg5.html, Last accessed 4th October 2011.
213. A.A. Aksut, W.J. Lorenz, and F. Mansfeld, "The Determination of Corrosion Rates by Electrochemical D.C. and A.C. Methods - Systems with Discontinuous Steady State Polarization Behavior", Corrosion Science, 22, 7 (1982): pp. 611-619.
214. E. Stupnišek-Lisac, S. Podbrščček, and T. Sorić, "Non-Toxic Organic Zinc Corrosion Inhibitors in Hydrochloric Acid", Journal of Applied Electrochemistry, 24, 8 (1994): pp. 779-784.
215. R.D. Marco, A. Jefferson, B. Kinsella, and W. Durnie, "Surface Analysis of Adsorbed Carbon Dioxide Corrosion Inhibitors", Corrosion, 57, 01 (2001).
216. M. Ozcan, Ä. Dehri, and M. Erbil, "Organic Sulphur-Containing Compounds as Corrosion Inhibitors for Mild Steel in Acidic Media: Correlation between Inhibition Efficiency and Chemical Structure", Applied Surface Science, 236, 1-4 (2004): pp. 155-164.
217. Y. Chen, T. Hong, M. Gopal, and W.P. Jepson, "EIS Studies of a Corrosion Inhibitor Behavior under Multiphase Flow Conditions", Corrosion Science, 42, 6 (2000): pp. 979-990.
218. M. Salasi, T. Shahrabi, E. Roayaei, and M. Aliofkhazraei, "The Electrochemical Behaviour of Environment-Friendly Inhibitors of Silicate and Phosphonate in Corrosion Control of Carbon Steel in Soft Water Media", Materials Chemistry and Physics, 104, 1 (2007): pp. 183-190.
219. H. Wang, W.P. Jepson, T. Hong, C. Kang, and H. Shi, "Characterization of Inhibitor and Corrosion Product Film Using Electrochemical Impedance Spectroscopy (EIS)", CORROSION 2001, paper no. 23, (Houston, TX:NACE, 2001).
220. M. Kissi, M. Bouklah, B. Hammouti, and M. Benkaddour, "Establishment of Equivalent Circuits from Electrochemical Impedance Spectroscopy Study of

Corrosion Inhibition of Steel by Pyrazine in Sulphuric Acidic Solution", Applied Surface Science, 252, 12 (2006): pp. 4190-4197.
221. M. Lagrenee, B. Mernari, M. Bouanis, M. Traisnel, and F. Bentiss, "Study of the Mechanism and Inhibiting Efficiency of 3,5-bis(4-methylthiophenyl)-4H-1,2,4-triazole on Mild Steel Corrosion in Acidic Media", Corrosion Science, 44, 3 (2002): pp. 573-588.
222. M. Mahdavian and S. Ashhari, "Corrosion Inhibition Performance of 2-mercaptobenzimidazole and 2-mercaptobenzoxazole Compounds for Protection of Mild Steel in Hydrochloric Acid Solution", Electrochimica Acta, 55, 5 (2010): pp. 1720-1724.
223. F. Bentiss, M. Traisnel, N. Chaibi, B. Mernari, H. Vezin, and M. Lagrenee, "2,5-Bis(n-methoxyphenyl)-1,3,4-oxadiazoles used as Corrosion Inhibitors in Acidic Media: Correlation between Inhibition Efficiency and Chemical Structure", Corrosion Science, 44, 10 (2002): pp. 2271-2289.
224. B. Mernari, H. El Attari, M. Traisnel, F. Bentiss, and M. Lagrenee, "Inhibiting Effects of 3,5-bis(n-pyridyl)-4-amino-1,2,4-triazoles on the Corrosion for Mild Steel in 1 M HCl Medium", Corrosion Science, 40, 2-3 (1998): pp. 391-399.
225. F. Bentiss, M. Lagrenee, M. Traisnel, and J.C. Hornez, "The Corrosion Inhibition of Mild Steel in Acidic Media by a New Triazole Derivative", Corrosion Science, 41, 4 (1999): pp. 789-803.
226. F. Bentiss, M. Traisnel, L. Gengembre, and M. Lagrenee, "A New Triazole Derivative as Inhibitor of the Acid Corrosion of Mild Steel: Electrochemical Studies, Weight Loss Determination, SEM and XPS", Applied Surface Science, 152, 3-4 (1999): pp. 237-249.
227. F. Bentiss, M. Traisnel, L. Gengembre, and M. Lagrenee, "Inhibition of Acidic Corrosion of Mild Steel by 3,5-diphenyl-4H-1,2,4-triazole", Applied Surface Science, 161, 1-2 (2000): pp. 194-202.
228. J.L. Mora-Mendoza and S. Turgoose, "Fe_3C Influence on the Corrosion Rate of Mild Steel in Aqueous CO_2 Systems under Turbulent Flow Conditions", Corrosion Science, 44, 6 (2002): pp. 1223-1246.
229. J.R. Park and D.D. Macdonald, "Impedance Studies of the Growth of Porous Magnetite Films on Carbon Steel in High Temperature Aqueous Systems", Corrosion Science, 23, 4 (1983): pp. 295-315.
230. X. Tang, L.Y. Xu, and Y.F. Cheng, "Electrochemical Corrosion Behaviour of X-65 Steel in the Simulated Oil-Sand Slurry. II: Synergism of Erosion and Corrosion", Corrosion Science, 50, 5 (2008): pp. 1469-1474.
231. J. Pacheco, F.C. Ibrahim, and R. Franco, "Testing Requirements of Corrosion Inhibitor Qualification for Pipeline Applications", CORROSION 2010, paper no. 325, (San Antonio, TX: NACE, 2010).
232. A. Crossland, R. Woollam, J. Vera, J. Palmer, G. John, and S. Turgoose, "Corrosion Inhibitor Efficiency Limits and Key Factors", CORROSION 2011, paper no. 62, (Houston, TX: NACE, 2011).
233. J. Marsh and T. Teh, "Conflicting Views - CO_2 Corrosion Models and Corrosion Inhibitor Availability Philosohies - The Influence on Subsea Systems And Pipelines Design", Offshore Europe, (Aberdeen, Scotland, U.K., 2007).
234. I.J. Rippon, "Carbon Steel Pipeline Corrosion Engineering: Life Cycle Approach", CORROSION 2001, (Houston, TX:NACE, 2001).
235. B. Hedges, D. Paisley, and R.C. Woollam, "The Corrosion Inhibitor Availability Model", CORROSION 2000, paper no. 34, (Orlando, FL:NACE, 2000).
236. Serene Energy, "Technical Overview on Oil and Gas Production - Causes of Sand Production", Available: http://www.i.sereneenergy.org/i/Causes-of-Sand-Production.html, Last accessed 16th August 2012.

237. G. Schmitt and M. Mueller, "Critical Wall Shear Stresses in CO_2 Corrosion of Carbon Steel", CORROSION 99, paper no. 44, (San Antonio, TX: NACE, 1999).
238. F. Donahue, A. Akiyama, and K. Nobe, "Theory of Organic Corroison Inhibitors Part 2: Solutions Containing Ring-Substituted Anilines", Journal of The Electrochemistry Society, 144, 10 (1967): pp. 1006-1011.
239. K. Babic-Samardzija, C. Lupu, N. Hackerman, A.R. Barron, and A. Luttge, "Inhibitive Properties and Surface Morphology of a Group of Heterocyclic Diazoles as Inhibitors for Acidic Iron Corrosion", Langmuir, 21, 26 (2005): pp. 12187-12196.
240. "Gamry Instruments., "Basics of Electrochemical Impedance Spectroscopy", Available: http://www.gamry.com/application-notes/EIS/, Last accessed 8th November 2012".
241. M. Uematsu and E. Franck, *Static dielectric constant of water and steam*. 1981: American Chemical Society and the American Institute of Physics for the National Bureau of Standards.
242. P. Bommersbach, C. Alemany-Dumont, J.P. Millet, and B. Normand, "Formation and Behaviour Study of an Environment-Friendly Corrosion Inhibitor by Electrochemical Methods", Electrochimica Acta, 51, 6 (2005): pp. 1076-1084.
243. G. Schmitt, "Drag Reduction by Corrosion Inhibitors – A Neglected Option for Mitigation of Flow Induced Localized Corrosion", Materials and Corrosion, 52, 5 (2001): pp. 329-343.
244. L.D. Paolinelli, T. Pérez, and S.N. Simison, "The Effect of Pre-Corrosion and Steel Microstructure on Inhibitor Performance in CO_2 Corrosion", Corrosion Science, 50, 9 (2008): pp. 2456-2464.
245. J.W. Palmer, "Corrosion Control by Film Forming Inhibitors", CORROSION 2006, paper no. 119, (San Diego, CA:NACE, 2006).
246. A.J. McMahon, L. Harris, and J.W. Martin, "Effects of Sand and Interfacial Adsorption Loss on Corrosion Inhibitor Efficiency", CORROSION 2005, (Houston, TX: NACE, 2005).
247. A. Suzuki, Y. Kebukawa, S. Nakashima, L.P. Keller, M.E. Zolensky, and T. Nakamura, "Infrared Micro-spectroscopy of Organic and Hydrous Components in Some Antarctic Micrometeorites", Lunar and Planetary Science, 36, (2005).
248. W.H. Durnie, B.J. Kinsella, R. de Marco, and A. Jefferson, "A Study of the Adsorption Properties of Commercial Carbon Dioxide Corrosion Inhibitor Formulations", Journal of Applied Electrochemistry, 31, 11 (2001): pp. 1221-1226.
249. A. Durdureanu-Angheluta, R. Ardeleanu, M. Pinteala, V. Harabagiu, H. Chiriac, and B.C. Simionescu, "Silane Covered Magnetite Particles. Preparation and Characterization", Digest Journal of Nanomaterials and Biostructures, 3, 1 (2008): pp. 33-40.
250. G.D. Chukin and V.I. Malevich, "Infrared Spectra of Silica", Journal of Applied Spectroscopy, 26, 2 (1977): pp. 223-229.
251. J.Z. Ai, X.P. Guo, J.E. Qu, Z.Y. Chen, and J.S. Zheng, "Adsorption Behaviour and Synergistic Mechanism of a Cationic Inhibitor and KI on the Galvanic Electrode", Colloids and Surfaces A: Physicochemical and Engineering Aspects, 281, 1-3 (2006): pp. 147-155.
252. J. Ai and X. Guo, "AFM and FTIR Studies of Organic Cation Adsorption on Carbon Steel Coupled with Stainless Steel", Surface and Interface Analysis, 38, 8 (2006): pp. 1218-1222.
253. W. Durnie, R.D. Marco, A. Jefferson, and B. Kinsella, "Development of a Structure-Activity Relationship for Oil Field Corrosion Inhibitors", Journal of The Electrochemical Society, 146, 5 (1999): pp. 1751-1756.

254. J.Z. Ai, X.P. Guo, and Z.Y. Chen, "The Adsorption Behaviour and Corrosion Inhibition Mechanism of Anionic Inhibitor on Galvanic Electrode in 1% NaCl Solution", Applied Surface Science, 253, 2 (2006): pp. 683-688.
255. R. Zvauya and J.L. Dawson, "Inhibition Studies in Sweet Corrosion Systems by a Quaternary Ammonium Compound", Journal of Applied Electrochemistry, 24, 9 (1994): pp. 943-947.
256. W. Durnie and M. Gough, "Characterization, Isolation and Performance Characteristics of Imidazolines: Part II Development of Structure - Activity Relationships", CORROSION 2003, paper no. 336, (San Diego, CA: NACE, 2003).
257. M. Gough, B.M. Hedges, W. Durnie, and L. Auty, "Characterization, Isolation and Performance Characteristics of Imidazolines", CORROSION 2002, (Denver, Co, 2002).
258. V. Jovancicevic, S. Ramachandran, and P. Prince, "Inhibition of Carbon Dioxide Corrosion of Mild Steel by Imidazolines and Their Precursors", Corrosion, (1999).
259. W. Durnie, R.D. Marco, B. Kinsella, A. Jefferson, and B. Pejcic, "Predicting the Adsorption Properties of Carbon Dioxide Corrosion Inhibitors Using a Structure-Activity Relationship", Journal of The Electrochemical Society, 152, 1 (2005): pp. B1-B11.
260. W. Durnie, "Modeling the Functional Behavior of Corrosion Inhibitors", CORROSION 2004, paper no. 401, (New Orleans, LA: NACE, 2004).
261. W. Durnie, M. Gough, and H.D. Reus, "Development of Corrosion Inhibitors to Address under Deposit Corrosion in Oil and Gas Production Systems", CORROSION 2005, (Houston, Tx, 2005).
262. F. Bentiss, M. Lebrini, and M. Lagrenee, "Thermodynamic Characterization of Metal Dissolution and Inhibitor Adsorption Processes in Mild Steel/2,5-bis(n-thienyl)-1,3,4-thiadiazoles/Hydrochloric Acid System", Corrosion Science, 47, 12 (2005): pp. 2915-2931.
263. D.J. Shaw, *Introduction to Colloid and Surface Chemistry*. 1992: Butterworth-Heinemann.
264. N. Ohno, J. Uehara, and K. Aramaki, "A SERS Study on Adsorption of Dibenzyl Disulfide, Sulfide, and Sulfoxide on an Iron-Deposited Silver Electrode in a Hydrochloric Acid Solution", Journal of The Electrochemical Society, 140, 9 (1993): pp. 2512-2519.
265. J. Uehara and K. Aramaki, "A Surface-Enhanced Raman Spectroscopy Study on Adsorption of Some Sulfur-Containing Corrosion Inhibitors on Iron in Hydrochloric Acid Solutions", Journal of The Electrochemical Society, 138, 11 (1991): pp. 3245-3251.
266. A. Kudelski, "Chemisorption of 2-Mercaptoethanol on Silver, Copper, and Gold: Direct Raman Evidence of Acid-Induced Changes in Adsorption/Desorption Equilibria", Langmuir, 19, 9 (2003): pp. 3805-3813.
267. N. Sheppard, "The Vibrational Spectra of Some Organic Sulphur Compounds and the Characteristic Frequencies of C-S Linkages", Transactions of the Faraday Society, 46, (1950): pp. 429-439.
268. G.A. Crowder, "The C-S Stretching Frequency in Thiol Acids and Esters", Appl. Spectrosc., 26, 4 (1972): pp. 486-487.
269. V.V. Tarabara, I.R. Nabiev, and A.V. Feofanov, "Surface-Enhanced Raman Scattering (SERS) Study of Mercaptoethanol Monolayer Assemblies on Silver Citrate Hydrosol. Preparation and Characterization of Modified Hydrosol as a SERS-Active Substrate", Langmuir, 14, 5 (1998): pp. 1092-1098.
270. A.-M. Fuller, F. Mackay, C. Mackenzie, C. Rowley-Williams, V. Magdalenic, and E. Perfect, "Applying Biochemistry Concepts to the Analysis of Oilfield

Produced Fluids", SPE Annual Technical Conference and Exhibition, (New Orleans, Louisiana, 2009).
271. C.J. Glover and J.A. Bullin, "Identification of Heavy Residual Oils by GC and GC-MS", Journal of Environmental Science and Health. Part A: Environmental Science and Engineering, 24, 1 (1989): pp. 57-75.
272. M.A. Gough and G.J. Langley, "Analysis of Oilfield Chemicals by Electrospray-Mass Spectrometry", Rapid Communications in Mass Spectrometry, 13, 4 (1999): pp. 227-236.
273. R.M. de Souza, A.L. Saraceno, C.L.P. da Silveira, and R.Q. Aucelio, "Determination of Trace Elements in Crude Oil by ICP-OES using Ultrasound-Assisted Acid Extraction", Journal of Analytical Atomic Spectrometry, 21, 11 (2006): pp. 1345-1349.
274. G.M. Graham, K.S. Sorbie, L.S. Boak, K. Taylor, and L. Blilie, "Development and Application of Accurate Detection and Assay Techniques for Oilfield Scale Inhibitors in Produced Water Samples", SPE International Symposium on Oilfield Chemistry, (San Antonio, Texas, 1995).
275. R.K. Henderson, A. Baker, K.R. Murphy, A. Hambly, R.M. Stuetz, and S.J. Khan, "Fluorescence as a Potential Monitoring Tool for Recycled Water Systems: A Review", Water Research, 43, 4 (2009): pp. 863-881.
276. A.-M. Fuller, F. Mackay, C.D. Mackenzie, C. Rowley-Williams, and E. Perfect, "Development of New Chemical Additive Detection Methods Inspired by the Life Sciences", SPE International Symposium on Oilfield Chemistry, (The Woodlands, Texas, USA, 2011).
277. K. Kuwata, M. Uebori, K. Yamada, and Y. Yamazaki, "Liquid Chromatographic Determination of Alkylthiols via Derivatization with 5,5'-dithiobis(2-nitrobenzoic acid)", Analytical Chemistry, 54, 7 (1982): pp. 1082-1087.
278. Thermo Scientific, "Instructions - Ellman's Reagent, Available: www.piercenet.com/instructions/2160311.pdf, Last accessed 29th November 2011".
279. M. Child, M. Heywood, and G. Yong, "Bronsted Acidity of Silanol Groups on Silica Immersed in Carbon Tetrachloride", J. Chem. Soc., Faraday Trans, 78, 1 (1981): pp. 2005-2010.
280. W. Pohle and P. Fink, "IR-spektroskopische Charakterisierung der Oberflochenkomplexe bei der Pyridinadsorption an Chemisch Modifiziertem SiO2 (Aerosil)", Zeitschrift fur Physikalische Chemie, 109, 2 (1978): pp. 205-220.
281. R. Lowry and I. Tinsley, "Rapid Colorimetric Determination of Free Fatty Acids", Journal of the American Oil Chemists' Society, 53, 7 (1976): pp. 470-472.
282. D. Kwon and J. Rhee, "A Simple and Rapid Colorimetric Method for Determination of Free Fatty Acids for Lipase Assay", Journal of the American Oil Chemists' Society, 63, 1 (1986): pp. 89-92.
283. T. Szauer and A. Brandt, "On the Role of Fatty Acid in Adsorption and Corrosion Inhibition of Iron by Amine-Fatty Acid Salts in Acidic Solution", Electrochimica Acta, 26, 9 (1981): pp. 1257-1260.
284. J.W. Munson and R. Bilous, "Colorimetric Determination of Aliphatic Acids", Journal of Pharmaceutical Sciences, 66, 10 (1977): pp. 1403-1405.
285. S.C. Slack and W.J. Mader, "A Colorimetric Procedure for Imidazolines", Journal of the American Pharmaceutical Association, 46, 12 (1957): pp. 742-744.
286. B. Miksic, A. Furman, and M. Kharshan, "Effectiveness of the Corrosion Inhibitors for the Petroleum Industry under Various Flow Conditions", CORROSION 2009, paper no. 573, (Atlanta, GA:NACE, 2009).